THE UNIVERSITY *of* EDINBURGH

Development of Electrochemical Sensing in Nuclear Pyroprocessing: A Study of the Cerium-Aluminium Binary System with Macro- and Microelectrodes

THE UNIVERSITY *of* EDINBURGH

Simon J. Reeves

2018

"The truth resists simplicity." - John Green

"You're always a little bit wrong." - Hank Green

Lay Summary

Nuclear fission provides a complementary energy source to renewables, meeting the global energy demand, whilst also reducing the amount of carbon dioxide emissions during the phasing out of fossil fuel energy sources. Research into future reactor technologies will also allow for some elements in current nuclear waste to be reused as fuel, significantly increasing the efficiency and the lifetime of nuclear fuel from the current one hundred years of new minable uranium. For this to be achieved, the waste must be processed in order to extract the required elements to generate fuel. This will also have the benefit of reducing the amount and radioactivity of the final waste that must be dealt with.

One of the proposed technologies for this is electrochemical pyroprocessing, which involves the waste being dissolved in a molten (liquid) salt at high temperatures (450 ^{o}C). The desired elements are selectively extracted using electrochemistry: applying a potential (voltage) or a current, to drive deposition of elements onto an electrode. It is very important to understand the fundamentals of these electrochemical processes, as well as have an appropriate electrode to act as a sensor which can monitor the state of the molten salt for process control. A crucial part of this system is to enable the extraction of actinides (e.g. uranium, plutonium and heavier elements which are produced inside the reactor), but not to allow the selective extraction of plutonium, as this could allow nuclear weapons to be produced. This can be achieved by electrochemically depositing these actinides as an alloy into an active metal electrode, which forces the actinides to be extracted together. Of the proposed active metal candidates, aluminium offers the best separation of actinides from other elements, and so is the active metal studied in this thesis.

This thesis studies the cerium-aluminium alloy system, which is a non-radioactive model of the plutonium-aluminium system due to the electrochemical similarity of cerium and plutonium as well as their similar alloying behaviour with aluminium. Macroelectrodes (similar to the electrodes that would be used for the industrial scale deposition), were found to give useful information on the fundamental alloying processes of insertion (cerium deposition into an aluminium electrode) and co-deposition (deposition of cerium and aluminium together onto a non-alloying (inert) electrode). However, alloying on macroelectrodes could not

be used to determine the cerium concentration in the molten salt, which prevents these macroelectrodes from being suitable for sensing and monitoring.

Microelectrodes have improved electrochemical properties which gives them several significant analytical advantages over macroelectrodes. The co-deposition response on microelectrodes was found to be much simpler to analyse than on macroelectrodes, and could be used reliably to determine the cerium concentration in the molten salt, which is desirable for sensing and monitoring. To avoid the need for the addition of aluminium into the molten salt, in-house produced aluminium microelectrodes were also studied. Due to the method of production, the aluminium microelectrodes had a protective surface oxide layer which prevented alloying. This oxide layer could be disrupted electrochemically, which allowed proof of principle studies to be performed which confirmed that these microelectrodes had an improved electrochemical response over macroelectrodes. Further development is required to fully remove this oxide layer, or prevent it from forming initially, in order to study alloying in greater detail with microelectrodes to fully realise their advantages for sensing and monitoring in pyroprocessing.

Abstract

Future nuclear fission reactors (GEN IV) are designed to include fast breeder reactor technologies, which can accept transuranics (elements heavier than uranium) as fuel. This has the potential of being more fuel efficient but requires the closing of the nuclear fuel cycle: full recycling of existing and newly generated nuclear waste to extract uranium and transuranic elements which can be reused as fuel. In the UK a system being investigated is electrochemical pyroprocessing which uses molten LiCl-KCl eutectic (LKE), which aims to recover uranium by electrodeposition on an inert (steel) electrode and the transuranics by electrodeposition as alloys with an active metal electrode (bismuth, cadmium or aluminium). Of the three active metal candidates, aluminium has the best separation efficiency of actinides and lanthanides, which is important as lanthanides are neutron poisons and so are not to be extracted. The development of pyroprocessing requires fundamental understandings of electrochemical alloy formation, as well as on-line monitoring tools to ensure the reprocessing occurs safely and efficiently. To that end, this thesis investigates cerium-aluminium alloying (a non-radioactive model system for plutonium-aluminium) on macro- and microelectrodes to understand the limiting factors during the alloying reaction at each electrode scale and also the circumstances under which the Ce^{3+} concentration can be reliably determined for on-line monitoring.

On a bulk aluminium macroelectrode one cerium-aluminium alloying reaction was observed. This reaction was kinetically limited by the phase change from cerium insertion into the aluminium, and resulted in lattice expansion and progressive roughening of the electrode surface. These factors made it difficult to reliably calculate the Ce^{3+} concentration. Li^{+} from the solution was also able to reduce and form alloys with aluminium, approximately 0.3 V more negative than the first cerium-aluminium alloying peak. Since lithium atoms are smaller than cerium, and there is an abundance of Li^{+} in the salt, lithium-aluminium alloy was found to form preferentially to cerium-aluminium alloy at these more negative potentials.

By co-depositing Al^{3+} and Ce^{3+} together on a tungsten electrode which is inert under these conditions (it does not alloy), the kinetic barrier to alloy formation by cerium insertion was decreased, which is beneficial to studying the thermodynamics of alloying. Studies of pure aluminium plating and pure cerium plating showed

each individual reaction was diffusion limited, with an increased contribution of convection to the mass transport at slow scan rates. Co-deposition on macroelectrodes with a low ratio of $[CeCl_3]$:$[AlCl_3]$ showed only one cerium-aluminium alloying peak. The co-deposition currents, and ratio of oxidation peaks charges, showed that co-deposition was occurring with both species under diffusion control, resulting in an amorphous alloy with a Ce:Al ratio that smoothly varied with the $[CeCl_3]$:$[AlCl_3]$ ratio. This was in contrast to the alloying behaviour of cerium with liquid bismuth, in which co-deposition occurred at specific ratios determined by the crystal phases that could be formed at the applied potentials, with higher co-deposition ratios being achieved at more negative potentials. Co-deposition on macroelectrodes with a high ratio of $[CeCl_3]$:$[AlCl_3]$ could result in up to five cerium-aluminium alloy peaks, corresponding to all five Ce_xAl_y crystalline phases predicted by the phase diagram. This phase change from amorphous to crystalline was promoted by the high Ce:Al ratio in the amorphous alloy resulting from the high $[CeCl_3]$:$[AlCl_3]$ ratio and by plating pure cerium on the surface, which could then insert into the alloy. Charge analysis of these peaks confirmed the expected stoichiometries of the crystal phase from these in-situ measurements which is important for rapid analysis, whereas all previous literature has relied on ex-situ techniques which cooled the alloy, possibly changing its composition and structure. In all circumstances of alloy formation on macroelectrodes, the rate of reduction of Ce^{3+} was time dependent and sensitive to convection. This significantly complicated analysis of the electrochemical signal, making it very difficult to reliably calculate the concentration of Ce^{3+}, which is required for on-line monitoring.

Co-deposition on in-house microfabricated tungsten microelectrodes resulted in steady state currents for both pure aluminium deposition and cerium-aluminium co-deposition (up to the beginning of lithium-aluminium alloying). Thus, unlike on macroelectrodes, the deposition rate occurred at the flux ratio of each species from solution and only one oxidation peak was observed corresponding to the amorphous cerium-aluminium phase, even at high $[CeCl_3]$:$[AlCl_3]$ ratios. The steady state alloying current meant that calculating the Ce^{3+} concentration was relatively simple from co-deposition on microelectrodes.

Co-deposition was highly beneficial for studying alloying, however to avoid the addition of Al^{3+} to the molten salt, in-house microfabricated thin film aluminium microelectrodes were also used to study alloying. Alloying on microfabricated thin film aluminium microelectrodes was hampered by the formation of a native aluminium oxide layer, which prevented cerium insertion into the aluminium. The oxide layer could be disrupted by reduction of lithium, which showed steady state currents (albeit with significant capacitance) could be achieved for alloying by cerium insertion. However, the full surface area of the microelectrode could not be attained and all microelectrodes lost their aluminium layer after multiple lithiation/de-lithiation cycles. These devices need further development to overcome the oxide layer, or prevent its formation, in order to

study alloying in greater detail with aluminium microelectrodes to fully realise their advantages for sensing and monitoring in pyroprocessing.

Declaration

I hereby declare that the work presented in this thesis is my own unless otherwise credited, and that the work has not been submitted for any other degree or professional qualification.

Simon J. Reeves

Acknowledgments

This PhD has, at times, been a stressful experience, and it would have been difficult to get through it without the following people.

First and foremost, thank you to Dr Justin Elliott and Hannah Levene, with whom I have worked closely to discuss ideas, design experiments, and to set-up an entire laboratory.

Thank you to Dr Damion Corrigan, your guidance at the start of my PhD was invaluable to deciding the path of my research.

Thank you to Dr Ewen Blair and Dr Ilka Schmuser for tirelessly fabricating microelectrodes which I promptly destroyed.

Thank you to both past and present residents of the Mount and Campbell groups' office for laughs and bizarre lunchtime conversations: Dr Richard Perry, Dr Charlotte Brady, Dr Andrew Piper, Ugne Mitrikeviciute, Dr Kate Fisher, Dr Hannah Johnston and Katie Ember.

Thank you to the rest of the Mount group: Ahmet Ucar, Dr Dimitrios Kampouris and Dr Eva Gonzalez-Fernandez.

Thank you to my supervisors Professor Andy Mount, Professor Anthony Walton and Dr Mike Harrison for feedback and guidance along the way.

Finally, thank you to my family for support and proofreading, as well as Hannah Paterson and Hannah Blacknell who have remained my good friends even after moving apart since our undergraduate days.

List of Nomenclature

Symbols

α	Transfer coefficient
ν	Scan rate
τ	Time taken for the short circuit reaction to complete
A	Surface area
c	Concentration
c_∞	Bulk concentration
D	Diffusion coefficient
d	Diameter
E	Potential
E^θ	Standard potential
E_f	Fermi level/energy
E_{onset}	Onset potential
E_p	Peak potential
F	Faraday's constant
I	Convolved current of a macroelectrode
i	Current

i_{lim}	Limiting macroelectrode current of one redox species at the onset potential of a second redox species
I_L	Limiting convolved current
i_L	Limiting current of a microelectrode
i_p	Peak current
J	Flux
k	Rate of electron transfer/ Rate of short circuit reaction
k^θ	Standard heterogeneous rate constant
n	Number of electrons
Q	Charge
R	Gas constant/ Apparent resistance
r	Radius
R_s	Solution resistance
T	Temperature
t	Time

Abbreviations

CA	Chronoamperometry/ Chronoamperogram
Ce:Al	Molar ratio of cerium to aluminium in deposited alloy
CV	Cyclic voltammetry/ Cyclic voltammogram
EDX	Energy dispersive x-ray spectroscopy
FP	Fission products
HOMO	Highest occupied molecular orbital
ICP-MS	Inductively coupled plasma mass spectrometry
Li:Al	Molar ratio of lithium to aluminium in deposited alloy

LKE	LiCl-KCl eutectic
LUMO	Lowest unoccupied molecular orbital
mAn	Minor actinides
MOX	Mixed oxide
NNL	National Nuclear Laboratory
OCP	Open circuit potential
PCV	Partial cyclic voltammetry/ Partial cyclic voltammogram
PSTAT	Potentiostat
PUREX	Plutonium Uranium Reduction EXtraction
PWR	Pressurised water reactor
RDE	Rotating disc electrode
RRDE	Rotating ring-disc electrode
TBP	Tributylphosphate
UPS	Uninterruptible power supply
XRD	X-ray diffraction

Contents

Chapter 1

Introduction

1.1 The Need for Nuclear Energy

The worldwide demand for energy is continuously increasing. The demand in 2050 has been estimated to be at least double what it was in 2000.[1,2] At the same time the awareness and impact of global climate change has resulted in many countries seeking alternatives to fossil fuels. Renewable energy sources, e.g. wind and solar, have low CO_2 emissions and are often referred to as low carbon energy sources. However, renewable energy sources are intermittent and will struggle to meet the increasing energy demand alone on a global scale in the timeframe needed to prevent the global average temperature from rising. To that end, nuclear fission is a promising solution for providing base load power (near constant output) with low CO_2 emissions,[3,4] as the predominant sources of carbon emissions are during plant construction and decommissioning.[3] There are, of course, dangers associated with nuclear fission, namely the radioactivity of waste which requires long term storage. There is also often negative public perception of nuclear fission due to nuclear related disasters such as Chernobyl and Fukushima.[5] Despite the public perception, nuclear fission is however actually a much safer energy source than fossil fuels in terms of negative health impacts per unit of energy generated. In order to combat the current dangers of nuclear fission, newer reactor designs, fuel sources and recycling technologies are being investigated in a number of countries such as France, South Korea, USA and the UK. These includes passive safety systems that do not require power to function, as well as being able to close the fuel cycle: fully recycling more of the waste to generate usable fuel, thereby decreasing the volume and radioactivity of waste for geological disposal.

1.2 Nuclear Fission

1.2.1 Conventional (Thermal) Reactors

A nuclear reactor works by bombarding target atoms with neutrons of a particular energy (typically "thermal neutrons", with energies of approximately 25 meV). When the neutron has been captured into the nucleus of the target atom, that new nucleus undergoes fission by which it splits apart into multiple atoms of smaller mass. The total mass of the new atoms will be less than the mass of the target atom, with the excess mass being converted to energy (according to $E = mc^2$) and new neutrons which can cause further fission if captured by another nucleus. Typically in a pressurised water reactor (PWR) the energy released is used to heat water and generate steam, which then drives a turbine producing electrical energy. The resulting lighter elements are called fission products (FP). ^{235}U is the primary isotope used for fission. Naturally occurring uranium contains ^{238}U at 99.3% abundance,[6] which does not readily undergo fission when bombarded with thermal neutrons. Uranium ore is leached with strong acid/alkali and converted to gaseous UF_6. The proportion of ^{235}U is increased from 0.7% to 5% by gas centrifugation, which separates molecules based on differences in mass. The ^{235}U proportion must be controlled so that fission is controlled and occurs at high efficiency.

Once ^{236}U is formed from neutron capture by ^{235}U, there is a probabilistic range of FP. The distribution of FP can be seen in Figure 1.1. The fissioning of a uranium nucleus means that it splits approximately in half. However there are many possible ways for the nucleus to split, generate new atoms of varying sizes, generate neutrons, and excess energy. This is why FP elements have atomic masses either above or below 120, which is roughly half the atomic mass of a uranium atom. The FP themselves are radioactive and therefore undergo radioactive decay once formed. This is termed a nuclear cascade, and again this results in a probabilistic distribution of elements.

Over the lifetime of the fuel the proportion of ^{235}U to ^{238}U decreases, lowering the fuel efficiency. This requires the fuel rods to be replaced in order to maintain a high energy output, despite there still being ^{235}U remaining. Transuranic elements (i.e. of higher atomic numbers) can be formed by the neutron capture of ^{238}U followed by beta decay (termed transmutation) rather than undergoing fission. These are often called the minor actinides (mAn) due to their small percentage in the composition of spent fuel.

The typical distribution of elements in spent fuel from a thermal neutron reactor can be seen in Figure 1.2. The majority is uranium, both ^{238}U and ^{235}U. About 1% are transuranic elements which are the main cause of the radioactivity of the waste as they continue to undergo radioactive decay and have long half lives. The remainder of the waste are the FP. These are the elements which are generated from fission, and by the decay

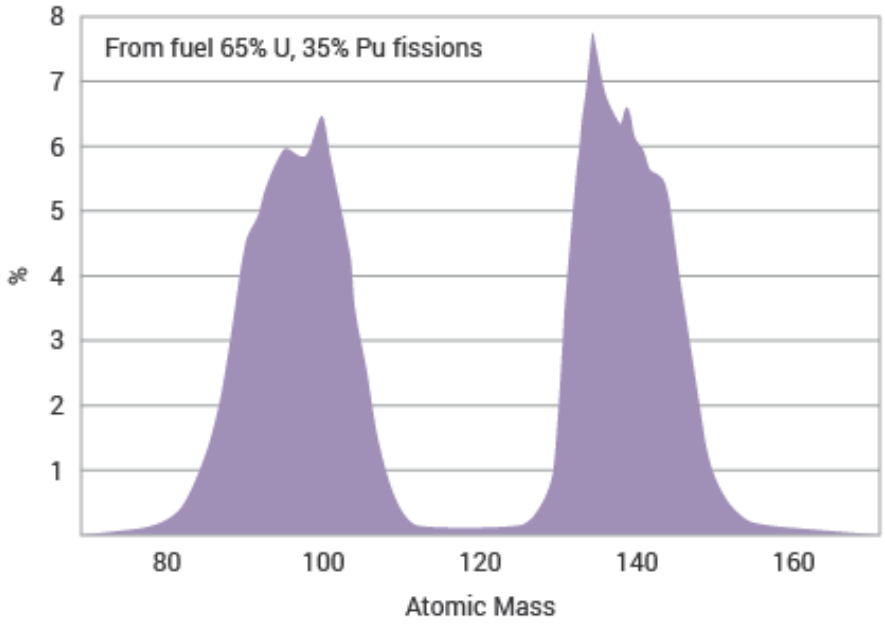

Figure 1.1: The "double-hump" distribution of fission products from ^{235}U using a thermal neutron source. [7]

of transuranics. These elements are also radioactive, as the isotopes generated may be unstable relative to the naturally occurring isotopes. This accounts for a large proportion of the periodic table, and these elements are very difficult to separate efficiently. The radioactivity is however far less than from the transuranics and so can be stored as intermediate level waste, rather than high level waste.

1.2.2 Fast Reactors

The newest reactor technologies (GEN IV) utilise passive safety systems, and aim to minimise waste and increase fuel efficiency by closing the fuel cycle.[9] The other major change in GEN IV reactors is a change to fast and/or breeder reactors. These use fast neutrons (approximately 1 MeV) rather than thermal neutrons (approximately 25 meV). These neutrons are generated from the same source, but now no moderator (which previously was used only to let the thermal neutrons through) is required, which simplifies the reactor design. Fast neutrons can be captured by ^{238}U and long lived transuranics, transmuting them into fissile elements (this is termed breeding if they generate enough new fissile material more quickly than fuel is used up)[10,11] whose FP are much shorter lived than FP from thermal neutron fission.

Fuels for fast reactors are to have plutonium as the major component as it is much more efficient at absorbing fast neutrons than uranium. Plutonium therefore undergoes fission more readily from fast neutrons and also generates more neutrons per fission event. This allows more energy to be gained from the same starting fuel, however it results in a hotter and more radioactive waste, which must be efficiently processed to separate the

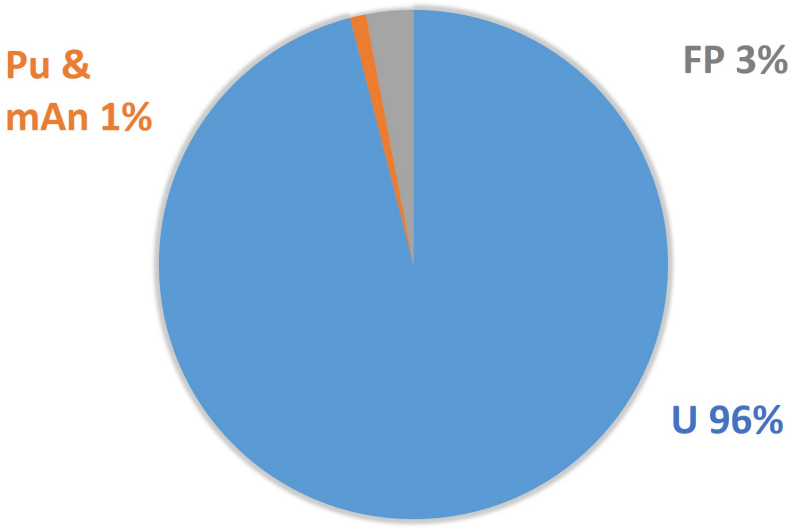

Figure 1.2: Typical composition of elements in spent nuclear fuel from thermal reactors. Replicated with permission from [8].

different levels of waste (low, intermediate and high in the UK classification system). The high level waste (mostly mAn) can then be reprocessed for fuel, or transmuted by further neutron bombardment to convert it to intermediate level waste, which has a shorter radioactive lifetime (hundreds of thousands, to thousands of years, a more manageable timescale for humans).[12, 13] The lifetime of nuclear fuel would also be greatly extended from hundreds of years of new minable uranium.[14] This would in turn require less mining of new uranium ore, which is one of the main contributors to carbon emissions. To achieve this, plutonium must be recycled from existing waste, as plutonium for fuel can only be obtained in sufficient quantities by transmutation of uranium, i.e. it has very low abundance in nature.

1.3 Waste Processing

1.3.1 Aqueous Based Processing

Current recycling of the waste from thermal reactors involves the PUREX (Plutonium Uranium Reduction EXtraction) process: an aqueous based process involving ligands (specifically tributylphosphate, TBP) which selectively bind to uranium and plutonium in the 4+ oxidation state (Figure 1.3).[15] Recovered uranium and plutonium can then be reprocessed for mixed oxide (MOX) fuel, or stored before further use. The main disadvantages of this process when moving to fast reactor waste is that minor actinides are not recovered and fast reactor waste generates far more heat and radiation than thermal reactor waste. This will cause the solvent to boil and break down the organic ligands. Research towards extraction of minor actinides is being

carried out to design ligands which are more selective to actinides than lanthanides,[16–18] however radiation damage of ligands remains a primary concern with such approaches.

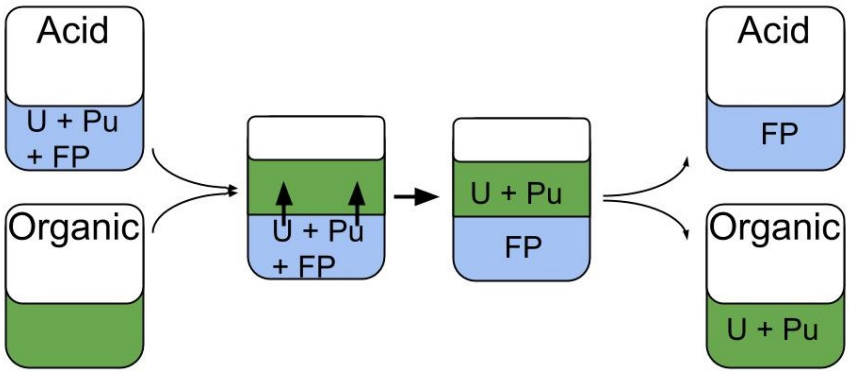

Figure 1.3: Illustration of the aqueous PUREX process for recovery of uranium and plutonium from thermal reactor waste. Replicated with permission from [8].

1.3.2 Nuclear Pyroprocessing

Pyroprocessing is being developed which involves the recycling of spent nuclear fuel by electrochemically reducing actinides from a molten salt system.[11,19] Such a method can provide a high fissile content fuel for reuse in a compact manner, located adjacent to a nuclear plant, removing the need for long-term storage and off-site transportation of highly radioactive material which is required in the PUREX process. There are a variety of salts proposed for different use cases, with operating temperatures ranging from 400 °C (LiCl-KCl eutectic, LKE) to over 800 °C ($CaCl_2$). All of these molten salts have a high irradiation resistance due to being made of inorganic ions and have a wide temperature window between their melting and boiling points (hundreds, if not thousands, of degrees). This makes molten salts excellent solvents for fast reactor waste. Since there is an energy cost to heating a molten salt, heat generated by the waste is actually a benefit in keeping the salt molten without requiring a constant energy input. Waste can be introduced into solution by anodic dissolution which makes pyroprocessing particularly suitable for metal and metal oxide waste, which are the predominant chemical forms of existing waste. Uranium and the transuranics can be extracted by one or a combination of: electrodeposition to a pure metal form; liquid-liquid extraction between the salt and a metal bath to form alloys; precipitation of metal oxides through control of oxygen thermodynamic activity; and fluoride volatilisation. The recovery of certain elements can then be tuned by application of these different extraction techniques.

The general scheme being researched within the UK can be seen in Figure 1.4. Here uranium, the main constituent of the waste, is primarily recovered by electrodeposition onto an inert steel electrode. The minor

actinides, as well as remaining uranium, are to be recovered using the liquid-liquid extraction process.[20] The main candidates for the metal bath are cadmium, bismuth and aluminium. The actinides can form alloys with these metal baths which are more stable than their pure metallic form, thus positively shifting the potential required for electrodeposition. This requires less energy and results in the reduction potentials for the actinides being very similar. This is a benefit for nuclear non-proliferation as plutonium cannot be recovered in a pure form.

Due to the chemical similarity of lanthanides and actinides, lanthanides will also form alloys at similar potentials. This is undesirable as lanthanides act as neutron poisons: they capture neutrons but do not then undergo fission, thus decreasing the efficiency of the reprocessed fuel. Dependent on reactor designs, differing levels of lanthanides are acceptable in the fuel. However in general it is preferred to aim towards 100% separation between actinides and lanthanides, which is a key focus of research into nuclear pyroprocessing.

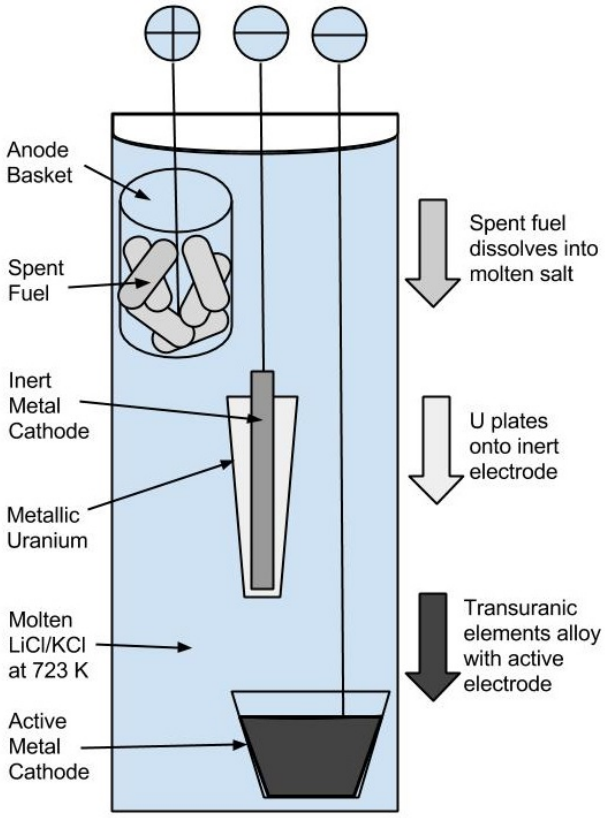

Figure 1.4: Illustration of electrochemical nuclear pyroprocessing. Replicated with permission from [8].

There are several chloride and fluoride salt candidates for pyroprocessing, each of which will have different solvent windows and impact the thermodynamic behaviour of the dissolved fission products. The LiCl-KCl eutectic (LKE) has the lowest melting point (353 °C) of these candidates, making it relatively simple to work with on the lab scale. It is also good for the plant scale as LiCl & KCl are cheap and the low melting

temperature reduces the energy costs required to run the system. LKE is often used in the literature and is the chosen salt system of the National Nuclear Laboratory (NNL), who are partially funding the research in this thesis. LKE therefore has been chosen as the salt medium in the work outlined below.

1.3.2.1 Active Electrode Candidates

The development of pyroprocessing requires investigation into the fundamentals of electroreduction of lanthanide and actinide species in the molten salt with different active electrodes. This will determine how best to recover selectively the actinides while also maintaining a sufficient throughput. There has been an industrial focus on cadmium as the active electrode material due to its high vapour pressure, which facilitates the back extraction of recovered material for fuel reprocessing. However the high vapour pressure also means it is lost from piping systems, posing a serious health risk due to its toxicity and a financial cost for replacement.

Bismuth is another promising active electrode material as it has similar properties to cadmium and is non-toxic. Aluminium offers the best separation efficiency of actinides from lanthanides,[21] however since aluminium is a solid at the proposed operating temperature, it may be that the rate of extraction will be slower due to slower diffusion of reduced species through a solid medium.

Recently there have been literature reviews of the thermodynamics of actinides and lanthanides on inert,[22] cadmium[23] and bismuth[24] electrodes. The reviews on cadmium and bismuth focus on the thermodynamics of Cd or Bi rich binary systems i.e. one redox species. Other redox species reduce the solubility of one another in the active electrode, which would result in the formation of solid intermetallic compounds at lower concentrations than the binary system. Knowledge of secondary alloys (i.e. those with higher concentrations of redox active metal) in the binary systems would be beneficial, as would understanding ternary systems.

There is no review for aluminium, although there is plenty of literature on key actinides[25–27] and lanthanides[21,28–34]. The literature often investigates a binary system (aluminium and one actinide/lanthanide) to map out the potentials at which different alloys/intermetallic compounds form. This is used during separation experiments using a mixture of actinide and lanthanides. Alloy formation is controlled by applying currents, with cut-off potentials employed to prevent reduction of lanthanides. Once a cut-off is reached, a lower current is applied. This is repeated until the current is below a certain threshold, or the potential ceases to change. The separation efficiency is then determined by ex-situ methods. While the studies do determine how to maximise the separation efficiency at the maximum rate, there is little investigation of the fundamental alloying processes.

In this work cerium is used as a non-radioactive surrogate for plutonium. There is far less literature on the binary system of cerium-aluminium[35–38] than other lanthanide-aluminium binary systems. In these studies multiple alloying peaks were observed, and assignments made to particular crystal structures from the cerium-aluminium binary phase diagram. Ex-situ x-ray diffraction (XRD) was used to confirm that electrodeposition (either reduction of cerium into an aluminium electrode and/or co-deposition of cerium and aluminium) at certain potentials resulted in crystalline phases, matching the observed cyclic voltammetry peak positions. However such ex-situ analysis gives samples hours to cool and reach equilibrium, and may not accurately reflect the present phases during cyclic voltammetry which occurs over seconds. In one case, electrodeposition of cerium was carried out on an aluminium electrode at a potential where only the least cerium rich crystal phase (out of five possible crystal phases) was expected to form.[36] However, XRD showed the two most cerium rich crystal phases were present, instead of the least cerium rich crystal phase. This behaviour was unexpected based on the theory that each crystalline phase will only form at a specific potential according to the free energy of formation (as is assumed from all other studies on this binary system) and no explanation was given for how this result may have arisen. In only one case was analysis of the charge passed during cyclic voltammetry performed.[37] In this case the ratio of cerium to aluminium for each oxidation peak lead to each peak being assigned to different crystal phases than those assigned by ex-situ XRD, highlighting that the short timescale cyclic voltammetry may be dominated by kinetic factors, whereas the XRD after electrodeposition (over hours) is likely measuring the system at thermodynamic equilibrium. In order to develop an electrochemical sensor, it is important to gain a deeper understanding of the phases formed during short timescales (e.g. during cyclic voltammetry) which has not been the focus in the existing literature, but will be a key focus of the work in this thesis. In addition, each study in the literature has only focused on a single concentration of cerium in the salt, or a single ratio of cerium to aluminium concentrations for co-deposition. For an electrochemical sensor it is necessary to understand how the cerium concentration, and ratio of cerium to aluminium concentrations for co-deposition, will affect the electrochemical response and if it may in fact also change the kinetics of crystal phase formation. This will also be investigated within this thesis.

1.3.2.2 Development of Sensors in Molten Salts

In order to maintain efficient operating conditions, as well as ensure safe operating conditions, it is desirable to develop in-situ methods of monitoring. In contrast to ex-situ monitoring, in-situ monitoring does not require a sampling system or transport of radioactive material. It can also significantly decrease the time between recording and understanding the data. Spectroscopic methods (UV/vis, near infrared and Raman) are under

investigation for monitoring concentrations of actinide ions in-situ.[39–44] This is promising, as characteristic absorption peaks obey the Beer-Lambert law, allowing simple conversion of adsorption to concentration. For measurement purposes, optical windows built into the reprocessing system are all that is required; no salt needs to be removed for monitoring to occur. It is however required that the optical window is both transparent to the wavelength being used for spectroscopy, and also that the optical window is chemically resistant to the salt. For example glass/quartz is initially transparent for UV/vis spectroscopy, but chemically reacts with the salt and becomes opaque over time.

Electrochemical monitoring is another promising in-situ method. Electrochemical monitoring will be controlled by the same parameters as electrochemical extraction, e.g. concentration and diffusion coefficients. In this way, using an aluminium (or other active metal) electrode for sensing would provide direct equivalent information on the processes occurring at an aluminum extraction electrode. In addition, a sensing electrode may be a different metal to the extraction electrode, e.g. tungsten may be used to observe electrodeposition of pure metals, which may be more easily resolved than electrodeposition of alloys. However, given the number of redox species that would be present in the salt, all at different concentrations, it may be difficult to identify the electrochemical response of a particular redox species of interest (e.g. plutonium) amongst all the other similar electrochemical reactions. Using an alloying electrode such as aluminium (instead of, or in combination with bismuth and/or cadmium), may help to identify particular redox species by observing a characteristic fingerprint of multiple alloying peaks of specific heights and peak separations. If the alloying response could also be used to determine the concentration of the redox species in solution, then a higher degree of confidence would be achieved in identification and quantification of a particular redox species by a combination of electrochemistry on active (e.g. aluminium) and inert (e.g. tungsten) sensing electrodes.

In order to improve the quality of the electrochemical information, microelectrodes would be employed for sensing. The theory behind microelectrodes will be covered in depth later (Chapter 2.2). In short, they have a much higher signal to noise ratio, have a lower limit of detection, and are less sensitive to convection. While an individual microelectrode has a small surface area, an array of microelectrodes can give a large area (and therefore current) while maintaining the improved performance, further improving the limit of detection. In addition, the analysis of microelectrode data, especially in more complex systems, is much simpler to analyse than macroelectrode data. This makes microelectrodes vastly superior as sensors over macroelectrodes. Microelectrodes are easily introduced into pyroprocessing as this only requires the addition of extra electrode ports. Electrochemistry can also be used to investigate the fundamentals of alloying processes (e.g. to determine the maximum loading capacity, the distribution of different phases, how to maximise the rate of reduction and alloy formation etc.) in addition to in-situ monitoring. The use of microelectrodes would also

avoid the issue of possible proliferation with an inert sensing electrode, as it would not be possible to recover large quantities of plutonium when performing pure metal deposition.

Microelectrodes were first made by encapsulation in glass, and ground down to expose a single face of the electrode metal to the solvent. Attempts were made to use such microelectrodes in molten chloride systems[45, 46], however they suffer from degradation of the glass layer causing variable responses over time. In this thesis, microelectrodes are made by microfabrication of layers on silicon substrates. This is done in order to control the chemical properties of each layer, to achieve a chemically resistant microelectrode which can function consistently for extended periods of time.

In practice, no one monitoring system would be used alone. It is always desirable to have complementary techniques, as each technique has its own advantages and disadvantages. Ex-situ methods would likely still be used, to increase the confidence that the pyroprocessing system is working in a safe and efficient manner.

1.4 Aims of this Thesis

In the context of the need to develop electrochemical sensing in molten salts systems, and gain a better understanding of the mechanisms of alloying, this thesis aims to:

1) Characterise the electrodeposition of aluminium and its alloys with cerium (a non-radioactive surrogate for plutonium) and lithium from LKE utilising macroelectrodes.

2) Determine the influence of kinetic factors which control electrochemical signals due to specific phase formation.

3) Analyse both the formation and decomposition of alloy phases in order to know how to identify a specific redox species from the observed electrochemistry.

4) Determine under what conditions the electrochemical alloying response can be accurately converted to a concentration of the redox species.

5) Utilising microelectrodes, repeat alloying experiments in order to understand how the change in mass transport properties affects the observed electrochemistry and mechanisms of alloy formation.

Chapter 2

Theory

2.1 Ambient/Aqueous Electrochemistry

2.1.1 Electron Transfer

Electrochemical reactions occur by the transfer of electrons to or from a redox active species near the surface of an electrode. In metals the large number of overlapping atomic orbitals results in an equally large number of energy levels. With a large enough number of atoms, the differences between energy levels are very small. The energy levels can then be described as a band of continuous energies, rather than a number of discrete energy levels (Band Theory).[47] Due to thermal energy, there is a spread of population at the higher energy bands. The Fermi level (E_f) is defined as the energy at which the probability of that energy being occupied is $\frac{1}{2}$.

A redox species will have a particular highest occupied or unoccupied energy level due to its electronic structure. Electron transfer occurs if the energy of the redox species is significantly above (HOMO, oxidation) or below (LUMO, reduction) the E_f of the electrode. The general expression for a reversible one electron transfer is given as:

$$ox + e^- \rightleftharpoons red \tag{2.1}$$

where ox is the oxidised species and red is the reduced species. This can be seen schematically in Figure 2.1. The rate of electron transfer is dictated by the difference between E_f and energy of the redox species orbital. An applied potential to the electrode changes its E_f. Thus the rate of electron transfer is governed by the

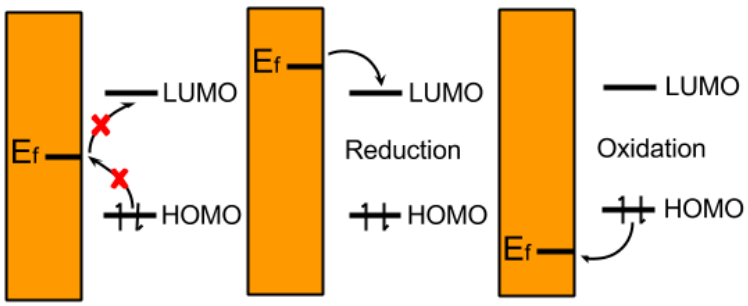

Figure 2.1: Schematic representation of E_f and the LUMO and HOMO of a redox species. If E_f is between the LUMO and HOMO energies, no reaction will occur. If E_f is greater than the LUMO energy, the redox species will be reduced. If E_f is below the HOMO energy, the redox species will be oxidised. Replicated with permission from [8].

applied potential, and so a redox species can be oxidised and/or reduced in order to study it. The rate of electron transfer, k, is given by the Butler-Volmer equation:[48]

$$k_{red} = k^{\theta} exp[-\alpha_{red} nF(E - E^{\theta})/RT] \tag{2.2}$$

$$k_{ox} = k^{\theta} exp[-\alpha_{ox} nF(E - E^{\theta})/RT] \tag{2.3}$$

where n is the number of electrons transferred, F is Faraday's constant, R is the gas constant, T is the temperature in K, E is the applied potential, E^{θ} is the the standard potential (i.e. the potential at which E_f is the same as the energy of the redox species and so no reaction occurs), k^{θ} is the standard heterogeneous rate constant and α is the transfer coefficient. The transfer coefficients are geometric factors which are determined by the position of the transition state in the reaction coordinate. $\alpha_{red} + \alpha_{ox} = 1$ and often each transfer coefficient is very close to $\frac{1}{2}$.

The measured current, i, is given by:[48]

$$i_{red} = -nFAk_{red}c_{ox} \tag{2.4}$$

$$i_{ox} = nFAk_{ox}c_{red} \tag{2.5}$$

where c_{ox} and c_{red} are the concentrations of each species at the electrode surface, and A is the surface area of the electrode. Other symbols have their usual meanings. For a fixed concentration it is only the rate of electron transfer that controls the measured current. Naturally as a reaction proceeds the local concentration

will decrease, and so will the measured current. At this point the mass transport of redox species to the electrode begins to influence the overall rate of reaction.

2.1.2 Mass Transport

There are three major categories of mass transport: diffusion, convection and migration. All will contribute to how the concentration of redox species at the electrode surface changes over time. In practice it is desirable to have only one of these be the contributing factor.

Migration is the movement of charged species due to the presence of an electric field. An applied potential at an electrode surface will generate an electric field that permeates into the solution. This will attract ions of the opposite charge and repel ions of the same charge, i.e. a negative potential (E_f above redox species energy) would attract positive ions and repel negative ions. A schematic representation can be seen in Figure 2.2. This type of mass transport is usually prevented by the addition of a background electrolyte to a neutral solvent. This background electrolyte is chosen to be at a higher concentration than the redox species, thus shielding the redox species from the electric field. The background electrolyte will also be chosen so as not to undergo a redox reaction within the electrochemical window of the solvent.

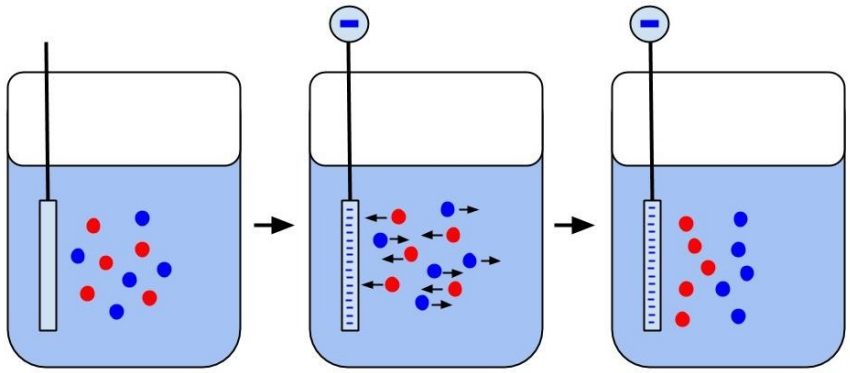

Figure 2.2: Schematic representation of migration under a negative applied potential. Blue circles are negative ions; red circles are positive ions. Replicated with permission from [8].

Convection is mass transport due to the macroscopic flow of the solvent. Figure 2.3 shows schematics of two forms of convection: natural (e.g. temperature gradients) and forced (e.g. stirring of solution). Natural convection is often difficult to control and can be chaotic in nature. This can be avoided by working in a water/heat bath to ensure minimal temperature gradients, or by creating larger forced convection which can be better mathematically described. In the case of rotating disc electrodes (RDEs) or rotating ring-disc electrodes (RRDEs) the electrode itself is the stirring mechanism and convection is used as the dominant form of mass transport to the electrode surface.

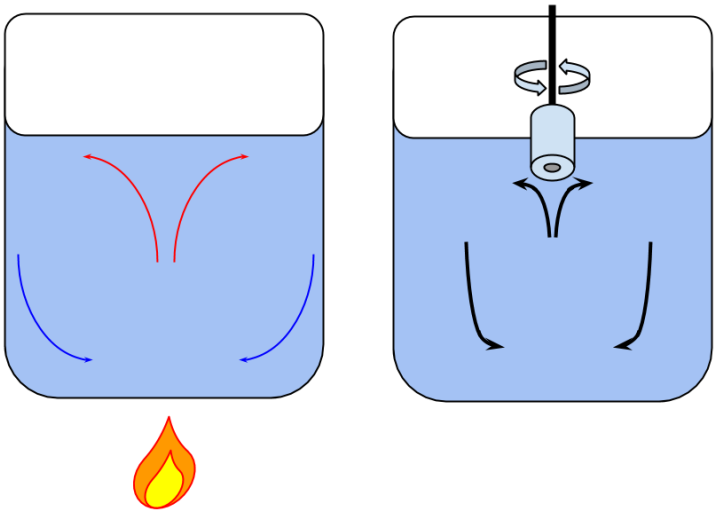

Figure 2.3: Schematics of convection in solution. (Left) Natural convection caused by temperature gradients. (Right) Forced convection caused by a rotating disc electrode. Replicated with permission from [8].

Diffusion is the process of mass transport caused by Brownian motion. When there is a concentration gradient, diffusion will naturally result in species spreading out to form a homogeneous mixture as in Figure 2.4. This can be expressed using Fick's first law of diffusion:

$$J = -D\frac{\partial c_\infty}{\partial x} \tag{2.6}$$

where J is the flux of species to the electrode surface (mol cm^{-2} s^{-1}), D is the diffusion coefficient (cm^2 s^{-1}), c_∞ is the bulk concentration (mol cm^{-3}) and x is the distance from the electrode surface (cm).

Fick's second law of diffusion describes how this occurs over time in 3D space:

$$\frac{\partial c_\infty}{\partial t} = D(\frac{\partial^2 c_\infty}{\partial x^2} + \frac{\partial^2 c_\infty}{\partial y^2} + \frac{\partial^2 c_\infty}{\partial z^2}) \tag{2.7}$$

Together these laws describe the dynamic shape of a diffusion field which grows over time as a concentration gradient forms at the electrode surface. This is of importance to the difference between macro- and micro-electrodes which will be covered later. It is common that diffusion is made to be the predominant form of mass transport, as will be the case in this work.

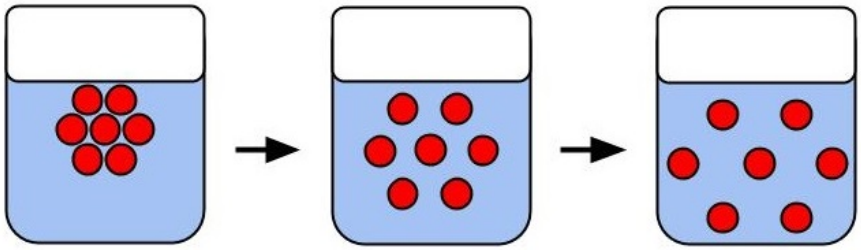

Figure 2.4: Schematic of diffusion from a heterogeneous to a homogeneous mixture. Replicated with permission from [8].

2.1.3 Electrical Double Layer

When a potential is applied to an electrode, a double layer is formed due to migration.[48] Figure 2.5 shows the structure of the double layer. There is a dense layer of background electrolyte ions close to the electrode surface. This layer is comprised of ions of the opposite charge (inner Helmholtz plane) adsorbed on the electrode, and counter ions (outer Helmholtz plane). The second layer is more diffuse, as the ions are not able to adsorb on the electrode but are still attracted to the electrode due to the electric field. This shields the bulk solution from the electric field, which causes redox species to experience a steep potential gradient closer to the electrode surface. This eliminates the possibility of electron transfer via quantum tunneling further from the electrode surface, ensuring that the electron transfer occurs only at the the electrode surface and follows Butler-Volmer kinetics.

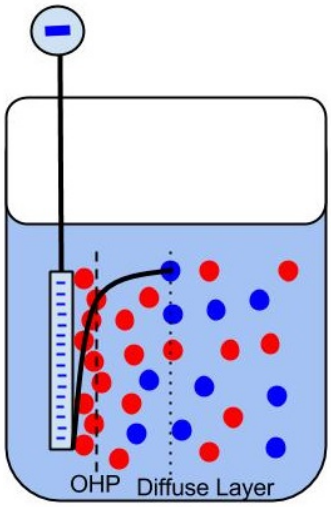

Figure 2.5: Schematic of the electric double layer. This consists of a densely packed layer at the electrode surface (OHP) and a more diffuse layer further from the electrode surface. At a certain distance from the electrode surface the ions exists as bulk due to being shielded by the double layer. The black line indicates the potential felt by ions in solution, decreasing further from the electrode surface. Replicated with permission from [8].

2.1.4 iR Drop

Any solution will have a resistance (R_s). This, in combination with the current being passed, affects the potential at the electrode (known as Ohmic or iR drop):

$$E_{measured} = E_{applied} - iR \tag{2.8}$$

This iR drop from solution resistance is the energy required to drive ions to the electrode by migration when forming the double layer. In addition to the solution resistance, there may be other elements of the electrical circuit that have a resistance during a redox reaction. The combination of resistances can be determined from cyclic voltammetry of a redox reaction at a variety of scan rates. In an ideal circuit (with no resistance) the peak current (i_p) is expected to increase with scan rate, but the peak potential (E_p) is not and so any observed change of E_p with the change in i_p is due to combination of all the resistances in the electrical circuit. A plot of E_p versus i_p should give a straight line correlation, with a gradient equal to the apparent resistance, R. A resistance correction can then be applied to the measured potentials. Since the potential offset scales with current, microelectrodes are far less affected by iR drop than macroelectrodes.

2.1.5 Three Electrode Cell

In electrochemistry a three electrode cell is used to be able to study redox reactions.[49] A schematic can be seen in Figure 2.6. The current is measured between the working and counter electrodes. The surface area of the counter electrode is much greater than the working electrode to ensure that it is the reaction at the working electrode that limits the current. The counter electrode is not able to maintain a stable potential when passing current and so a separate reference electrode must be used. The potential applied at the working electrode is measured versus this reference electrode. The reference electrode has an electrochemical reaction at equilibrium, which has a fixed/stable potential. The working electrode potential is then known relative to this reference reaction. This allows measured potentials to be compared between experiments, as potential is a relative, rather than absolute, scale.

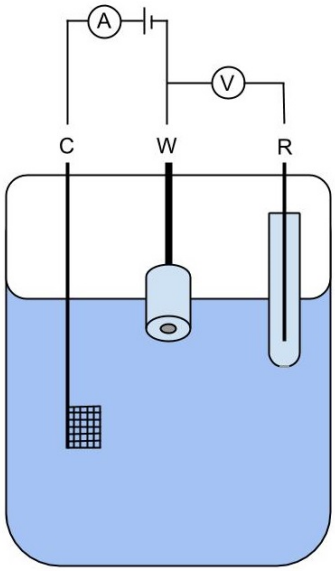

Figure 2.6: Schematic of a three electrode cell with a working electrode (W), reference electrode (R) and counter electrode (C). A voltmeter (V) measured the potential between the working and counter electrodes. An ammeter (A) measures the currents between the working and counter electrodes. Replicated with permission from [8].

2.2 Macro- and Microelectrodes

The advantages of microelectrodes stem from their enhanced mass transport relative to macroelectrodes.[50–52] This is due to the shape of their diffusion fields, which can be seen in Figure 2.7. On a macroelectrode the diffusion field grows linearly whereas on a microelectrode the diffusion field grows hemispherically. In both cases the diffusion field grows over time as the local concentration is depleted and redox species must diffuse from further away. On macroelectrodes the diffusion field has a constant surface area and so the distance redox species must travel also increases, leading to a drop off in current over time. The microelectrode diffusion field has an increasing surface area, which increases at the same rate as the distance redox species must travel. These two effects cancel out, resulting in a constant rate of mass transport (steady state/limiting current) which is time independent.

This radial diffusion also occurs at the edges of macroelectrodes, however the area of the edge is very small on a macroelectrode and so linear diffusion dominates. Once the radius decreases to the scale of tens of μm, the surface becomes more "edge like" and radial diffusion dominates. Once sufficiently small the surface becomes "all edge", and the radial diffusion is purely hemispherical.

For both sizes of electrode the capacitive (non Faradaic) current is proportional to the electrode surface area. On macroelectrodes the Faradaic current (the current due to the redox process) is proportional to the surface

area, and so the ratio of Faradaic to capacitive current (the signal to noise ratio) is constant regardless of surface area. For microelectrodes the Faradaic current is proportional to r , whereas the area for a disc is $4\pi r^2$. Since capacitive current remains proportional to area for microelectrodes, as the microelectrode area decreases, the capacitive current decreases more rapidly than the Faradaic current, leading to an increased signal to noise ratio. This is beneficial for detecting redox species at very low concentrations.

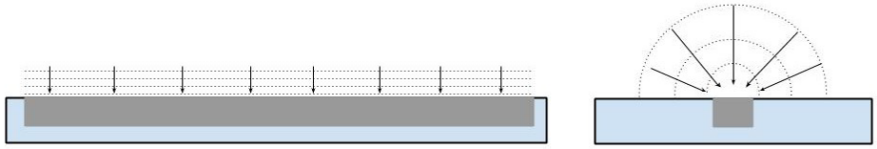

Figure 2.7: Schematic of diffusion fields. (Left) Linear at macroelectrode surface. (Right) Hemispherical at microelectrode surface. Replicated with permission from [8].

2.3 Electrochemical Techniques

2.3.1 Soluble-Soluble Versus Soluble-Insoluble

For many redox reactions, both the oxidised and reduced forms are soluble. In this case species travel to the electrode under mass transport, undergo electron transfer and then travel away from the electrode under mass transport. These are termed "soluble-soluble" reactions. It is also possible that the product of the reaction is not soluble in solution. In such a reaction, the oxidised species travels to the electrode surface under mass transport control, is reduced to a neutral species, and then stays on the electrode surface. For metals this is termed a plating reaction, with the oxidation being a stripping reaction. This is also the case for alloy formation, where one metal may be on the electrode and not undergo a redox reaction but a second metal can be reduced into the first.

2.3.2 Cyclic Voltammetry

In cyclic voltammetry, the potential is scanned from a starting potential to a lower or upper vertex potential (depending on the direction of the scan) and back again (Figure 2.8). The potential can be scanned in a number of ways, but in the simple case the potential is scanned linearly at a constant scan rate (ν, $V\,s^{-1}$). The resulting cyclic voltammogram (CV) is plotted as the current versus potential. In this work CVs are almost exclusively scanned negatively on the forward scan, and positively on the back scan, in order to reduce redox species in solution. When scanning through the potentials at which a redox reaction can occur, the initial current is controlled by the electron transfer kinetics, a peak is reached (mixed control) where the local

concentration has decreased and mass transport is required to maintain the current, and after the peak the current is dictated by mass transport. For macroelectrodes this generates a peak, for microelectrodes this generates a limiting current.

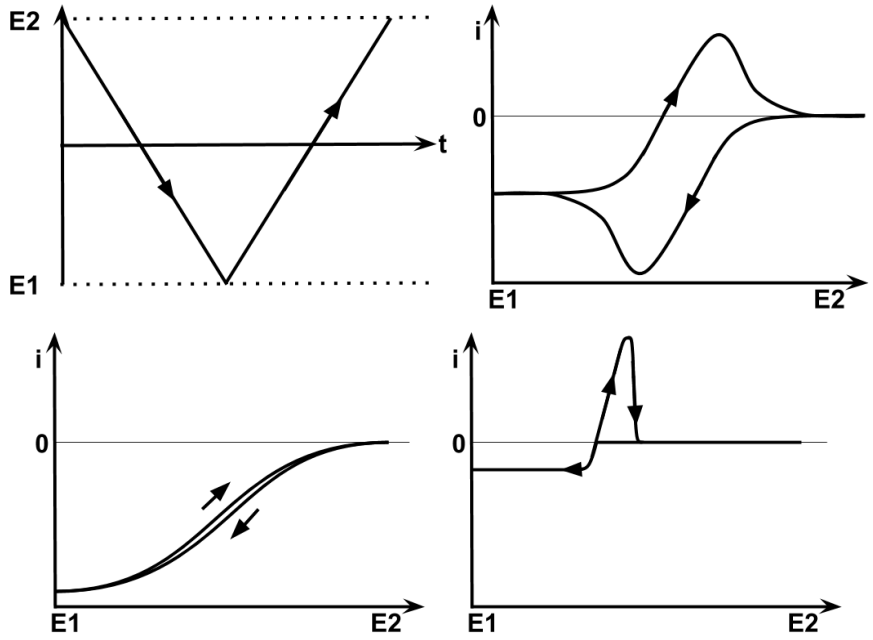

Figure 2.8: (Top Left) Triangular sawtooth wave commonly used in cyclic voltammetry. The potential is scanned linearly with time from one potential, to another, before scanning in the opposite direction. (Top Right) Typical CV of a soluble-soluble reaction on a macroelectrode. (Bottom Left) Typical CV of a soluble-soluble reaction on a microelectrode. As both reactions are diffusion limited, the peaks becomes limiting currents. (Bottom Right) Typical CV of a plating/stripping reaction on a microelectrode. The reduction is diffusion limited and so displays a limiting current. The shape of the stripping peak is sharper than for a soluble-soluble oxidation, but does not change on macro- versus microelectrodes.

The potential at which a redox reaction will occur is dictated by the Nernst equation:[48]

$$E = E^{\theta} + \frac{RT}{nF}\, ln(\frac{c_{ox}}{c_{red}}) \tag{2.9}$$

Thus by changing the concentration of redox species the potential at which the reaction will occur will shift.

The peak current when diffusion is the dominant form of mass transport is given by:[48]

$$\frac{|i_p|}{\sqrt{\nu}} = X(nF)^{\frac{3}{2}} Ac\sqrt{\frac{D}{RT}} \tag{2.10}$$

where X has a value of 0.4463 for a soluble-soluble reaction (Randles-Sevick equation, which is valid for the reduction and oxidation reaction) and 0.61 for a plating reaction (Delahay equation, only valid for the

reduction reaction). Other symbols have their usual meanings. By performing a CV at multiple scan rates, it is possible to confirm that the i_p versus $\nu^{0.5}$ correlation is linear and thus that the reaction in controlled by diffusion.

For a disc microelectrode the steady state, or limiting, current is given by:[53]

$$|i_L| = 4nFcDr \tag{2.11}$$

where r is the radius of the microelectrode in cm. For a soluble-soluble reaction both the oxidation and reduction reactions will display limiting currents. A plating reaction will give a limiting current, however a stripping reaction will still be peak shaped, as in Figure 2.8, as it is controlled by electron transfer rather than diffusion.

It is possible to convolve macroelectrode CVs to allow for the effect of linear diffusion, to resemble microelectrode CVs. Since the decrease in current due to diffusion occurs with respect to $t^{0.5}$ (Equation 2.14), the current can be partially integrated with respect to time:[48]

$$I(t) = \frac{1}{\sqrt{\pi}} \int_0^t \frac{i(u)}{\sqrt{t-u}}\, du \tag{2.12}$$

This yields a convolved current (I), with units of A $s^{0.5}$. For diffusion controlled peaks, this will result in limiting convolved currents, I_L. This must be solved numerically, and is a built in function of the NOVA software used to record and analyse electrochemistry data in this thesis. The limiting convolved current is described by:[48]

$$|I_L| = nFAcD^{0.5} \tag{2.13}$$

2.3.3 Chronoamperometry

In chronoamperometry (CA) a rest potential (where no Faradaic current would pass) is applied to allow the formation of the double layer. The potential is then changed to reduce/oxidise the redox species, and the current is measured over time, with $t = 0$ set as the beginning of the second potential. Assuming the applied potential results in diffusion limited current, the current on a macroelectrode is given by the Cottrell equation:[48]

$$|i| = nFAc\sqrt{\frac{D}{\pi t}} \tag{2.14}$$

On a disc microelectrode the current can be described by:

$$|i| = nF4\pi r^2 c\sqrt{\frac{D}{\pi t}} + 4nFcDr \tag{2.15}$$

This is the Cottrell equation in addition to the steady state current. At short timescales the macro- response dominates as the initial diffusion field is linear. At longer timescales the diffusion field becomes hemispherical, and the steady state (micro-) current dominates. A benefit of this combination of linear and hemispherical diffusion regimes is that a current time transient from a microelectrode can be fit, to determine $c * D$ and r. Thus as long as one of those parameters is known, the other two can be determined simultaneously.

2.4 Molten Salt Electrochemistry

Molten salts are liquids containing only ions. In the case of this work, with LiCl-KCl eutectic (LKE), all the ions are inorganic and so melt at high temperature due to the energy required to overcome the lattice enthalpy. Molten salts can contain organic ions which melt at much lower temperatures (around room temperature) and are generally called ionic liquids in order to distinguish them from the inorganic molten salts. Molten salts are able to dissolve many ionic redox species, and in this work metal chlorides are used so that the solvent and redox species share the same counter ions.

Molten salt electrochemistry has many other applications in addition to nuclear pyroprocessing. The most well known of these is probably the Hall–Héroult process for the production of aluminium, which uses aluminium oxide in a cryolite molten salt (Na_3AlF_6-Al_2O_3).[48] There is also interest in the use of molten salts to produce graphene and carbon nanostructures.[54–57]

The electrochemical theory outlined in Section 2.1 is valid for ambient conditions in neutral solvents (e.g. water) and dissolved background electrolyte at low concentration. While this theory has not yet been proved valid for molten salt systems, which are liquids with only permanent dipoles, controlled by Coulombic interactions, it has been able to describe molten salt electrochemistry so far.

When molten, LKE has a viscosity similar to water[58] as well as a high conductivity[59] due to being comprised of ions. The eutectic is used because the melting point is lower than each individual salt as can be seen in Figure 2.9. The eutectic occurs at a molar ratio of 59.2 moles of LiCl to 40.8 moles of KCl.

This corresponds to a mass ratio of 45 g of LiCl to 55 g of KCl, per 100 g of LKE. The depression of the melting point is due to the increased entropy gained by mixing the salts. The melting point at the eutectic composition is 353 °C (626 K). Nuclear pyroprocessing research in the UK has been agreed to operate in LKE at an operating temperature of 450 °C (723 K), which will be the main temperature used in this thesis.

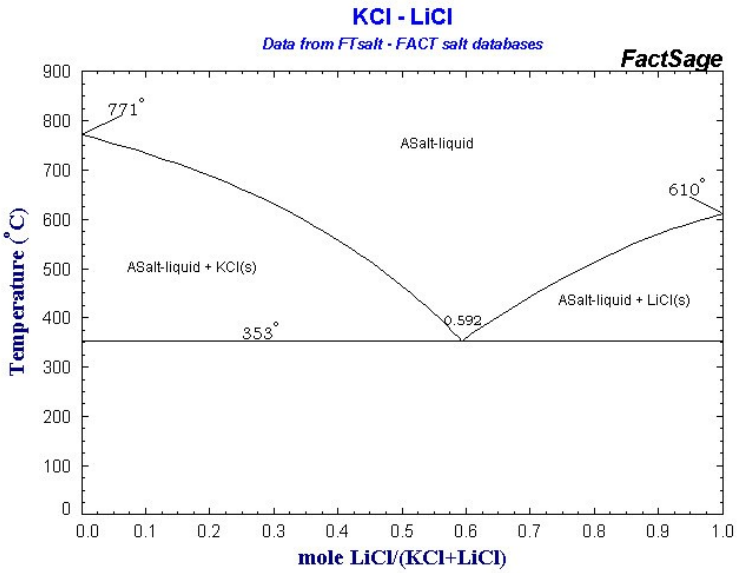

Figure 2.9: Phase diagram for the binary mixture of LiCl and KCl.[60]

If a sufficient potential is applied, the solvent itself can undergo electrochemical redox reactions. The solvent window of LKE is approximately 4 V and can be seen in Figure 2.10. Chloride is oxidised to chlorine at approximately +1.2 V. Chlorine gas is able to leave the system, thus why no reduction current is seen. Lithium ions are reduced to lithium metal at approximately -2.6 V. Lithium metal can then be re-oxidised to lithium ions.

Due to the radioactivity of actinides, it is commonplace to use surrogates to be able to study actinide behaviour with more safe material. This allows for implementation of experimental protocols that can be more easily tweaked with non active material, before replicating the experiment with active material. For this purpose the lanthanides are excellent surrogates, due to their chemical similarity. In this work cerium is used as an electrochemical surrogate for plutonium. This is due to each element having the same oxidation state in the chloride (3+) and similar reduction potentials.[19, 61] It also forms the same number of intermetallic compounds with aluminium and these have similar stoichiometries (Figure 2.11). Therefore understanding of the cerium-aluminium system can be carried out more safely, and then applied to the plutonium-aluminium system.

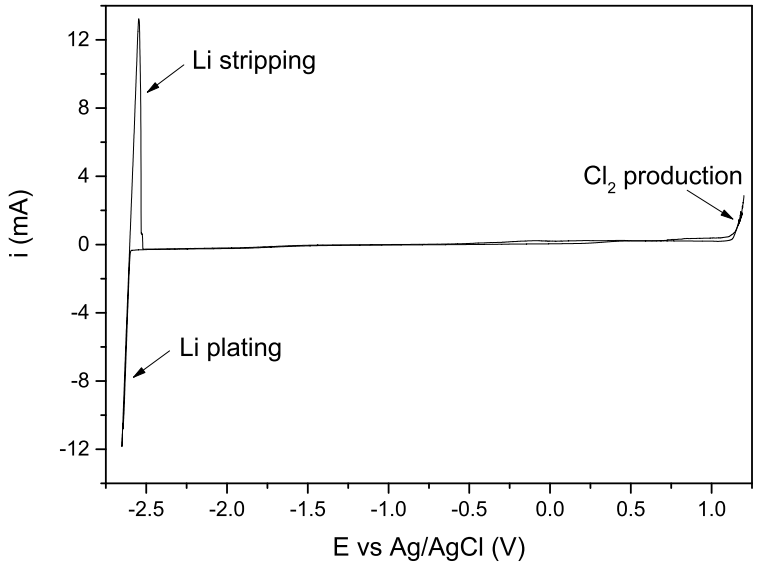

Figure 2.10: Typical CV of LKE on a tungsten macroelectrode.

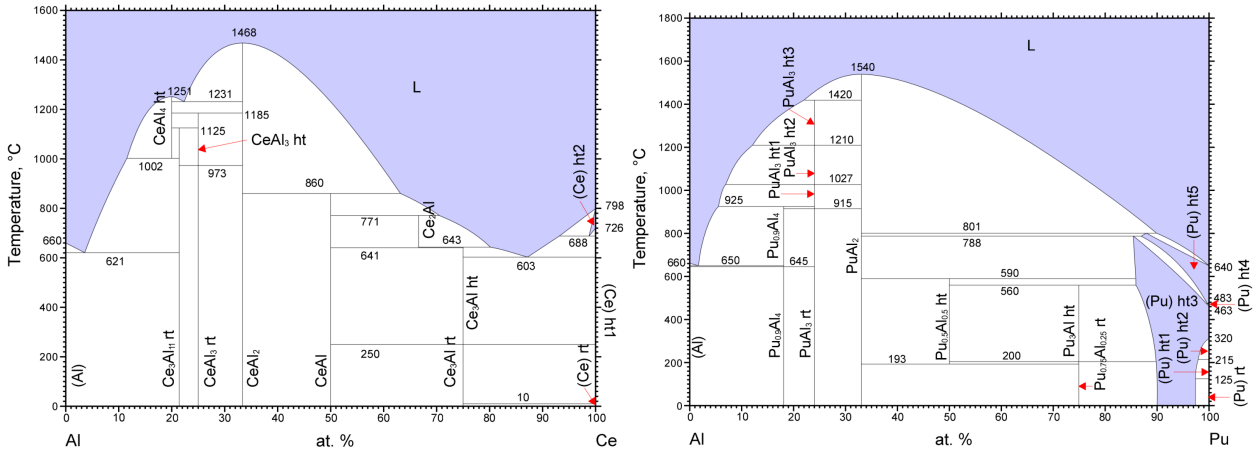

Figure 2.11: Phase diagrams for the (Left) Cerium-aluminium binary system.[62] (Right) Plutonium-aluminium binary system.[63]

Chapter 3

Experimental Methods and Materials

3.1 Macroelectrode Molten Salt Electrochemistry

LKE was prepared with 22.5 g of LiCl ≥99% (Sigma-Aldrich, Dorset, UK) and 27.5 g KCl (Alfa Aesar, Heysham, UK). Other salts used were: $AlCl_3$ (99.99%, Sigma-Aldrich), $CeCl_3$ (≥99.99%, Sigma-Aldrich), AgCl 99% (Sigma-Aldrich) and Al_2O_3 (99.99%, Acros Organics, Fisher Scientific, Perth, UK). All salts are 50 g of LKE + redox species. Concentrations will be given for redox species in Figure captions. Where no concentrations are given, the salt was LKE only.

Working electrodes were either aluminium wire (99.95%, d = 1 mm or 250 μm, Goodfellow, Cambridge, UK) or tungsten rods (99.95%, d = 2 mm, Goodfellow). Counter electrodes were always tungsten rods (d = 2 mm) immersed deeper into the salt than the working electrode to ensure a greater surface area.

The reference electrode was made by loading a mullite tube (inner d = 4 mm, outer d = 6 mm, Multi-Lab Ltd, Glasgow, UK) with 1 g of LKE + 1wt% AgCl. A length of silver wire (99.9%, d = 1 mm, Sigma-Aldrich) was inserted into the salt, with enough length to extend out of the mullite tube. The mullite tube was sealed with silicoset 158 (RS Components, Glasgow, UK).

Salts were held in glassy carbon crucibles (Sigradur GAT 10, HTW-Germany, Thierhaupten, Germany) during experiments. These crucibles were chosen for their resistance to corrosion and resistance to thermal shock. This crucible would then sit in a quartz cell (H. Baumbach & Co., Ipswich, UK) with a borosilicate lid (H. Baumbach & Co.) with multiple ports for inserting electrodes. Mullite tubes open at both ends were used to sparge the salt with argon gas (99.998% BOC, Guildford, UK). The temperature of the salt was

monitored using a K-type thermocouple (RS Components, UK) and recorded using a UTC-USB (Omega Engineering, Manchester, UK) connected to a PC.

Vertical tube furnaces (Carbolite, Derbyshire, UK and Severn Thermal, Dursley, UK) were used to heat the salt. The Carbolite furnaces were located in the laboratory environment, and required a constant flow of argon through the cell to maintain an inert atmosphere. In this case, high-vacuum grease (Dow Corning, Midland, Michigan, USA) was applied between the glass lid and quartz cell, to minimise the ingress of air into the system. Severn Thermal furnaces were located inside gloveboxes (MBraun, Garching, Germany) which were filled with argon gas. In this case the cells did not require a constant flow of argon and high-vacuum grease was not applied.

A Faraday cage (a steel mesh in the shape of the quartz cell) was inserted between the furnace and the quartz cell. This was grounded to reduce the noise generated by the heating coils. It was not practical for the Faraday cage to fully surround the electrochemical cell, as would usually be done for aqueous based electrochemistry, however external electromagnetic radiation was not found to be a significant concern.

Electrochemical measurements were performed with an Autolab Metrohm potentiostat PGSTAT128N (Eco-Chemie, Utrecht, Netherlands). This was controlled by NOVA 1.11 software (EcoChemie) on a computer. Data was analysed using a combination of NOVA 1.11 and Origin 2015 (Origin Lab, Northampton, MA, USA).

3.2 Microelectrodes

Optical microscopy was performed by using a top lit microscope Yenway ISH500 (Microscope Systems Limited, Glasgow, UK) and Yetxam software to capture images. A variety of zoom levels (50X→1000X), were used to inspect microelectrodes before and after use. Electrical connection to microelectrodes was achieved by spot welding of flat nosed micro alligator (RS Components, UK) to tungsten macroelectrodes. The crocodile clips has a large flat surface area for connection to the microelectrode bond/contact pads.

3.2.1 Tungsten Microelectrode Fabrication

Microelectrodes were fabricated in-house by Ewen Blair and Ilka Schmueser at the Scottish Microelectronics Centre. The schematic for microfabrication can be seen in Figure 3.1.

The final electrode can be seen in Figure 3.2. Further information on microelectrode design and microfabrication procedures can be found in [64]. Although the schematic shows a square microelectrode, microdisc

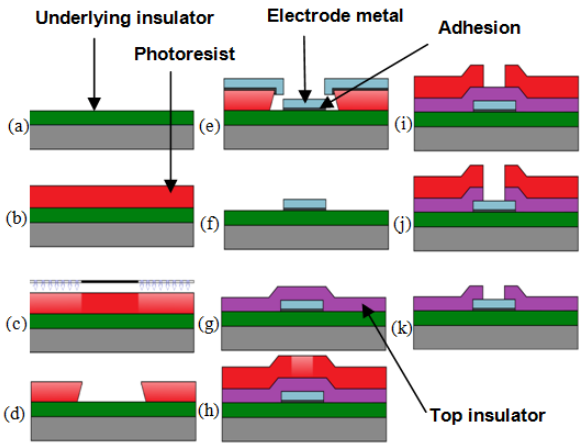

Figure 3.1: Cross section schematic of photolithography. (a) An insulator (Si_3N_4) is deposited on top of a silicon substrate. (b-d) Negative photoresist is deposited, patterned, then etched to leave a cavity. (e-f) An adhesion layer (TiN) is deposited, followed by deposition of metal (W). The photoresist is then removed. (g) Another layer of insulator (Si_3N_4) is deposited. (h-l) Positive photoresist is deposited, patterned and etched to create a hole in the top insulator to expose the metal. The photoresist is removed. Replicated with permission from [64].

electrodes were used exclusively in this work. A range of disc sizes were produced, (r = 5, 10, 15, 25, or 50 µm). In this work microelectrodes were used which had tracks of metal connecting the contact pad to the exposed microelectrode. This would either be thin track (TT) or super thin track (STT). These were designs to combat particular failure mechanisms, and should not have any effect on voltammetric electrochemical measurements.

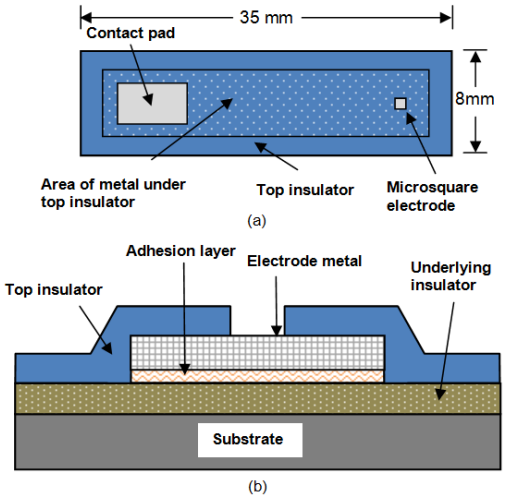

Figure 3.2: (a) Top down view of the microelectrode. In this work the microelectrodes are disc rather than square geometries. Electrical contact is made to the contact pad. (b) Cross section view of the microelectrodes. Figure taken from [64].

3.2.2 Thin Film Aluminium Microelectrodes

To produce microelectrodes with a fixed volume of aluminium, aluminium was deposited on top of existing tungsten STT microelectrodes. This was done by patterning a layer of photoresist to expose a hole that has a radius 5 μm greater than the radius of the underlying tungsten microelectrode. This was done to prevent difficulties in aligning so that aluminium always covered the entire tungsten surface. For the following devices there is a 200 nm layer of aluminium, sitting in a 500 nm well. It is known that deposition over a step height results in a thinner film over that step height than of deposition on a flat surface.[64] It is unclear whether or not the wall of the well is covered with aluminium, and therefore whether the ring above the well is electrically connected to the aluminium inside the well. This will not impact experimental studies as in Chapter 7 it will be seen that measured currents are well below expected values for the inner circle area.

Figure 3.3 shows an optical image of an aluminium microelectrode. The green material is Si_3N_4 on top of SiO_2 and purple material is Si_3N_4 on top of patterned tungsten. The Si_3N_4 has different thicknesses over each section, which affects its optical properties thus resulting in different colours. The aluminium (bright metal) has a clearly visible ring around the inner disc. When tungsten is visible, it is a much duller metal.

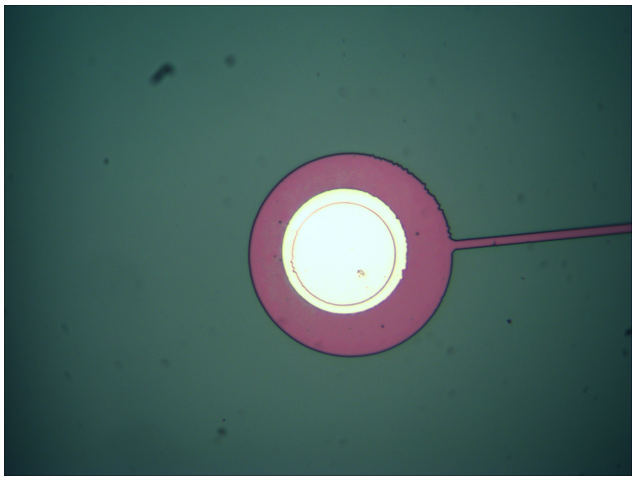

Figure 3.3: Optical microscopy (400X magnification) of an aluminium microelectrode. The central disc has a radius of 25 μm, and is 300 nm recessed from the surrounding pink/purple Si_3N_4. The surrounding aluminium ring is approximately 5 μm wide and sits on top of the Si_3N_4.

3.3 Experimental Protocol

A schematic of the cell assembly can be seen in Figure 3.4. LKE and redox species are weighed out in a carbon crucible. This is placed within the quartz cell, with the borosilicate lid on top. This lid had several inlets/ports (seven on the top and two on the side). Electrodes are held in inlets using screw on high

temperature plastic with o-rings. The reference electrode rapidly fails when subjected to large temperature gradients and the reference electrode is always immersed into the salt before heating starts. The salt is heated to target temperature with an immersed thermocouple (inside a mullite tube), usually one to two hours are required. Once at the target temperature: the counter electrode is immersed to maximum depth; the working electrode is immersed to a shallower depth. For experiments in an external furnace (surrounded by air), a flow of argon was continuously passed through the cell to remove air from the cell. High-vacuum grease was applied between the glass lid and quartz to ensure an airtight seal. For experiments in gloveboxes (purely argon environment, O_2 <0.1 ppm, H_2O <0.1ppm), high-vacuum grease was not used and argon was not actively passed through the cell.

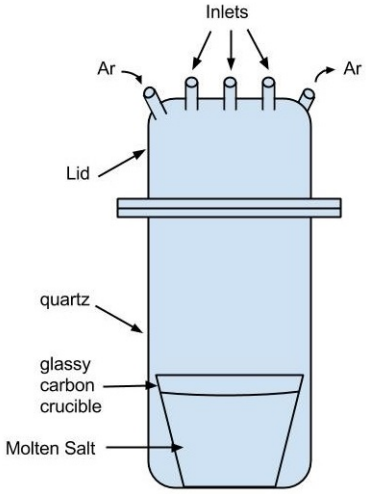

Figure 3.4: Schematic of the cell used to perform molten salt electrochemistry. Replicated with permission from [8].

Prior to running electrochemical measurements, a procedure is run to electrochemically dry the salt. This is done by performing ten CVs between the solvent window, while sparging the molten salt with argon gas. This produces lithium metal and chlorine gas which are mixed into solution and can react with species generated by the presence of water. This improves the observed electrochemistry of redox species which are to be studied. Further information on this procedure can be found in [8].

Chapter 4

Development of Methods for Characterising Electrodeposition and Alloying of Cerium and Aluminium on Macroelectrodes

4.1 Introduction

Aluminium is one of the proposed active electrode materials for the pyroprocessing of spent fuel. It is therefore important to investigate the fundamental processes that occur when spent fuel elements are reduced and alloyed with aluminium. For the purposes of pyroprocessing, macroelectrodes will be used to maximise the rate of recovery of certain elements. It is therefore important to understand how alloying occurs on an aluminium macroelectrode in order to improve the efficiency of the extraction. It is also important to determine if a similar electrode could be used as a sensor, since if a concentration of some species can be determined on the sensing electrode then it is possible to extract it with the extraction electrode as the reduction potentials would be the same. Thus the potentials required for extraction at the active metal electrode can be determined by measuring in the salt with the same active metal. It is then important to know how well an aluminium macroelectrode functions for such analysis. While there are electrochemical equations for analysing soluble-soluble reactions,[48, 53] it is unclear whether these equations can be applied

to plating/stripping and alloying reactions. There are far fewer equations found in the literature for these plating/stripping reactions, which are required to form the basis of on-line monitoring in pyroprocessing.

The following groups of elements have been previously extensively studied electrochemically on either an aluminium electrode and/or by co-deposition of their chloride with aluminium chloride on an inert electrode in LKE: lanthanides[31–34, 38, 65–78], actinides[26, 27, 79–81], and other metals[82–85]. In this work the electrodeposition and alloying of cerium into aluminium is being studied. Cerium is used as a non radioactive electrochemical surrogate for plutonium. There are far fewer studies of the LiCl-KCl-$CeCl_3$ system on an aluminium electrode[28, 36], and co-deposition with LiCl-KCl-$CeCl_3$-$AlCl_3$ on an inert electrode[35, 37, 38] available in the literature. The common findings are that only one alloying is observed on a bulk aluminium macroelectrode during CVs. By holding a relatively negative potential for tens of seconds, followed by measuring open circuit potential (OCP) time transients, two distinct potential plateaux were observed and attributed to the oxidation of two distinct Ce_xAl_y intermetallic compounds. Holding a reducing potential just negative of the observed alloying peak for hours followed by cooling and x-ray diffraction (XRD), three or four intermetallic compounds were found to have formed, although there was disagreement on which crystal phases had formed. For co-deposition, (where a thin film of aluminium is deposited prior to alloying), three intermetallic compounds (out of a maximum of five) were observed to form during CVs. By holding a relatively negative potential for hours followed by cooling and XRD, all five intermetallics were measured to have formed. It is interesting to note that co-deposition shows the formation of intermetallic compounds occurs at particular potentials (related to the free energy of their formation), however by reducing cerium on a bulk aluminium electrode for long periods of time at a potential where only one intermetallic should form, it was found that more intermetallics did form. This suggests that the formation of intermetallics is not solely controlled by the applied electrochemical potential, but that constant reduction may be able to increase the content of cerium which can then allow the formation of intermetallics due to the chemical potential, i.e. decreasing the free energy of intermetallic formation below zero due to increasing the concentration of the reactants (in this case, cerium dissolved in aluminium). This point was not noted in the literature itself, but was arrived at by understanding the results of all existing literature on the electrochemical formation of cerium-aluminium alloys from LKE.

The work in this chapter will look at the solvent window of the aluminium electrode in LKE, thus investigating lithium-aluminium alloying (which has applications in other technological fields). It will also delve deeper into the fundamental processes occurring during electrodeposition and alloying of cerium with the aim of determining if the reactions are kinetically or thermodynamically limited. This will help to determine if common analytical electrochemical expressions are applicable to alloying reactions and ultimately what useful

information can be gained from a sensing aluminium macroelectrode. This work will also inform differences in response when aluminium and cerium are co-deposited as a thin film, which will be covered in more depth in Chapter 6.

4.2 Bulk Aluminium Macroelectrodes

4.2.1 Bulk Aluminium Macroelectrode in LKE

It is of importance to determine the potential window available when using aluminium as an electrode. A typical CV of LKE on an inert electrode, in this case tungsten, can be seen in the left hand graph of Figure 4.1. There are two electrochemical features in the CV: at the positive end there is the oxidation of chloride at approximately 1.2 V; at the negative end there is plating and stripping of lithium at approximately -2.5 V. This gives a total solvent potential window of approximately 3.7 V in LKE. The right hand graph in Figure 4.1 also shows typical CVs of an aluminium wire in LKE with no added redox species. Above -1.2 V the positive current rapidly increased (α'), indicating the oxidation of Al^0 to Al^{3+} (stripping). The reverse reaction (α) was also seen, i.e. the reduction of Al^{3+} back to Al^0 (plating). These currents increased with scan rate as expected. Negative of -2 V there was an increase in the reduction current (β). Below -2.3 V the reduction current increased rapidly and a nucleation loop was seen (γ). On the reverse sweep, there was a sharp oxidation peak (γ') followed by a broad peak/shoulder (β'). Both the β/β' and γ/γ' reactions are attributed to lithium reduction/oxidation processes.

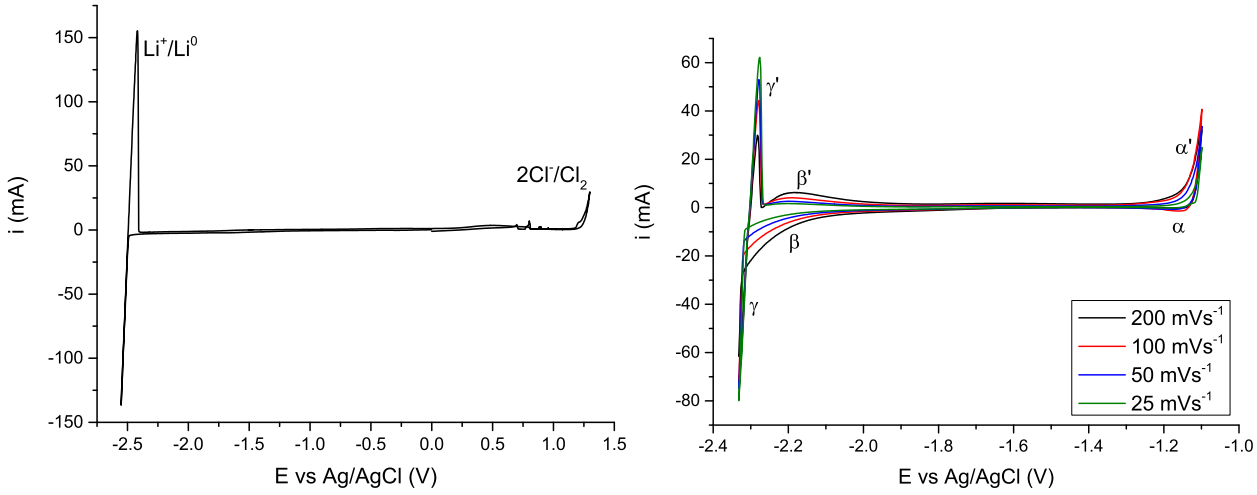

Figure 4.1: (Left) CVs of a tungsten macroelectrode (d = 2 mm), ν = 200 mVs^{-1}. (Right) CVs of a bulk aluminium macroelectrode (d = 1 mm) immersed in LKE. T = 723 K.

Figure 4.2 shows the phase diagram for the lithium-aluminium binary system. At the operating temperature of 723 K the following states are thermodynamically stable depending on the local composition: pure Al, lithium dissolved in aluminium, LiAl, Li_3Al_2, aluminium dissolved in lithium, and pure lithium. It should be noted that the phase diagram assumes that the system is at equilibrium (thermodynamic control), however the electrochemical system is not at equilibrium (phase change kinetic control). There is also a difference between the global composition (volume of aluminium electrode versus quantity of reduced lithium) and the local composition (lithium concentration in the surface layer of the electrode). This makes it difficult to determine whether reaction β is the formation of lithium dissolved in aluminium (alloy), the LiAl or Li_3Al_2 intermetallic compounds, or aluminium dissolved in lithium (alloy), since all are predicted to exist between the compositions of pure aluminium (α/α') and pure lithium (γ/γ'). Formation of these alloys/intermetallic compounds requires a phase change, i.e. insertion into a host metal lattice and/or nucleation followed by crystal growth, which may be sufficiently slow to not be observed, or not occur at all, during the CV as the composition at the electrode surface varies from pure aluminium to pure lithium. The phase diagram is however useful in determining the phases that should form, if the system were given enough time to reach equilibrium and crystallisation to occur, i.e. during chronoamperometry or chronopotentiometry at longer timescales.

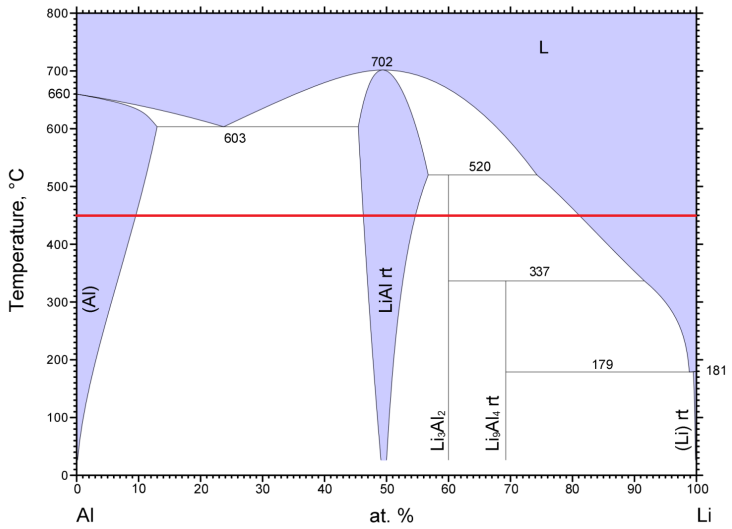

Figure 4.2: Lithium-aluminium binary phase diagram.[86] Red line marks the operating temperature of experiments. White areas are mixed phase zones, blue areas are single phase zones.

The β/β' reaction was attributed to the formation of a lithium-aluminium alloy since it was the first reaction observed in the CVs and lithium-aluminium alloy is the first possible phase that can be formed according to the phase diagram. The reduction β had reduction currents proportional to $\nu^{0.5}$ (left hand graph in Figure 4.3) which indicated the reaction was controlled by mass transport. Since Li^+ is the solvent ion it is unlikely

to become diffusion limited, however the reaction may have been be controlled by diffusion of lithium metal within the aluminium. The oxidation currents also increased with scan rate but this proportionality deviated slightly from $\nu^{0.5}$.

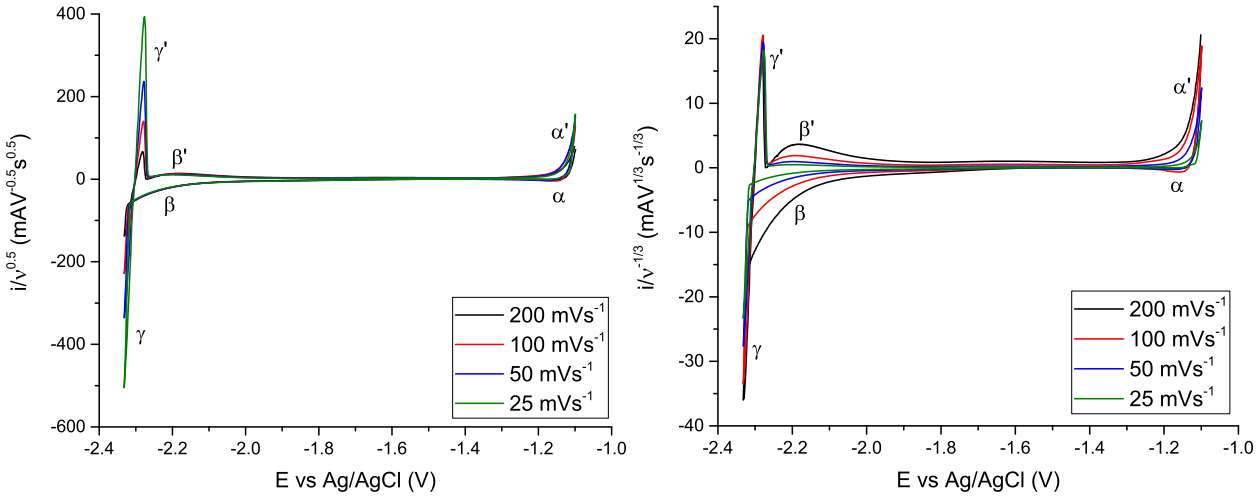

Figure 4.3: CVs from the right hand graph of Figure 4.1 with the current divided by ν^x. (Left) $x = 0.5$, showing that β is a diffusion limited reaction. (Right) $x = -\frac{1}{3}$, showing that the stripping of pure lithium (γ') is heavily influenced by amount of alloy formed before lithium plating occurs (β).

The γ/γ' reaction was attributed to the plating of pure metallic lithium rather than the formation of a high lithium content lithium-aluminium alloy due to no other reaction being observed at more negative potentials. The approximate +0.2 V shift of the lithium plating potential relative to the tungsten electrode deposition can be explained by the lithium-aluminium surface of the electrode being "lithium-like" which decreases the energy required to plate lithium. This same shift was seen for bismuth alloying into a platinum microelectrode versus plating on an inert tungsten microelectrode, due to bismuth-platinum alloys having formed.[8,87] The nucleation loop can be explained as an overpotential being required to initiate lithium plating onto a mixed lithium-aluminium surface, before some metallic lithium is able to insert into the lithium-aluminium layer and increase the lithium content, stabilising the pure lithium layer and causing a positive shift in its oxidation potential. It should be noted that the potential at which the γ reaction started became more negative at higher scan rates. This was due to less time spent reducing lithium during reaction β at faster scan rates, as so there was less lithium in the lithium-aluminium surface, requiring more energy (more negative potentials) to initiate pure lithium plating. The gradients of γ at each scan rate were the same, which was further evidence that this reaction was due to pure lithium plating, which would not be diffusion limited, rather than formation of lithium-aluminium alloy which would likely be diffusion limited by Li^0 diffusion inside the aluminium. It is interesting to note that the peak current of γ' decreased with scan rate, which is the opposite of expected behaviour. This can be explained by less time spent producing lithium-aluminium alloy

at higher scan rates, and so when pure lithium metal was plated a lot more of that pure metal can insert into the alloy leaving less lithium to be stripped on the back scan. This effect is so great that it inverts the usual proportionality $i_p \propto \nu^{0.5}$ to $i_p \propto \nu^{-\frac{1}{3}}$ (right hand graph of Figure 4.3). The value of $-\frac{1}{3}$ was determined by a plot of $ln(i_{p\,\gamma'})$ versus $ln(\nu)$ which yielded a gradient of -0.34 ± 0.06. This inversion of proportionality has been observed within the group in other systems which have one metal plating onto an alloy containing itself (Al onto Pt, Bi onto Pt), which may make this behaviour a useful diagnostic tool for understanding electrochemistry on alloyed electrodes. Whether the relationship is always $i_p \propto \nu^{-\frac{1}{3}}$ would need to be investigated for this diagnostic use, but it is not within the scope of this thesis.

4.2.2 First Cerium-Aluminium Alloying Reaction on a Bulk Aluminium Macroelectrode

In this work cerium is being studied as a non-radioactive surrogate for plutonium, as both undergo a concerted three electron reduction at similar potentials.[22] Typical CVs of $CeCl_3$ on a bulk aluminium macroelectrode can be seen in Figure 4.4. The peaks A/A' were the first (most positive) alloying reaction seen, and was tentatively attributed to the formation of Ce_3Al_{11}, the first intermetallic compound seen in the aluminium-cerium phase diagram (Figure 4.5).[62] Unlike the aluminium-lithium binary system, there is no thermodynamically stable amorphous cerium-aluminium alloy (either cerium dissolved in aluminium or aluminium dissolved in cerium), only thermodynamically stable crystalline intermetallic compounds (Ce_xAl_y) with particular stoichiometries. The onset potentials of reduction, and the initial reductive currents, were independent of scan rate, whilst the reduction peak potentials ($E_{p\,A}$) and currents ($i_{p\,A}$) varied with scan rate. This pointed towards the reduction being kinetically limited, due to nucleation of the Ce_3Al_{11} crystal phase. The oxidation peak A' was much more symmetrical, which was consistent of a small iR drop. This pointed towards the oxidation being a thermodynamically controlled reaction. The background current (non Faradaic current passed before the onset of Faradaic current) was found to be linear with potential, and was subtracted by using the baseline of the forward scan between -1.45 and -1.55 V on each CV. On all future macroelectrode CVs the background current behaviour is very similar. Presented CVs will have already been background corrected.

From the Delahay equation (Equation 2.10) the peak current will vary with the square root of the scan rate if it is diffusion limited. Figure 4.6 shows that a basic linear regression of i_p versus $\nu^{0.5}$ yielded a straight line fit as expected by a diffusion limited soluble-insoluble reaction. From the slope of the reduction data

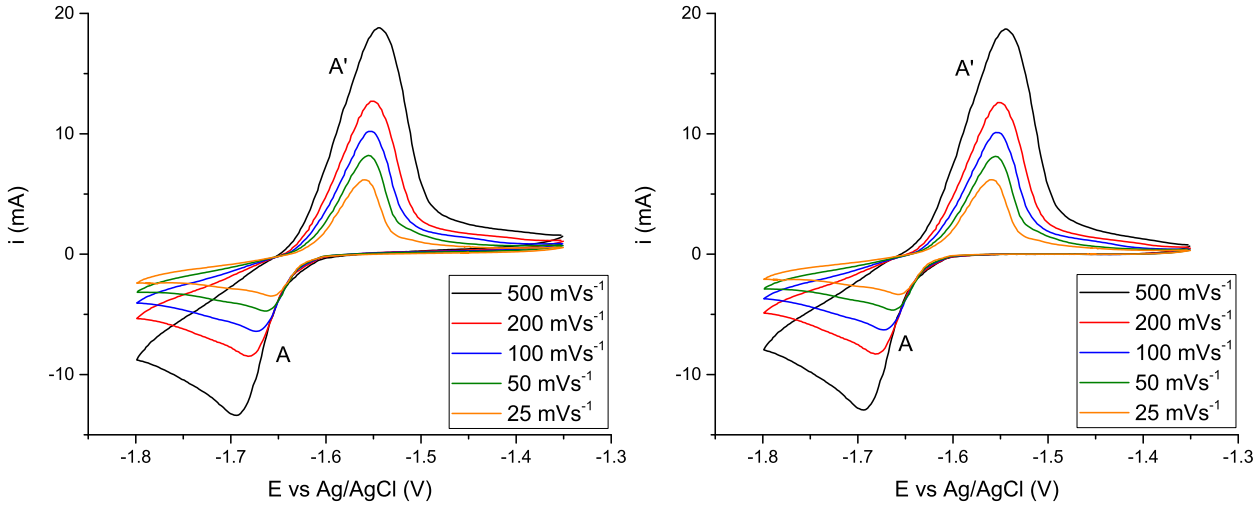

Figure 4.4: CV of $[CeCl_3]$ = 55.4 mM on a bulk aluminium macroelectrode, d = 1 mm, T = 723 K. (Left) Before and (Right) after linear background subtraction using -1.45 to -1.55 V.

the concentration of $CeCl_3$ was calculated to be 25.57 ± 0.43 mM, which was approximately 46% of the amount added. It is highly likely that there is some significant kinetic factor for cerium inserting into the solid aluminium lattice, which lowers the rate of cerium reduction. It has also been observed in experiments performed with optical windows (not shown) that bubbles form on the aluminium surface which could not be removed, resulting in a smaller surface area. If the smaller surface area was taken into account, the calculated concentration should approach the amount added.

Semi-integral convolution (Equation 2.12) provides another method of checking whether a reaction is under diffusion control. In effect the mathematical operation converts macroelectrode data to resemble microelectrode data by integrating with respect to $t^{0.5}$. If the reaction was purely under diffusion control, a reduction peak in the CV should become a limiting current in the convolved CV. Figure 4.7 shows the convolved CVs of Ce^{3+}/Ce^0 on aluminium. The reduction convolved current did lose its peak shape, but did not become limiting (or even give a straight line), and continued to increase in magnitude as the potential became more negative. This remained the case for all scans performed. This, as well as the current after $E_{p\,A}$ in Figure 4.4 not decreasing as rapidly as expected by a diffusion limited reaction, implied that the alloying reaction was under diffusion control of Ce^{3+}at $E_{p\,A}$, but after the peak the kinetics of cerium insertion (and thus kinetics of a phase change), in combination with an increasing surface area, was controlling the rate of reduction. As the reaction switches from being controlled by electron transfer to mixed control ($E_{p\,A}$) a diffusion field is expected to form as diffusion becomes a significant factor in the overall rate of reaction. This is why diffusion control is observed from the plot of $i_{p\,A}$ versus $\nu^{0.5}$ in Figure 4.6. At more negative potentials, as more cerium insertion occurs the surface would have roughened, which increased the active

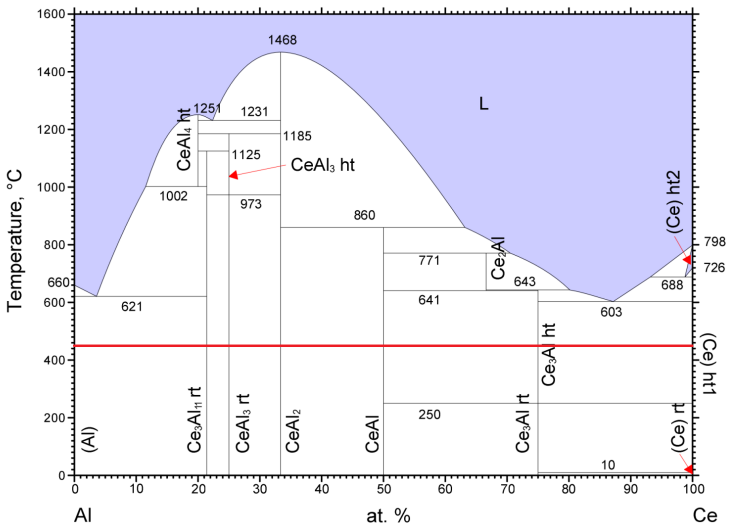

Figure 4.5: Cerium-aluminium binary phase diagram.[62] Red line marks the operating temperature of experiments. White areas are mixed phase zones, blue areas are single phase zones.

surface area and may have lowered the kinetic barrier for the formation of a Ce_xAl_y phase in the surface layer for repeat CVs. If the phase formation was significantly slower than diffusion of Ce^{3+} to the electrode, then this kinetic barrier would dictate the rate of reaction. As further cerium insertion occurred and this kinetic barrier lowered, the reduction current in the CV remained greater than expected as the diffusion field was not limiting the reaction, i.e. there is more Ce^{3+} at the surface than would be expected for a pure plating reaction. It was difficult to measure this kinetic barrier, especially as it changed with repeated use of the electrode. In such a large volume electrode there is likely to always be more bulk aluminium that has a large kinetic barrier to alloying, alongside aluminium nearer the interface that has a lowered kinetic barrier due to multiple alloying/de-alloying cycles. The global kinetic barrier would then be a mixture of the two local kinetic barriers.

While the reduction currents proved difficult to analyse to obtain the $CeCl_3$ concentration, the oxidation reaction may provide some useful information about alloying behaviour. The measured E_p were affected by iR drop. At higher scan rates with higher currents, the voltage required to drive the reduction reaction shifted negatively. Conversely the oxidation peak potentials shifted positively. For a purely thermodynamically controlled reaction, the only resistance expected in the voltammetry would be due to the solution resistance, R_s. R (the apparent resistance) for each reaction was determined by a plot of E_p versus i_p for each scan rate (Figure 4.8). The apparent resistance for the reduction, $R_A = 4.41 \pm 0.23\ \Omega$, was significantly greater than that of the oxidation, $R_{A'} = 0.89 \pm 0.08\ \Omega$. If both reactions were purely controlled by the thermodynamics then the apparent resistances would be small and very similar. While the reduction reaction was affected

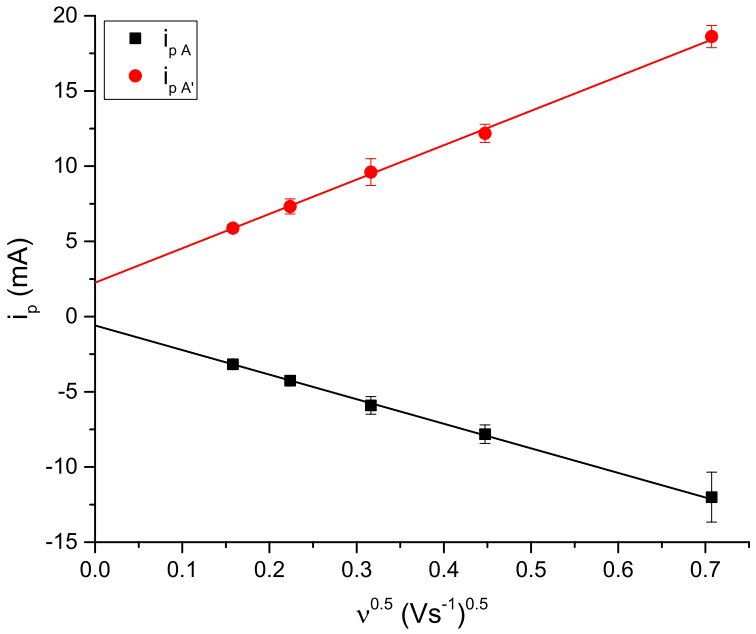

Figure 4.6: i_p versus $\nu^{0.5}$ for the cerium intermetallic reaction A/A' seen in Figure 4.4. Solid lines are linear regressions extrapolated to $\nu^{0.5} = 0$.

by iR drop, there were also kinetic factors which cause the higher apparent resistance of the reduction reaction. $R_{A'}$ was greater than $R_{\alpha'}$ (stripping of pure aluminium off a tungsten electrode, Figure 4.18) and so the apparent resistance of alloy oxidation was not solely due to R_s. This implied that there was some contribution of kinetics to the oxidation reaction, as the aluminium structure must have changed during de-alloying of cerium, however this kinetic factor appeared to be far less than for the reduction reaction. The oxidation reaction looked to be controlled more by thermodynamics than kinetics, as the peak was very symmetrical. Therefore $R_{A'}$ may be used to perform iR drop correction for further analysis.

Figure 4.9 shows the effect of performing iR correction using $R_{A'}$. The iR corrected CVs confirmed that peak A' was highly symmetrical and thus mostly thermodynamically controlled. The thermodynamic peak shape for the oxidation of a monolayer is given by:[8]

$$i = \frac{2i_p}{\left(1 + cosh\left[\frac{nF\{E-E_p\}}{RT}\right]\right)} \tag{4.1}$$

Figure 4.10 shows CVs iR drop corrected with $R_{A'}$ and then normalised ($i/i_{p\,A'}$). The oxidation peaks did not completely superimpose, rather the peak width broadened at higher scan rates. As they did not superimpose over different scan rates, this indicated that there was some difference in surface energies/surface coverage which was expected from a kinetically limited alloy formation which spent less time forming the alloy at

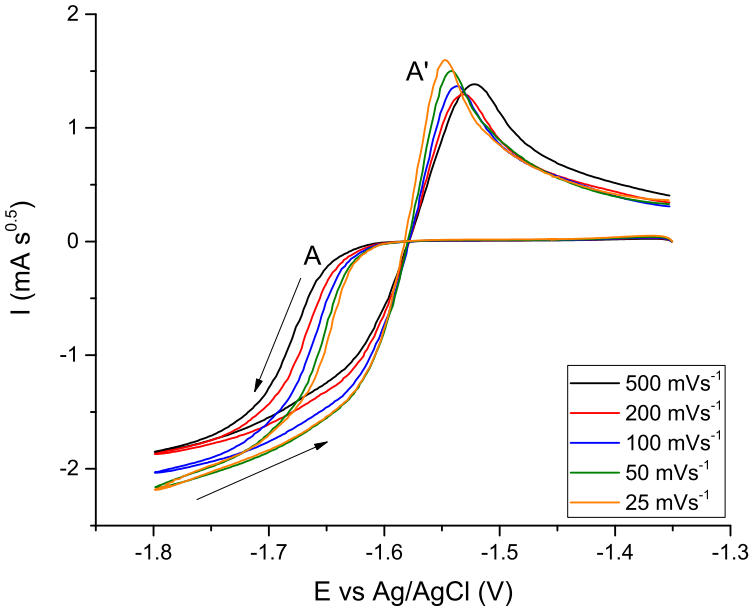

Figure 4.7: Semi-integral convolution of Figure 4.4.

faster scan rates. By fitting the oxidation peaks to Equation 4.1, n (which determines the peak width) was obtained for each scan rate (Table 4.1).

From the peak fitting, n was found to increase as the scan rate decreased as expected. The oxidation reaction Ce^0/Ce^{3+} is known to be single step 3 electron transfer[22] and so for a monolayer of alloy the peak fit would give $n = 3$. The increasing values of n from the fits indicated a more homogeneous energy distribution rather than a real change in n. This can be rationalised as follows: at slower scan rates more total charge was passed during reduction, i.e. more alloy/intermetallic was formed and there was more time for coalescence of nucleation sites. Since the aluminium volume was effectively infinite on the timescales of these CVs, the diffusion depth of reduced cerium was almost certainly more than a monolayer, however the equation appeared to still be valid due to the low errors of the fits. The large volume of aluminium led to a larger volume of well connected alloy/intermetallic grains, thus a narrower distribution of energies and a sharper peak, which resulted in a a fitted n greater than expected for the redox reaction ($n = 3$ for Ce^{3+}). The fastest scan rates of 500 mVs^{-1} had an n value of less than 3. At short timescales it was more likely that only a monolayer depth of alloy was formed, however it was less likely to be a complete homogeneous layer, hence a wider distribution of energies (and wider peak) than expected.

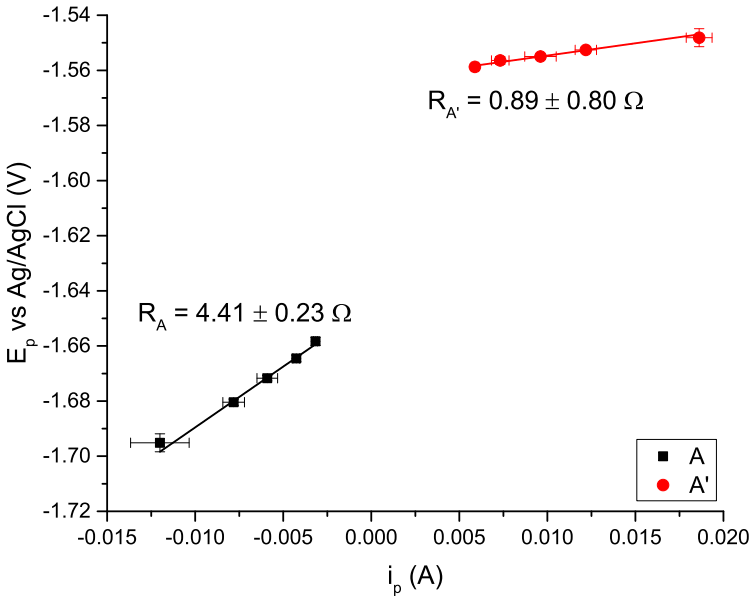

Figure 4.8: E_p versus i_p for the reaction of $CeCl_3$ on an aluminium electrode (Figure 4.4). The gradient of the linear regression gives the apparent resistance of the reaction.

Table 4.1: Fit values for peak A' in Figure 4.10 using Equation 4.1

Scan Rate (mVs^{-1})	500	200	100	50	25
n	2.77 ± 0.02	3.17 ± 0.02	3.49 ± 0.02	3.84 ± 0.02	4.21 ± 0.02
χ^2	7.30×10^{-4}	3.70×10^{-4}	3.52×10^{-4}	4.09×10^{-4}	3.97×10^{-4}
R^2	0.992	0.997	0.997	0.996	0.997

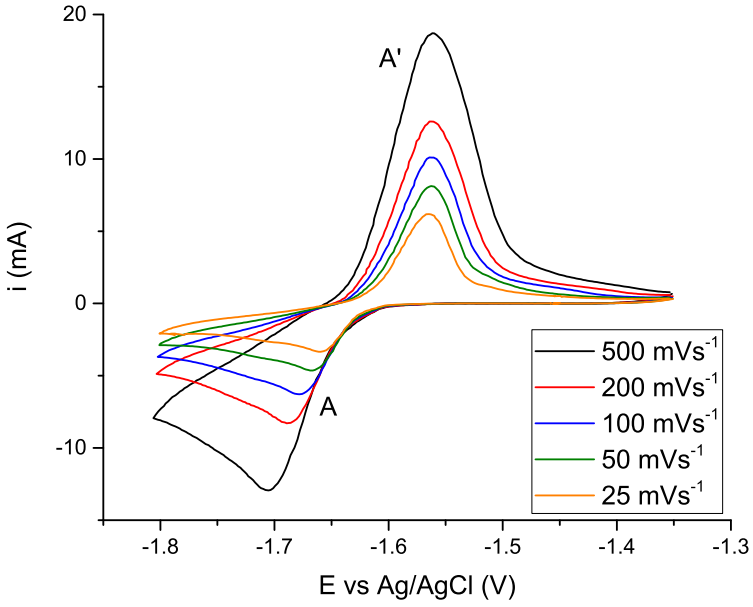

Figure 4.9: CVs of $[CeCl_3] = 55.4$ mM on a bulk aluminium macroelectrode ($d = 1$ mm) after iR drop correction using $R_{A'} = 0.89\ \Omega$.

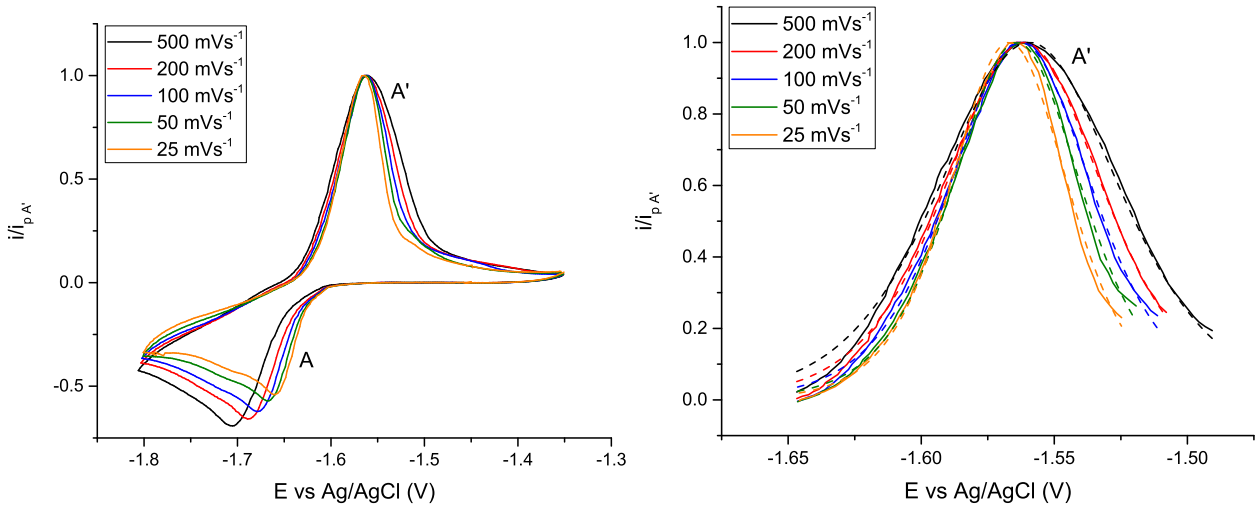

Figure 4.10: (Left) Normalised iR drop corrected CVs from Figure 4.9 using $R_{A'} = 0.89\ \Omega$. (Right) Peak fits (dashed lines) of A' using Equation 4.1.

Since there were significant differences between the reduction and oxidation reactions, it is worthwhile to determine the efficiency of the reaction. This is defined as:

$$Efficiency = |\frac{Q_{oxidation}}{Q_{reduction}}| * 100 \tag{4.2}$$

where Q is the charge passed for each reaction. This specific equation assumes that the reduction is the forward (first) reaction, and oxidation is the reverse (second) reaction. An efficiency of <100% would signify incomplete oxidation due to kinetics of a plating/stripping or alloying reaction, or some of the reduced species became detached from the electrode (e.g. dendrites which are mechanically unstable). The efficiency for the A/A' reaction for each scan rate is shown in Figure 4.11. Average values and standard deviations were obtained from all 10 CVs at each scan rate, excluding the first CV at each scan rate as these gave efficiency values $\gg$100%.

The efficiency increased linearly with scan rate. 100% efficiency would be reached at approximately 930 mVs^{-1} if the trend remained linear over the whole range of scan rates. A possible explanation for this trend in an alloying reaction is that the alloy was mechanically unstable and nano-rough, and so could detach from the electrode surface leaving less cerium to be oxidised on the reverse scan. At slower scan rates the alloy would form deeper into the aluminium, resulting in rougher and less mechanically stable alloy at the surface which detach more easily. This is important for bulk extraction as it is desirable to recover elements quickly without forming mechanically unstable deposits. For this purpose it would be necessary to investigate the relationship between the mechanical stability of the alloy and the rate of formation of the alloy, e.g. by using chronopotentiometry at a number of applied currents to completely fill an aluminium electrode. However this is not within the scope of this thesis.

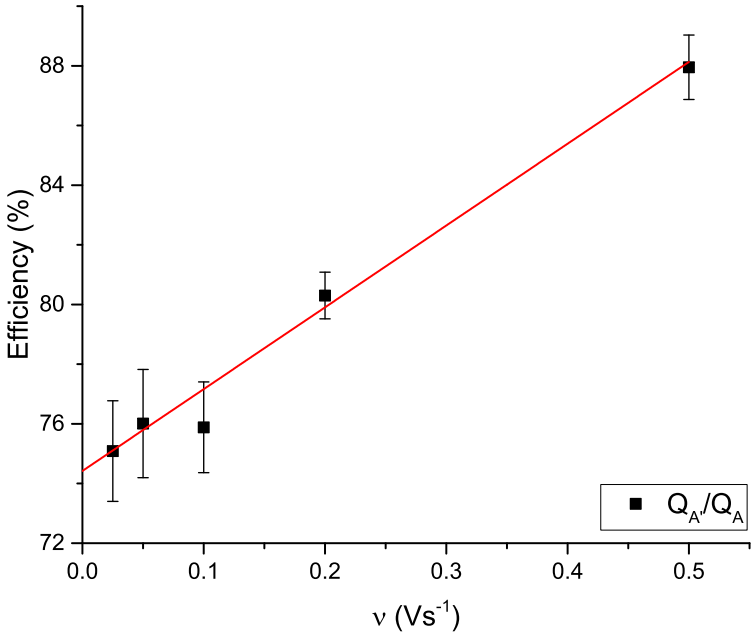

Figure 4.11: Efficiency versus ν for the CVs from Figure 4.4. Red line is a linear regression. Error bars are 1σ based on 9 CVs.

4.2.3 Cerium-Aluminium Alloying on a Bulk Aluminium Macroelectrode Using Wider Potential Windows

For the purposes of sensing, it is important to know if more than one set of reactions can be observed over the entire aluminium potential window. For example, if the A/A' reaction were due to Ce_3Al_{11}, then formation of more cerium rich intermetallic compounds may give separate reaction peaks. In a real refining system there will be multiple signals corresponding to different analytes. It would be useful to be able to see the formation of multiple crystalline intermetallics for each analyte, giving a "fingerprint" that could be more easily identified or at least prevent misidentification of another species. It is known from XRD studies of constant potential and long time deposition from LKE-$CeCl_3$-$AlCl_3$ systems that at -1.9 V crystalline Ce_3Al_{11} and $CeAl_3$ will have formed, and at -2.1 V crystalline $CeAl_3$, $CeAl_2$ and CeAl will have formed.[38] It is interesting to note that no Ce_3Al_{11} was detected from the deposit formed at -2.1 V which indicates that if a high enough concentration of cerium is present within aluminium there can be a complete conversion of low cerium content intermetallics to higher cerium content intermetallics. Liu *et al.* found from co-deposition CVs that three sets of reduction/oxidation reactions were observed between the aluminium and cerium plating reactions.[37] From reduction of $CeCl_3$ into an aluminium electrode at a constant potential of -1.6 V for 1 hour, followed by XRD after cooling, Ce_3Al and CeAl (the two most cerium rich Ce_xAl_y intermetallic compounds) were found to have been formed, despite only one alloy reaction in the CV run to -1.6 V.[36]

The formation of more cerium rich intermetallic compounds were investigated by scanning more negatively (Figure 4.12). Only one new reaction was observed on these wider potential windows that could correspond to a reaction of cerium: δ/δ'. The reduction (δ) showed a linear increase in reductive current with potential after the curved increase of β. The corresponding oxidation (δ') was a peak. The couple δ/δ' was attributed to pure cerium metal plating/stripping due to the similarity to the potentials seen on a tungsten electrode (Figure 4.20). It was not attributed to more cerium rich intermetallics, as they would be expected to give well defined peaks as seen for A/A'. This appearance of the pure metal deposition on top of metal-aluminium alloys has been observed previously on aluminium electrodes.[33, 66, 84]

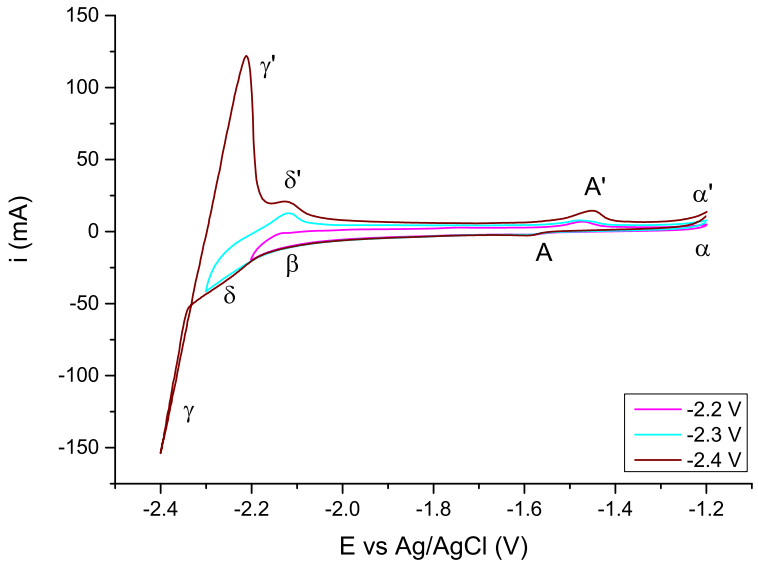

Figure 4.12: CVs of [$CeCl_3$] = 55.4 mM on a bulk aluminium macroelectrode, d = 250 μm, ν = 100 mVs^{-1}, T = 723 K.

Figure 4.13 shows the effect of decreasing the lower vertex potential (the potential at which the CV scan is reversed). Very small features around -1.8 V (B/B') were observed that may have been the formation/decomposition of $CeAl_3$, it being the second intermetallic compound that is expected to be formed. This is consistent with Wang *et al.*[38] that the first two intermetallics can form when the potential is negative of -1.9 V. The reduction peak was only observed on a single scan, whereas the oxidation peak was observed over a few potential windows. When the lower vertex potential was more negative that -2.2 V, the oxidation δ' was observed on the reverse scan, and the B' reaction was not longer observed. Due to the large volume of the aluminium wire, it may have been difficult to reach the concentration of cerium in aluminium necessary to form $CeAl_3$, i.e. if the cerium is able to diffuse to regions of lower cerium concentration only a small amount of $CeAl_3$ would form. Since the diffusion coefficient of cerium in aluminium is unknown, it is difficult to say how far cerium could diffuse away from the interface and thus how thick the alloy layer is

versus the radius of the electrode. The formation of more cerium rich intermetallic compounds were negligible in these experiments, and so only one crystalline intermetallic formed due to the large contribution of kinetics in the insertion of cerium into aluminium.

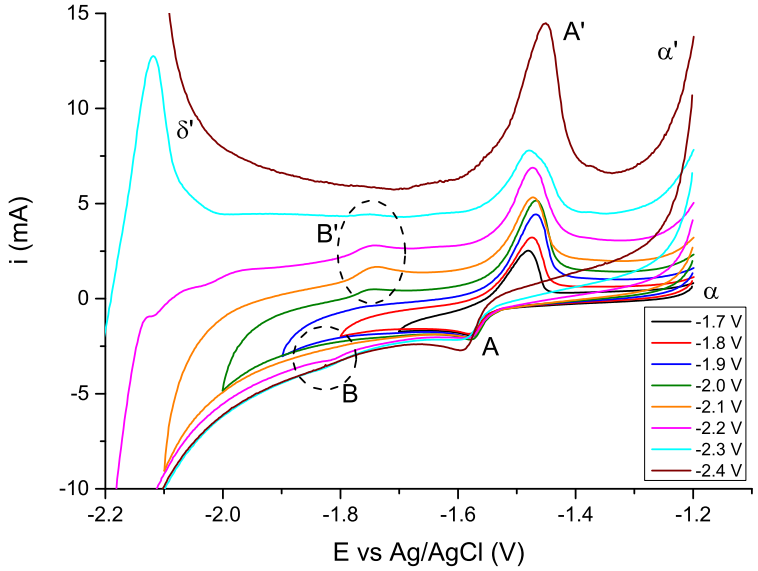

Figure 4.13: CVs of $[CeCl_3]$ = 55.4 mM on a bulk aluminium macroelectrode, d = 250 μm, ν = 100 mVs^{-1}, T = 723 K as lower vertex potential is scanned negatively.

The cerium-aluminium alloy oxidation peak potential A' stayed roughly constant at different lower vertex potentials, whereas the lithium oxidation peak potential γ' shifted positively at more negative lower vertex potentials. This implied that the lithium oxidation was controlled by kinetics of electron transfer, but the cerium-aluminium alloy oxidation was controlled by the thermodynamics. A feature of soluble-insoluble (alloying/plating) reactions that should be noted is that while the cerium reduction peak height A was almost unchanged as the lower vertex potential is decreased, the oxidation peak height A' increased due to an increase in deposition time and therefore an increase in the quantity of cerium reduced.

Figure 4.14 shows the moles of cerium oxidised from A' as a function of both lower vertex potential and time. From -1.7 to -2.1 V the trend was linear as expected by diffusion limited reduction of Ce^{3+}. Negative of -2.1 V the quantity of cerium oxidised deviated significantly from linear behaviour. These potentials corresponded to observations of lithium alloying as well as pure cerium plating. Since cerium insertion into aluminium is slow due to a large kinetic barrier, and so the alloy formation may not have been diffusion limited by Ce^{3+}, applying the potential required for pure cerium plating would result in more cerium being reduced than at all intermetallic compound formation potentials. This "excess" cerium may then spontaneously alloy with the aluminium, in the same way as with lithium metal plated onto lithium-aluminium alloy. It was also possible that when lithium-aluminium alloy was oxidised, cerium was more readily able to insert into the lithium

vacancies, i.e. there was a lower kinetic barrier to replace the metal in the alloy than to insert a metal into pure bulk aluminium. The large currents from lithium insertion were also likely to result in roughening the aluminium electrode more rapidly than through cerium insertion. This would have resulted in a larger area for further cerium insertion after oxidation of the lithium-aluminium alloy.

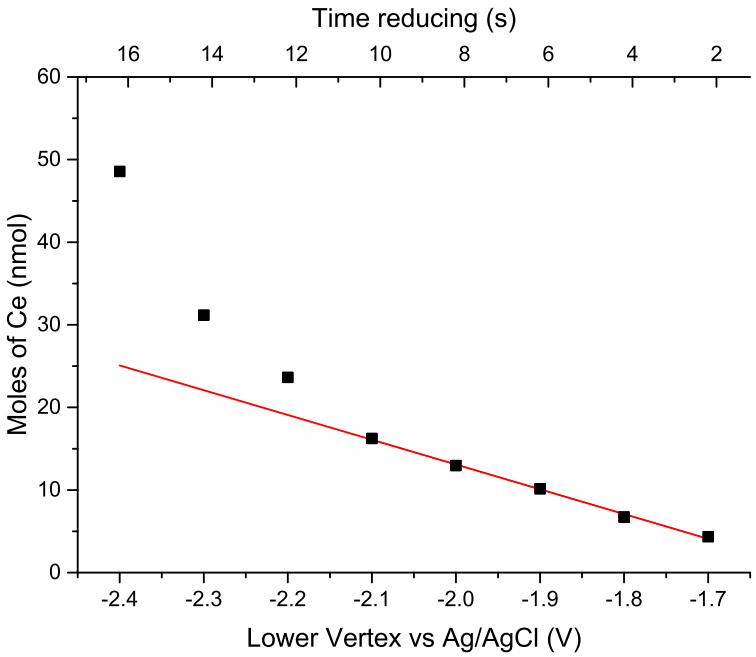

Figure 4.14: Moles of cerium oxidised as a function of lover vertex (inversion) potential, from CVs in Figure 4.13 and . Red line is a linear regression fitted between -1.7 and -2.1 V, extrapolated to -2.4 V.

4.3 $AlCl_3$ and $CeCl_3$ Co-deposition on Tungsten Macroelectrodes

The bulk aluminium macroelectrode electrochemistry was complicated by kinetic factors during the CV: slow cerium insertion into the aluminium lattice and roughening of the surface area. To better understand the thermodynamics of the cerium-aluminium alloying system, and determine if the $CeCl_3$ concentration can be determined, it is beneficial to co-deposit $AlCl_3$ and $CeCl_3$. By reducing both species together, the alloy composition should be dictated by the ratio of flux of each species to the electrode surface. This should lower the kinetic barrier to the intermetallic formation, allowing more intermetallics to be observed. This in turn would allow a study of how the $CeCl_3$ concentration affects the electrochemical response, which is critical for real time monitoring.

4.3.1 Electrochemical Dissolution to Introduce $AlCl_3$ to LKE

The introduction of a specific amount of $AlCl_3$ into the melt was difficult due to the set up used in this work, which consisted of flowing argon through a cell inside a furnace surrounded by air. Initial attempts added $AlCl_3$ to LKE powder before melting. Residual oxygen/water in the salt resulted in substantial formation of Al_2O_3 thus the true concentration of $AlCl_3$ was not known. Similarly adding $AlCl_3$ powder to pre-cleaned solidified LKE also resulted in the same reaction occurring, as the cell had to be exposed to air in order to add the $AlCl_3$. Previous work in the group oxidised an aluminium electrode into LKE as a cleaning step to remove residual oxygen and water as Al_2O_3.[88] In the current work this technique was used to introduce a known quantity of $AlCl_3$ into a pre-cleaned salt by passing a fixed current for a set amount of time. 205.2 mA for 15 minutes was chosen to reach an $AlCl_3$ concentration of 21 mM (Figure 4.15). In later work 292.8 mA for 10 minutes was used to reach 20 mM $AlCl_3$. In cases where other concentrations were desirable, the time was scaled, rather than the stripping current.

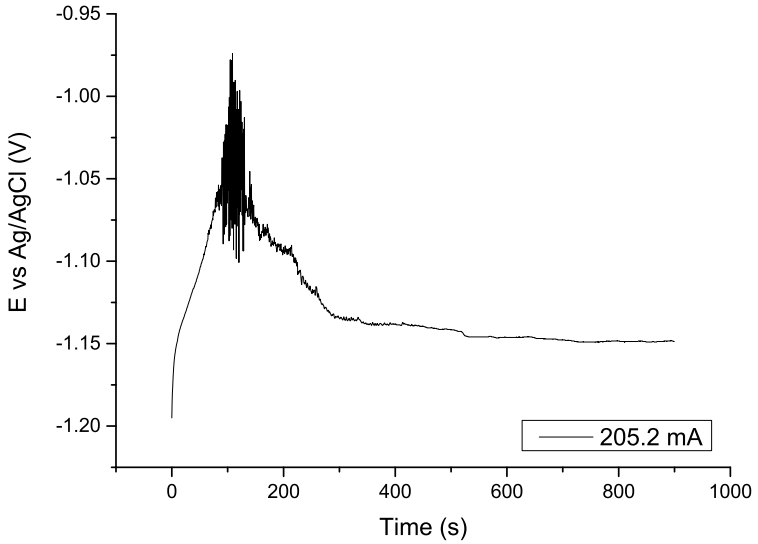

Figure 4.15: Electrochemical dissolution of a bulk aluminium macroelectrode by constant current oxidation to produce $[AlCl_3] = 21$ mM.

Prior to performing the electrochemical dissolution stripping of aluminium, CVs were first performed on the aluminium electrode to confirm it was immersed and not in contact with any other electrodes. The spikes in the potential seen within the first 200 s were not always observed on strippings of other aluminium electrodes. It may be that the spikes in potentials were caused by the native oxide, Al_2O_3, which is less conductive that aluminium, thus a higher voltage was required to maintain the stripping current. The native oxide may be partially removed by CVs to the aluminium solvent window (Al^{3+}/Al^0 at the positive end and Li^+/Li^0 on the negative end) before electrochemical dissolution, thus different numbers of CVs beforehand may be the

reason why the spikey region was not always observed. The spikey region of Figure 4.15 is still of interest as the mechanism by which the passivating Al_2O_3 layer is removed, or loses its passivity, is required for the performance of aluminium microelectrodes (Section 7.3).

The potential that was tended to at longer timescales is slightly more positive than the aluminium OCP (approximately -1.3 V). This positive offset of potential was consistent with aluminium oxidation and dissolution and was related to the surface area of the electrode; if immersed further the potential shifted negatively and vice versa. Since a large current was being passed, if the initial immersion depth was small the potential tended upwards rapidly after some time, and could reach the positive potential limit of the solvent window: +1.2 V. It was therefore important to maximise the area of aluminium immersed in the salt before beginning the electrochemical dissolution, to avoid oxidation of the solvent.

4.3.2 LKE-$AlCl_3$ on Tungsten Macroelectrodes

Figure 4.16 shows typical CVs on a tungsten electrode in LKE-$AlCl_3$. α/α' was attributed to the reaction of Al^{3+}/Al^0,[38, 89] β was attributed to the reduction of lithium ions to form amorphous lithium-aluminium alloy, and γ/γ' was attributed to the formation of Li_xAl_y intermetallic, the same reactions as on a bulk aluminium macroelectrode (Figure 4.1). These reactions (except for β) have previously been reported around these potentials on inert electrodes.[35, 38, 90] The reactions β and γ/γ' here had peak shapes and were much more symmetrical than those observed for lithium reductions on a bulk aluminium macroelectrode, highlighting the improved ability of co-deposition to lead to thermodynamically controlled phase formation. It was not possible to discern an oxidation β' peak. Two potential windows were studied: one with only the plating/stripping reaction of $AlCl_3$; the second covering the aluminium plating/stripping and Li_xAl_y intermetallic reactions.

Table 4.2 shows the efficiency of the aluminium plating/stripping reactions in Figure 4.16. The efficiency was 100% within experimental error at all scan rates.

Table 4.2: Efficiency of the α/α' (Al^{3+}/Al^0) reaction in Figure 4.16 over the narrow potential window.

Scan Rate (mVs^{-1})	500	200	100	50
Efficiency (%)	99.5 ± 5.4	92.8 ± 5.1	94.1 ± 6.2	89.2 ± 5.2

Figure 4.17 shows i_p versus $\nu^{0.5}$ for the reactions observed in Figure 4.16. For the reaction β, the slope was zero within experimental error, hence this reaction was found to be scan rate independent. For the α/α' and γ/γ' reactions, the linear regression indicated diffusion control of the reduction reactions. The α reduction would be limited by the diffusion of Al^{3+}. The greater gradient for γ suggests that this reduction was limited

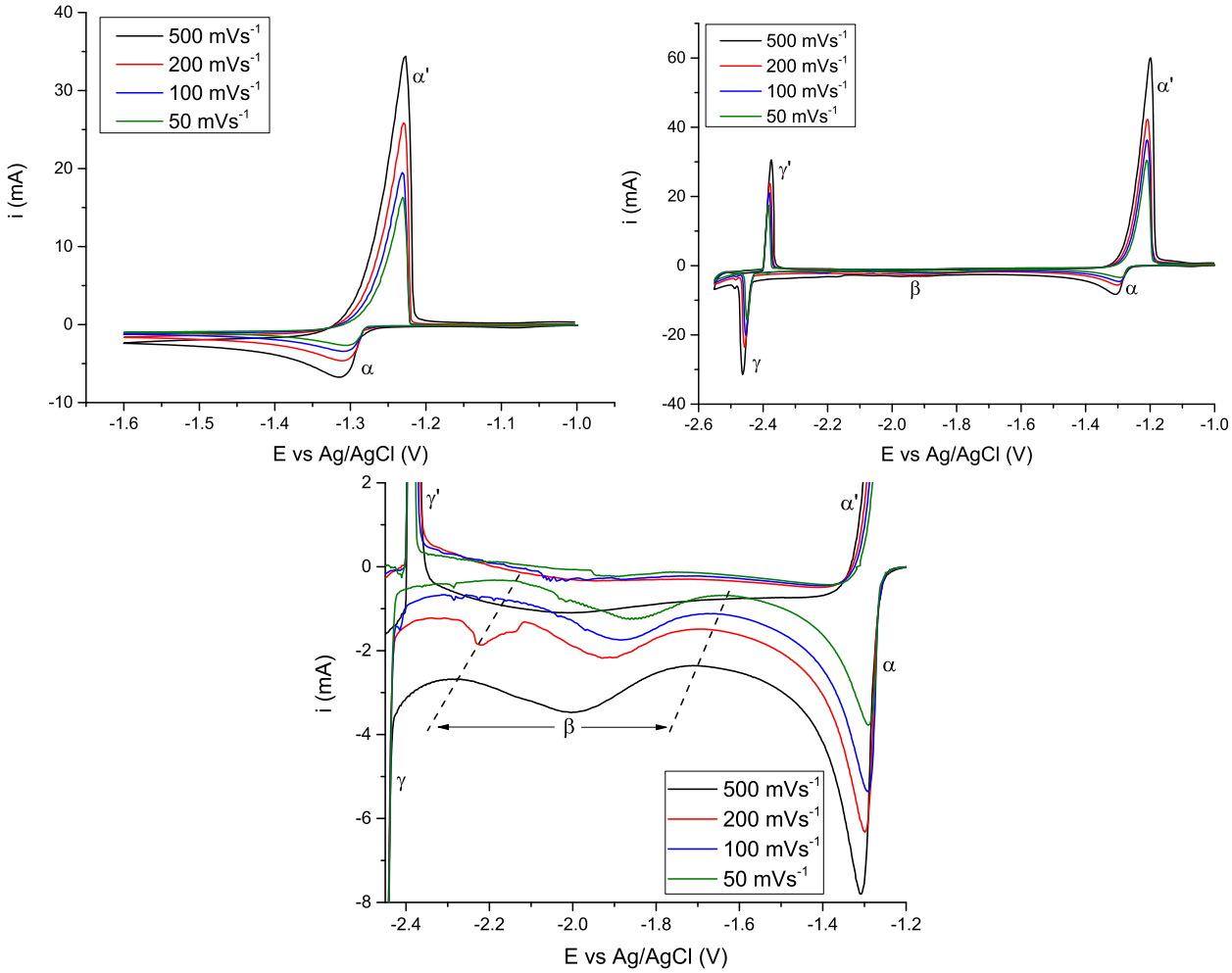

Figure 4.16: CVs of $[AlCl_3] = 21$ mM on a tungsten macroelectrode, $T = 723$ K. (Top Left) Potential window -1 to -1.6 V. (Top Right) Potential window -1 to -2.55 V. (Bottom) Zoom in of (Top Right).

by diffusion of lithium metal inside the aluminium, which must have been faster than the diffusion of Al^{3+} for the current to decrease.

It can be seen in Figure 4.16 that peak positions changed as a function of scan rate. As with the alloying reaction (Figure 4.4), there was some apparent resistance to the reactions which caused iR drop. Figure 4.18 shows the plots of E_p versus i_p for each reaction. The apparent resistances were found to be $R_\alpha = 2.20 \pm 0.18\ \Omega$ and $R_{\alpha'} = 0.16 \pm 0.01\ \Omega$ over the narrower potential window. Over the wider potential window the apparent resistances were $R_\alpha = 3.54 \pm 0.15\ \Omega$, $R_{\alpha'} = 0.37 \pm 0.01\ \Omega$, $R_\gamma = 0.89 \pm 0.01\ \Omega$, and $R_{\gamma'} = 0.81 \pm 0.01\ \Omega$. $R_{\alpha'}$ had the smallest values which were similar in magnitude to the resistance observed from stripping bismuth from a tungsten electrode (approximately 0.2 Ω).[8] This is of a reasonable magnitude for the solution resistance, R_s. Apparent resistances above this value must then have been due to phase changes kinetics, i.e. overpotential nucleation of aluminium on tungsten and/or insertion of lithium into

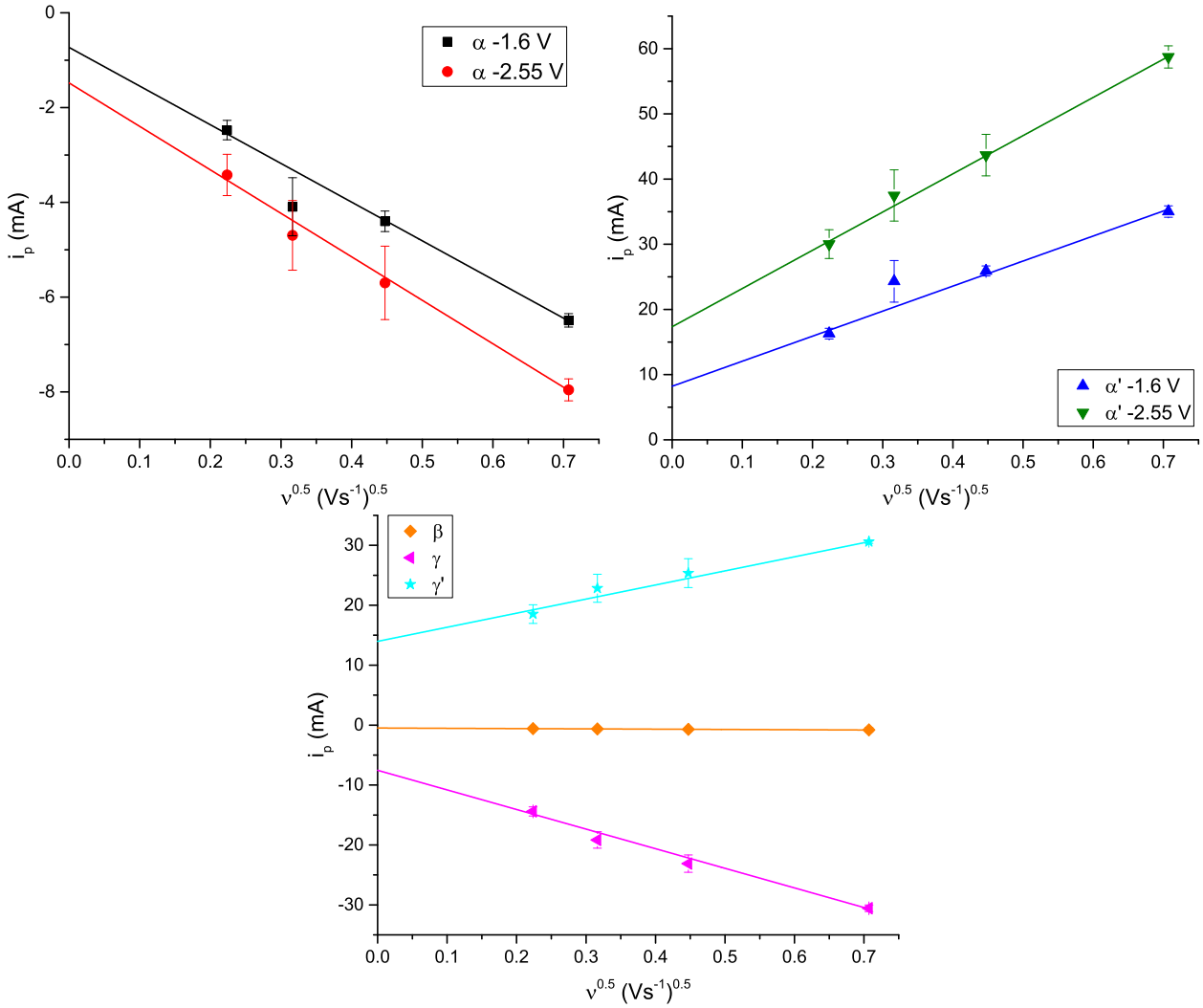

Figure 4.17: i_p versus $\nu^{0.5}$ for the reactions α/α', β and γ/γ' over both potentials windows in Figure 4.16. Solid lines are linear regressions extrapolated to $\nu^{0.5} = 0$.

the aluminium lattice. Similar kinetic limitations have been observed for the nucleation of solid plutonium onto tungsten during plating.[91] It appeared that repeat measurements lead to a change in the system, e.g. roughening of the tungsten surface due to repeated metal plating/stripping reactions, which caused R_α and $R_{\alpha'}$ to increase. It is therefore important to analyse the system every time a new experiment is performed to obtain accurate apparent resistances for iR correction, which complicates analysis for on-line monitoring.

For the oxidation of pure aluminium, iR correction showed that the peak was thermodynamically controlled, although the peak was not symmetrical. The reduction was clearly kinetically controlled as the apparent resistance was much higher and the currents at each scan rate after the onset potential followed the same curve (similar to the reduction of Ce^{3+} into an aluminium electrode). This was almost certainly the kinetics of nucleation of a solid aluminium film on the tungsten surface. The β reaction appeared to have a very

large resistance of over 600 Ω. This is unlikely to be a real resistance, but rather the peak potential become more positive at slower scan rates, due to a decrease in the potential required to initiate lithium reduction by alloying into thicker aluminium film. This idea was reinforced by the onset potential of β shifting significantly more positive with decreasing scan rate than the onset potentials for α and γ. R_{γ} and $R_{\gamma'}$ were very similar to each other, although were both significantly larger than the resistances for aluminium stripping. This implied some degree of phase change kinetics to these reactions, as also evidenced by the initial currents after the onset potential following the same curve. By having similar resistance it would seem that the kinetic barrier was equal in the forward and backward reaction. Although there was a kinetic barrier to lithium insertion, it was much smaller than the kinetic barrier to cerium insertion ($\Delta R \approx 3\ \Omega$). This makes sense as lithium has a much smaller metallic radius, and so would disrupt the aluminium lattice to a lesser extent.

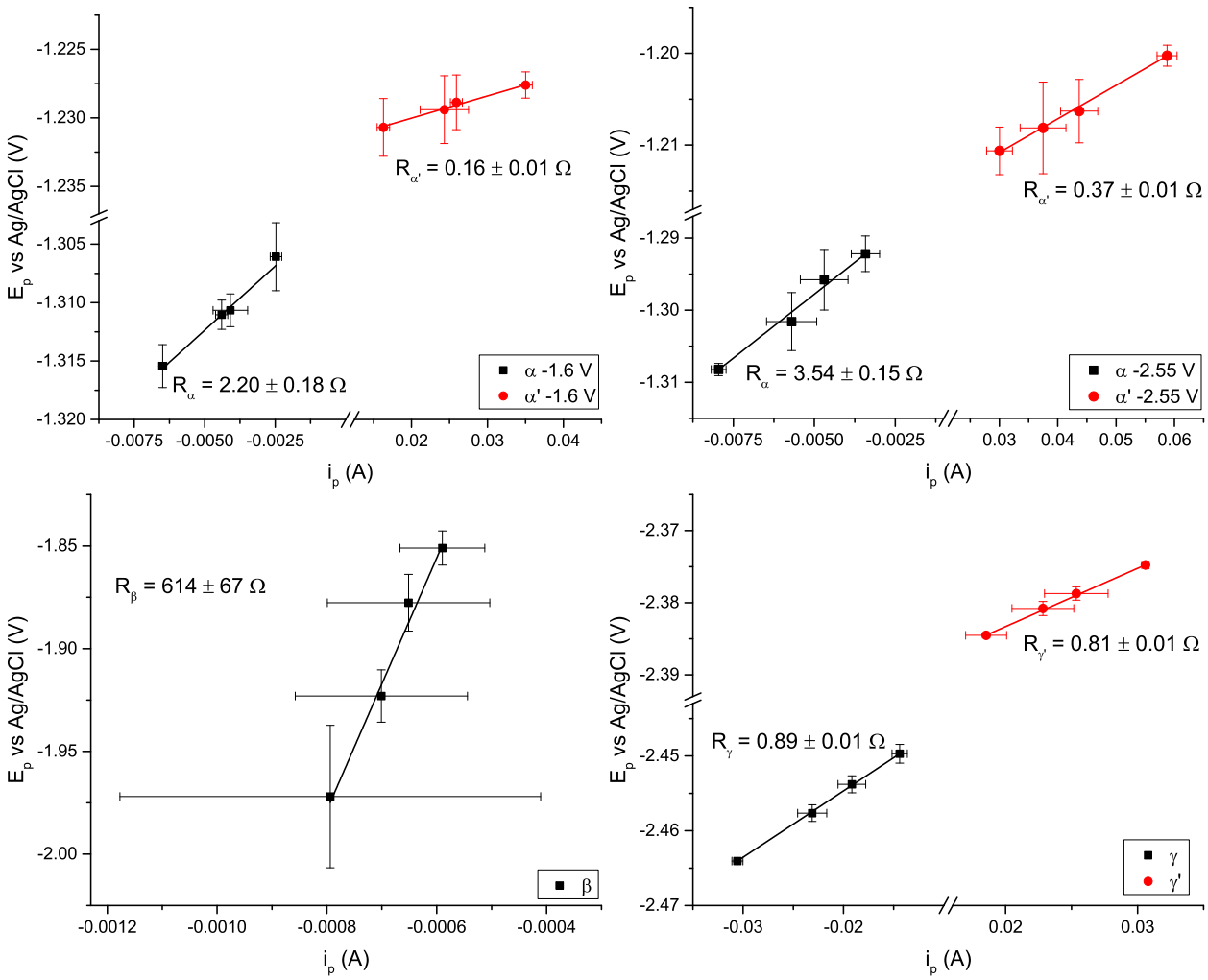

Figure 4.18: E_p versus i_p from Figure 4.16. (Top Left) The α/α' reactions over the narrow potential window. (Top Right) The α/α' reactions over the wider potential window. (Bottom Left) The β reaction. (Bottom Right) The γ/γ' reactions.

An attempt was made to fit the monolayer expression (Equation 4.1) to the α', γ and γ' peaks after iR correction using their respective R (not shown). This was not successful as the peaks were asymmetrical: for α' the current curved upwards to the peak before falling sharply; for γ/γ' the current rose very sharply to the peak current before curving downwards. It was however possible to fit peak β using Equation 4.1. n was scan rate independent with an average value of 1.16 ± 0.15. This is the expected value for the formation of a lithium-aluminium alloy monolayer as well as the formation of the LiAl intermetallic.

The convolved CVs over both potential windows are shown in Figure 4.19. Over both potential windows, α displayed a limiting convolved current (I_L) rather than a peak, which was consistent with diffusion control of Al^{3+}. $|I_L|$ increased slightly as the scan rate decreased; at the slowest scan rate (50 mVs^{-1}) the current looked significantly more peak shaped, indicating a more significant contribution of convection to the current over longer timescales and possible increase of surface area due to the metal deposit being rough.[92] β retained a peak shape at the two slower scan rates, but was smeared out at the two faster scan rates. This peak was not expected to show a limiting convolved current as it was not controlled by diffusion (scan rate independent peak current). The γ reduction peak did not display a limiting convolved current, rather it still had a peak shape. There was a rapid decrease of $|I|$ after the peak, however it did not reach a limiting value, rather it continued to curve. This implied that at these potentials lithium was able to reduce and rapidly insert into the pre-deposited aluminium where it was limited by diffusion of lithium metal in aluminium. After the peak, a limiting convolved current would have been expected regardless of whether the reaction was limited by Al^{3+} (complete lithium insertion) or lithium metal (incomplete lithium insertion). The lack of a limiting convolved current may have been due to surface roughening and loss of material due to the mechanical instability of a thin alloy layer undergoing rapid volume expansion.

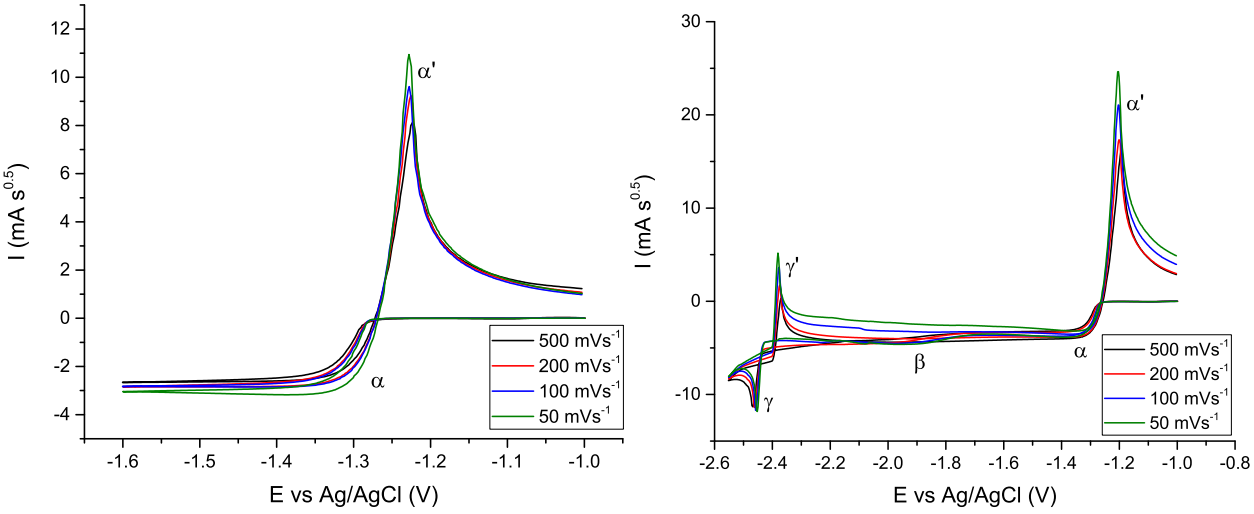

Figure 4.19: Convolved CVs over the (Left) narrow potential window (Right) wide potential window of Figure 4.16

By analysing the charge passed on the forward and backward scans, the molar ratio of Li:Al in the deposit can be found. On the forward (reductive) scan Li:Al can be determined in the co-deposition region:

$$\text{Li:Al}_{\text{co-deposit}} = \frac{n_{Al}}{n_{Li}} * \frac{\text{Q}_{\text{Li co-deposited}}}{\text{Q}_{\text{Al co-deposited}}} = \frac{n_{Al}}{n_{Li}} * \frac{\nu * \int_{-1.7}^{-2.55} (i - i_{lim\,\alpha})\,\text{d}V}{\nu * i_{lim\,\alpha} * (2.55 - 1.7)} \tag{4.3}$$

where $i_{lim\,\alpha}$ is the current due to aluminium reduction at the onset potential of the lithium reduction. The charge due to one species must be divided by its n in order to convert from charge to moles. Thus to obtain the molar ratio, the charge ratio is multiplied by the inverse of the n ratio. By taking into account the pre-deposited aluminium, Li:Al can be determined over the entire reductive scan:

$$\text{Li:Al}_{\text{total-deposit}} = \frac{n_{Al}}{n_{Li}} * \frac{\text{Q}_{\text{Li co-deposited}}}{\text{Q}_{\text{Al co-deposited}} + \text{Q}_{\text{Al pre-deposited}}} = \frac{n_{Al}}{n_{Li}} * \frac{\nu * \int_{-1.7}^{-2.55} (i - i_{lim\,\alpha})\,\text{d}V}{\nu * (i_{lim\,\alpha} * (2.55 - 1.7) + \int_{-1.3}^{-1.7} i\,dV)} \tag{4.4}$$

Li:Al can also be determined from the backward (oxidative) scan by taking a ratio of the peak areas:

$$\text{Li:Al}_{\text{ox}} = \frac{n_{Al}}{n_{Li}} * \frac{\text{Q}_{\gamma'}}{\text{Q}_{\alpha'}} = \frac{n_{Al}}{n_{Li}} * \frac{\nu * \int_{-2.4}^{-2.3} i\,\text{d}V}{\nu * (\int_{-1.35}^{-1.15} i\,\text{d}V + \int_{-2.2}^{-1.35} i\,dV)} \tag{4.5}$$

where the integral between -2.2 and -1.35 V, is negative charge due to deposition of aluminium after the oxidation of lithium alloy. This removes excess aluminium charge from the aluminium stripping peak, which was not part of the lithium alloy, leading to a more accurate Li:Al overall.

$\text{Li:Al}_{\text{co-deposit}}$ was found to be 1.50 ± 0.36. This indicated the formation of Li_3Al_2, the second intermetallic. The lower apparent $R_\gamma = 0.89 \pm 0.01\ \Omega$ for lithium insertion was much lower than the apparent $R_A = 4.41 \pm 0.23\ \Omega$ for cerium insertion, which implied that lithium insertion had a much lower kinetic barrier. This suggested that the pre-deposited aluminium was significantly involved in alloying with lithium, thus ignoring the pre-deposited aluminium charge overvalued Li:Al. $\text{Li:Al}_{\text{total-deposit}}$ was found to be 0.79 ± 0.22 which was in agreement with $\text{Li:Al}_{\text{ox}} = 0.87 \pm 0.14$ (as both are global measures of the charge), indicating that the global composition of the alloy was LiAl, the first intermetallic. Thus on a aluminium thin film electrode, β is the formation of lithium dissolved in aluminium (as observed on the bulk aluminium macroelectrode), whereas the γ/γ' reaction is the formation of the LiAl intermetallic rather than the plating of pure lithium observed on a bulk aluminium electrode. This can be explained by the much larger volume on a bulk electrode, which stabilises lithium metal on the surface (deposited approximately +0.2 V of its deposition potential on inert electrodes) by allowing some pure lithium to alloy with the large volume of aluminium. It

may however be the case that γ/γ' on the bulk aluminium macroelectrode was also the formation of the LiAl intermetallic (due to the similarity in potential). The reason that no other reaction was observed at more negative potentials may have been due to the fast insertion of lithium into the large volume of aluminium, thus at potentials for pure lithium plating on an inert substrate the rate of lithium reduction, and therefore current, would not change.

4.3.3 LKE-$CeCl_3$ on Tungsten Macroelectrodes

The reduction of Ce^{3+} on tungsten is known to be a one step three electron transfer plating/stripping reaction.[22] Figure 4.20 shows CVs of $CeCl_3$ in LKE on a tungsten electrode over a number of scan rates. δ was the reduction (plating) reaction; δ' was the oxidation (stripping) reaction.

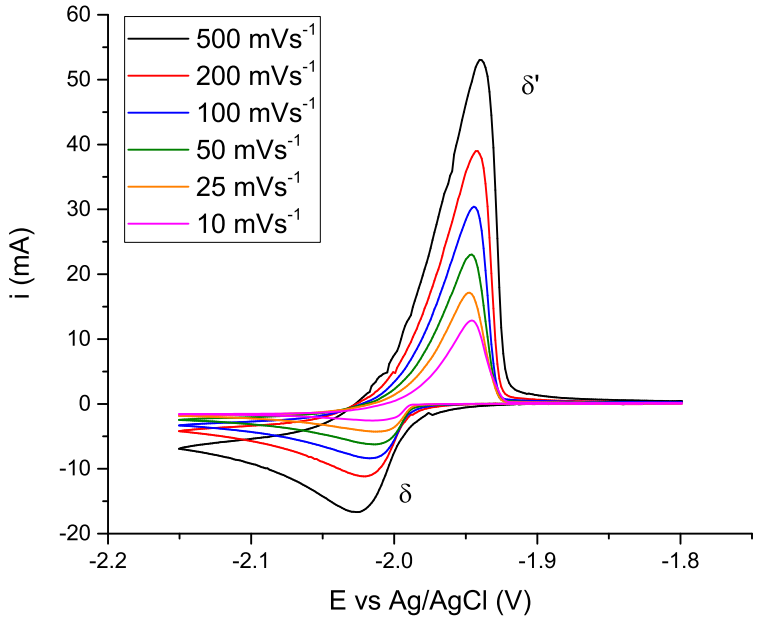

Figure 4.20: CVs of $[CeCl_3]$ = 20 mM on a tungsten macroelectrode, T = 723 K.

Table 4.3 shows the efficiency of the cerium plating/stripping reaction in Figure 4.20. As with pure aluminium plating/stripping, the efficiency was 100% within experimental error for all scan rates studied.

Table 4.3: Efficiency of the Ce^{3+}/Ce^0 reaction in Figure 4.20.

Scan Rate (mVs^{-1})	500	200	100	50	25	10
Efficiency (%)	104 ± 3	110 ± 2	105 ± 4	102 ± 2	100 ± 1	94 ± 2

Figure 4.21 shows the plot of i_p versus $\nu^{0.5}$. The linear regression indicated that the reduction reaction was under diffusion control of Ce^{3+}.

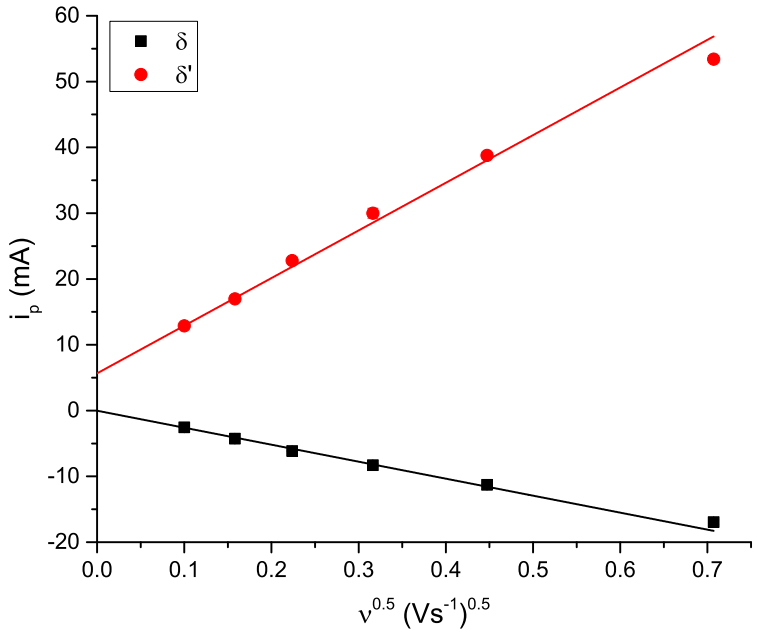

Figure 4.21: i_p versus $\nu^{0.5}$ for the reaction δ/δ' in Figure 4.20. Solid lines are linear regressions extrapolated to $\nu^{0.5} = 0$.

The apparent resistance for the cerium reduction and oxidation was determined via the same method as for previous reactions. Figure 4.22 shows plots of E_p versus i_p to calculate the apparent resistances. $R_\delta = 1.22 \pm 0.08\ \Omega$ (cerium plating) was less than $R_\alpha = 2.20 \pm 0.18\ \Omega$ (aluminium plating) implying that there was a lower kinetic barrier to nucleation of cerium on tungsten versus nucleation of aluminium on tungsten. $R_{\delta'} = 0.23 \pm 0.01\ \Omega$ (cerium stripping) was similar to $R_{\alpha'} = 0.16 \pm 0.01\ \Omega$ (aluminium stripping), as well as $R = 0.18\ \Omega$ found for bismuth stripping off tungsten.[8] This was evidence that the only resistance affecting pure metal stripping was that of solution resistance, $R_s \approx 0.2\ \Omega$. The apparent resistances affecting oxidation of lithium ($R_{\gamma'} = 0.81 \pm 0.01\ \Omega$) and cerium ($R_{A'} = 0.89 \pm 0.80\ \Omega$) from aluminium alloys were significantly higher than solution resistance, implying that there was still a contribution of phase change kinetics to the oxidation of alloys.

Figure 4.23 shows the convolved CVs of $CeCl_3$. As with the convolved CVs of $AlCl_3$ (Figure 4.19) there was a limiting convolved current, and its magnitude increased slightly as scan rate decreased. At 10 mVs^{-1} the response was far more peak like than a limiting current. This peak shape even after convolution at slower scan rates has also been seen with other species, e.g. $BiCl_3$, UCl_3, $SmCl_3$ and $EuCl_3$.[92] This is expected to be caused by the increased contribution of convection to the mass transfer at longer timescales, as well as an increasing surface area during the scan as a rough metal film is deposited.

Figure 4.24 shows how I_L current changed as a function of scan rate. For the three fastest scan rates used (500, 200 and 100 mVs^{-1}) I_L was the same within experimental error. At slower scan rates (50 mVs^{-1} and

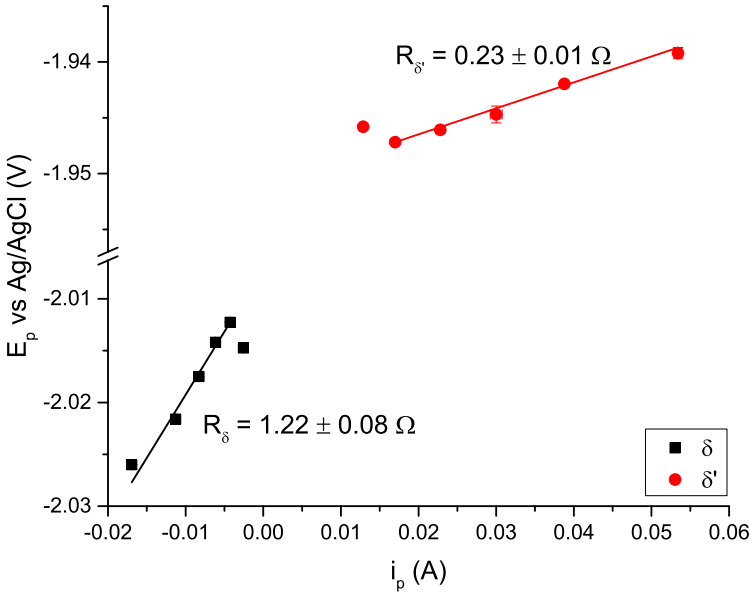

Figure 4.22: E_p versus i_p for reaction δ/δ' (Figure 4.20). Data from the slowest scan rate, 10 mVs^{-1}, was not used for linear regression as it deviated significantly from the other data.

below), $|I_L|$ increases quite substantially, indicating that convection had a large influence on the mass transfer. I_L at the faster scan rates (100 mVs^{-1} and above) is evidently not affected by convection to the same extent, and was constant within experimental error. By estimating the immersion depth of the tungsten working electrode, and therefore the electrode surface area, the $CeCl_3$ concentration was calculated, using the diffusion controlled I_L, to be on the same order of magnitude as the 20 mM added. Thus if the electrode area was known exactly, the $CeCl_3$ concentration could be calculated accurately at scan rates where the contribution of convection to the mass transport is known to be negligible. Using convolved current may result in a more precise concentration value, as I_L can be measured over a potential range, whereas calculating concentration from a CV uses only a single peak current value for each scan rate.

It is interesting to note that while Figure 4.21 indicated purely diffusion control of the reduction reaction, the convolution shows evidence of the contribution of convection. The plot of i_p versus $\nu^{0.5}$ only uses a single point on the CV which is known as the mixed control region, where electron transfer kinetics becomes less significant and mass transport becomes more significant in terms of controlling the overall rate of reaction. At fast scan rates the influence of convection at this point will be small, thus only diffusion should determine the peak current. Past the peak potential, the current is controlled purely by mass transport and the convection will contribute more to the mass transport, especially at slower scan rates. It may be possible to use the convolved CVs to determine the convective contribution to mass transport, which is important for CVs performed over wide potential windows.

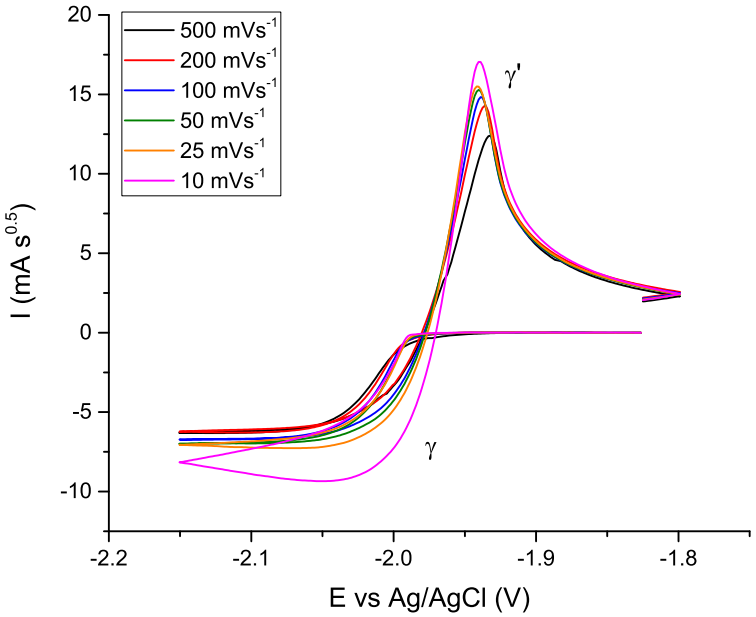

Figure 4.23: Convolved CVs of Figure 4.20

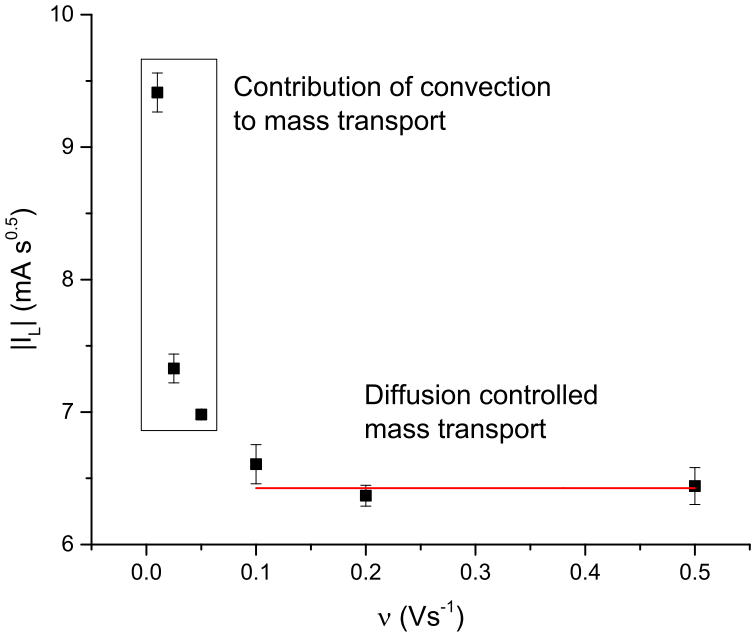

Figure 4.24: I_L versus ν for Figure 4.23.

4.3.4 LKE-$AlCl_3$-$CeCl_3$ Co-deposition on Tungsten Macroelectrodes

Figure 4.25 shows CVs when both $AlCl_3$ and $CeCl_3$ are present in the melt. The plating of aluminium, α, was observed followed by cerium-aluminium alloying, A. When the potential window was widened, the CV had an overall curve shape to it, with several oxidation reactions occurring at negative currents. Repeat scans at wide potential windows gave poor repeatability, whereas over narrow potential windows (<1 V) there was good repeatability. Some new oxidation peaks were observed that were attributed to decomposition of Ce_xAl_y intermetallics (B' and C'), however no formation peaks were observed. There was also a large oxidation peak at approximately -2.25 V, δ', which corresponded with the same oxidation peak of pure cerium metal on a bulk aluminium macroelectrode (Figure 4.12). At approximately -2.45 V lithium-aluminium alloying (LiAl, γ/γ') was observed. This occurred at similar potential as with only $AlCl_3$ present in the salt (Figure 4.16).

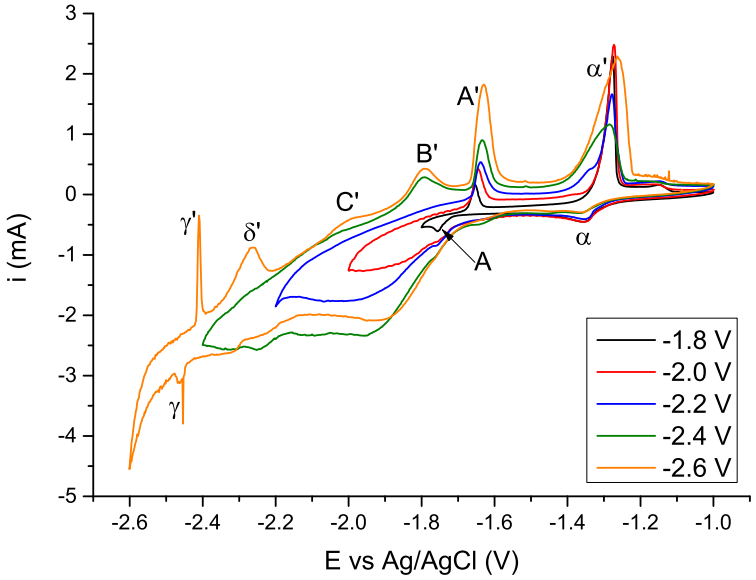

Figure 4.25: CVs of LKE containing [$AlCl_3$] = 21 mM and [$CeCl_3$] = 21.5 mM on a tungsten macroelectrode over different potential windows, ν = 100 mVs^{-1}, T = 723 K.

As the potential window was widened $i_{pA'}$ increased, as was seen when cerium was reduced/oxidised on a bulk aluminium macroelectrode (Figure 4.13). This was expected as both aluminium and cerium were reduced for longer, hence the total amount of Ce_xAl_y intermetallic would increase. The aluminium stripping peak α' broadened and $i_{p\alpha'}$ decreased as the potential window widened. When the window was wide enough for lithium-aluminium alloying, γ/γ', $i_{p\alpha'}$ increased but the peak remained broad. The peak broadening can be explained by an increased proportion of alloyed aluminium to bulk aluminium, which resulted in a wider range of surface energies. Formation of cerium-aluminium alloy is expected to result in a large volume expansion, thus some material may have been lost due to mechanical detachment. The volume expansion of lithium-aluminium alloying was expected to be less, as lithium has a smaller metallic radius than cerium.

Thus once potentials are reached where lithium-aluminium alloying can occur, there would be less material loss from volume expansion during alloying, leading to an increase in $i_{p\,\alpha'}$.

Figure 4.26 shows comparative CVs performed over the LKE solvent window, before and after the addition of $CeCl_3$ to LKE-$AlCl_3$. $CeCl_3$ was added by opening the cell to air and pouring in $CeCl_3$ granules. This unfortunately let some oxygen and water from the atmosphere into the system, which was expected to convert some $AlCl_3$ to Al_2O_3 irreversibly, which explains the decrease in the size of the aluminium plating/stripping (α/α') reaction. When $CeCl_3$ was present the γ/γ' reaction was not observed, which contradicts what was seen when looking at a narrower potential window (Figure 4.25). The curve shape to currents observed in the shorter potential window was not present over the full solvent potential window, and repeat CVs over the solvent windows gave good repeatability, in contrast to the poor repeatability of wide potential window scans that did not go to the solvent limits. The cerium plating/stripping (δ/δ') reaction was more clearly visible over the full solvent potential window. Four intermetallic oxidation peaks were observed: A', B', C' and D'. Three intermetallic formation peaks were observed: A, C and D. From literature,[35,37,38] and later in this thesis, it is known that B should appear around -1.9 to -2.0 V.

After two hours had passed (Figure 4.27), it was observed that the aluminium plating/stripping (α/α') reaction had decreased in current significantly, and had changed peak shape in an unexplained fashion. In addition, the intermetallic oxidation peaks decreased in size, and the cerium stripping peak δ' changed shape and peak position. This resulted in the observation of a fifth intermetallic oxidation peak, E'. The formation peak E was not observed, but is likely to have a very similar potential to the plating of pure cerium. It has been noted in the literature that $AlCl_3$ is volatile from LKE.[31,37,38,70,72,73,84,93,94] This is because solid $AlCl_3$ has a sublimation temperature of approximately 180 °C,[95] approximately 250 °C colder than the working temperature of these experiments. This presents a possible mechanism for the loss of $AlCl_3$, but has not been investigated in the literature.

In the literature of co-deposition of $CeCl_3$ and $AlCl_3$,[35,37,38] each species were roughly equimolar, as was done in these experiments. These concentrations however are an order of magnitude smaller than in the literature, which may affect the alloying that can be observed. In no literature experiments which utilised $AlCl_3$ was the volatility investigated. Concentrations of $AlCl_3$ given were approximately the amounts that were added, but no references were made to the time taken to perform the experiments, thus there were no quantifications of how much $AlCl_3$ may have been lost. Since only equimolar studies have been performed in the literature, it is unclear how the molar ratio of [$CeCl_3$]:[$AlCl_3$] affects the alloy produced by co-deposition. That investigation will be performed in this thesis (Chapter 6) once the loss of $AlCl_3$ is understood.

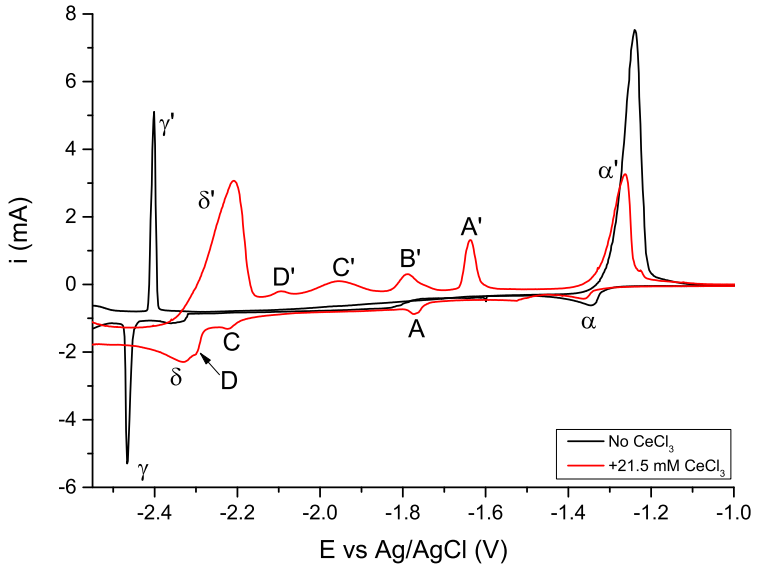

Figure 4.26: CVs of LKE containing [$AlCl_3$] = 21 mM before and after addition of [$CeCl_3$] = 21.5 mM on a tungsten macroelectrode, ν = 200 mVs^{-1}, T = 723 K. The CVs were performed over the entire solvent potential window (+1.1→-2.8 V).

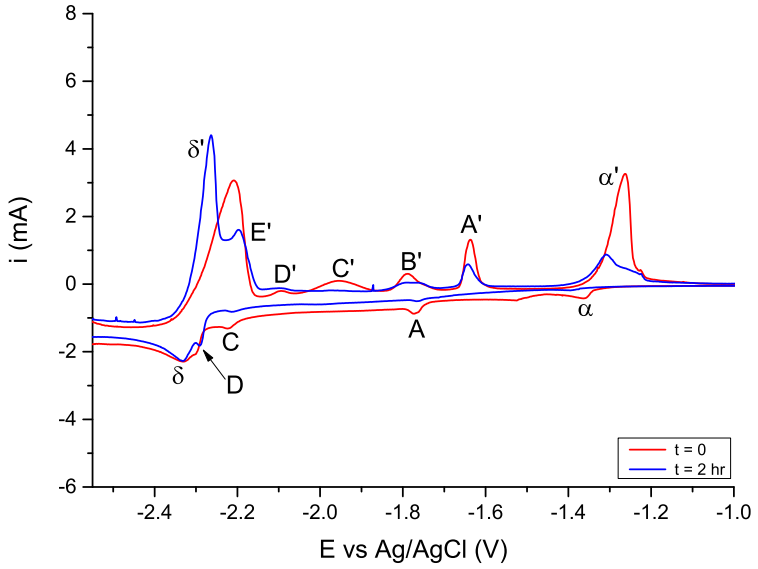

Figure 4.27: CVs of LKE containing [$AlCl_3$] = 21 mM and [$CeCl_3$] = 21.5 mM on a tungsten macroelectrode at two time points after addition of $CeCl_3$. ν = 200 mVs^{-1}, T = 723 K. The CVs were performed over the entire solvent potential window (+1.1→-2.8 V).

4.4 Conclusions

From reduction of $CeCl_3$ on a bulk aluminium macroelectrode only one cerium-aluminium intermetallic was observed with reliability. This formation/reduction reaction was found to be significantly influenced by phase change kinetics negative of the peak potential, not purely controlled by diffusion of Ce^{3+} to the electrode surface. The efficiency of the alloying reaction was found to be greater at higher scan rates, which was explained by less coalescence of intermetallic crystal grains, which resulted in more mechanically stable deposits. Although bulk aluminium macroelectrodes show electrochemistry due to an analyte, the inability to accurately calculate the $CeCl_3$ concentration due to the reaction not being governed purely by diffusion of Ce^{3+}, precludes its use as an on-line monitoring sensor.

The reduction of Al^{3+} and Ce^{3+} on an inert electrode were each governed purely by diffusion of ions in LKE. Over wide potential windows, or at slow scan rates, convection became a significant contribution to the flux. When co-deposited, a maximum of five intermetallic compounds were observed, which agreed with the number expected from the cerium-aluminium phase diagram, four of which have been confirmed to form in the literature via ex-situ analysis after long term reduction on a bulk aluminium macroelectrode. The intermetallics were observed via their oxidation peaks, however not all the corresponding reduction peaks were observed.

$AlCl_3$ was observed to decrease in concentration over time from LKE, which may be explained by its volatility due to operating approximately 250 °C above the sublimation point of $AlCl_3$. The rate of loss was sufficiently high to prevent certain measurements of a specific $[CeCl_3]$:$[AlCl_3]$ ratio, as the ratio was changing significantly during the measurement. Thus investigation into co-deposition was hampered.

Investigation of the loss of $AlCl_3$ will be the focus of the next chapter. This will allow investigation of how the $[CeCl_3]$:$[AlCl_3]$ ratio in the salt affects the ratio of Ce:Al in the co-deposit and the electrochemical features observed. The loss of $AlCl_3$ will allow the $[CeCl_3]$:$[AlCl_3]$ ratio to vary such that $AlCl_3$ will start in excess, but then become equimolar and then finally $CeCl_3$ will be in excess.

Co-deposition would not be performed in a real pyroprocessing system for on-line monitoring, as the repeat addition of a chemical would complicate the sensing technique. It is however promising for a method of further investigation of relevant alloying processes before the use of thin film aluminium microelectrodes, as co-deposition results in more information-rich electrochemistry.

Chapter 5

Methods of Introducing $AlCl_3$ to LKE and the Effect on Electrochemistry

5.1 Introduction

In the previous chapter, $AlCl_3$ was added by electrochemical dissolution of an aluminium electrode. This was done rather than by addition of $AlCl_3$ powder due to experimental constraints, specifically it was the only way (at the time) that the $AlCl_3$ could be introduced while maintaining an inert atmosphere to prevent the reaction of $AlCl_3$ with water to form hydroxides and oxides. $AlCl_3$ also sublimes at approximately 180 ^oC,[95] which is approximately 160 ^oC before the LKE melting temperature, therefore some $AlCl_3$ is expected to be lost via sublimation during heating of the furnace. In addition it is noted in the literature that $AlCl_3$ is volatile from LKE[35, 37, 38] as it retains molecular character, and so the $AlCl_3$ concentration may be changing with time, although the rate of volatilisation in this system has not been measured in the literature. This method also allowed controlled addition of Al^{3+} by monitoring the charge passed. This is the same way in which nuclear waste would be introduced into the salt by electroreduction of oxides followed by oxidation of the metals. It is known that by oxidising aluminium at the working electrode, a counter reaction must be occurring at the counter electrode. For the currents used during electrochemical dissolution at the working electrode, lithium plating at the counter electrode is the only reaction that would be able to balance the charge being passed. This is likely to impact the electrochemistry performed since lithium reduction is the most negative reaction that can occur in LKE. There is a driving force for the lithium metal to re-oxidise by reducing other metal chloride species: $CeCl_3$ and $AlCl_3$ in this work. This is similar to short circuit reactions

which can occur in batteries. This "short circuit" reaction will cause the concentration of Al^{3+} introduced to solution to decrease over time, thus the rate of the "short circuit" reaction must be investigated. Both methods of Al^{3+} addition, electrochemical and chemical, therefore have potential drawbacks. This chapter presents a systematic study to give insight into the importance of these effects.

More recently gloveboxes have been available to carry out work, thus allowing the introduction of $AlCl_3$ powder to precleaned LKE in an inert atmosphere, thus avoiding hydrolysis reactions. This will allow a study of the loss of $AlCl_3$ during furnace heating and whether further loss of $AlCl_3$ does indeed occur due to volatility (gas formation) once the $AlCl_3$ is dissolved in LKE. The rate of loss due to volatility can then be compared to the rate of loss due to the "short circuit" reaction to understand which method of addition is more useful for studying the co-deposition of $CeCl_3$ and $AlCl_3$ where the ratio of $[CeCl_3]$:$[AlCl_3]$ would, ideally, remain quantifiable and fixed over time. The quantities of $AlCl_3$ added from both electrochemical dissolution and powder addition (and so the theoretical maximum concentrations), are given in legends as $[AlCl_3]_0$.

5.2 Simultaneous Measurements of Potential at the Tungsten Counter Electrode

Measuring the counter electrode potential provides diagnostic information about the chemical species generated in the system. During potentiostatic measurements (CV, CA) the potential at the counter electrode gives information on the counter redox reaction that is required to maintain the current being passed at the working electrode. It should be noted that such a measurement is not a standard output of the computer controlled potentiostats used. In order to perform these measurements, two potentiostats were used: the first was connected as normal to perform CVs, the second potentiostat was connected via its reference electrode connection to the solution's reference electrode, and via its working electrode connection to the solution's counter electrode. Figure 5.1 shows a schematic representation of how the potentiostats were connected to the electrochemical cell. To ensure all current flowed through PSTAT1, PSTAT2 was set to measure the OCP of the counter electrode. This was done by setting the cell to closed on both hardware and in software, and by not connecting the counter electrode connection of PSTAT2. One critical element of the set up was that the potentiostats did not share a power supply. This is due to the way that the potentials are generated with respect to ground within these potentiostats. If the potentiostats shared a power supply, then they shared a common ground, leading to interference once potentials were being applied. PSTAT2 was therefore powered through an uninterruptible power supply (UPS), which was isolated from mains power.

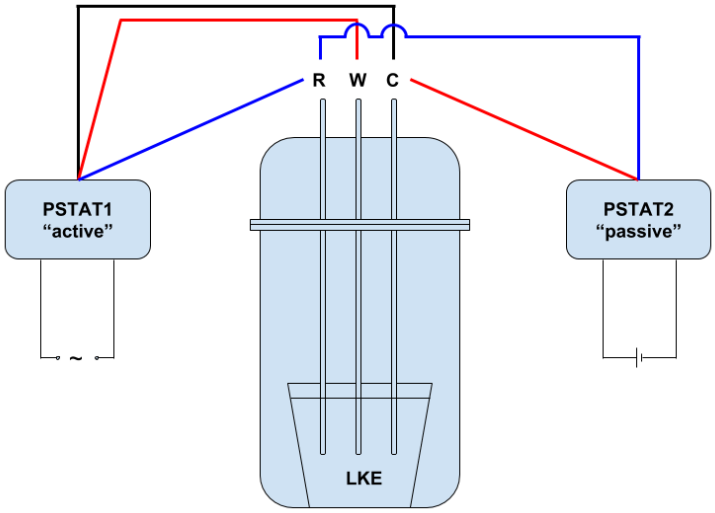

Figure 5.1: Schematic of potentiostat set-up required to simultaneously perform electrochemistry and measure the potential at the counter electrode. Red = working electrode connection, blue = reference electrode connection, black = counter electrode connection. PSTAT1 is powered by the mains supply and drives the electrochemistry; PSTAT2 is powered by an uninterruptible power supply (UPS) or other battery and measures the counter electrode potential.

5.2.1 During CVs on a Bulk Aluminium Macroelectrode

As discussed in the previous chapter it is expected that the oxidation of aluminium at the working electrode to produce $AlCl_3$ ($Al^0 \rightarrow Al^{3+} + 3e^-$) must also produce lithium metal at the counter electrode ($3Li^+ + 3e^- \rightarrow 3Li^0$). Figure 5.2 shows CVs performed on an aluminium electrode using PSTAT1 and the potential at the counter electrode recorded on PSTAT2. When Li^+ reduction (β) began at approximately -1.9 V, the counter electrode potential slowly increased. It is only once γ/γ' was reached at approximately -2.2 V, and the currents were much larger, that the counter electrode potential increased far more rapidly to reach a reaction that could balance the current. Over the course of the γ/γ' reaction on the aluminium working electrode, the counter electrode potential was observed to rapidly switch between Cl_2 evolution (approximately +1.2 V) and lithium plating (approximately -2.5 V): the extremes that mark the solution potential window on tungsten (Figure 4.1). When the aluminium working electrode reduced Li^+ to Li^0 (either β or γ), the counter electrode potential increased towards Cl_2 evolution. Since there is very little reduction of Cl_2 back to Cl^- (since Cl_2 is a gas that is mostly lost from the solution) the counter electrode potential must switch to lithium reduction to balance the oxidation of lithium at the working electrode. When the working electrode strips and then plates aluminium, the counter electrode can switch between large positive and negative balancing currents by small fluctuations around the lithium plating/stripping potential. This is why the counter electrode spends much longer at pure lithium potentials than at the Cl_2 evolution potential. During the second and third CVs, when the aluminium stripping and plating currents were greater, the counter electrode rested at the

pure lithium potentials for much longer. Thus the length of time the counter electrode spends at potentials can be diagnostic of the species in solution.

PSTAT2 monitored the counter electrode potential transient once the CVs had finished. The counter electrode potential initially rested at the lithium plating potential on tungsten, before slowly relaxing back towards the OCP of tungsten in LKE (approximately -0.45 V), although it did not reach that value within the time that monitoring was performed. This implies that lithium metal was lost from the counter electrode gradually, either by some chemical reaction/dissolution or by convection of the solution. This work has demonstrated the expected behaviour of the counter electrode potential when the working electrode potential is scanned during CVs, and establishes the use of the counter electrode potential as a diagnostic tool for understanding the speciation in, or the state of, the system.

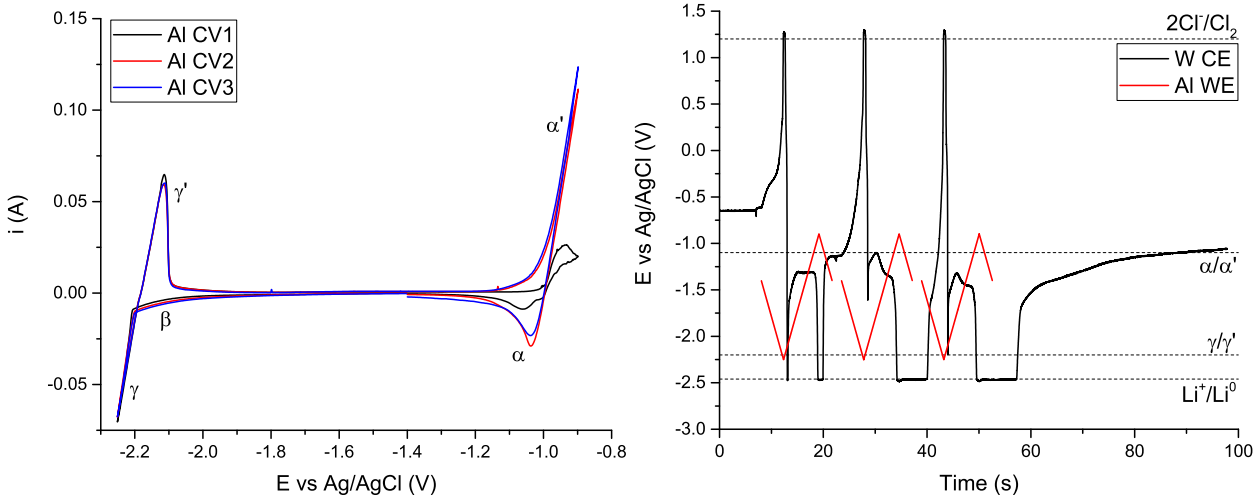

Figure 5.2: (Left) CVs on an aluminium electrode in LKE, $\nu = 200$ mVs^{-1}, $T = 723$ K . (Right) The corresponding potentials of the aluminium working electrode and tungsten counter electrode over time. As the working electrode scanned negatively, the counter electrode scanned positively and vice versa. When specific potentials are reach (marked with dotted lined) the counter electrode jumps between chlorine evolution and lithium plating, in order to balance the current being passed at the working electrode.

5.2.2 During Electrochemical Dissolution of a Bulk Aluminium Macroelectrode

Figure 5.3 shows the potentials on the aluminium working electrode and tungsten counter electrode when $AlCl_3$ is added to the salt by electrochemical dissolution. The potential of the aluminium electrode remained above the potential required for aluminium oxidation and below the potential for chloride oxidation, therefore aluminium oxidation was the reaction occurring at the working electrode. The potential at the counter electrode remained below that required for reduction of lithium ions to lithium metal. This then confirmed

that this method of $AlCl_3$ addition to the salt also results in the production of lithium metal, which would cause the loss of Al^{3+} from solution due to a "short circuit" reaction: $Al^{3+} + 3Li^0 \rightarrow Al^0 + 3Li^+$.

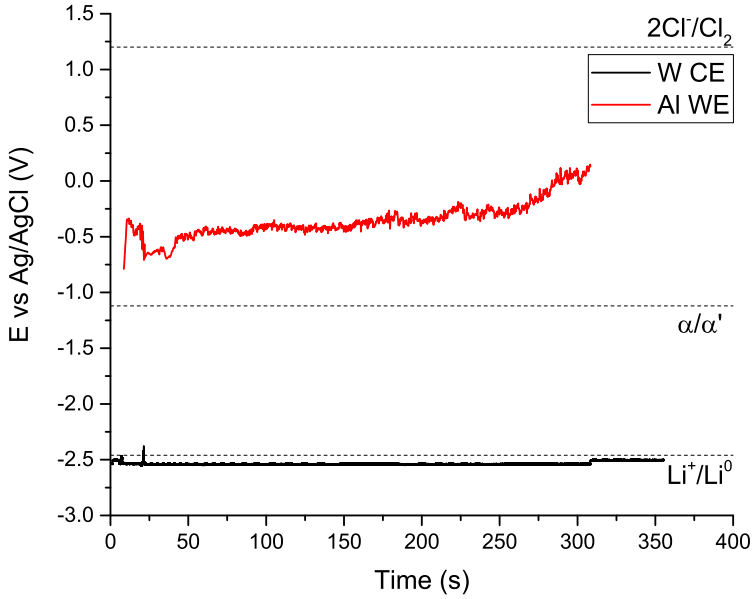

Figure 5.3: Potentials measured at the aluminium working electrode and tungsten counter electrode during electrochemical dissolution. $i = +292.8$ mA, $t = 300$ s, $T = 723$ K.

5.2.3 During CVs of Electrochemically Generated $AlCl_3$ in LKE on Tungsten Macroelectrodes

Figure 5.4 shows the CVs and counter electrode potential measurements in LKE after electrochemical dissolution of $AlCl_3$. In these CVs both the working and counter electrodes were tungsten rods. The CVs showed reactions previously observed: α/α' (aluminium plating/stripping), γ/γ' (lithium-aluminium alloying) and Li^+/Li^0. The counter electrode potential however did not appear to change in response to the current being passed at the working electrode, instead resting at approximately -2.5 V. The counter electrode potential did however "spike" up and down when the working electrode scanned to lithium plating, then lithium stripping. The size of the counter electrode potential "spike" was dependent on the magnitude of the current: in CV 1 when the lithium stripping current was small, the counter electrode potential "spike" was small. In CVs 2 and 3, the lithium stripping peak was larger and so was the size of the counter electrode potential "spike". Upon closer inspection (bottom graph in Figure 5.3), these "spikes" were found to be potential transients, as they occurred over roughly 4 s (2 s of lithium stripping followed by 2 s of lithium plating on the working electrode), and so were electrochemical phenomena, rather than noise due PSTAT resistor switching, which would have only been one or two data points long. Other potential transients at

the counter electrode were also observed when the working electrode crossed the potentials for the α/α' and γ/γ' reactions. The blue lines on the bottom graph in Figure 5.3 are the time points at which the working electrode started a reduction or oxidation reaction. The time points matched up very well with the counter electrode potential transients. Thus the counter electrode potential was still responding to the required current passed through the system (as expected); it was baselined on the lithium plating/stripping potential due to the large quantity of Li^0 in the system, and was able to pass the required currents by small changes in potential above and below the lithium plating/stripping potential.

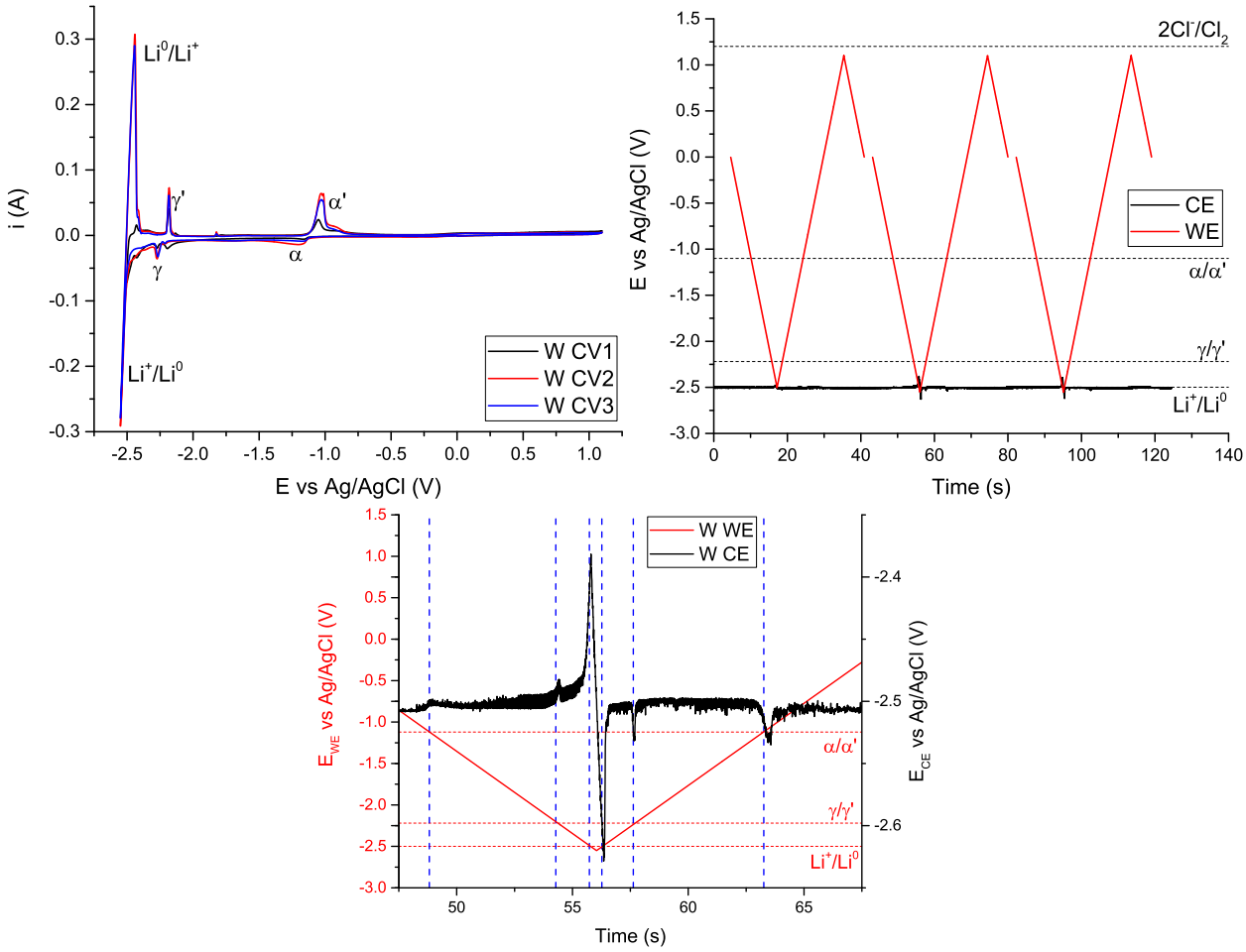

Figure 5.4: (Top Left) CVs on a tungsten electrode in LKE with $[AlCl_3]_0 = 10$ mM added by electrochemical dissolution, $\nu = 200$ mVs^{-1}, $T = 723$ K. (Top Right) The potentials of the working and counter electrodes over time. (Bottom) Zoomed image of counter electrode potentials during CV 2. Blue vertical dotted lines indicate time points at which the working electrode crosses over the formal potential of each reaction, marked by the red horizontal dotted lines. The red horizontal dotted lines that show the formal potentials of each reaction are lined up with the working electrode potential (left hand) axis.

CVs were run again, but swapping over which tungsten rod was used as the working and counter electrodes. The same behaviour as in Figure 5.4 was observed. The OCP on the electrodes after performing CVs were

-1.1 V (Al^{3+}/Al^0) for the working electrode, and -2.5 V (Li^+/Li^0) for the counter electrode, regardless of which tungsten rod was the working electrode and which was the counter electrode. The electrodes were also physically moved to different locations in the salt, which had no effect on the observed OCPs. Since electrochemical dissolution has produced equal amount of Al^{3+} and $3Li^+$, the salt is effectively a battery and the "short circuit" reaction ($Al^{3+} + 3Li^0 \rightarrow Al^0 + 3Li^+$) has an EMF of 1.4 V. In absence of an applied potential from the PSTAT, the OCP measurements read the electromotive force (EMF) of the solution and then display the potential at each electrode relative to the reference electrode, thus acting as voltmeters.

5.2.4 During CVs of Chemically Dissolved $AlCl_3$ in LKE on Tungsten Macroelectrodes

Figure 5.5 shows CVs and potential measurements of LKE-$AlCl_3$ salt (in an inert atmosphere glovebox), where the $AlCl_3$ was added as powder to solidified LKE that had been electrochemically cleaned. The reactions of $AlCl_3$ on the tungsten electrode were the same as previously observed (Figure 4.16). There was an additional peak partially merged with the Li^+/Li^0 peak that may be a more lithium rich Li_xAl_y. The aluminium stripping peak was substantially larger from chemical addition than from electrochemical dissolution of an equivalent $[AlCl_3]_0$ over the same potential window. Thus is appeared that the true $[AlCl_3]$ from chemical addition is greater for the same amount of time since addition, and that with a thicker aluminium layer being deposited, more lithium-aluminium alloying behaviour can be observed. When reductive currents were passed at the working electrode, the counter electrode potential went to oxidation reactions as expected. Thus by adding $AlCl_3$ chemically, there was not an equal amount of lithium metal, and so the counter electrode reactions were due to other species in solution. Strangely when oxidative currents were passed at the working electrode, the counter electrode was able to rest at potentials (approximately -0.2 V and approximately 0.3 V) which did not correspond to any observable electrochemical reaction in the CV.

Repeat CVs in LKE-$AlCl_3$ (Figure 5.6) showed that peaks did grow in the the region of -0.75 to 0 V. These measurements were taken every 5 minutes. It was clear that any contaminants were not oxides or oxychlorides, as the sparge cleaning method has been found to fully chloridise such species,[8] especially with $AlCl_3$ present.[67, 81, 96, 97] These contaminants may instead be species such as $FeCl_3$, $NiCl_2$, or $CrCl_2$ which have been observed to react at similar potentials[87, 98, 99] and may have been impurities in the $AlCl_3$ powder, or resulting from corrosion of metal on the underside of the sample container lid. Assuming less than 100% reaction efficiency, repeat electrochemistry negative of these potentials would cause a build up on the electrode surface. This would reduce the available surface area for aluminium plating and lead to an

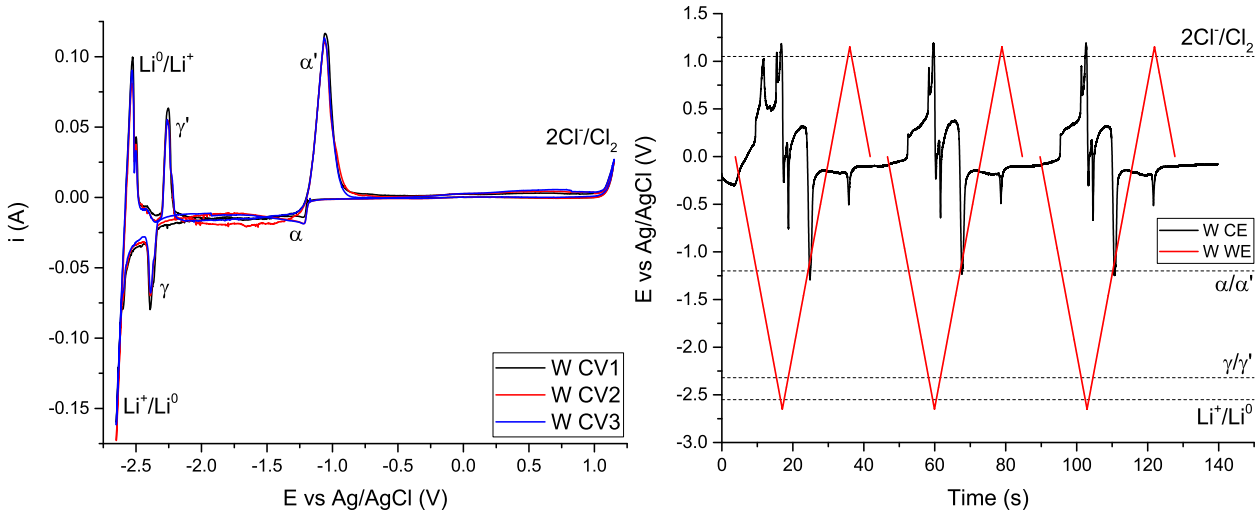

Figure 5.5: (Left) CVs on a tungsten electrode in LKE with $[AlCl_3]_0 = 20$ mM, $\nu = 200$ mVs^{-1}, $T = 723$ K. (Right) The potentials of the working and counter electrodes over time.

increased quantity of reduced aluminium as aluminium alloys (Al-Fe, Al-Ni, Al-Cr), hence the decreasing size of the aluminium stripping peak (α') as the unknown oxidation peaks increased over time.

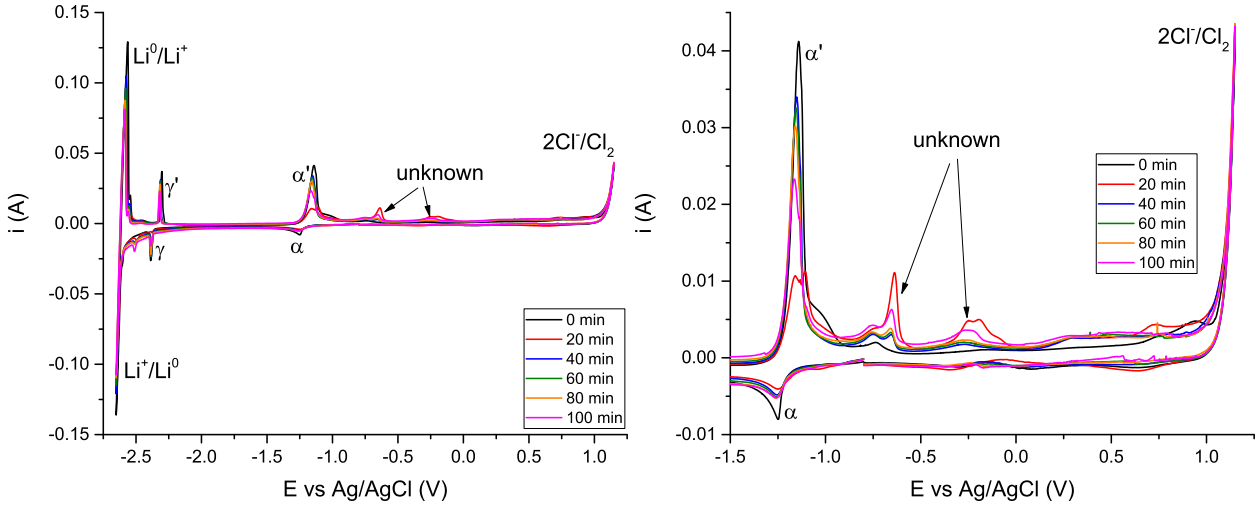

Figure 5.6: CVs performed continuously on a tungsten electrode in LKE with $[AlCl_3]_0 = 20$ mM, $\nu = 200$ mVs^{-1}, $T = 723$ K. (Left) Full solvent window. (Right) Zoomed in version, focusing on the unknown reactions.

Figure 5.7 shows CVs performed during sparge cleaning. In this method, argon gas is bubbled to mix the solution with forced convection. This has the effect of increasing the flux of redox species to the electrode surface. The expected reactions were clearly seen, i.e. the solvent window reactions, α/α', and γ/γ'. These reactions were at larger currents than observed when not sparging (Figure 5.5) due to the forced convection. If the unknown reactions were due to redox species present at low concentration, the increased flux of sparging

would be expected to increase the currents due to their reactions, as happened with the α/α' and γ/γ' reactions. However there was no evidence of the contaminants in these sparged CVs.

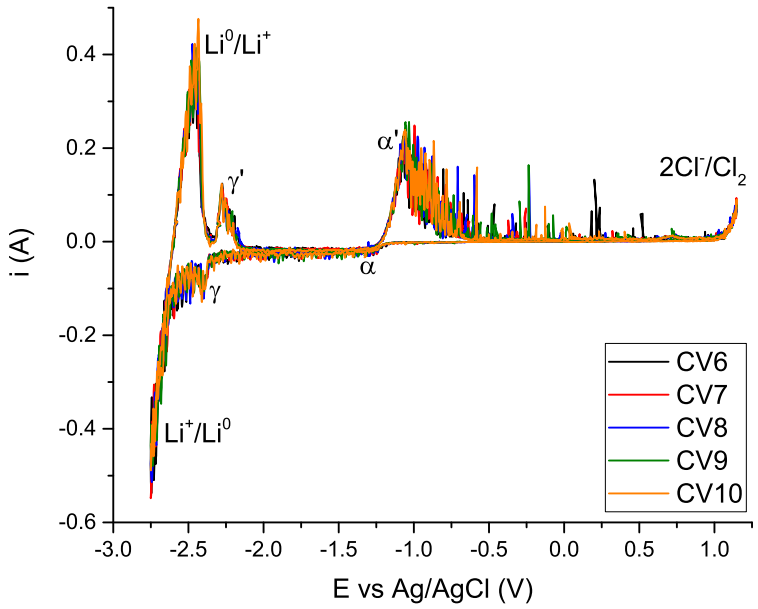

Figure 5.7: CVs while sparging argon gas on a tungsten electrode in LKE with $[AlCl_3]_0 = 20$ mM, $\nu = 200$ mVs^{-1}, $T = 723$ K.

Figure 5.8 shows CVs and potential measurements after sparge cleaning was performed. The contaminant peaks were not observed, however, the counter electrode potential continued to rest at the potentials of these unknown reactions. Further CVs were performed, with the unknown peaks growing back in, as in Figure 5.6. It may be that the contaminant redox species were at such a low concentration that they were below the limit of detection of the macroelectrode CV. If their reactions are not fully reversible, then over repeat CVs their total electrode coverage would have increased. The alloying reactions then became more visible, as this involved aluminium which was at a detectable concentration. It has been observed during this work (although not shown in this thesis) that when $AlCl_3$ was lost from the LKE-$AlCl_3$ system, the $AlCl_3$ concentration can be so low that the α/α' reaction was not observable (as the Faradaic current for this reaction was similar in magnitude to the background current). However the γ/γ' (alloying) reaction was clearly observable, thus the presence of $AlCl_3$ could be confirmed even below the limit of detection of the plating/stripping reaction.

It seems that performing CVs to the solvent window alone (and generating strong reductant and oxidant species, Li^0 and Cl_2 respectively) did not remove the reduced species from the electrode surface (Figure 5.6), as the peaks grew in over time when scanning over the entire solvent potential window. By sparging, it may have been that the physical agitation that aided mechanical loss of the unknown deposits.

If the contaminants were at such a low concentration that they could not be detected on the working electrode,

their reactions could still have provided enough current for periods of time when the working electrode was passing small currents, as long as the counter electrode area was significantly larger than the working electrode area. This in turn might explain why the OCP was approximately -0.1 V on the counter electrode, rather than -1.1 V (the Al^{3+}/Al^0 potential in this solution), despite $AlCl_3$ being the highest concentration redox species.

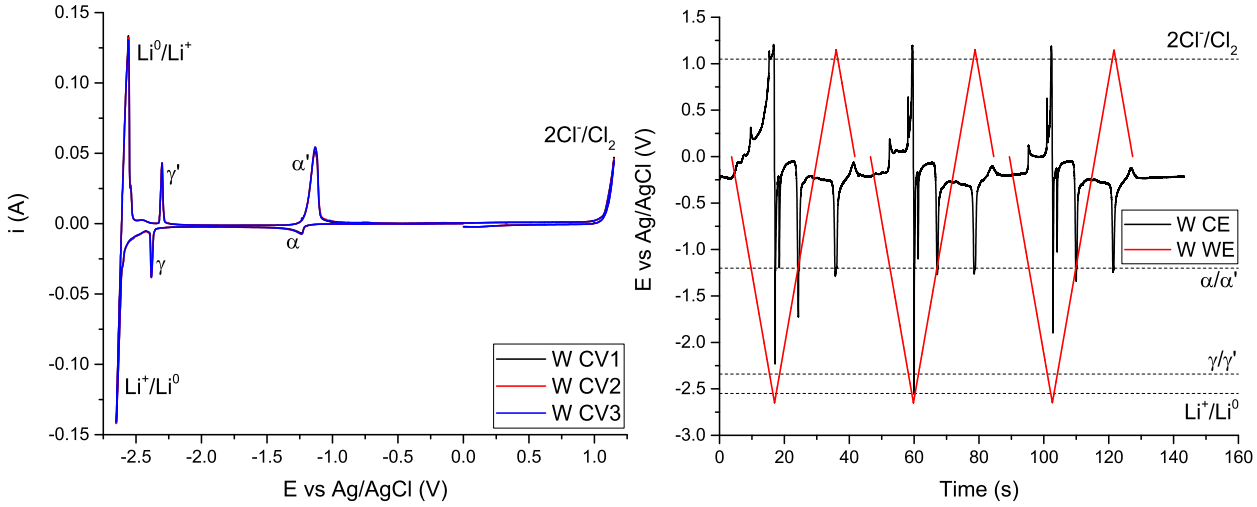

Figure 5.8: CVs on a tungsten electrode in LKE with $[AlCl_3]_0 = 20$ mM, $\nu = 200$ mVs^{-1}, $T = 723$ K after sparge cleaning.

While the counter electrode behaviour appeared to be influenced by unknown reaction contaminants, the salt containing $AlCl_3$ added as powder avoided generating lithium metal, and so avoided one mechanism of $AlCl_3$ concentration change. Whatever these unknown reactions were, sparge cleaning was an effective method for cleaning the surface of the electrodes, allowing electrochemistry to be performed without significant influence of these reactions for a time.

5.2.5 During CVs of $BiCl_3$ in LKE on Tungsten Macroelectrodes

$BiCl_3$ is a well studied redox species in the group[8] and its electrochemistry is well understood. Here it is being used as an alternative redox species to see the behaviour of the counter electrode potential when plating/stripping on a tungsten electrode. Figure 5.9 shows CVs and potential measurements before and after electrochemically cleaning LKE-$BiCl_3$. LKE was not pre-cleaned before addition of $BiCl_3$, and so water based impurities were expected to be present. As with the CVs performed on an aluminium electrode (Figure 5.2) when the working electrode current was negative, the counter electrode potential scanned positive and vice versa. Owing to the presence of two reactions attributed to $BiCl_3$: $Bi^{3+} + 3e^- \rightarrow Bi0$ (ε/ε') and

$xLi^+ + xe^- + yBi^0 \rightarrow Li_xBi_y$ (η/η'), the counter electrode potential rested on these reactions, rather than the solvent window reactions, as long as the working electrode current was sufficiently small.

After cleaning, the currents passed at the working electrode were smaller. The counter electrode rested at the bismuth reactions for longer rather than the solvent window reactions to balance the current. When the CVs finished, the counter electrode potential transient tended to the formal potential of ε/ε', the same as the OCP on the working electrode. During this transient in the salt before cleaning, there were two potential plateaux between ε/ε' and η/η'. These plateaux disappeared after the salt was cleaned. This highlighted that minor species/reactions (in this case oxides, hydroxides, or oxychlorides from water based impurities) can have an impact on the electrochemistry occurring at an electrode, even if their currents are too small to observe peaks in the CVs. Thus measuring the counter electrode potential is a possible diagnostic tool for determining a salt's electrochemical cleanliness.

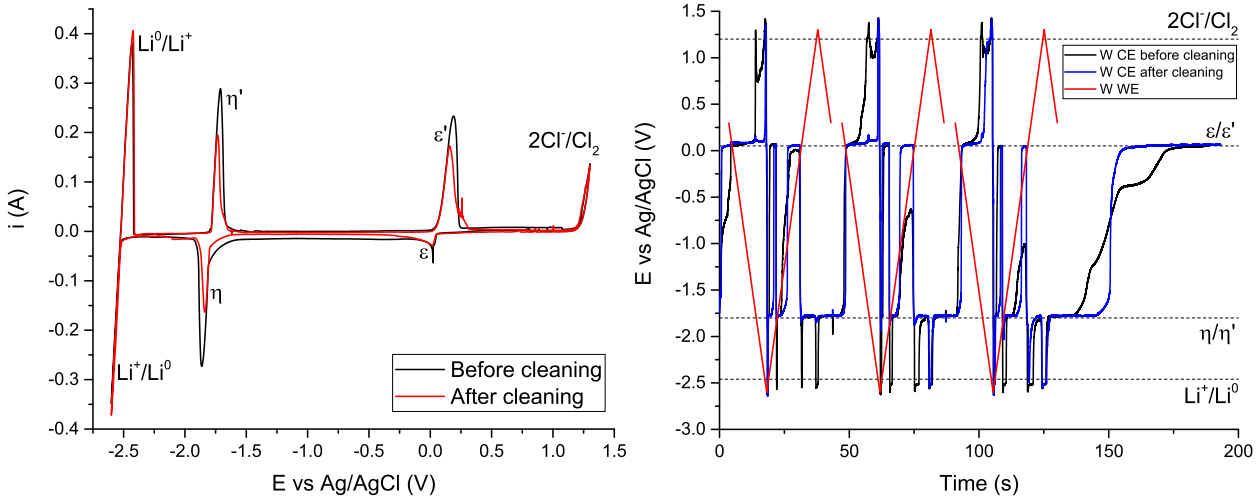

Figure 5.9: (Left) CVs on a tungsten electrode in LKE with [$BiCl_3$] = 20 mM, ν = 200 mVs^{-1}, T = 723 K. (Right) The potentials of the working and counter electrodes over time.

In these LKE-$BiCl_3$ studies, the counter electrode potential rested at reactions that were clearly visible in the CVs in order to balance the current being passed at the working electrode. The reaction, and time spent there, were dependent on the magnitude, and time, of the current passed at the working electrode. Since counter electrode potentials in the electrochemically cleaned LKE-$BiCl_3$ salt rested only on observable reactions in the CV, it is very unlikely that the unknown reactions in the LKE-$AlCl_3$ salt are due to contaminants from the LKE salt itself. It is most likely that the unknown reactions were due to aluminium alloying with transition metal contaminants from the $AlCl_3$ powder. These alloying reaction currents increased over time due to increasing surface roughness of the metal remaining on the tungsten surface, due to <100% reaction efficiency of the metal causing a build up over time. Since sparge cleaning (production of reductant and

oxidant, Li^0 and Cl_2 respectively, which are efficiently mixed by sparging) removed these unknown reactions from the CVs, it is possible to perform electrochemistry without significant influence of these unknown reactions, as long as the salt is sparge cleaned once these reactions become visible.

5.3 Monitoring $AlCl_3$ Concentration

The goal of Chapter 6 will be to co-deposit $CeCl_3$ and $AlCl_3$ together, to see if this offers improved resolution of intermetallic peak formation and if $CeCl_3$ concentration can be accurately calculated from the electrochemistry. In order to do this, it is important to know what the relative concentration of $CeCl_3$ and $AlCl_3$ are, as the change in relative ratios is likely to impact on the observed electrochemistry. Thus it is important to know how the $AlCl_3$ concentration changes over time, i.e. is it so slow that it can be assumed to be at constant concentration during experiments, or is the concentration changing too quickly for such an assumption, and if that change in concentration can be taken into account. For this purpose, the rate of loss of $AlCl_3$ from the system will be measured as a result of addition by: electrochemical dissolution (primary loss mechanism is the "short circuit" reaction with lithium metal); and powder (primary loss mechanism is the sublimation during heating and possible volatilisation from molten LKE).

5.3.1 $AlCl_3$ Added By Electrochemical Dissolution

It has been shown that electrochemical dissolution has resulted in the formation of large quantities of lithium metal which fixes the potential at the counter electrode (Figure 5.4). It is expected that the following "short circuit" reaction then occurs throughout the solution: $3Li^0 + Al^{3+} \rightarrow 3Li^+ + Al^0$, i.e. the lithium metal chemically reacts with aluminium ions to produce lithium ions and aluminium metal. This is expected to happen since the reduction potential of lithium is significantly more negative than that of aluminium, $\Delta E \approx$ -1.4 V. There are two other reactions which may lead to the loss of $AlCl_3$ from solution: reaction with water based impurities to form Al_2O_3; and the reaction of $AlCl_{3(\mathrm{LKE})}$ to $AlCl_{3(g)}$ (volatilisation). These other two reactions will be investigated in Section 5.3.2, where $AlCl_3$ is added in powder form and so loss of Al^{3+} from the "short circuit" reaction is avoided.

Figure 5.10 shows CVs performed every 5 minutes after electrochemical dissolution of an aluminium electrode to a target concentration of $[AlCl_3]_0$ = 20 mM. Over the first 10 hours the peak currents decreased in magnitude and the peak potentials shifted negatively. Both of these observations fitted with the expected behaviour of a decreasing concentration by the Nernst and Delahay equations (Equations 2.9 and 2.10 respectively). Between hours 10 and 26 $E_{p\,\alpha'}$ continued to shift negatively, however $E_{p\,\alpha}$ was shifting slightly

positive. Interestingly, both $i_{p\,\alpha}$ and $i_{p\,\alpha'}$ were slightly increasing in magnitude. Since the Delahay equation (Equation 2.10) describes only the plating peak current, only the plating peak will be used for analysis of concentration change.

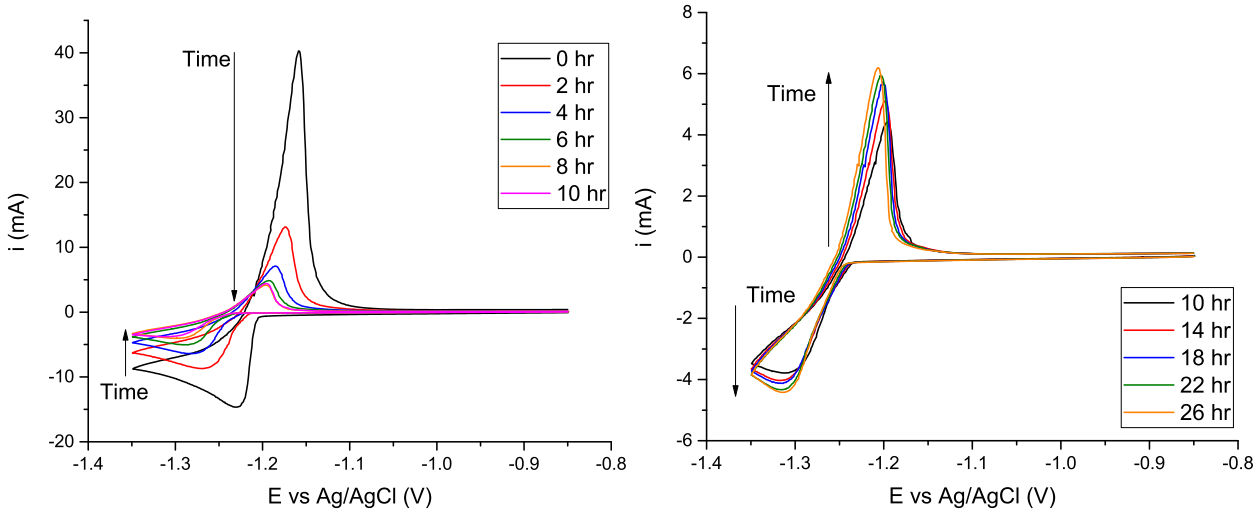

Figure 5.10: CVs performed every 5 minutes on a tungsten rod after electrochemical dissolution of an aluminium electrode. $[AlCl_3]_0 = 20$ mM, $\nu = 200$ mVs^{-1}, $T = 723$ K.

Figure 5.11 shows $|i_{p\,\alpha}|$ and $E_{p\,\alpha}$ over time. Over the first 11 hours, both decreased quite rapidly, before $|i_{p\,\alpha}|$ and $E_{p\,\alpha}$ increased very slowly, as seen from the CVs (Figure 5.10). The time taken to reach the minimum $|i_{p\,\alpha}|$ (in this case 11 hours) was termed τ. It is quite clear that the relationship between peak current and time over the first 11 hours was not linear, thus the kinetics of loss of $AlCl_3$ from the system was not 0^{th} order. For determination of the kinetics, concentration would be plotted versus time. Since here the initial concentration was not known, and so the concentration at any time t was also not known, peak current was instead plotted versus time, since $|i_{p\,\alpha}|$ is proportional to concentration as given by Equation 2.10. Data after time τ did not obey Equation 2.10 and so was not analysed in order to determine the rate of $AlCl_3$ loss. The reason for $|i_{p\,\alpha}|$ increasing after time τ was most likely caused by surface roughening of tungsten after many plating/stripping cycles, increasing the surface area (and reducing the energy required) for aluminium to plate.

The left hand graph in Figure 5.12 shows the peak current versus time as $\ln|i_{p\,\alpha}|$ and $\frac{1}{|i_{p\,\alpha}|}$ in order to test for 1^{st} and 2^{nd} order kinetics, respectively, of $AlCl_3$ loss. The linear fit was poor for 1^{st} order, but was good for 2^{nd} order, thus it was more likely that the loss of $AlCl_3$ followed 2^{nd} order kinetics over the first 11 hours. After that point ($t > \tau$) $i_{p\,\alpha}$ was clearly not due to 2nd order kinetics. It has been found that lithium metal exists in LKE as colloidal clusters.[100] The reaction of $3Li^0$ with Al^{3+} is much more likely in the case of

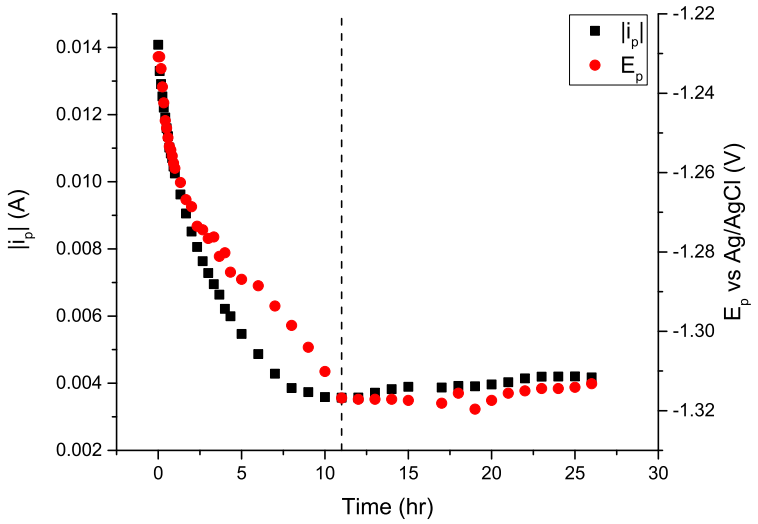

Figure 5.11: $|i_{p\,\alpha}|$ and $E_{p\,\alpha}$ over time from Figure 5.10. The dashed line at 11 hr indicates the time taken to reach the minimum $|i_{p\,\alpha}|$ (at time τ), which also happens to be when $E_{p\,\alpha}$ ceased to shift negatively.

lithium metal clusters, as this simplifies a four atom collision and reaction (since Al^{3+} reduces via a single step 3 electron transfer) to a two species collision and reaction, hence why the reaction kinetics are 2nd order.

The right hand graph in Figure 5.12 shows the plot of $E_{p\,\alpha}$ versus $ln|i_{p\,\alpha}|$, the equivalent plot for the Nernst equation (Equation 2.9). This showed a roughly linear relationship over the first 30 data points (equivalent to the first 11 hours). The expected Nernst slope of this plot is $\frac{RT}{nF}$, which for Al^{3+} is 0.0208. The linear fit for this data had a slope of 0.0502, however for repeat volatility studies the slope was often much closer to $\frac{RT}{nF}$ (Table 5.1).

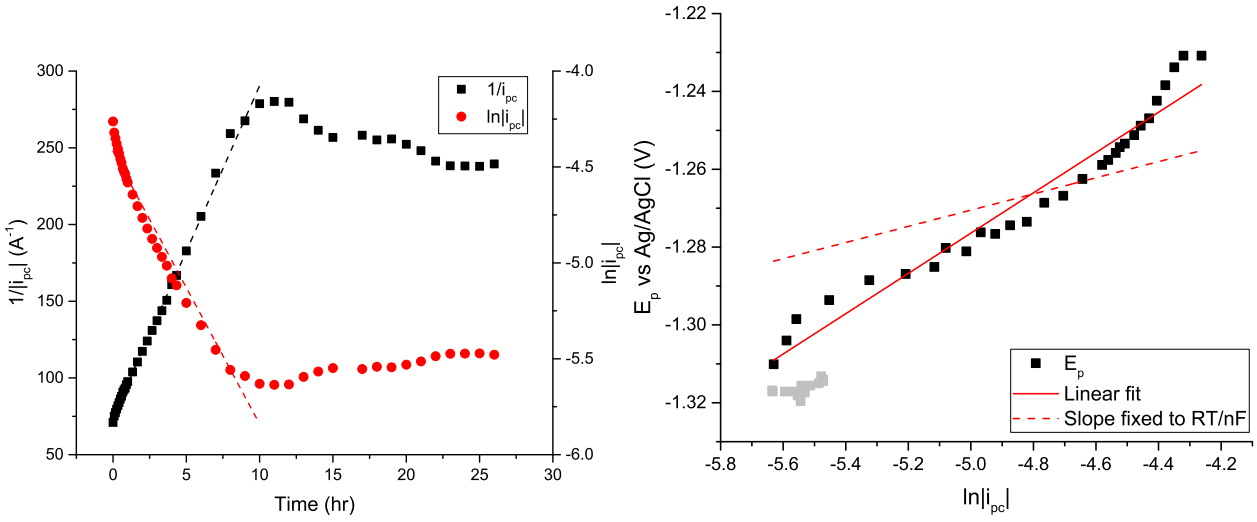

Figure 5.12: (Left) $i_{p\,\alpha}$ versus time to test for 1st and 2nd order reaction kinetics (Right) $E_{p\,\alpha}$ versus $ln|i_{p\,\alpha}|$ to test for a Nernstian response. Grey data points were excluded from the linear fit as $t > \tau$ (end of expected Nernstian response).

Table 5.1 summarises repeat studies of $AlCl_3$ loss after electrochemical dissolution, where $\frac{i_{p\,\alpha}t=\tau}{i_{p\,\alpha}t=0}$ is the percentage of $AlCl_3$ remaining after the "short circuit" reaction completed ($t = \tau$), relative to when CVs were started after electrochemical dissolution ($t = 0$). In several repeat experiments, $|i_{p\,\alpha}|$ was found to reach a minimum, then increase significantly before decreasing again. In these cases the time from 0 to τ (the first minimum $i_{p\,\alpha}$) was analysed, as this time domain consistently behaved as 2^{nd} order. For $\frac{i_{p\,\alpha}t=\tau}{i_{p\,\alpha}t=0} = 40.5$, the rate constant, k, is particularly high, τ is quite low, and the Nernst slope is high. That experiment was performed by electrochemical dissolution into LKE which had not been pre-cleaned, thus a lot of the lithium metal rapidly reacted with water based impurities, preventing the $AlCl_3$ concentration from dropping as dramatically from the "short circuit" reaction. All other studies performed in the glovebox had a Nernst slope for $E_{p\,\alpha}$ versus $ln|i_{p\,\alpha}|$ much closer to the theoretical $\frac{RT}{nF} \times 10^3 = 20.8$, which indicated that the gloveboxes result in a much better controlled environment than flowing argon through the cell when outside of the gloveboxes. The times taken to reach a "stable" $i_{p\,\alpha}$ (at $t = \tau$) were quite variable, however in general, as $\frac{i_{p\,\alpha}t=\tau}{i_{p\,\alpha}t=0}$ increased, the time taken to complete the "short circuit" reaction, τ, decreased. The length of time between electrochemical dissolution and starting CVs was on the order of minutes, so variability in measurement start times cannot be the reason that τ varied by hours. While sparge cleaning was performed in the same manner, and judged to be sufficient by visual inspection of the CVs, there may have been differing quantities of water based impurities that remained in each salt. If lithium metal reacts with oxides preferentially to $AlCl_3$, then more $AlCl_3$ would remain in the salt. Variable concentrations of water based impurities could then be the major cause of irreproducability in these experiments.

Table 5.1: Summary of repeat experiments investigating the loss of $AlCl_3$ added to LKE by electrochemical dissolution. $\frac{i_{p\,\alpha}t=\tau}{i_{p\,\alpha}t=0}$ is the percentage of aluminium remaining after the completion of the short circuit reaction.

$\frac{i_{p\,\alpha}t=\tau}{i_{p\,\alpha}t=0}$ (%)	τ (hr)	2nd order k	Nernst slope$\times 10^3$	Furnace Set-Up
0.8	13.5	41.0 ± 0.8	21.3 ± 0.5	Glovebox
6.6	12.7	28.0 ± 0.4	28.3 ± 0.4	External
7.7	26	30.8 ± 0.8	29.9 ± 0.9	External
9.3	15.8	63.3 ± 1.7	20.8 ± 0.2	Glovebox
13.3	7	57.9 ± 0.9	31.1 ± 0.7	External
25.3	11	21.6 ± 0.3	50.2 ± 0.2	External
40.5	3	141.8 ± 10.8	93.0 ± 4.0	Glovebox
51.8	4	51.3 ± 2.6	25.1 ± 0.9	External

The overall goal of this chapter is to determine the $[CeCl_3]$:$[AlCl_3]$ ratio of the system. Concentration would need to be calculated from the plating peak current. However this is problematic due to the difficulty in accurately determining the area of the macroelectrode, thus concentrations cannot be easily calculated from the macroelectrode peak currents. Once the $AlCl_3$ has reached a "stable" concentration, i.e. when the peak

current has left the zone of 2nd order kinetics ($t > \tau$), it was possible to employ microelectrodes to determine D and c simultaneously. This was be done by the use of chronoamperometry (CA). The response of CA on a microelectrode disc is given by Equation 2.15:

$$i = nF4\pi r^2 c\sqrt{\frac{D}{\pi t}} + 4nFcDr$$

The first part of this equation is the macro response from linear diffusion, which dominates at short timescales. The second part of the equation is the micro response from hemispherical diffusion which dominates at long timescales. Since they each have a different dependency on D it is possible to fit this equation to data and simultaneously determine D and c. This cannot be achieved on macroelectrodes, as only linear diffusion occurs, which is the first part of the equation, the Cottrellian response. Any CA fitting using only the Cottrell equation would result in a mutual dependency of D and c.

Figure 5.13 shows CVs and CAs of the $AlCl_3$ reaction on a microelectrode. The limiting current (i_L) of the CV was approximately -40 nA, which helped to verify that the steady state response being tended towards in the CA was accurate. From the CA (fixed $n = 3$, fixed $r = 15$ μm, fits $R^2 > 0.99$, $\chi^2 = 7\text{x}10^{-19}$), $c = 0.58 \pm 0.02$ mM and $D_{Al^{3+}} = 4.16 \pm 0.02$ x 10^{-5} cm^2 s^{-1} at 723 K. In the literature the diffusion coefficient of Al^{3+} has been found to be 2.79 ± 0.05 x 10^{-5} cm^2 s^{-1}at 773 K,[90] 0.65 ± 0.07 x 10^{-5} cm^2 s^{-1} at 943 K,[101] 3.1 x 10^{-5} cm^2 s^{-1} at 723 K,[102] and 1.33 x 10^{-5} cm^2 s^{-1} at 723 K[85], so the value obtained here was sensible. This is of similar magnitude to many other species in LKE, but critically for co-deposition studies, the diffusion coefficient of Al^{3+} is higher than that of Ce^{3+} (1 x 10^{-5} cm^2s^{-1} at 723 K).[22]

This "stable" concentration obtained from CA was 2.9% of the target concentration of 20 mM, however from the macroelectrode CVs the $i_{p\alpha}$ at $t = \tau$ was 9.3% that of $i_{p\alpha}$ at $t = 0$. It is obvious that since the electrochemical dissolution takes 10 minutes, and rapid loss was seen over the first few minutes of every repeat study, a significant amount of the $AlCl_3$ must have been lost before the first CV could be performed. Thus $i_{p\alpha}$ at $t = 0$ was for an $AlCl_3$ concentration of less than 20 mM. By determining the concentration at a particular time with microelectrode CA, it should be possible to convert the peak current to concentration at any other time by a simple ratio of currents, since peak current is directly proportional to concentration. In theory the CA measurements on microelectrodes could be taken at any point over the 2nd order kinetics time domain, as long as the rate of loss is not so rapid as to prevent multiple CAs from being run to ensure repeatability.

As will be seen in Section 5.3.2, volatility of $AlCl_3$ from LKE, at most, takes place on the timescale of days to reach the same loss of $AlCl_3$. It is then almost certain that the majority of loss of $AlCl_3$ added

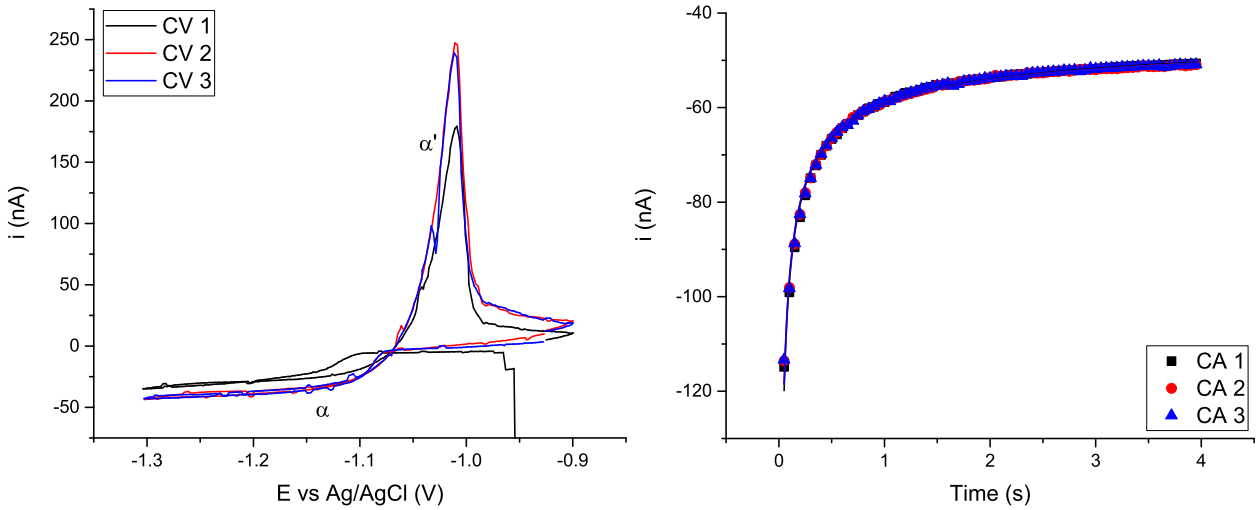

Figure 5.13: (Left) Typical CVs on a tungsten microelectrode, $\nu = 100$ mVs^{-1} (Right) CA at -1.3 V, data sampling interval 0.05 s, solid line is the fit according to Equation 2.15. Performed at $t > \tau$, $r = 15$ μm, $T = 723$ K

electrochemically was due to the "short circuit" reaction of $AlCl_3$ with $3Li^0$. Although the $AlCl_3$ and $3Li^0$ should be initially present in equal concentrations, it appeared that they did not fully react. Lithium appeared to preferentially react with water based impurities (which were not fully removed/reacted with by previous sparge cleaning), causing an imbalance between $AlCl_3$ and $3Li^0$ in the salt, and so more $AlCl_3$ remained at the end of the "short circuit" reaction. CV monitoring after the "short circuit" reaction ($t > \tau$) showed the end of 2^{nd} order kinetics, instead changes in peak currents and peak potentials were affected by changes in surface area/energy due to repeat plating/stripping restructuring the tungsten surface, or volatilisation of $AlCl_3$.

5.3.2 $AlCl_3$ Added Chemically

Figure 5.14 shows CVs performed repeatedly with $AlCl_3$ in LKE that was added in as powder. Over time the aluminium plating/stripping peak diminished in current and area, and a new oxidation peak grew in at a slightly more positive potential. After sparge cleaning (right hand Figure, 21.75hr), this new peak disappeared and the magnitude of the pure plating/stripping peak returned, but not to the same maximum as at $t = 0$. Figure 5.6 shows repeat CVs run after sparge cleaning. These CVs show peaks growing in which were attributed to contaminants. If these contaminants were $FeCl_3$, $CrCl_2$ or $NiCl_2$ then aluminium will alloy with them, which will in turn affect $i_{p\alpha}$. This makes it very difficult to determine if the $AlCl_3$ concentration change is due to volatilisation from the salt, as the aluminium plating/stripping peak current change is not solely determined by the $AlCl_3$ concentration change. Full window CVs taken directly after each sparge clean

(21.75 and 27.27 hours) did indicate a lower $AlCl_3$ concentration, however it was not clear if this was due to volatility of $AlCl_3$ (being pushed to the LKE-gas interface by the sparging gas) or due to reactions with trace amount of oxygen in the sparging gas.

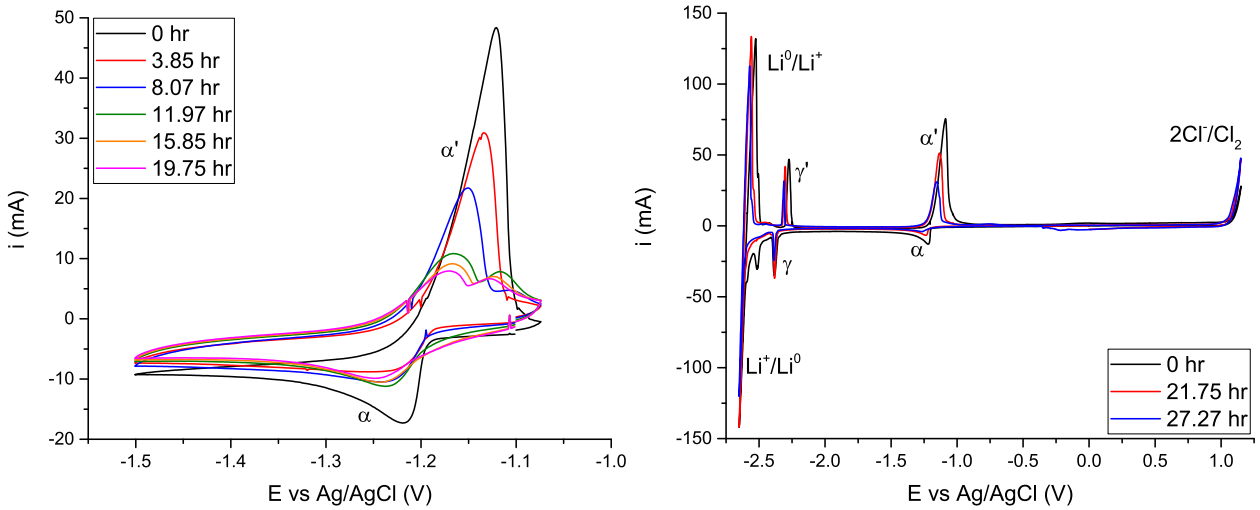

Figure 5.14: CVs of $[AlCl_3]_0 = 20$ mM over time on a tungsten electrode, $\nu = 200$ mVs^{-1}, $T = 723$ K. (Left) Repeat CVs over approximately 20 hr. (Right) comparison of full window CVs performed at the beginning of the experiment and directly after sparge cleaning at 21.75 and 27.27 hr.

Various LKE-$AlCl_3$ salts were prepared and left molten for differing times. Once cooled the salts were ground up and analysed by inductively coupled plasma mass spectrometry (ICP-MS). This technique determines the number of Al^{27} atoms in the sample, but cannot distinguish chemical environment (no oxidation state or bonding information), thus cannot determine if they are present as $AlCl_3$ or Al_2O_3. Figure 5.15 shows the aluminium concentrations from ICP-MS analysis for four LKE samples kept molten for different lengths of time. Samples were taken from Salt 1 each day by inserting a borosilicate glass rod into the molten salt. Since the glass rod was at room temperature, salt flash froze onto the rod and the rod was removed after a few seconds. The flash frozen salt was much more brittle than slowly cooled salt, and so the salt could easily be removed from the glass rod. In each salt the mass of $AlCl_3$ powder added to the LKE was the quantity required for a target $[AlCl_3]$ of 20 mM. It is unclear why the results from the first 2 days showed a greater concentration of $AlCl_3$ than was added by mass, and indeed why the concentration seemed to increase upon melting especially as this was the expected timeframe where the most $AlCl_3$ loss was expected due to 170 ^{o}C of temperature ramping where the $AlCl_3$ could sublime before the salt melted. This data point seems anomalous and may arise from a non-homogeneous concentration so soon after melting.

It did appear that the concentration of $AlCl_3$ decreased after several days (3-7 days after melting). It was possible that some water/oxygen was introduced as the argon supply to the glovebox was very close to running out and so some aluminium oxide may have crashed out as Al_2O_3. Unfortunately this experiment could not

be repeated due to time constraints. Alternatively, excess metallic lithium generated during sparge cleaning of the LKE before addition of $AlCl_3$ could have caused a "short circuit" reaction in the same manner as the salts with Al^{3+} added by electrochemical dissolution. During sparge cleaning chlorine gas would be pushed to the surface and lost from the system, thus the salt becomes "unbalanced" and not all the metallic lithium could be oxidised back to lithium ions. Aluminium in the form of Al_2O_3, or floating Al^0 generated by a "short circuit" reaction, would not necessarily be homogeneously distributed, thus not accurately sampled by the glass rod insertion technique, but should be accurately sampled in the cooled salts as no separation was performed before grinding the salt into a homogeneous powder. Thus if the $AlCl_3$ loss was indeed due to some volatility mechanism, it implies that the dissolved $AlCl_3$ retains a lot of covalent Al-Cl bonding rather than forming strongly ionic species such as $KAlCl_4$. The rate of volatility at least appeared to be much slower than the "short circuit" reaction of $AlCl_3$ and Li^0 (days rather than hours) and so studies in the next Chapter with $AlCl_3$ powder, which are performed on the order of hours, can be assumed to have a constant $[CeCl_3]$:$[AlCl_3]$ ratio over their experimental timeframes.

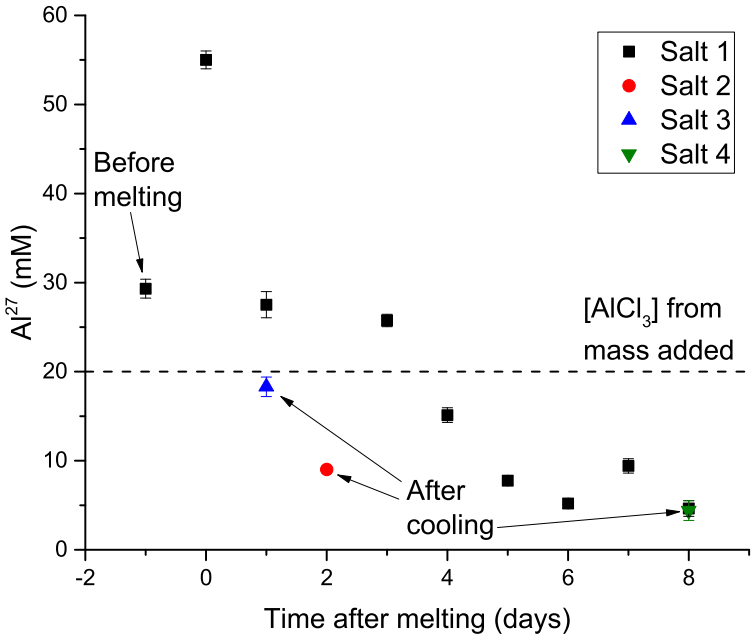

Figure 5.15: Concentration of aluminium in LKE from ICP-MS.

5.4 Conclusions

This work has highlighted that while electrochemical dissolution seems to be a good method for adding redox species quantitatively in-situ, a large quantity of liquid metallic lithium is also produced which disperses throughout solution leads to a "short circuit" type reaction with generated Al^{3+} which caused the redox

species to reduce back to metal, and precipitate from solution. Such a process would severely hamper the recovery of elements during pyroprocessing, for which electrochemical dissolution is the proposed method for introducing nuclear waste.[103, 104] Even if a frit was employed to prevent the metallic lithium generated at the counter electrode from mixing with the rest of the solution, the lithium is highly reactive and would likely increase the corrosion rate of the frit and other components around the counter electrode. This method could work more effectively in other salts where the charge balancing products were solid (e.g. $CaCl_2$, in the temperature range between the $CaCl_2$ melting point 775 °C and the Ca^0 melting point 840 °C), and so remained on the counter electrode. The rate of the short circuit reaction would then be much less and the products of electrochemical dissolution would not mix as efficiently.

Measuring the counter electrode potential has highlighted the ability to detect the potentials of species present at low concentrations, or perhaps the formation of intermediate species, which are broken down during sparge cleaning and not normally observed on the working electrode electrochemistry. This type of measurement may be useful as a diagnostic of salt cleanliness.

The rate of the Al^{3+} and lithium metal "short circuit" reaction was found to typically take tens of hours to finish. The decrease in aluminium plating peak current relative to the start of the measurements ($\frac{i_{p\,\alpha}t=\tau}{i_{p\,\alpha}t=0}$) was found to vary between 1% and 30%. The variability was attributed to the differing levels of water based impurities remaining after sparge cleaning LKE prior to electrochemical dissolution of the aluminium electrode. With more water based impurities remaining, some of the generated lithium metal likely reacted with the water based impurities and so unbalanced the quantity of lithium metal to aluminium ions, thus the $AlCl_3$ concentration never reached 0. Due to the difficulty in determining macroelectrode area, it was difficult to convert measured peak currents into concentrations, which is the ultimate aim of an on-line monitoring sensor. From chronoamperometry measurements on a microelectrode it was possible to determine D and c simultaneously. The values obtained made qualitative sense for the system, and were of the same order of magnitude as literature values, however repeat studies would be required to have good confidence in the exact diffusion coefficient value. While this was a useful experiment, it is not practical to run chronoamperometry microelectrode prior to every $CeCl_3$ and $AlCl_3$ co-deposition measurement on a macroelectrode, owing to the issues of microelectrode yield and lifetime which are still being improved.[64, 105, 106]

While the exact concentration of $AlCl_3$ may not have been known at all times during the "short circuit" reaction, this method of addition will be used in the next chapter to probe how a varying $[CeCl_3]$:$[AlCl_3]$ ratio will impact on co-deposition electrochemistry. Such an experiment can only employ rapid electrochemical measurements (narrow potential window CVs at reasonably fast scan rates) owing to the high rate of the "short circuit" reaction.

The addition of $AlCl_3$ powder in a glovebox (well maintained argon atmosphere) does also appear to suffer from loss of $AlCl_3$. This appears to be due to volatility of $AlCl_3$ from LKE, however the rate of loss is at least significantly slower than the "short circuit" reaction (days rather than hours). This will allow more complex electrochemical measurements to be performed at "fixed" $[CeCl_3]$:$[AlCl_3]$ ratios.

Chapter 6

Co-deposition of $CeCl_3$ and $AlCl_3$ on Macroelectrodes

6.1 Introduction

As discussed in Chapter 4, the use of a bulk aluminium macroelectrode presents difficulty with the study of cerium-aluminium alloy formation. As cerium is a large atom relative to aluminium, the alloying process induces stress in the aluminium lattice and thus there is a kinetic reaction barrier for cerium insertion. In principle, the co-deposition of cerium and aluminium together will avoid the kinetic barrier of insertion, leading to higher cerium content in the alloy and electrochemistry which is simpler to analyse. While this co-deposition method does indeed show more information (Figure 4.27), the "short circuit" reaction of Al^{3+} and Li^0 after electrochemical dissolution of an aluminium electrode made studying a fixed $[CeCl_3]$:$[AlCl_3]$ difficult.

The aim of this chapter is to understand how co-deposition is affected by the $[CeCl_3]$:$[AlCl_3]$ ratio, as this would inform what is controlling the alloying reaction, e.g. diffusion of Al^{3+} or diffusion of Ce^{3+}. It is possible to use the "short circuit" reaction after electrochemical dissolution of an aluminium electrode (established in Chapter 5) to study how the increasing $[CeCl_3]$:$[AlCl_3]$ ratio (by the decreasing $AlCl_3$ concentration) affects the observed electrochemistry of the cerium-aluminium alloying. This was done in the same manner as the study of the $AlCl_3$ concentration change (Section 5.3.1): an aluminium electrode was electrochemically dissolved into an LKE-$CeCl_3$ salt, CVs were performed every few minutes at a single scan rate, but over a wider potential window to include cerium-aluminium alloying. This allows for a qualitative sense of how the

electrochemistry is influenced by the increasing [$CeCl_3$]:[$AlCl_3$] ratio, as the exact value of the ratio at any point in time is difficult to determine on macroelectrodes.

With the more recent availability of an inert atmosphere glovebox set-up, it was possible to add $AlCl_3$ powder a pre-cleaned LKE-$CeCl_3$ salt. Although some of the $AlCl_3$ volatilises during the furnace heating phase (Section 5.3.2), once the salt is molten, the $AlCl_3$ concentration is stable over experimental timeframes, thus studies of fixed [$CeCl_3$]:[$AlCl_3$] ratios have also been performed. Addition via $AlCl_3$ powder now allows for a more thorough investigation of the co-deposition electrochemistry at a specific [$CeCl_3$]:[$AlCl_3$] ratio, as more electrochemistry can be performed at a single concentration ratio. The quantities of $AlCl_3$ added from both electrochemical dissolution and powder addition (and so the theoretical maximum concentrations), are given in legends as $[AlCl_3]_0$, although the true concentrations (which are difficult to calculate accurately) will be lower.

6.2 Variable [$CeCl_3$]:[$AlCl_3$] Ratio: Study of Cerium-Aluminium Alloying with $AlCl_3$ added via Electrochemical Dissolution

It is of interest to study alloy formation with different [$CeCl_3$]:[$AlCl_3$] ratios. The loss of $AlCl_3$ can be used to probe these ratio changes, however since the change is rapid, only relatively simple (rapid) experiments can be performed. CVs were performed every few minutes at a single scan rate, but over a wider potential window than when only studying the Al^{3+} and Li^0 "short circuit" reaction: $3Li^0 + Al^{3+} \rightarrow 3Li^+ + Al^0$. It is possible that lithium metal reacts with Ce^{3+} to form cerium metal: $3Li^0 + Ce^{3+} \rightarrow 3Li^+ + Ce^0$. That cerium metal would then react with Al^{3+} to regenerate Ce^{3+} and form aluminium metal: $Ce^0 + Al^{3+} \rightarrow Ce^{3+} + Al^0$. Thus the end point of the reaction is the same as if Ce^{3+} was not present, and the $CeCl_3$ concentration is therefore constant as the $AlCl_3$ concentration decreases.

CVs performed over a two hour period can be seen in Figure 6.1. In the first 28 minutes a number of reactions were observed: aluminium plating (α) and stripping (α' and α"), two cerium-aluminium alloying reactions (A/A' and B/B') and lithium-aluminium alloying (β/β'). $i_{p\,\alpha''}$ became larger over time, whereas $i_{p\,\alpha'}$ became smaller over time, which implied that each peak was due to a distinct structure of aluminium and that the ratio of each structure was changing over time. Since the stripping current is limited by the electrode kinetics, which causes the CVs to follow the same currents, as the peak currents changed, so did the peak potentials. Thus these peaks overlapped significantly more over time and became difficult to resolve. α" has not been reported in the literature and has only been observed in this work when cerium has alloyed with aluminium, i.e. not observed when only plating/stripping aluminium or when lithium has alloyed with aluminium. α"

can be understood to be a new structure of aluminium formed by oxidation of cerium-aluminium alloy. This new aluminium structure was likely much rougher and less compact than bulk aluminium, thus being easier to oxidise than bulk aluminium. As the $AlCl_3$ concentration decreased, the aluminium layer would be thinner and so more of the aluminium would be alloyed with cerium, causing more of this rough aluminium to be present during stripping.

Across the entire experiment the first cerium-aluminium alloy peaks, A/A', were clearly observable. The second cerium-aluminium alloy peaks, B/B', were initially observable but became smaller within the first 10 minutes. Since this reaction was only visible for a few CVs it will not be analysed in detail. Once the β/β' currents increased the potential window was narrowed (right hand graph in Figure 6.1).

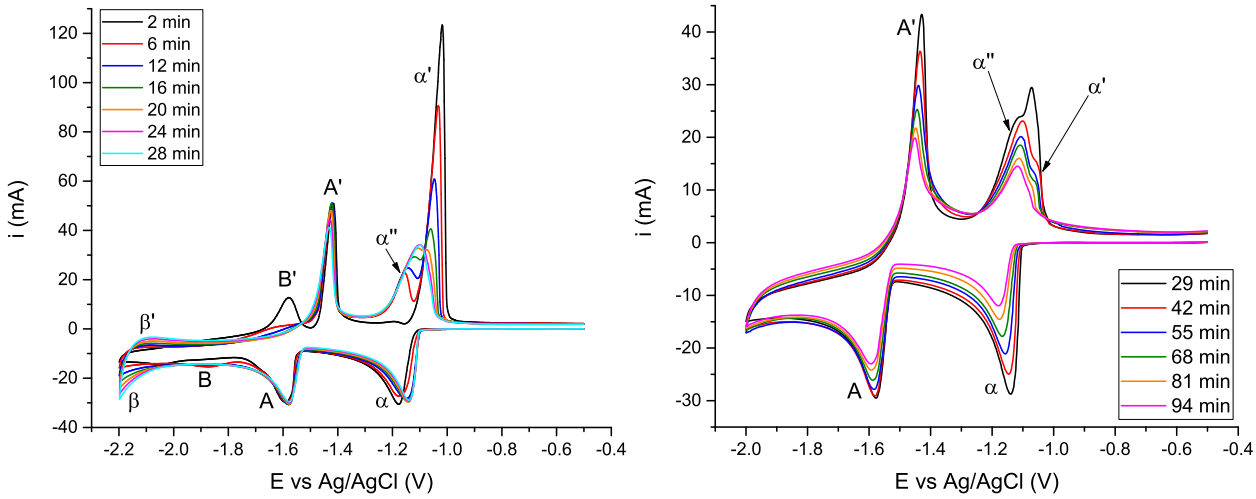

Figure 6.1: CVs of LKE containing $[CeCl_3]$ = 20 mM, $[AlCl_3]_0$ = 20 mM, ν = 200 mVs-1, T = 823 K (Left) The first 28 minutes (Right) After the first 28 minutes. The potential window was narrowed at 28 minutes to avoid the reduction of Li^+ which was observed in the wider potential window (<-2.1 V) after a few minutes had passed.

6.2.1 Peak Analysis

Figure 6.2 shows the peak currents for each reaction over time. Over the first 20 minutes $i_{p\,\alpha}$ was variable, which can be understood as the time required for Al^{3+} to diffuse from the aluminium electrode to the tungsten working electrode (variable local concentration), combined with some degree of the "short circuit" reaction occurring in solution. After 20 minutes the $AlCl_3$ concentration became homogeneous in solution and decreased rapidly as expected, due to the "short circuit" reaction with lithium metal. $i_{p\,A}$ (the total current due to cerium and aluminium reduction) also decreased, but less rapidly. By subtracting the current due to aluminium (denoted as $i_{lim\,\alpha}$, although it was not strictly a "limiting" current) at the onset potential of peak A ($E_{onset\,A}$, where the current was only due to aluminium reduction) from $i_{p\,A}$, the current due only

to cerium reduction, $i_{p\,Ce^{3+}}$, was obtained. $|i_{p\,\alpha}|$ was initially greater than $|i_{p\,Ce^{3+}}|$, but became less than $|i_{p\,Ce^{3+}}|$ after 54 minutes. $i_{p\,Ce^{3+}}$ was effectively constant at approximately -20 mA over this experimental timeframe, which suggested that the rate of cerium reduction was always controlled by the flux of cerium to the electrode, rather than by the quantity of aluminium pre-deposited, which decreased as the $AlCl_3$ concentration decreased. Since the quantity of cerium reduced during co-deposition must be constant, as it is controlled by the flux of cerium, the rate of any cerium insertion reaction must also be constant. Since the amount of pre-deposited aluminium decreased quite rapidly, the total amount of cerium reduced by the insertion reaction must have been very small, i.e. not filling the whole pre-deposited volume of aluminium, in order for $i_{p\,Ce^{3+}}$ to be constant.

The geometric surface area was not measured for this experiment, however it was estimated to be 0.664 cm^2 (1 cm immersion of an $r = 0.1$ cm tungsten rod). For the added $CeCl_3$ concentration of 20 mM, this surface area would be expected to give $i_{p\,Ce^{3+}} \approx$ -20 mA. Thus it appears that if the geometric area of the tungsten rod is known, the $CeCl_3$ concentration can be calculated from co-deposition, as long as Ce^{3+} diffusion is the limiting factor.

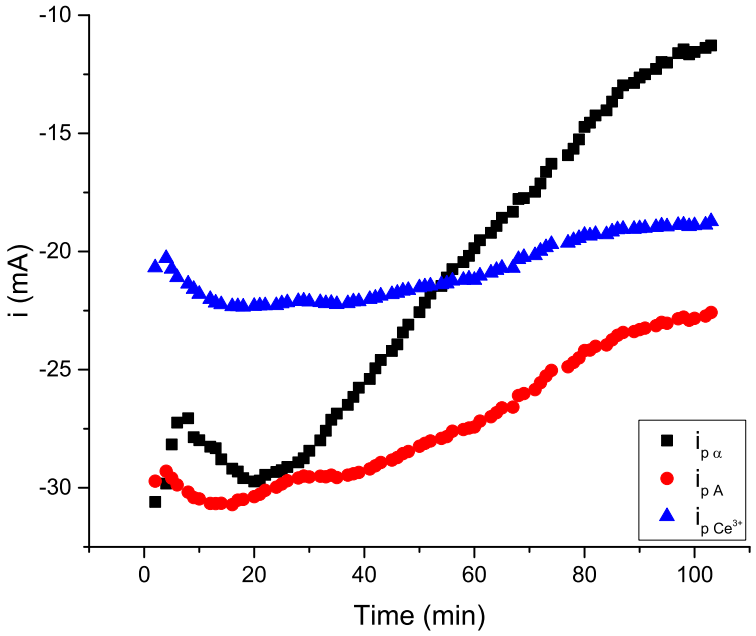

Figure 6.2: Reduction peak currents over time from Figure 6.1. $i_{p\,Ce^{3+}}$ was calculated by subtracting the current at $E_{onset\,A}$ from $i_{p\,A}$.

Figure 6.3 shows how $E_{p\,\alpha}$ and $E_{p\,A}$ changed over time. Both reduction peak potentials shifted positively over the first 20 minutes, which matched the variability in $i_{p\,\alpha}$ (Figure 6.2). Again this was explained as an initially non homogeneous concentration of $AlCl_3$ directly after electrochemical dissolution; as the local concentration of Al^{3+} increased, so did $i_{p\,\alpha}$ and $E_{p\,\alpha}$. This positive shift of potential is consistent with an

increasing concentration due to the Nernst equation (Equation 2.9). At approximately 30 minutes (when the potential window was narrowed), the reduction peak potentials did shift negatively, indicating that the $AlCl_3$ concentration was then homogeneous and therefore the "short circuit" reaction was the dominant factor of $AlCl_3$ concentration change from that time onward. At 80 minutes, both $E_{p\,A}$ and $E_{p\,\alpha}$ became constant, despite $i_{p\,\alpha}$ having continued to decrease. If the $AlCl_3$ concentration had become constant, neither the peak potential or the peak current should have changed, whereas if concentration was still decreasing then both should have changed. Since only the peak current was changing, this implied that there was some variable in the system which was continuing to change which affected the current but not the potential, e.g. electrode surface area. Since $E_{p\,A}$ followed the same trend as $E_{p\,\alpha}$, the potential required to reduce cerium to form cerium-aluminium alloy was affected by the $AlCl_3$ concentration. It may be that the potential required for co-deposition changes with quantity of aluminium pre-deposited, or changes with the $[CeCl_3]$:$[AlCl_3]$ ratio.

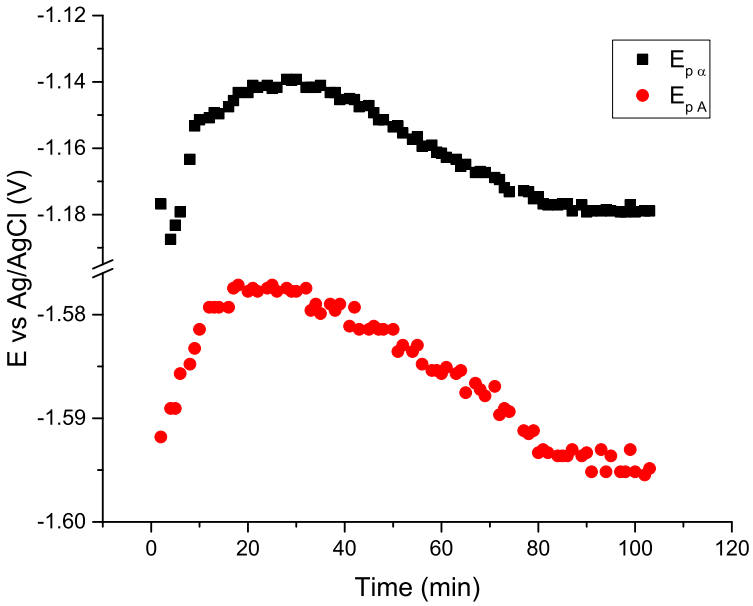

Figure 6.3: $E_{p\,\alpha}$ and $E_{p\,A}$ over time from Figure 6.1.

6.2.2 Molar Ratio during Co-deposition Potentials

During work on bismuth-cerium co-deposition it was found that both bismuth and cerium-bismuth alloying gave flat limiting convolved currents.[8] By taking a ratio of these currents, the m value (the molar ratio of cerium to bismuth being deposited at each time interval) could be calculated. This informed the stoichiometry of the co-deposited cerium-bismuth alloy (Ce_mBi). It is of interest to know if this same analysis works for the cerium-aluminium alloying system (as alloying in solid aluminium may not be expected to result in rapid

phase formation as was the case in liquid bismuth) and thus if different [$CeCl_3$]:[$AlCl_3$] ratios show different molar ratios and thus different co-deposit stoichiometries.

Figure 6.4 shows convolved CVs of cerium aluminium co-deposition at two times after electrochemical dissolution. In each case the aluminium reduction (α) gave a flat limiting convolved current, however the cerium-aluminium alloying reaction (A) did not. At 2 minutes the convolved current A was peak-like before it became a straight line on a slope (increasing with potential). At 41 minutes the convolved current of A did not show the same peak-like shape, instead going directly to a straight line on a slope. This peak-like response in the convolved current was observed for the cerium-bismuth alloying case. By decreasing the quantity of deposited bismuth prior to cerium reduction (by starting the CV closer to the onset potential of cerium reduction, or by decreasing the [$CeCl_3$]:[$BiCl_3$] ratio), the size of the convolved peak diminished. The peak in the convolved data was explained to be reduced cerium rapidly inserting into pre-deposited bismuth (a liquid at these temperatures, thus with a low kinetic barrier to insertion), after which the current was controlled by co-deposition at the surface. By reducing the quantity, and therefore volume, of pre-deposited bismuth, there was less cerium that could rapidly insert into the bismuth and therefore the peak decreased in size. This cerium-aluminium data can also be explained with the same mechanism of cerium insertion into pre-deposited aluminium, as the quantity of aluminium was greatest at 2 minutes (thus some cerium insertion occurred), leading to a peak-like (non diffusion limited) response. Once the $AlCl_3$ concentration decreased, the volume of pre-deposited aluminium was less and so less of the cerium insertion occurred, hence the peak-like response disappears over time.

The slope of the convolved cerium-aluminium alloying current A, was also observed when reducing cerium onto a bulk aluminium macroelectrode (Figure 4.7). In both cases the convolved current was equal on the forward and backward scan for the cerium-aluminium alloying reaction, however there was an obvious slope, i.e. it was not flat, therefore the current after $i_{p\,A}$ in the CVs decreased slowly than was expected from the reaction being limited by diffusion. This implied that even during co-deposition, alloying of cerium and aluminium results in a rough surface with increasing surface area as further alloying occurs.

The associated m values (molar ratio of Ce:Al being deposited at each data point) can be seen in Figure 6.5. These were calculated using:

$$m = \frac{I_A - I_{L\,\alpha}}{I_{L\,\alpha}} = \frac{I_A}{I_{L\,\alpha}} - 1 \tag{6.1}$$

The full derivation for this equation can be found in [8]. This analysis has not been performed in the literature, but has proved to be very useful in studying the cerium-bismuth and lithium-bismuth binary

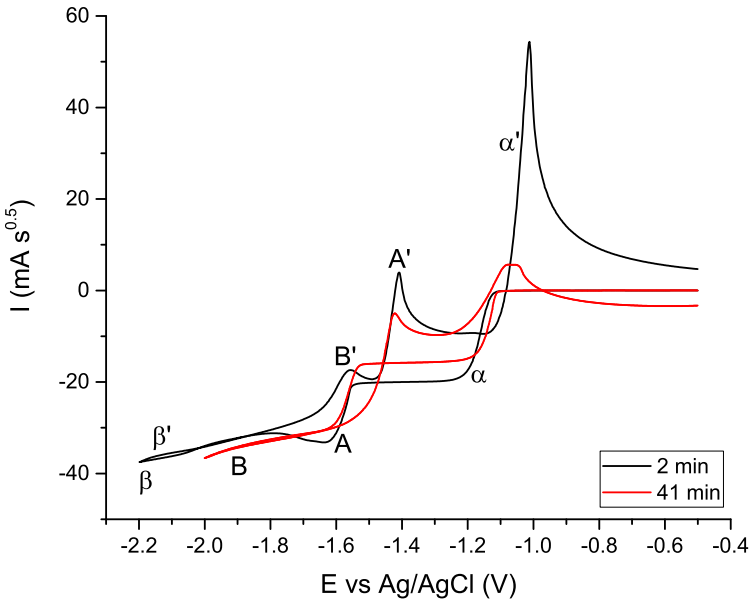

Figure 6.4: Convolved CVs of Figure 6.1

systems. This equation effectively takes the ratio of convolved current due to cerium and convolved current due to aluminium. Since aluminium and cerium both have $n = 3$, no correction is needed to convert current ratio to molar ratio. The m value is not necessarily the flux ratio:

$$\frac{J_{Ce^{3+}}}{J_{Al^{3+}}} = \frac{[CeCl_3] * \sqrt{D_{Ce^{3+}}}}{[AlCl_3] * \sqrt{D_{Al^{3+}}}} \tag{6.2}$$

which would only equal the m value if both species are individually being reduced under diffusion control. In the case of cerium-bismuth co-deposition, the m value was equal to the stoichiometry of a Ce_xBi_y crystal phase over one potential window, but then became equal to a different Ce_xBi_y crystal phase at more negative potentials, despite the predicted flux ratio being greater than all observable Ce_xBi_y phases. Thus, in the case of cerium-bismuth co-deposition, the phases being co-deposited were controlled by the applied potential.

Since the convolved current for reaction A was not limiting, the m value could not give a constant value during co-deposition potentials. As with the bulk aluminium macroelectrode, this was explained by formation of alloy increasing the surface area, which caused the alloying current to be greater than expected for the reaction under control of Ce^{3+} diffusion. This increased surface area meant that $I_{L\,\alpha}$ was overvalued at co-deposition potentials, causing the m value calculation to become invalid. While the m values could not give an exact measure of the co-deposition ratio over the co-deposition potentials, around $E_{p\,A}$ (where the calculation was most valid as the electrode area had not significantly increased) the m value did increase over time as expected from the increasing $[CeCl_3]$:$[AlCl_3]$ ratio. The m value (Figure 6.5), even at 2 minutes

with the lowest $[CeCl_3]$:$[AlCl_3]$ ratio, was approximately 0.5 at $E_{p\,A}$. The m value continued to increase to approximately 1.5 at $E_{p\,A}$ at 103 minutes. This was great enough for the formation of four crystalline Ce_xAl_y intermetallics: Ce_3Al_{11}, $CeAl_3$, $CeAl_2$ and CeAl, however only the peaks corresponding to Ce_3Al_{11} were observed over this potential window. The fact that m increased smoothly over time, rather than exhibiting specific values, points towards the co-deposition ratio being controlled by the flux of each individual species. It is likely then that A/A' is related to an amorphous cerium-aluminium phase rather than a specific crystal phase, despite no thermodynamically stable amorphous phase according to the phase diagram (Figure 2.11).

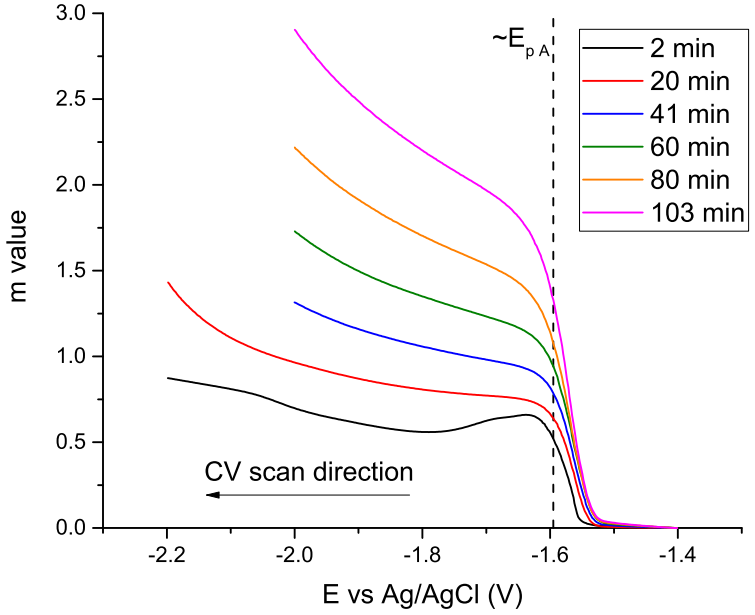

Figure 6.5: Molar ratio (m) of cerium to aluminium reduced over the course of CVs in Figure 6.1.

6.2.3 Molar Ratio of Deposited Alloy

It is important to note that the m value is the ratio of cerium to aluminium depositing at each point in time, not the ratio of cerium to aluminium that has been deposited. From the reduction currents, the Ce:Al ratio in the alloy over the course of the CV can be determined. This can be done by looking at the co-deposition regime, i.e. ignoring pre-deposited aluminium:

$$\text{Ce:Al}_{\text{co-deposit}} = \frac{Q_{\text{Ce co-deposited}}}{Q_{\text{Al co-deposited}}} = \frac{\nu * \int_{-1.5}^{-2.0} (i - i_{lim\,\alpha})\, dV}{\nu * i_{lim\,\alpha} * (2 - 1.5)} \tag{6.3}$$

where $\int_{-1.5}^{-2.0} (i - i_{lim\,\alpha})\, dV$ is the integral of current only due to Ce^{3+} reduction over the peak A and $i_{lim\,\alpha}$ is the current due to aluminium reduction at $E_{onset\,A}$, and assumed to be constant for the remainder of the

reductive scan. This charge analysis during the reductive scan is novel; in the literature charge analysis is performed only on the oxidative scan.[37]

The Ce:Al ratio of the alloy taking into account the pre-deposited aluminium is:

$$\text{Ce:Al}_{\text{total-deposit}} = \frac{Q_{\text{Ce co-deposited}}}{Q_{\text{Al co-deposited}} + Q_{\text{Al pre-deposited}}} = \frac{\nu * \int_{-1.5}^{-2.0} (i - i_{lim\,\alpha})\, dV}{\nu * (i_{lim\,\alpha} * (2 - 1.5) + \int_{-1.1}^{-1.5} i\, dV)} \tag{6.4}$$

where $\int_{-1.1}^{-1.5} i\, dV$ is the integral of the current over peak α up to $E_{onset\,A}$. Thus this expression integrates current over the entire cathodic scan region of the CV to find the total amount of aluminium and cerium deposited. In both ratios of the reduction charge, integrals are performed relative to the existing baseline, i.e. relative to $i = 0$.

Figure 6.6 shows the plots of Equations 6.3 and 6.4 as a function of the potential being scanned during the CV. Over time the $[CeCl_3]$:$[AlCl_3]$ ratio increased, which corresponded with increased $\text{Ce:Al}_{\text{co-deposit}}$ and $\text{Ce:Al}_{\text{total-deposit}}$ values. Over the course of the CVs, $\text{Ce:Al}_{\text{co-deposit}}$ increased rapidly, but then decreased further negative of the peak potential. It is important to note that much like the m value calculation, the current at $E_{p\,A}$ ($i_{lim\,\alpha}$) is assumed to remain constant over the co-deposition potentials during this calculation. However this does not appear to be the case as the convolved currents indicate an increase in electrode surface area once alloying occurs. Thus Ce:Al values negative of $E_{p\,A}$ are inaccurate, and must be analysed with a large degree of uncertainty in the absolute values. Since $\text{Ce:Al}_{\text{total-deposit}}$ is a global average of both metals, it is averaging together the co-deposit layer and the pre-deposited aluminium layer, giving values far less than $\text{Ce:Al}_{\text{co-deposit}}$. Even if cerium insertion into the pre-deposited aluminium was occurring, it is unlikely that the alloy would be homogeneous during the CV. Therefore $\text{Ce:Al}_{\text{total-deposit}}$ was very unlikely to represent the local environment. However, the $\text{Ce:Al}_{\text{total-deposit}}$ values were greater than 0.333... at $E_{p\,A}$ at 103 minutes, which implied that it should have been possible to form a second intermetallic phase, $CeAl_3$, despite there being no observed peaks for this formation in the CVs.

Ce:Al can also be determined from the oxidation peak areas:

$$\text{Ce:Al}_{\text{ox}} = \frac{Q_{A'}}{Q_{\alpha' + \alpha''}} = \frac{\nu * \int_{-1.6}^{-1.3} i\, dV}{\nu * \int_{-1.3}^{-1.0} i\, dV} \tag{6.5}$$

This integral is performed relative to a linear baseline generated between the start and end potentials of integration. On the back scan, there is a region between $E_{p\,A'}$ and $E_{p\,\alpha'}$ where more aluminium can plate. This reduction charge on the back scan is also obtained (when possible), and subtracted from the oxidation charge of the aluminium stripping peak(s). In this case the two aluminium stripping peaks had a high degree

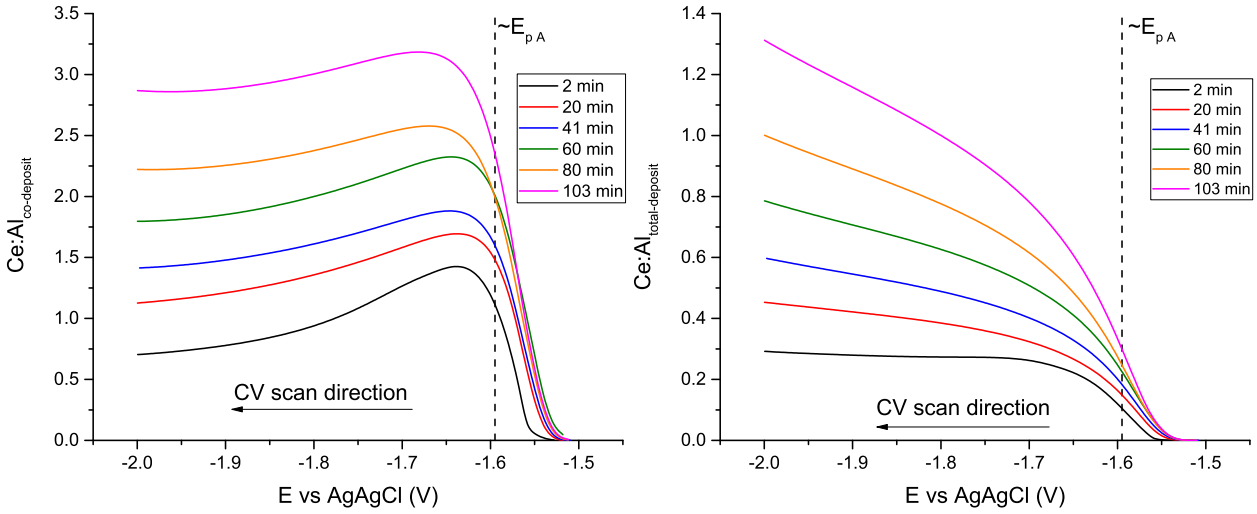

Figure 6.6: Ratio of cerium to aluminium (Ce:Al) during alloying in Figure 6.1. (Left) Ratio of co-deposit only, ignoring pre-deposited aluminium. (Right) Ratio of total deposit, including pre-deposited aluminium.

of overlap, and so their total areas were evaluated together. If the two stripping peaks were well separated, then $\frac{Q_{A'}}{Q_{\alpha''}}$ would have been a better representation of the Ce:Al ratio in the alloy, as α" was attributed to aluminium that had alloyed with cerium, whereas α' was attributed to bulk (unalloyed) aluminium. In this instance $Ce{:}Al_{ox}$ was a measure of the global composition, much like $Ce{:}Al_{total\text{-}deposit}$.

Figure 6.7 shows the $Ce{:}Al_{ox}$ values over time. These values were greater than those of $Ce{:}Al_{total\text{-}deposit}$ at $E_{p\,A}$, despite both of these calculations describing the global average of the alloy. As the $[CeCl_3]{:}[AlCl_3]$ ratio increased, the α" peak dominated the aluminium stripping reactions, thus $Ce{:}Al_{ox}$ became a better description of the alloy and the calculated values became more similar to $Ce{:}Al_{co\text{-}deposit}$. Since $Ce{:}Al_{co\text{-}deposit}$ and $Ce{:}Al_{total\text{-}deposit}$ rely on the assumption that $i_{lim\,\alpha}$ remains constant throughout the CV, which has been determined to not be the case in these macroelectrode experiments, these Ce:Al values could not be calculated accurately for the entire reductive scan. Charge analysis of the reductive scan would be beneficial where the surface area does not increase significantly during alloying, e.g. the cerium-bismuth system. $Ce{:}Al_{ox}$ has the benefit of not requiring a constant surface area, as it is a ratio of everything that had deposited, however it does assume that $Q_{\alpha'+\alpha''} \simeq Q_{\alpha''}$ which is only valid if either: very little aluminium is pre-deposited, or cerium rapidly inserts into pre-deposited aluminium.

The $Ce{:}Al_{ox}$ values are greater than the m values (at $E_{p\,A}$), which implies that the increase in the m value negative of $E_{p\,A}$ was real effect, and not simply due to an increase in surface roughness. While the exact m values and Ce:Al values differed, they all showed a smooth increase over time as the $[CeCl_3]{:}[AlCl_3]$ ratio increased. This combined m value and charge analysis work then reinforces that the cerium must have been

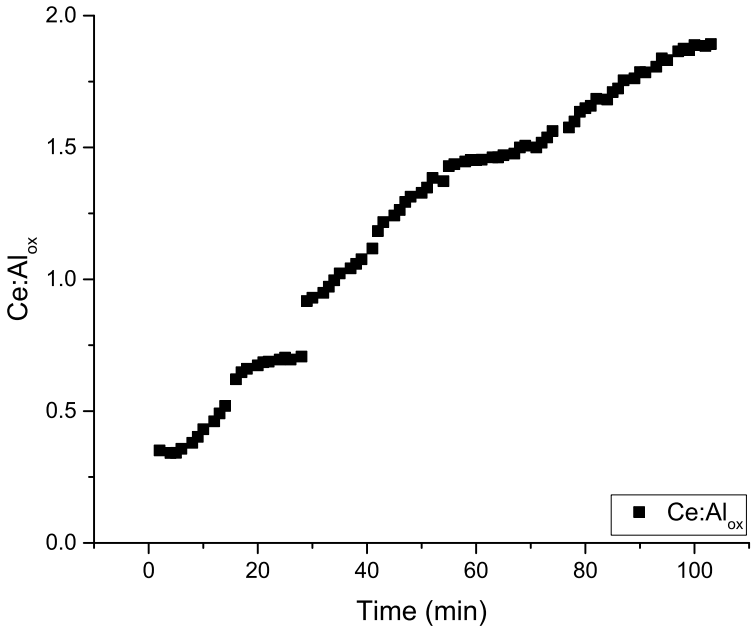

Figure 6.7: Ce:Al_{ox} values calculated from the oxidation peak areas from Figure 6.1

controlled by its flux (i.e. mass transport controlled), rather than by the formation of a specific crystal phase. For this to be the case an amorphous cerium-aluminium alloy must have formed, which is likely kinetically stabilised by the slow diffusion of cerium inside solid aluminium. This is in contrast to cerium-bismuth alloying, where phase changes occurred rapidly inside liquid bismuth, resulting in specific crystal phase formation, with the possible phases being controlled by the applied potential.

Figure 6.8 shows the n value (peak width) over time by fitting peak A' with Equation 4.1. The n values started at approximately 5.5, which was greater than the expected $n = 3$, indicating a homogeneous phase of alloy. Over time the n values tended towards 3, and reached this value at approximately 54 minutes. Interestingly this was similar to the time that $|i_{p\,\alpha}|$ became less than $|i_{p\,Ce^{3+}}|$. This decrease in n was expected, as the quantity of aluminium plated became smaller as the $AlCl_3$ concentration decreased. Thus the quantity of alloy became more similar to that of a monolayer, which is the assumption made in Equation 4.1 from which the n value was obtained.

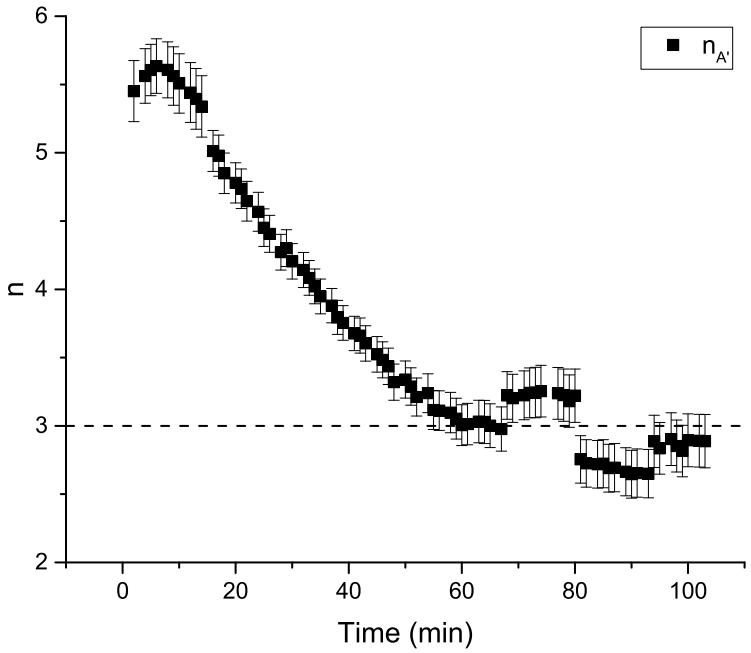

Figure 6.8: n values (peak widths) obtained by fitting peak A' with Equation 4.1.

6.3 Fixed $[CeCl_3]$:$[AlCl_3] \geqslant$ 1:1

In these experiments $AlCl_3$ powder is added to a pre-cleaned LKE-$CeCl_3$ salt in an argon filled glovebox. Thus, once molten, the $[CeCl_3]$:$[AlCl_3]$ ratio will be fixed (over the few hours that the experiment is run) and so more detailed electrochemical experiments at a particular $[CeCl_3]$:$[AlCl_3]$ ratio can be performed. Changes in electrochemistry can then be shown to be due to difference in phase change kinetics (or some other factor) rather than a rapidly changing flux ratio. This section uses a $[CeCl_3]$:$[AlCl_3]$ ratio similar to that of Section 6.2 at $t = 0$ min. Later in Section 6.4 the $[CeCl_3]$:$[AlCl_3]$ ratio is more similar to that of Section 6.2 at $t = 100$ min. Thus these two flux ratios were being investigated in further detail, using a wider range of electrochemical analysis. The concentration ratios given are minimum estimates, due to the difficulty in accurately determining the $AlCl_3$ concentration.

6.3.1 Cyclic Voltammetry

Figure 6.9 shows typical CVs performed covering the potential window of aluminium and the first observable cerium-aluminium alloy reaction (A/A'). There was no α" peak, which may have been due to the narrower potential window used; less alloyed aluminium was produced relative to bulk aluminium and so there was very little unstable aluminium to be oxidised. There was an extra feature, α"', which was positive of the main aluminium stripping peak α'. This feature has been observed in some experiments with LKE-$AlCl_3$

in the course of this work, thus was not a result of cerium alloying, but possibly due to a small amount of Al_2O_3 formation from surface oxide on the tungsten electrode. The cerium-aluminium alloy formation (A) appeared to be kinetically limited as with the reduction of Ce^{3+} into a bulk aluminium macroelectrode (Figure 4.4), since the current before $E_{p\,A}$ tracked along the same values, but $E_{p\,A}$, and therefore $i_{p\,A}$, varied with scan rate. $E_{p\,A'}$ appeared to stay constant with scan rate, implying the oxidation of the alloy was thermodynamically controlled, again agreeing with previous measurements on the reaction of Ce^{3+} into a bulk aluminium macroelectrode (Section 4.2.2).

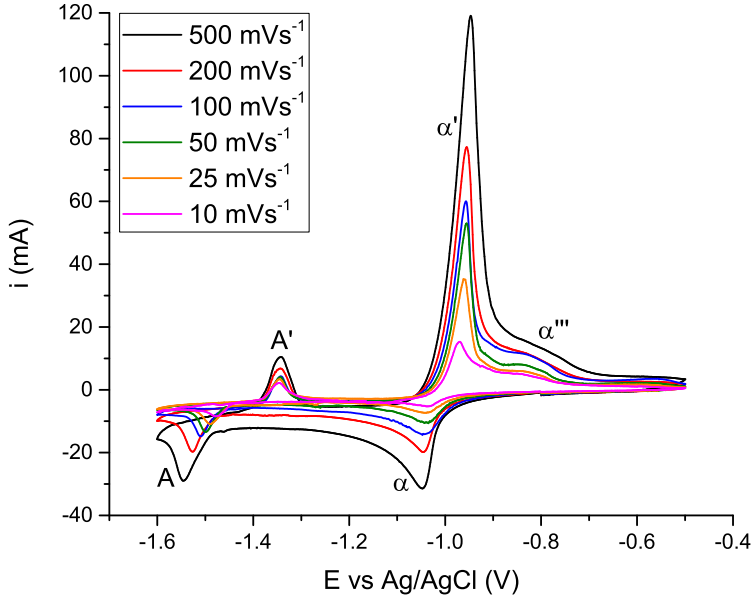

Figure 6.9: CVs on tungsten electrode, $[CeCl_3] = 20$ mM, $[AlCl_3]_0 = 20$ mM, $T = 723$ K.

Figure 6.10 shows the plot of i_p versus $\nu^{0.5}$. The aluminium plating peak current ($i_{p\,\alpha}$) followed previously observed behaviour (Figure 4.17) indicating diffusional control. The slopes from $i_{p\,A}$ and $i_{p\,Ce^{3+}}$ were also linear, indicating diffusion control at the peak potential, but the slopes were shallower since the diffusion coefficient of Ce^{3+} is less than that of Al^{3+}.

Figure 6.11 shows the E_p versus i_p plots to determine the apparent resistance for each peak in Figure 6.9. The relationship between E_p and i_p for the aluminium stripping peak (α') was not strictly linear, however a linear fit yielded an apparent resistance similar to previous measurements of pure aluminium stripping (Figure 4.18), which corresponded to the solution resistance, R_s. The apparent resistance of aluminium plating (R_α, impacted by nucleation kinetics) was significantly lower than previous measurements in a LKE-$AlCl_3$ system (Figure 4.18, $\Delta R \approx 3\ \Omega$). This highlights just how variable these electrochemical processes can be in molten salt systems, and hence why this analysis must be performed for each experiment rather than assuming previously obtained values are always valid. R_A matched the result from reduction of Ce^{3+} into a

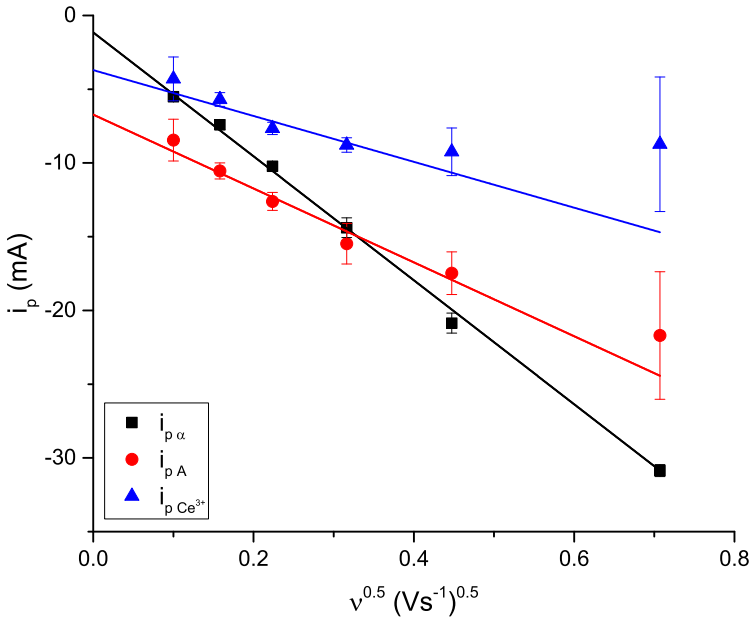

Figure 6.10: i_p versus $\nu^{0.5}$ for the reduction peaks in Figure 6.9. $i_{p\,Ce^{3+}}$ was calculated by subtracting $i_{lim\,\alpha}$ (at $E_{onset\,A}$) from $i_{p\,A}$.

bulk aluminium macroelectrode (Figure 4.8). Since the apparent resistances matched, this implied that even during a co-deposition experiment there was a significant amount of cerium insertion into aluminium, since aluminium was pre-deposited and so built up a layer that can be inserted into. Unlike the reduction of Ce^{3+} into a bulk aluminium macroelectrode, there was no linear correlation between E_p and i_p for the oxidation cerium-aluminium alloy from co-deposition, however there should still have been an apparent resistance due to R_s.

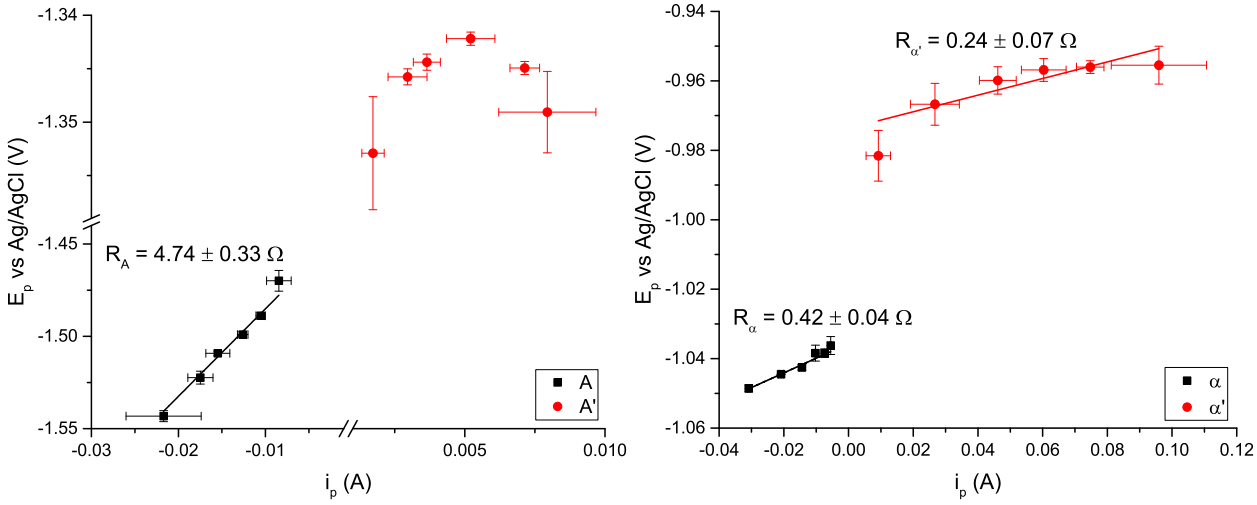

Figure 6.11: E_p versus i_p for peaks observed in Figure 6.9.

If cerium insertion was occurring, then there should be some relationship between the amount of aluminium

pre-deposited ($Q_{\alpha\, pre-deposit}$) and $E_{onset\, A}$ and/or $E_{p\, A}$. Figure 6.12 shows how the quantity of aluminium plated up to the cerium reduction onset potential ($E_{onset\, A}$) varied with the inverse of the square root of scan rate. This linear relationship intersected the origin, which was expected from the aluminium plating being controlled by Al^{3+} diffusion. At the slowest scan rate 10 mVs^{-1}, which is 10 $V^{-1}s$ on the $\nu^{-0.5}$ axis, there was the largest variation in charge which can be understood by the greatest influence of convection during the scan.

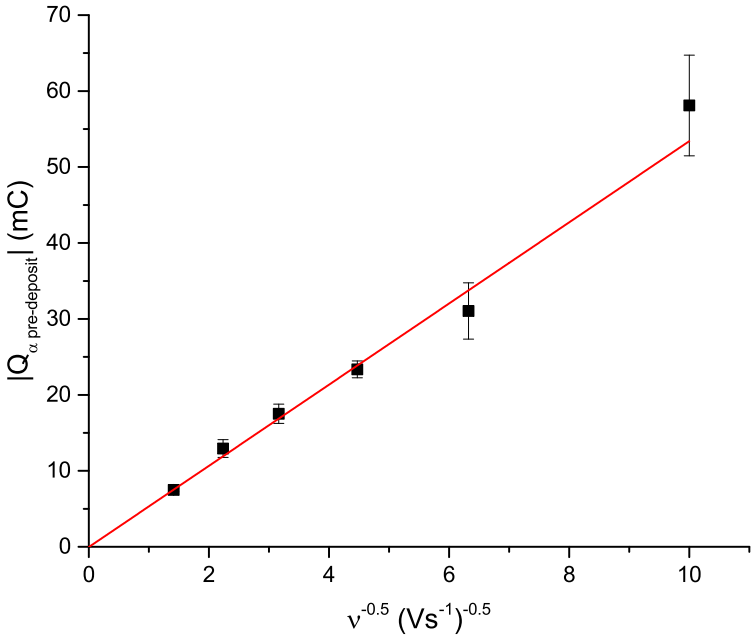

Figure 6.12: Charge passed during aluminium plating (pre-deposited) versus the reciprocal of the square root of scan rate from Figure 6.9.

Figure 6.13 shows how $E_{p\, A}$ changed as a function of the charge of aluminium plating from Figure 6.9. As $Q_{\alpha\, pre-deposit}$ increased (at slower scan rates) $E_{p\, A}$ shifted positively. This implied that the layer thickness (as dictated by the mass transport of Al^{3+}) does change the thermodynamics of the cerium insertion reaction, i.e. with more pre-deposited aluminium (at slower scan rates) there was a greater drive to form an alloy and hence $E_{p\, A}$ shifted positively, although the relationship is not linear.

Figure 6.14 shows the Ce:Al ratios calculated from analysis of the reduction and oxidation charges in the same manner as Section 6.2.3. $Ce{:}Al_{ox}$ and $Ce{:}Al_{total\text{-}deposit}$ were again very similar, since they are an average measure of the global composition. They were constant within experimental error, and were $<0.272727...$ which would have been expected value if the entire deposit was homogeneous Ce_3Al_{11}. These values were smaller than in the experiments in which $AlCl_3$ was added by electrochemical dissolution (Figure 6.7), which were $>0.272727...$ even at the earliest measurement time, and continued to increase as time (and the $[CeCl_3]{:}[AlCl_3]$ ratio) increased. Since $AlCl_3$ was added in powder form in this experiment, the

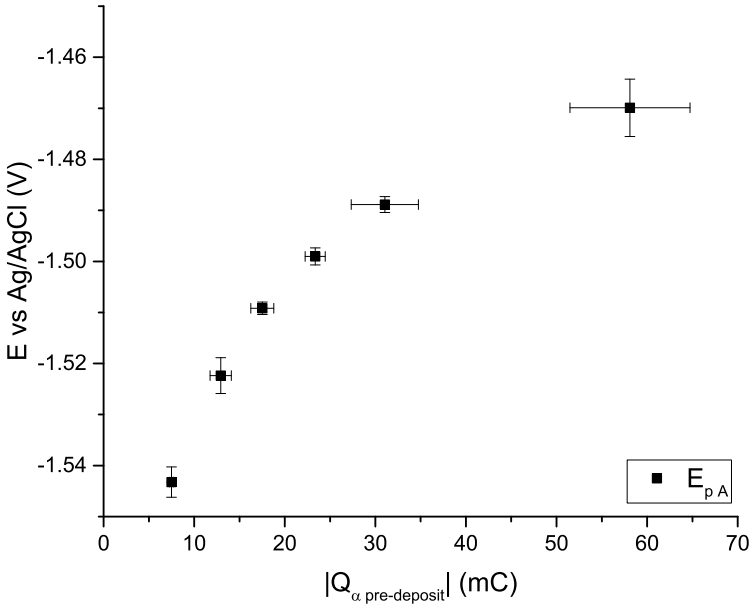

Figure 6.13: $E_{p\,A}$ as a function of the charge passed during aluminium plating ($Q_{\alpha\,pre-deposit}$) from Figure 6.9.

[$CeCl_3$]:[$AlCl_3$] ratio was likely greater, and since the diffusion coefficient of Al^{3+} is greater than Ce^{3+}, the m value (the molar ratio of co-deposition) would be <0.5 (the m value at $E_{p\,A}$ two minutes after electrochemical dissolution in Figure 6.5). Unfortunately the linear background of these CVs decreased in slope with scan rate, which prevented background correction and in turn prevented convolution from being performed, thus m values could not be determined for this system for comparison. An m value at least <1 would agree with the observation of a large bulk aluminium stripping peak (α') but no alloyed aluminium stripping peak (α"); more aluminium was being deposited than cerium, and so there was not very much alloying occurring, which makes $Ce{:}Al_{\text{co-deposit}}$ a more valid description of the alloy in these circumstances. $Ce{:}Al_{\text{co-deposit}}$ increased at slower scan rates and was always $>0.272727...$, and >0.5 at the slowest scan rates. This was similarly seen for the experiment where the [$CeCl_3$]:[$AlCl_3$] ratio was increasing due to the "short circuit" reaction (Figure 6.3). Again this suggested that amorphous cerium-aluminium alloy was able to form electrochemically by deposition of Al^{3+} and Ce^{3+} both under their respective mass transport control.

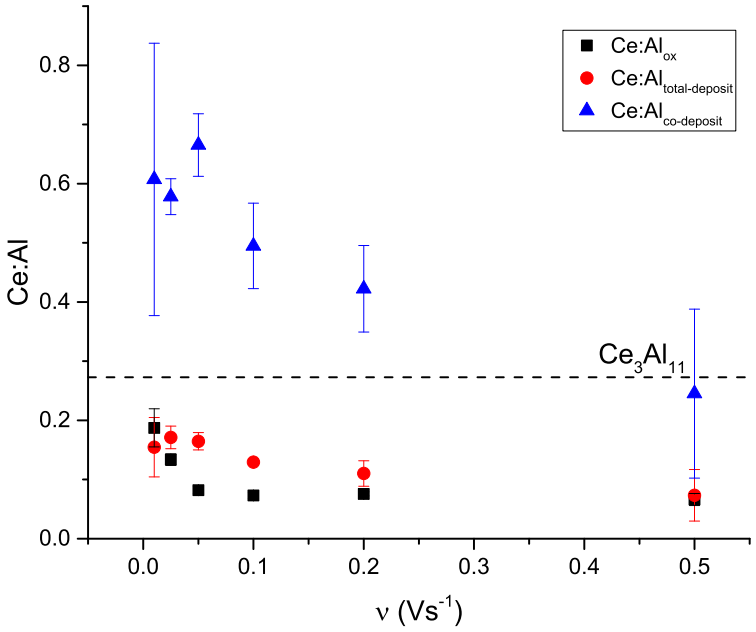

Figure 6.14: Ce:Al ratios calculated from the reduction and/or oxidation charges from CVs in Figure 6.9.

6.3.2 Partial Cyclic Voltammetry

Partial cyclic voltammograms (PCVs) have a start potential during a reaction, rather than at a point of no Faradaic current, and have an end potential when no Faradaic current is flowing. Thus there is a non-integer (partial) number of cycles. This was done so that the pre-deposited aluminium layer was minimised, to enable comparison of alloying by co-deposition without insertion at different scan rates. Thus the currents for reaction A should be mainly/purely the co-deposition regime rather than also including insertion of cerium into pre-deposited aluminium. Initial currents in PCV are due to setting up the aluminium diffusion field, giving a Cottrell type current-time transient. While this type of CV has been performed in the literature, they are usually still referred to as CVs and there is no alternative name used. PCV is being used as an alternative name here, to aid discussions of the differences in responses between CVs and PCVs.

Figure 6.15 shows PCVs over the same potential window as the CVs. As a result of starting the CV closer to $E_{onset\,A}$, $E_{p\,A}$ changed with scan rate far less, indicating that the apparent resistance due to phase change kinetics was far less with a thinner aluminium layer. This makes sense if considering two possible regimes for the cerium reduction: 1) reduction of Ce^{3+} into existing aluminium on the surface. This is like the case of Ce^{3+} reduction into a bulk aluminium macroelectrode. 2) co-reduction and Ce^{3+} and Al^{3+} together. These two regimes may have different kinetic factors involved in the formation of an amorphous cerium-aluminium alloy or Ce_xAl_y crystalline phase. Indeed, depending on the rate at which Ce^{3+} can be inserted

into aluminium, different thicknesses of aluminium may change the energy (and so potential) required to initiate Ce^{3+} reduction.

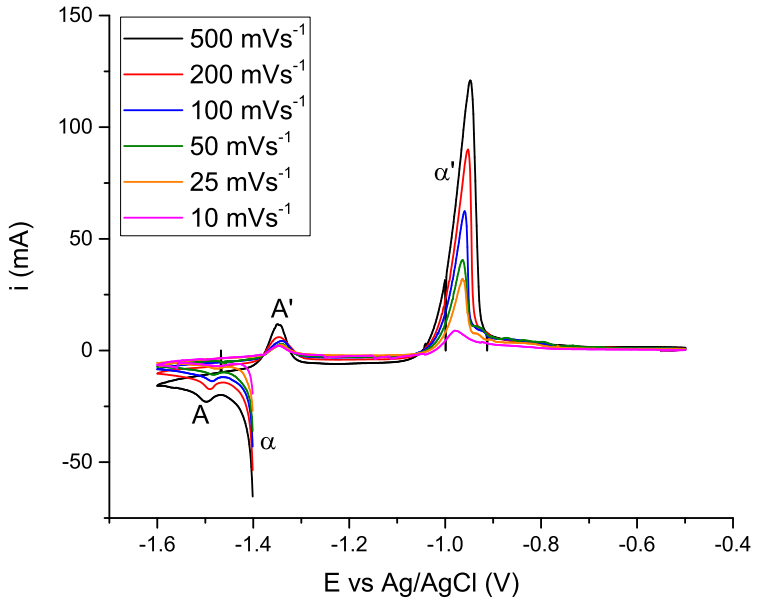

Figure 6.15: PCVs on tungsten electrode, $[CeCl_3] = 20$ mM, $[AlCl_3]_0 = 20$ mM, $T = 723$ K.

Figure 6.16 shows the plot of i_p versus $\nu^{0.5}$. Both $i_{p\,A}$ and $i_{p\,Ce^{3+}}$ had linear correlations, indicating diffusion control of the reaction at the peak potential. $i_{p\,Ce^{3+}}$ showed a much shallower gradient for the PCVs (-0.0039±0.0001) than for the CVs (-0.0156±0.0038), however for the peak to be limited by diffusion of Ce^{3+}, the gradients should be the same. This disparity is likely caused by the method of determining the current due to aluminium reduction, taken as the minimum $|i|$ just before $E_{onset\,A}$. In the CVs the aluminium diffusion field was well established before cerium reduction occurs, and so the aluminium reduction current at $E_{onset\,A}$ can be considered equal to the aluminium reduction current at $E_{p\,A}$. In the PCVs the aluminium diffusion field was less well established before cerium reduction occurs, and so the aluminium reduction current was still decreasing rapidly at $E_{p\,A}$, thus $i_{p\,Ce^{3+}}$, and its slope versus $\nu^{0.5}$, were undervalued for the PCVs.

Figure 6.17 shows the E_p versus i_p plots to determine the apparent resistances from the PCVs (Figure 6.15). $R_{\alpha'}$ was roughly the same as for the CVs (Figure 6.11), however E_p and i_p correlated much more linearly. Again there was no correlation between E_p and i_p for peak A'. R_A dropped significantly by performing PCVs, $\Delta R \approx 3\ \Omega$, confirming that the kinetic barrier to alloying decreased by minimising the amount of alloying by insertion relative to co-deposition.

By using Equation 4.1 the A and A' peaks were fitted for both CVs and PCVs at each scan rate. The resulting n values (which controls the peak width) are shown in Figure 6.18 and were all greater than the expected value of 3. The greatest difference between n values occurred at 200 and 100 mVs^{-1}; n_A values from the

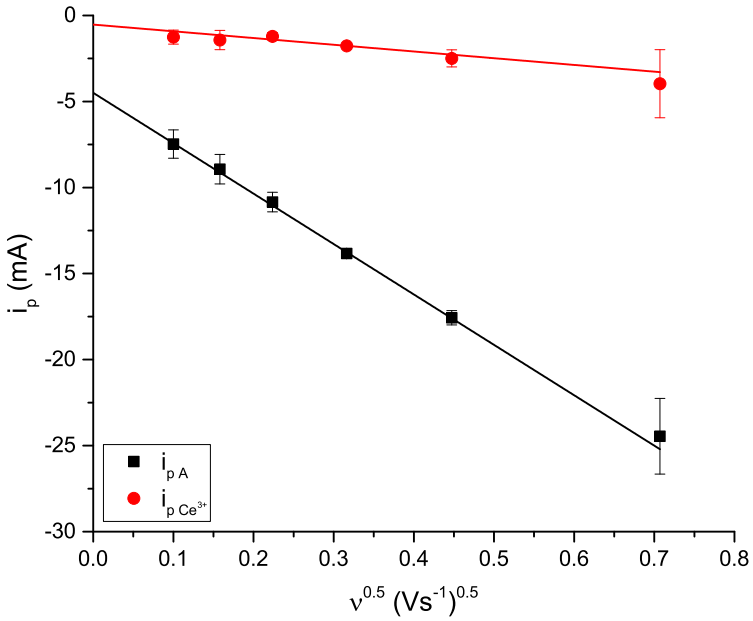

Figure 6.16: i_p versus $\nu^{0.5}$ for the alloying reaction in Figure 6.15. $i_{p\,Ce^{3+}}$ was calculated by subtracting $i_{lim\,\alpha}$ (at $E_{onset\,A}$) from $i_{p\,A}$.

PCVs were the highest, indicating the greatest phase homogeneity occurred by co-deposition with minimal insertion. $n_{A'}$ values from the PCVs were the lowest, which can be explained by the high phase homogeneity during reduction (n_A) resulting in mechanically unstable alloy, which detached during the PCV, thus there was less alloy, and a lower homogeneity of alloy, remaining on the back scan. $n_{A'}$ and n_A values from the CVs were much more similar to each other, and were between the values from the PCVs. This suggested that when co-deposition and insertion occur (in CVs), the overall phase structure, and therefore mechanical stability, of the alloy does not change significantly over the course of the CV.

Figure 6.19 shows the Ce:Al ratios calculated in the same manner as performed previously (Section 6.2.3). Due to $i_{lim\,\alpha}$ being overestimated during co-deposition potentials (as described earlier in this section), $Ce{:}Al_{co\text{-}deposit}$ and $Ce{:}Al_{total\text{-}deposit}$ had negative values at all scan rates other than at 25 mVs^{-1}, for which their values were lower than $Ce{:}Al_{ox}$, although all these values at 25 mVs^{-1} had a large error. By minimising the amount of pre-deposited aluminium, $Ce{:}Al_{ox}$ is a more valid description of the alloy and should be equivalent to $Ce{:}Al_{co\text{-}deposit}$ and $Ce{:}Al_{total\text{-}deposit}$ if $i_{lim\,\alpha}$ could be accurately determined. These $Ce{:}Al_{ox}$ values were approximately the same as the $Ce{:}Al_{ox}$ values from the equivalent CVs, but were significantly less than the $Ce{:}Al_{co\text{-}deposit}$ values from the equivalent CVs. Since these CVs and PCVs were performed in the same salt (with minimal time between each voltammetry) the m value should have been the same for each. Since the average $Ce{:}Al_{co\text{-}deposit}$ and $Ce{:}Al_{total\text{-}deposit}$ values at 25 mVs^{-1} agree with the $Ce{:}Al_{ox}$ values at higher scan rates, this implied an m value of approximately 0.1. The $Ce{:}Al_{co\text{-}deposit}$ values from the CVs implied an

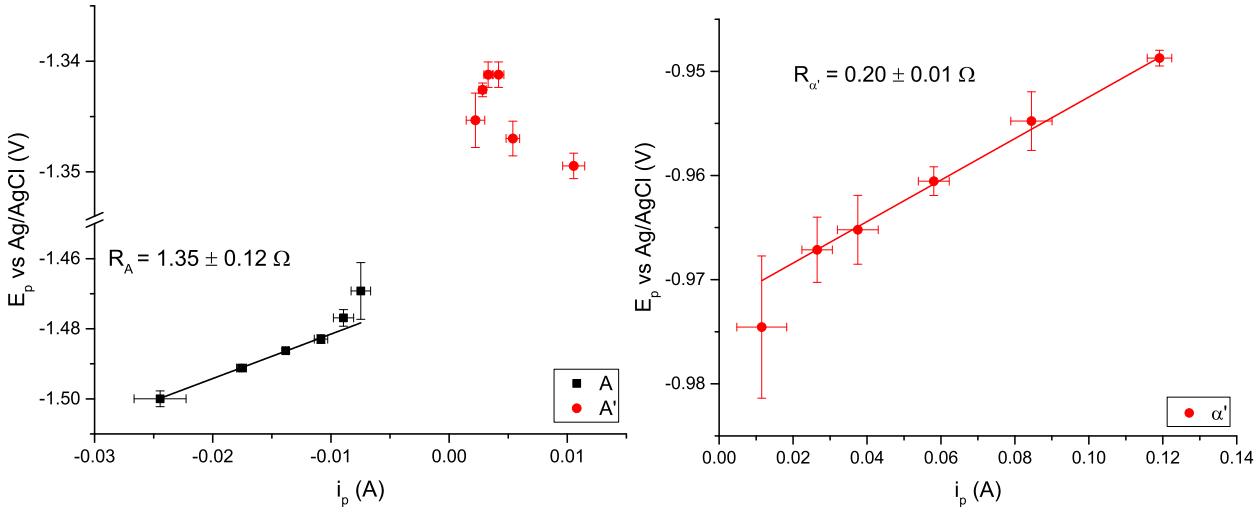

Figure 6.17: E_p versus i_p for peaks observed in Figure 6.15.

m value of approximately 0.5. This difference may have been caused by the mechanical stability of alloy produced from purely co-deposition being lower than that of an alloy produced from insertion, causing more of the alloy to be lost (due to the convective flow of molten salt) during PCVs. This agrees with the higher $n_{A'}$ values from PCVs (Figure 6.18) indicating that the crystal grains are larger from pure co-deposition, which made these deposits less mechanically stable (more brittle). It seemed to be that a pre-deposited aluminium layer resulted in smaller, more numerous crystal grains (possibly by there being a volume for cerium to insert into), which were more mechanically stable (less brittle). Again there is no direct evidence that any crystal phase was formed, but more likely an amorphous cerium-aluminium alloy which could have varying Ce:Al ratios depending on the experimental conditions.

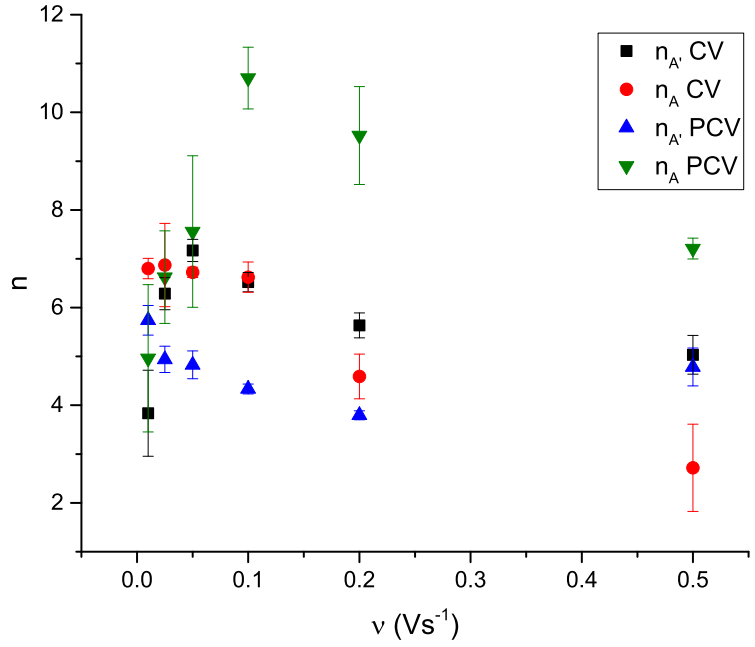

Figure 6.18: n values (peak widths) obtained by fitting peaks A and A' from Figures 6.9 and 6.15 with Equation 4.1.

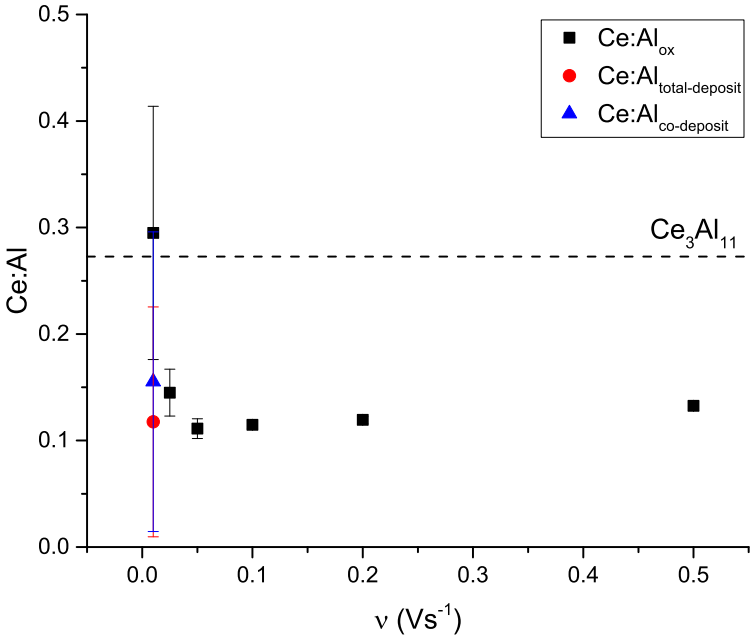

Figure 6.19: Ce:Al values calculated from the reductive and/or oxidative charges from PCVs in Figure 6.15.

6.3.3 Wider Potential Window PCVs

Figure 6.20 shows PCVs performed to a variety of lower vertex potentials, all starting 0.3 V positive of the lower vertex potential. The reduction peak B was observed in these PCVs only when the starting potential was close to $E_{p\,B}$. As with the CVs over a similar potential window (Figure 6.1), this reduction peak was only observed with a [$CeCl_3$]:[$AlCl_3$] ratio close to 1:1. When PCVs were scanned to more negative potentials (<-2.1 V), a peak corresponding to lithium alloying was observed (γ/γ'). There appeared to be another lithium reaction negative of γ/γ', which may be the formation of another lithium-aluminium alloy. The observation of the γ/γ' reaction implied that cerium was below its solubility limit in aluminium. Since no pure cerium plating was observed, the surface was not very cerium rich, and so lithium alloying appeared to be more favourable. It will be seen that in a 4:1 [$CeCl_3$]:[$AlCl_3$] ratio salt (Figure 6.24) the cerium plating/stripping reaction (δ/δ') is observed instead of the lithium-aluminium alloying reaction (γ/γ').

The aluminium stripping peak area, $Q_{\alpha''+\alpha'}$, diminished as the PCVs were started at more negative potentials. This was unexpected as the total potential scanned (time spent scanning) prior to the aluminium stripping onset potential increased, thus the reductive charge passed due to aluminium (which is diffusion limited) would have increased. Interestingly, once lithium alloying was observed, the total aluminium oxidation peak area became much larger. This can be explained by the cerium-aluminium alloy being mechanically unstable, thus causing more loss of aluminium on wider potential windows. If the lithium-aluminium alloy was more mechanically stable, and lithium-aluminium alloying became more dominant at more negative starting potentials, then more aluminium would have remained on wider potential windows.

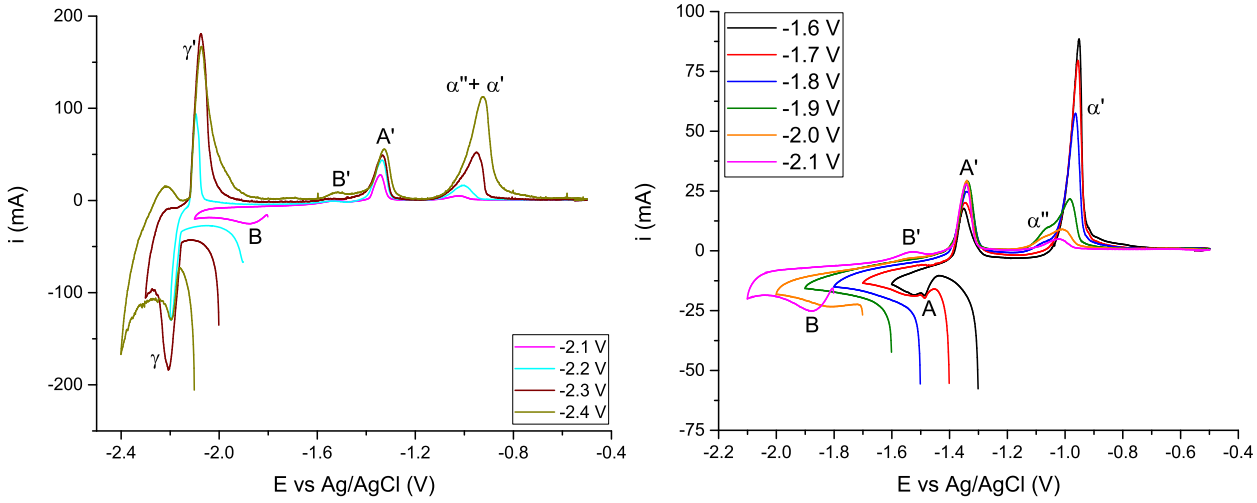

Figure 6.20: PCVs on tungsten electrode over a number of potential windows. Constant 0.3 V separation between start and lower vertex potentials. [$CeCl_3$] = 20 mM, [$AlCl_3$]$_0$ = 20 mM, ν = 200 mVs^{-1}, T = 723 K. Legend gives the lower vertex potential of the PCVs.

Figure 6.21 shows PCVs run to varying lower vertex potentials, but always starting at -1.4 V (just positive of $E_{onset\,A}$). The same reactions were observed in these PCVs as in the PCVs run previously. Only two cerium-aluminium alloy phases were observed at this [$CeCl_3$]:[$AlCl_3$] ratio of approximately 1:1. The B' peak was observed on all PCVs scanned more negative than $E_{p\,B}$. The aluminium stripping peak α' remained very sharp across all potential windows. $i_{p\,\alpha'}$ and $Q_{\alpha'}$ decreased slightly over the first few potential windows, but when lithium alloying was observed (γ/γ', <-2.1 V) $i_{p\,\alpha'}$ and $Q_{\alpha'}$ increased significantly. This was also the case in the previous PCVs with 0.3 V between the start and lower vertex potentials.

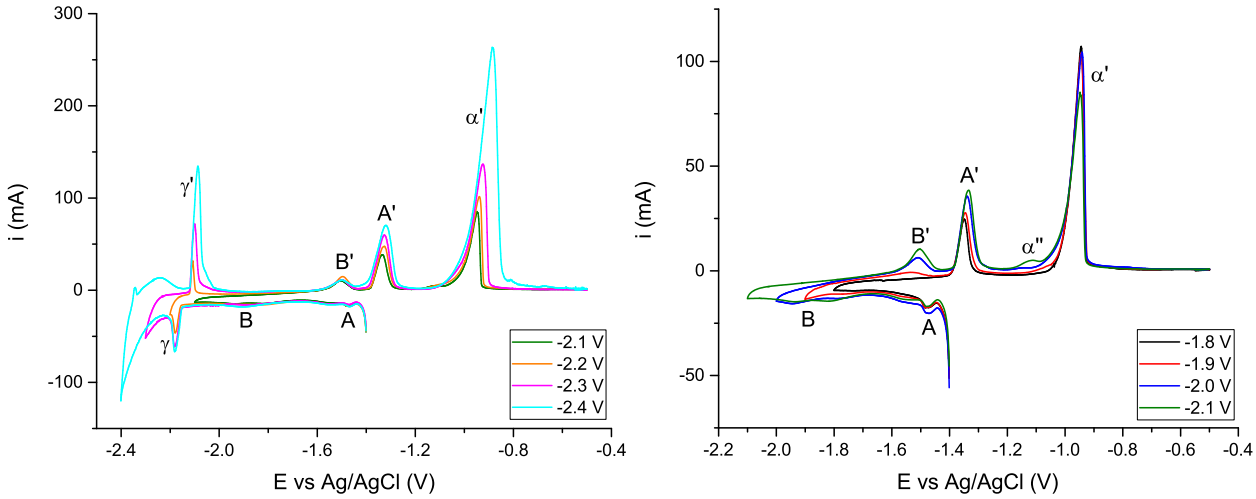

Figure 6.21: PCVs on tungsten electrode over a number of potential windows. Constant start potential at -1.4 V. [$CeCl_3$] = 20 mM, [$AlCl_3$]$_0$ = 20 mM, ν = 200 mVs^{-1}, T = 723 K. Legend gives the lower vertex potential of the PCVs.

Figure 6.22 shows the Ce:Al$_{ox}$ values of the alloy produced by PCVs, using either a constant separation between the start and lower vertex potentials, or a constant start potential. Ce:Al$_{ox}$ was calculated as $\frac{Q_{A'}}{Q_{\alpha''+\alpha'}}$ for peak A' and $\frac{Q_{B'}+Q_{A'}}{Q_{\alpha''+\alpha'}}$ for peak B'. In both types of PCV, the Ce:Al$_{ox}$ values increased for wider potential windows. At potentials more negative than the lithium-aluminium alloying reaction, the Ce:Al$_{ox}$ values decreased for wider potential windows. This implied that lithium preferentially alloyed with incoming aluminium, which makes sense as lithium ions from the solvent have an effectively infinite flux and lower n value (so more can be reduced for the same charge). Thus the total aluminium peak area, cannot be attributed only to cerium-aluminium alloying at those potential windows, and those Ce:Al$_{ox}$ values must therefore be undervalued at these widest potential windows.

The Δ0.3 V PCVs show far greater Ce:Al$_{ox}$ values than the PCVs always started at -1.4 V. This is because the Δ0.3 V PCVs often started at potentials where co-deposition of cerium and aluminium is occurring, whereas in the -1.4 V PCVs there is always a pre-deposited layer of aluminium before cerium reduction occurs. This

implied that cerium insertion into pre-deposited aluminium was slow, therefore $Ce{:}Al_{ox}$ (which is a global average) was different to the local Ce:Al in the co-deposited alloy layer.

In the literature, CVs have been performed at this $[CeCl_3]$:$[AlCl_3]$ ratio of approximately 1:1,[35,37] although the absolute concentrations are approximately ten times the concentrations used in this work. In the literature additional peaks C/C' were observed, but pure cerium plating/stripping (δ/δ') was observed instead of (and at the same potentials of) lithium-aluminium alloying (γ/γ'). This is the only $[CeCl_3]$:$[AlCl_3]$ ratio studied in literature, however it is clear from Section 5.3.1 that this ratio affects the observed electrochemistry. Studies of an approximately 4:1 ratio in Section 6.4 will shed light on how the co-deposition electrochemistry over a wide potential window is affected by an increasing concentration (and therefore flux) ratio.

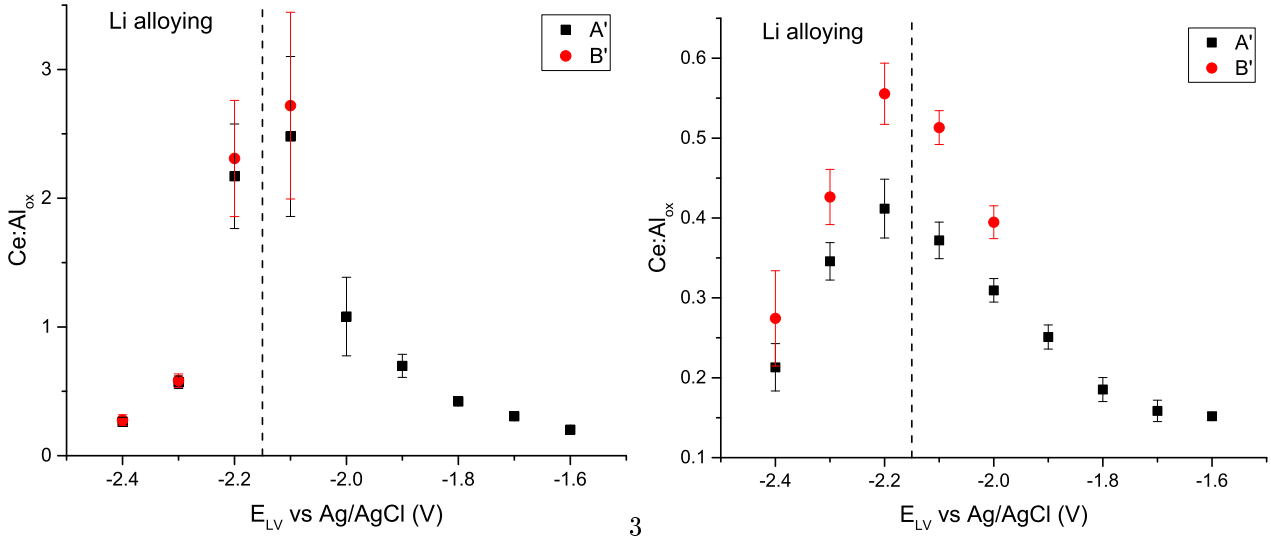

Figure 6.22: $Ce{:}Al_{ox}$ ratios as a function of the lower vertex potential of PCVs (Left) PCVs with 0.3 V between start and lower vertex potential, Figure 6.20. (Right) PCVs with a constant start potential of -1.4 V, Figure 6.21.

Figure 6.23 shows n values from fitting cerium oxidation peaks from both sets of PCVs with Equation 4.1. The n values for the Δ0.3 V PCVs, in the potential windows where only cerium and aluminium were reduced, decreased initially before increasing. This can be thought of as measuring the ratio of cerium insertion into aluminum versus co-deposition. If only one of these alloying mechanisms is occurring then the homogeneity of the alloy is high, leading to very similar surface energies and hence a sharp peak with a high n value. In these PCVs there are 0.3 V of reduction which must be "shared" between the two mechanisms. When the lower vertex potential was -1.8 V, and the start potential was -1.5 V (approximately $E_{p\,A}$), the lowest n value was obtained. This was because this PCV "shared" the 0.3 V relatively equally between both mechanisms as some aluminium is pre-deposited and so cerium insertion and co-deposition are occurring. For PCVs started more positively, more of the 0.3 V was spent pre-depositing aluminium and so cerium insertion is the

dominant mechanism. For PCVs started more negative, very little (if any) aluminium was pre-deposited and so co-deposition was the dominant mechanism.

The n values for the PCVs which always started at -1.4 V showed a trend of decreasing with the lower vertex potential. In these PCVs there was always pre-deposited aluminium, thus at less negative potentials the cerium insertion contributed significantly to the alloy formation. As the lower vertex potential became more negative, the ratio of co-deposition versus insertion increased. Thus there were regions of alloy with distorted aluminium lattice (from cerium insertion) which had different energies than regions of alloy made by co-depositing cerium and aluminium together. Since the n values continued to decrease, and did not increase even at quite negative potentials where co-deposition had been occurring for a long time, this implied that the pre-deposited layer of aluminium was never completely converted to cerium-aluminium alloy since this is a slow reaction with a large kinetic barrier.

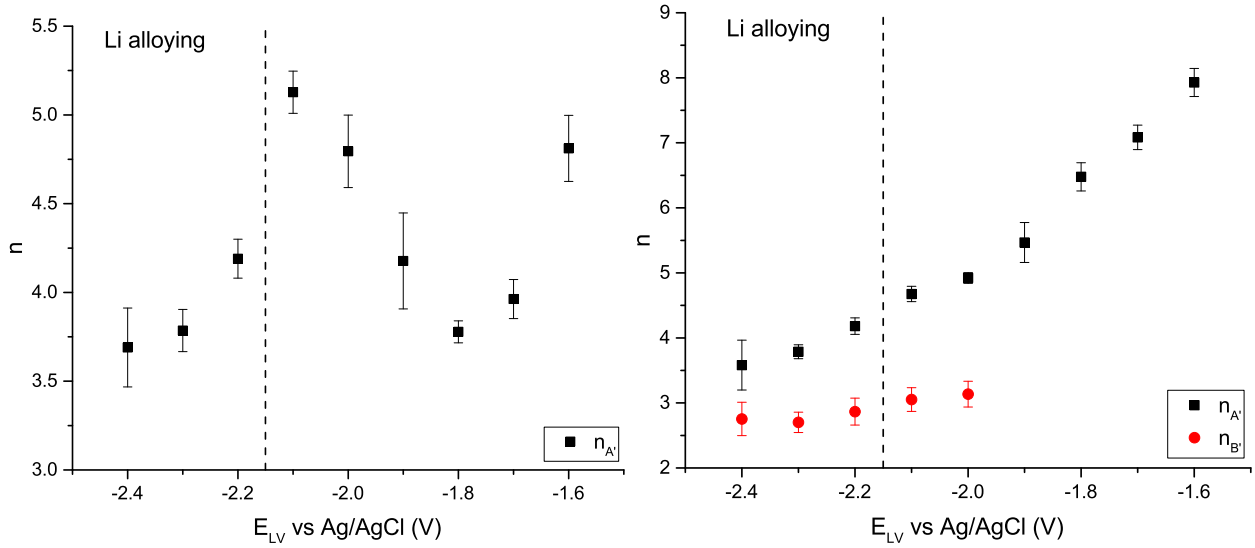

Figure 6.23: n values (peak width) from fitting peaks A' and B' with Equation 4.1, as a function of the lower vertex potential of PCVs (Left) 0.3 V between start and lower vertex potential. (Right) Constant start potential of -1.4 V. Figures 6.20 and 6.21 respectively.

6.4 Fixed $[CeCl_3]$:$[AlCl_3] \geqslant$ 4:1

6.4.1 CV and PCV

Figure 6.24 shows typical PCVs for a salt with a 4:1 molar ratio of $[CeCl_3]$:$[AlCl_3]$. In this potential window cerium plating/stripping (δ/δ') was observed, but no lithium alloying (γ/γ') was observed. (It should be noted that these two reactions occur at very similar potentials). This is the opposite of what was observed

in similar PCVs with a 1:1 molar ratio salt (Figure 6.21). In the ternary phase diagram of Li-Ce-Al there are no miscible ternary alloys, only immiscible lithium-aluminium and cerium-aluminium alloys at 550 °C.[107] Thus with a greater $[CeCl_3]$:$[AlCl_3]$ ratio, the Ce:Al in the alloy from the 4:1 is greater than from the 1:1 salt, which prevents reduction of Li^+ as there is little "free" aluminium to alloy with lithium. Since pure cerium plating was observed, the cerium alloying reactions cannot have been diffusion limited by Ce^{3+}, otherwise reaching the cerium plating potential would not have resulted in extra current being passed. This makes sense as the $CeCl_3$ concentration was 80 mM in the 4:1 salt, but only 20 mM in the 1:1 salt. Therefore the diffusion of Al^{3+} must have been limiting the alloying reactions at this higher concentration ratio.

In the 4:1 salt, the PCVs starting at -1.3 V (with aluminium pre-deposition) had three observable oxidation peaks (A', B' and C') between the pure aluminium (α') and pure cerium (δ') stripping peaks. This was one more than was observed in similar PCVs in the 1:1 salt. When the start potential was more negative (-1.5 V and below, co-deposition mechanism dominated) a fourth oxidation peak, D', was also observed. As the start potential became more negative, a fifth alloy oxidation peak, E', was resolved from the main cerium stripping peak δ'. As the start potential became more negative, $i_{p\,\delta'}$ increased while i_p of every other peak decreased. Thus at more negative starting potentials, less time was spent co-depositing, so the total quantity of cerium-aluminium alloy was less, which caused smaller oxidation peaks. More of the cerium that was reduced was then in the form of pure cerium, hence $i_{p\,\delta'}$ increased.

Interestingly, reduction peak C was observed when the starting potential was -1.3 or -1.5 V, whereas peak B was only observed when the starting potential was more negative than peak A (starting potential at -1.5 V). As the starting potential was made more negative, peak C was no longer observed, despite the starting potential being more positive than $E_{p\,C}$. This implied that the appearance of a reduction peak is related to the local Ce:Al in the alloy, and whether formation of a different phase is kinetically limited. For example if the local Ce:Al was <0.5 (by starting at less negative potentials), then co-deposition could be forming crystalline Ce_3Al_{11} and $CeAl_3$, and amorphous cerium-aluminium alloy. At $E_{p\,C}$ the potential would have induced a phase change and some of the existing phases would be electrochemically converted to $CeAl_2$ which has a kinetic component, thus affecting the current that can be passed. If however, the local Ce:Al was >0.5 (by starting at more negative potentials) then Ce_3Al_{11}, $CeAl_3$ and $CeAl_2$ could form via crystallising from an amorphous cerium-aluminium alloy. If $CeAl_2$ was present before $E_{p\,C}$ was reached, passing this potential does not change the rate at which $CeAl_2$ was formed and so no reduction peak was observed. By plating cerium, the conversion of an amorphous cerium-aluminium alloy to specific crystalline intermetallic Ce_xAl_y phases may have been promoted. With no amorphous cerium-aluminium alloy, conversion between crystal phases on the back scan must occur by cerium, hence observing oxidation peaks. If however, an amorphous

cerium-aluminium phase remained, then conversion between crystalline phases could occur by the "excess" cerium returning to the amorphous phase which would not result in oxidation. Thus the observation of multiple alloying peaks implies the formation of crystalline Ce_xAl_y intermetallic compounds (but does not rule out the presence of amorphous material), whereas the lack of these peaks in the 1:1 concentration PCVs (Figures 6.21 and 6.20) seems to imply only amorphous deposition of cerium-aluminium alloy. This lack of peaks after A/A' will also be observed for co-deposition on a microelectrode with a high Ce:Al ratio in the alloy (Section 7.2).

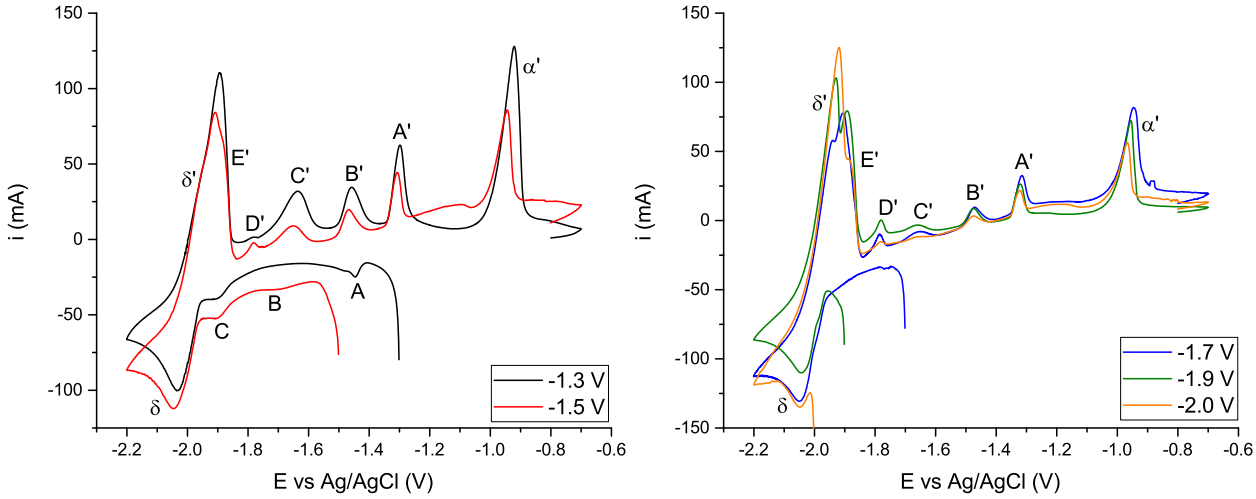

Figure 6.24: PCVs on tungsten electrode over a fixed potential window, but varying the start potential between -1.3 and -2.1 V in 0.1 V increments (for clarity, not all are shown). $[CeCl_3]$ = 80 mM, $[AlCl_3]_0$ = 20 mM, ν = 200 mVs^{-1}, T = 723 K. The legends show the start potential of each PCV. (Left) D' grew in only when the PCV started sufficiently negative. (Right) E' becomes resolvable from δ'.

Figure 6.25 shows the $Ce:Al_{ox}$ ratios calculated from the oxidation peak areas in the PCVs. $Ce:Al_{ox}$ at each start potential was scan rate independent within experimental error, and so an average was taken across all scan rates (200, 100, 50 and 25 mVs^{-1}). As before, integration of the peaks was performed relative to a baseline between the start and end potentials of the peak. For the pure aluminium stripping peak, α', the end potential was taken as the point where the current after the peak was a linear change with potential (at approximately -0.85 V). For the pure cerium stripping peak, δ', the start potential was taken as the point where the current before the peak was a linear change with potential (at approximately -2.05 V). For peak A', $Ce:Al_{ox}$ was the same at all starting potentials within experimental error, with an average value of 0.27 ± 0.05. This was within experimental error of the value for the first intermetallic Ce_3Al_{11}. For the other alloy peaks, $Ce:Al_{ox}$ was calculated by summing the alloy oxidation peak areas, e.g. for peak C':

$$Ce:Al_{ox} = \frac{Q_{C'} + Q_{B'} + Q_{A'}}{Q_{\alpha'}} \tag{6.6}$$

The alloy oxidation peaks are summed together, since if the alloy were all $CeAl_2$ (for peak C'), then this oxidation reaction only oxidises enough cerium to convert $CeAl_2$ to $CeAl_3$. Thus the total quantity of cerium oxidised from peaks C', B' and A' should equate to the total amount of the cerium in the alloy at potentials negative of peak C'. In the literature this was performed for peaks A', B' and C' from CVs over very similar potential windows.[37] It was found in the literature that the $Ce:Al_{ox}$ values increased for wider potentials windows, and were generally greater than expected for the number of observable phases, i.e. $Ce:Al_{ox}$ for peak C' was approximately 1, which would allow for the formation of four crystalline intermetallics, despite only three oxidation peaks being observed. This lead to the following attributions: peak A' as $CeAl_3$, peak B' as $CeAl_2$ and peak C' as CeAl. In this work, since five oxidation peaks were observed between pure cerium and pure aluminium, the following attributions were made which accounted for all crystalline phases predicted in the phase diagram (Figure 2.11): peak A' as Ce_3Al_{11}, peak B' as $CeAl_3$, peak C' as $CeAl_2$, peak D' as CeAl, and peak E' as Ce_3Al.

The $Ce:Al_{ox}$ values for peaks A', B', C' and D' showed a general trend of decreasing as the start potential of the PCVs was made more negative. At the more negative starting potentials, the $Ce:Al_{ox}$ values were within experimental error of the values for the Ce_xAl_y intermetallics that have been attributed to these peaks: both in this work, and in the literature by a combination of electrochemistry and ex-situ XRD.[35, 36] This matching of $Ce:Al_{ox}$ to Ce_xAl_y phases was true except for peak D', which had a very small area and did not significantly change the $Ce:Al_{ox}$ values relative to peak C'. As a result the $Ce:Al_{ox}$ value for peak D' was only within experimental error for CeAl at the least negative starting potentials.

For peak E' $Ce:Al_{ox}$ was 1.25 ± 0.28, which was not within experimental error of 3, the expected value for Ce_3Al. This was due to peaks E' and δ' overlapping, thus the baseline used for integration significantly undervalued the areas of each individual peak, $Q_{\delta'}$ and $Q_{E'}$. The start and end points of the baseline used for integrating peak E' were the minima between $i_{p\,\delta'}$ and $i_{p\,E'}$, and $i_{p\,E'}$ and $i_{p\,D'}$. In the bottom right graph of Figure 6.25, $Q_{\delta'+E'}$ was obtained by integrating the combined δ' and E' peaks between approximately -2.05 and approximately -1.85 V to obtain the total charge of cerium. At starting potentials of -1.3 and -1.4 V (where the E' peak dominates since $i_{p\,E'}$ decreased and $i_{p\,\delta'}$ increased when PCVs started at more negative potentials), $Ce:Al_{ox}$ from the charge of all cerium peaks was 3 within experimental error, confirming that peak E' is indeed Ce_3Al. Ideally the cerium charge due to alloy versus pure metal would be obtained by applying peak functions to the overlapping peaks, to allow more accurate $Ce:Al_{ox}$ values to be obtained at all starting potentials. However, this was not performed due to time constraints, as well as not having a peak function to describe pure metal stripping (which is asymmetrical).

This charge analysis has shown that by increasing the $[CeCl_3]$:$[AlCl_3]$ ratio, the Ce:Al ratio in the amorphous

alloy was increased. By increasing the Ce:Al ratio significantly, (and plating cerium metal), the formation of crystalline Ce_xAl_y phases was promoted. Otherwise amorphous alloy is produced electrochemically, which has an increasing Ce:Al ratio due to the flux of Ce^{3+} being greater than the flux of Al^{3+}.

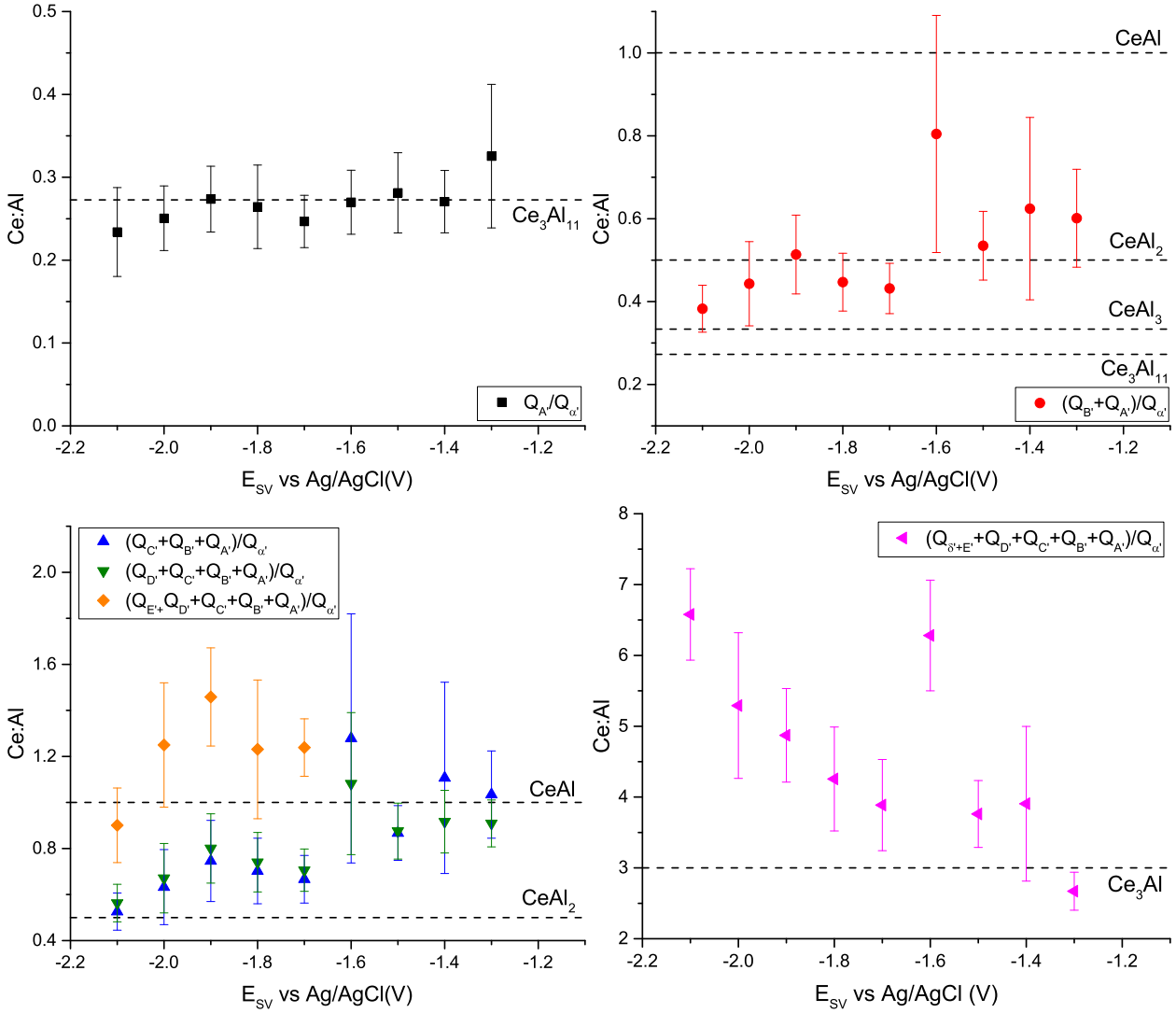

Figure 6.25: $Ce:Al_{ox}$ calculated from oxidation peak areas in Figure 6.24. Legend displays which oxidation peaks were summed: the first peak referred to in the equation is the peak for which the calculation is being performed. (Top Left) Peak A'. (Top Right) Peak B'. (Bottom Left) Peaks C', D' and E'. (Bottom Right) Combined peaks δ' and E'.

6.5 Conclusions

Co-deposition of $CeCl_3$ and $AlCl_3$ has resulted in the ability to observe multiple peaks due to electrochemical formation of cerium-aluminium phases. This was in contrast to cerium reduction into a bulk aluminium macroelectrode where only one alloy phase is observed electrochemically. During co-deposition CVs, a layer

of aluminium was pre-deposited before both species were co-deposited. There was some evidence that this pre-deposited layer mixes with the co-deposited layer, such that the overall reaction was limited by similar phase change kinetics as for cerium insertion into a bulk aluminium macroelectrode (similar apparent resistances of the first alloying peak). By performing CVs which start closer to the onset potential of alloying (PCVs) the quantity of pre-deposited aluminium was decreased or eliminated entirely. This results in alloying which occurred via co-deposition only.

At a low flux ratio (1:1 salt) only one extra alloy peak was observed. At more negative potentials, lithium alloying was observed rather than pure cerium plating, which can be used to determine if the reaction was controlled by Ce^{3+} or Al^{3+}. If Ce^{3+} controlled, there was extra aluminium which was free to alloy with lithium. If Al^{3+} controlled, not all Ce^{3+} at the electrode was reduced and so at the pure cerium plating potential more cerium can be reduced, which allowed extra current to be passed and the cerium plating/stripping reaction was observed.

At a higher flux ratio (4:1 salt) a maximum of five alloy peaks were observed. From analysis of the oxidation charges, these peaks corresponded to the crystalline Ce_xAl_y intermetallics predicted by the cerium-aluminium phase diagram. This has confirmed findings in the literature, which used ex-situ XRD to match the potentials to crystal phases. This in-situ method of charge analysis is beneficial for confirmation, as the ex-situ methods may have allowed nucleation and growth of crystal phases by cooling the samples slowly before analysis was performed (hours between alloy formation, thus ex-situ analysis may have shown different phases than those formed initially by using electrochemistry over seconds).

With macroelectrodes, the obtained alloying electrochemistry, and Ce:Al values, increased smoothly with time/potential rather than only depositing at fixed ratios according to the expected crystal phases. This implied that there is a metastable amorphous cerium-aluminium alloy which can form electrochemically, but is not predicted thermodynamically from the phase diagram. It should be noted that the co-deposition ratio was not the same as the expected flux ratio, which implied that there was still some kinetic barrier to alloy formation even for pure co-deposition.

By having a high flux ratio (as in the 4:1 salt), cerium plating was observed which indicated that the alloying reactions were not diffusion controlled by Ce^{3+}, i.e. the cerium reduction current during alloying was then that expected by its possible flux. By plating cerium, and increasing the Ce:Al ratio more rapidly, the formation of crystalline phases was promoted, which seemed to have also resulted in the loss of the amorphous phase.

The reaction A/A' does not appear to change in potential or shape for amorphous versus crystalline deposition, thus its presence alone cannot be taken as evidence for either phase in the deposit. It is necessary to

observe other peaks, either other cerium-aluminium alloy peaks and cerium plating, or lithium-aluminium alloy peaks, in order to determine whether the deposition is producing an amorphous or crystalline phase.

The next chapter will use microelectrodes, which have much greater efficiency of mass transport to better probe the rate determining step of the alloying reaction during co-deposition. It would be of benefit to use other analytical methods, such as in-situ x-ray or neutron diffraction that can determine the crystal phases that are formed electrochemically under these non-equilibrium conditions, as ex-situ methods may allow for the phases to change significantly before analysis can occur.

Chapter 7

Studies of Cerium-Aluminium Alloying on Microelectrodes

7.1 Introduction

In the previous chapter, a $[CeCl_3]$:$[AlCl_3]$ ratio of 4:1 was used for macroelectrode co-deposition, which enabled five oxidation peaks to be observed (A' through E') between those of pure aluminium stripping (α') and pure cerium stripping (δ'). These were attributed to each of the five Ce_xAl_y intermetallics predicted from the binary phase diagram. It was not possible to observe all the corresponding reduction peaks to the Ce_xAl_y intermetallics (could not observe all corresponding A to E peaks) over a single potential window. The peak height, shape, and peak potential for all peaks were highly dependent on kinetic deposition factors which were in turn affected by the starting potential of the PCVs. This makes determination of the phases formed from the Ce:Al ratios, and converting observed currents into concentrations of $CeCl_3$, quite challenging. Since concentration monitoring is the final goal of developing a sensor, co-deposition on macroelectrodes would not be suitable for on-line monitoring. This chapter will focus on the use of microelectrodes to investigate cerium-aluminium alloying by co-deposition, as well as alloying on fixed volume thin film aluminium microelectrodes.

It is hoped that co-deposition on microelectrodes will result in CVs that are easier to analyse and less sensitive to the CV parameters (start and end potentials), since mass transfer steady state currents are obtained much more rapidly, co-deposition should be constant, occurring at either the flux ratio, or at the solubility limit of cerium in aluminium. This should result in minimal kinetic influence to alloying during the CV, making it easier to analyse the thermodynamics of phase formation. This will help to inform how best to analyse data

to obtain the $CeCl_3$ concentration from the electrochemistry by understanding the relationship between the $CeCl_3$ concentration in the salt and the Ce:Al ratio in the alloy.

Chapter 4 covered the use of bulk aluminium macroelectrodes. While the i_p versus $\nu^{0.5}$ relationship did show that the alloying reaction was controlled by Ce^{3+} diffusion at the peak potential, the shape of the reduction peak after the peak potential indicated deviation from diffusion control. The current was greater than expected from diffusion control, which was attributed to the increasing roughness of the electrode surface as alloying occurs, since cerium atoms are quite large, the aluminium layer would undergo significant expansion upon alloying. This chapter will also look at microfabricated thin film aluminium microelectrodes with the aim of identifying whether, in this case, limiting currents of cerium-aluminium alloying show diffusion control during the entire CV and therefore how accurately the $CeCl_3$ concentration can be calculated.

In this chapter tungsten super thin track (STT), tungsten thin track (TT), and aluminium covered tungsten thin track (TT) microelectrodes have been used. STT and TT architectures are different in their yield and lifetimes, but have not been observed to produce different electrochemistry for voltammetry measurements.

7.2 $CeCl_3$ and $AlCl_3$ Co-deposition on Tungsten Microelectrodes

7.2.1 Aluminium Plating/Stripping on Tungsten Microelectrodes

The typical CV response of co-deposition on a tungsten microelectrode can be seen in Figure 7.1. Both the aluminium plating current (α) and the co-deposition current (A) were limiting, indicating both reactions were under diffusion control. The corresponding oxidation reactions A' and α' were also observed.

Figure 7.2 shows typical CVs on a microelectrode only covering the plating/striping of aluminium. The limiting current was independent of scan rate, which was expected for diffusion limited response on a microelectrode. There was a slight positive shift of the oxidation peak at lower scan rates. Repeat scans at each individual scan rate showed good repeatability, i.e. the same limiting currents and oxidation peak potentials. This oxidation peak shift was not due to the reference electrode, as the onset potential of plating did not change. It was most likely due to the quantity of aluminium deposited, which increased at slower scan rates. If the deposited layer was thick enough then it was more like bulk aluminium than surface aluminium and hence more stable, thus required more positive potentials to be oxidised.

In this experiment $AlCl_3$ was added via electrochemical dissolution. From work in Chapter 5 it is known that this method of addition leads to varying [$AlCl_3$] over time due to the "short circuit" reaction with lithium metal. Using the diffusion coefficient of $D_{Al^{3+}} = 4.16 \pm 0.02$ x 10^{-5} cm^2 s^{-1} calculated from microelectrode

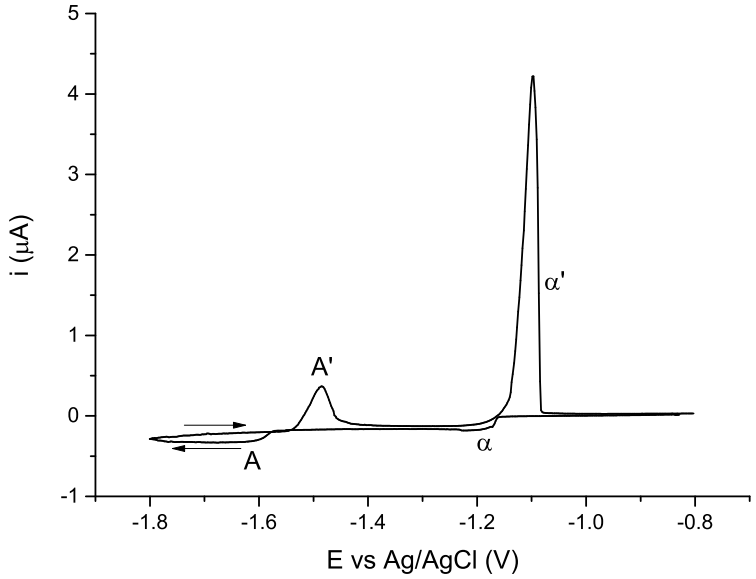

Figure 7.1: Typical CV of aluminium and cerium co-deposition on a tungsten microelectrode (STT, r = 15 μm), [$AlCl_3$] ≈ 2 mM, [$CeCl_3$] = 10.8 mM, ν = 100 mVs^{-1}, T = 808 K.

chronoamperometry in Section 5.3.1, a concentration of 2.37 ± 0.01 mM was calculated. However this experiment was performed at 808 K, rather than 723 K at which the chronoamperometry was performed. At this higher temperature the diffusion coefficient would be greater due to a decreased LKE viscosity, so the actual concentration in this salt was less than the calculated value. The exact concentration of $AlCl_3$ was not required since the m value/flux ratio can be calculated from the ratio of limiting currents (Figure 7.4) and [$AlCl_3$] was approximated to 2 mM.

7.2.2 Co-deposition at a Low Flux Ratio

Figure 7.3 shows typical CVs on a microelectrode only covering the alloying of cerium with aluminium. Since $i_{L\,\alpha}$ was constant up to $E_{onset\,A}$ over a wider potential window (Figure 7.1), it was valid to assume $i_{L\,\alpha}$ remained constant regardless of the CV (or PCV) starting potential. The CV was started at -1.4 V (more negative than the aluminium plating potential), in order to minimise the difference in pre-deposited aluminium film thickness prior to cerium reduction between scan rates. The CV was started at -1.4 V rather than, e.g. -1.55 V, so that any background currents could be observed and corrected for, to obtain accurate cerium reduction current values. The microelectrode was held at -1 V for 30 s between each CV to remove all deposited aluminium. Once background currents were removed, the limiting current of co-deposition was scan rate independent within experimental error. Using Equation 2.11, [$CeCl_3$] =10.4 ± 2.1 mM was calculated from the average limiting current. This was within experimental error of the quantity added (10.8 mM), which shows that the alloy reaction is limited by diffusion of Ce^{3+} rather than by diffusion of Al^{3+}.

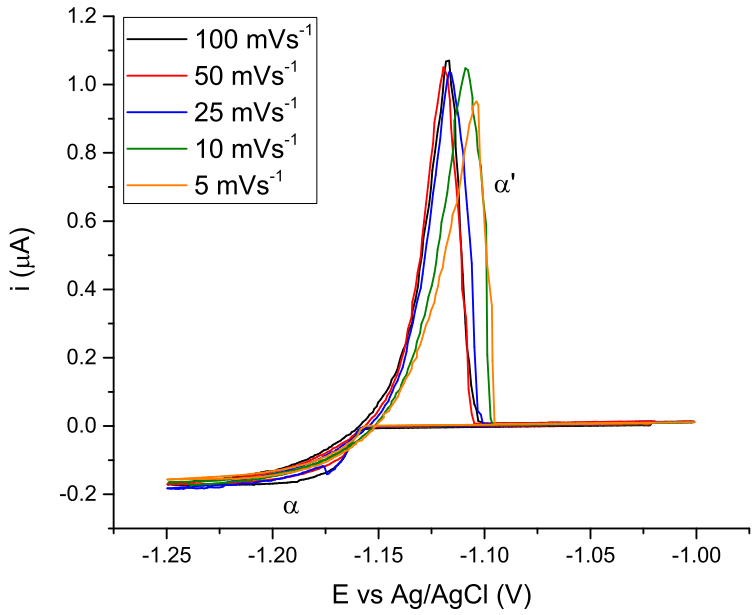

Figure 7.2: CV of aluminium plating/stripping reaction on a tungsten microelectrode (STT, $r = 15$ μm), [$AlCl_3$] ≈ 2 mM, $T = 808$ K.

Figure 7.4 shows the m value calculated from A and α currents from Figures 7.2 and 7.3. This was independent of scan rate, since $i_{L\,A}$ was independent of scan rate, with an average value of 2.0 ± 0.4. From macroelectrode work (Section 6.4) and the cerium-aluminium phase diagram,[62] the thermodynamically stable ratios of Ce:Al for a crystalline $Ce_x Al_y$ phase would be 1 or 3. Since the m value was between these values, the co-deposition current must be limited by the flux of cerium, producing an amorphous cerium-aluminium alloy. It should be noted that all macroelectrode work resulted in m values which increased over time/potential, whereas this microelectrode work shows constant m values. This is the expected behaviour of microelectrodes, which are less affected by convection and would appear to have a constant surface area as co-deposition occurs, which significantly simplifies analysis of the electrochemistry.

Figure 7.5 shows the Ce:Al ratios and efficiencies of the A/A' and α/α' reactions observed in Figures 7.2 and 7.3. Between 25 and 100 mVs^{-1} the Ce:Al ratio remained roughly constant at approximately 0.7. Below 25 mVs^{-1} the Ce:Al ratio increased to approximately 1.1. Since these Ce:Al values are lower than the m value, it implied that cerium did not insert into the pre-deposited aluminium, but only co-deposited with new aluminium on the surface. The efficiency of aluminium plating and stripping was constant within experimental error with an average value of approximately 90%. The efficiency of the alloying reaction increased with scan rate, from approximately 60% to approximately 75%. At faster scan rates there is less of a preference for plating at the edge (higher current densities, which in turn produces more dendritic, less

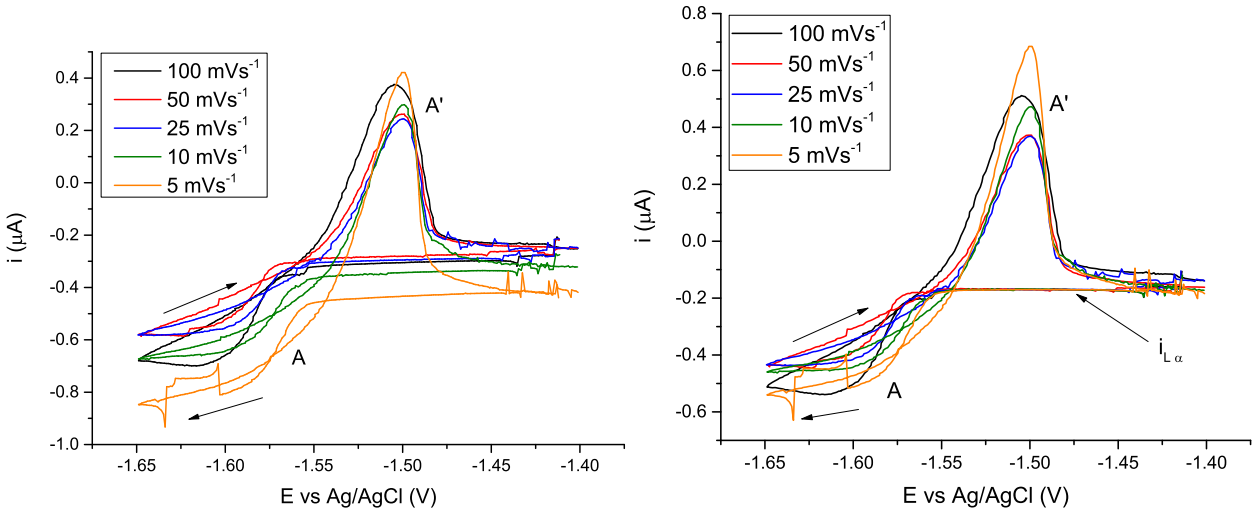

Figure 7.3: CV of the Ce^{3+} alloying reaction on a tungsten microelectrode (STT, $r = 15$ μm), [$AlCl_3$] ≈ 2 mM, [$CeCl_3$] = 10.8 mM, $T = 808$ K. (Left) Raw data. (Right) Background corrected using -1.475 to -1.525 V as the linear baseline, followed by adding -170.9 nA ($i_{L\,\alpha}$) from Figure 7.2.

mechanically stable, deposits), thus the alloy deposit would have been less dendritic resulting in a greater efficiency.[8]

Figure 7.6 shows n values obtained from fitting A' peak in Figure 7.3 with Equation 4.1. At all scan rates the n value (which controls the peak width) was greater than 3, and increased at slower scan rates. Since these values were above the expected $n = 3$ for cerium, the alloy must have been homogeneous with well interconnected grain structure, lowering the spread of energies and thus narrowing the peak. These n values were all greater than the macroelectrode experiment with a varying [$CeCl_3$]:[$AlCl_3$] ratio (Figure 6.8), where n was ~5.5 at a low concentration ratio and tended towards 3 at a high concentration ratio. This highlights how the improved diffusion properties at microelectrodes affect the co-deposited alloy grain structure.

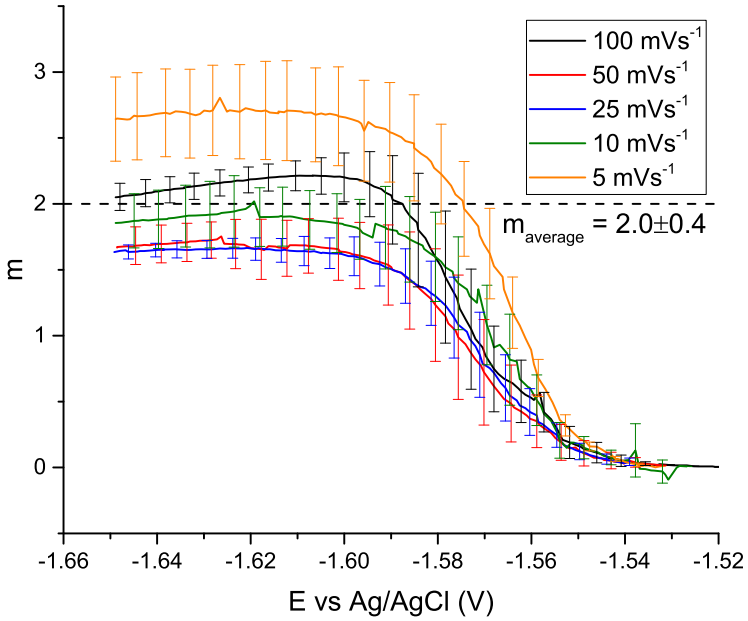

Figure 7.4: m values calculated using the current, A, from Figure 7.3 and average aluminium $i_{L\,\alpha}$, from Figure 7.2. Every 5th error bar is shown for clarity. Average m value calculated using all scan rates between -1.6 and -1.65 V, where steady state behaviour was achieved.

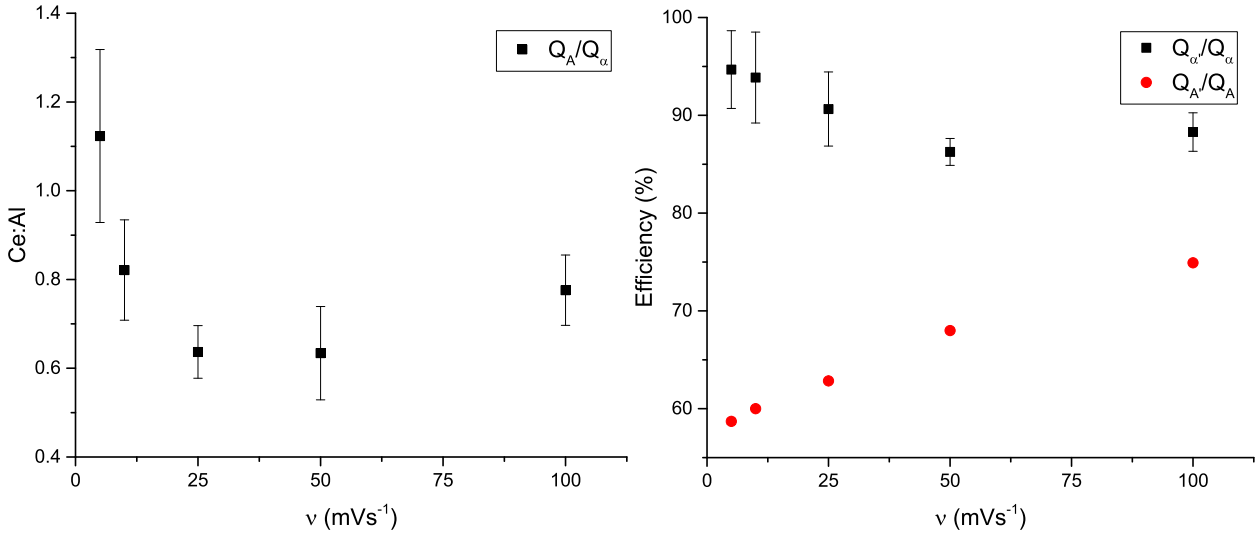

Figure 7.5: (Left) Ratio of cerium to aluminium deposited by comparing reduction charges of cerium and aluminium in Figure 7.3. (Right) Efficiency of the cerium and aluminium reactions by taking the ratio of oxidation to reduction charge for each reaction. $Q_{\alpha'}/Q_{\alpha}$ calculated from Figure 7.2 and $Q_{A'}/Q_{A}$ calculated from Figure 7.3.

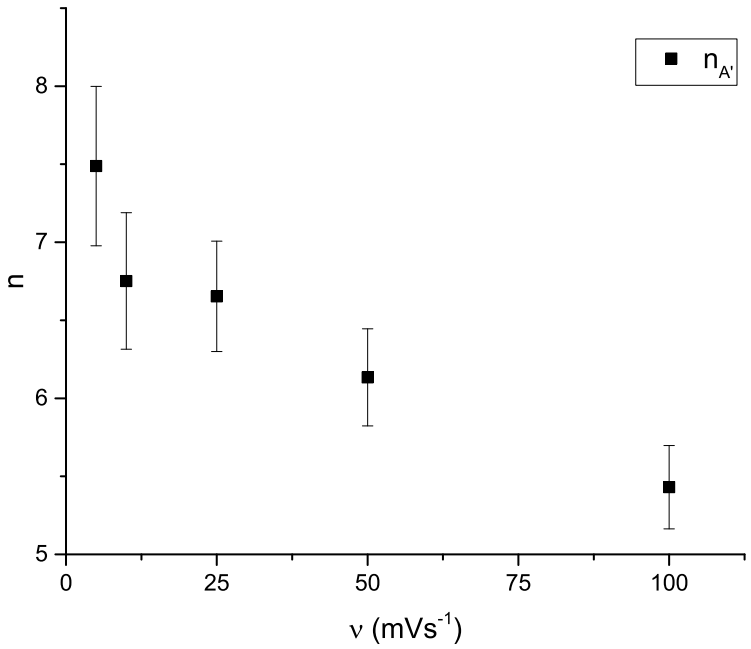

Figure 7.6: n values obtained from fitting A' peak in Figure 7.3 with Equation 4.1.

7.2.3 Co-deposition at a High Flux Ratio

In the previous section, the concentration ratio was approximately 4.5:1 and the co-deposition was limited by the flux of Ce^{3+}. In this section the $CeCl_3$ concentration has been doubled, increasing the concentration ratio to approximately 10:1. This gives a flux ratio of close to 3:1, which is the stoichiometry of the most cerium rich crystal phase (Ce_3Al), which may cause the reaction to become limited by the flux of Al^{3+}.

Figure 7.7 shows typical CVs of $AlCl_3$ and $CeCl_3$ co-deposition over multiple potential windows. The aluminium plating current, $i_{L\,\alpha}$, was consistent over each potential window at approximately -200 nA. Between -1.55 and -1.7 V, the co-deposition current $i_{L\,A}$ was limiting (approximately -860 nA), however at potentials below -1.7 V the current increased with potential. This may have been due to an increase of the electrode surface area as the alloy is deposited dendritically, as evidenced by the spikes in current. This increase of surface area is further evidenced by $i_{L\,A}$ during the back scan being greater than during the forward scan. Potentials negative of -1.8 V correspond to the reduction of lithium to form lithium-aluminium alloy (as seen in Figure 4.16). This provides an alternative explanation for the increase in current, due to the formation of a ternary amorphous lithium-cerium-aluminium alloy, or a combination of lithium-aluminium and cerium-aluminium alloy.

The alloy oxidation peak (A') grew in as the potential window widened, which was expected as more time was spent depositing cerium and aluminium. This peak was very sharp and symmetrical indicating thermodynamic control, unlike the peaks observed on macroelectrodes (Figure 6.21) where the peak was asymmetrical and therefore significantly influenced by phase change kinetics. There was initially a small aluminium stripping pre-peak (α") which was also seen on the macroelectrode co-deposition experiments (Figure 6.1). As with the macroelectrode data, α" was attributed to aluminium that was previously alloyed and therefore significantly roughened, thus was more easily oxidised than bulk aluminium (α'). As the potential window widened, and the expected cerium content of the alloy increased, the size of α" increased and seemed to have merged with peak α', which can be understood as more time was given for cerium to insert into bulk aluminium. Spikes in current were observed in peaks α" and α', which were attributed to detachment of aluminium dendrites causing local chaotic flow of solution, similar to the CVs performed while sparging with argon gas (Figure 5.7).

In this experiment 20 mM of $AlCl_3$ was added chemically. However the added mass of $AlCl_3$ cannot be used to know the concentration accurately in solution (Figure 5.15). Using $D_{Al^{3+}} = 4.16 \pm 0.02$ x 10^{-5} cm^2 s^{-1} obtained from microelectrode chronoamperometry (Figure 5.13), the concentration of $AlCl_3$ in this experiment was calculated to be 1.74 mM. The expected i_L current for Ce^{3+} reduction, assuming it was a plating reaction and therefore diffusion limited, was approximately -580 nA (for 20 mM $CeCl_3$ and $D_{Ce^{3+}} = 9.99$ x 10^{-6} cm^2

s^{-1}).[22] The measured $i_{L\,A}$ for the alloying current (aluminium and cerium reduction) was approximately -860 nA, therefore $i_{L\,Ce^{3+}}$ was approximately -660 nA. Since $i_{L\,Ce^{3+}}$ was a similar value to that expected value for a pure plating reaction, this suggested that the reaction was Ce^{3+} diffusion limited. The slightly larger $i_{L\,Ce^{3+}}$ value (by -80 nA) was most likely due to an increase in effective surface area due to non uniform plating of aluminium on the electrode surface, i.e. preferential edge plating on the microelectrode. This was evidenced by the increase in alloying current A on the back scan, which became more pronounced over wider potential windows.

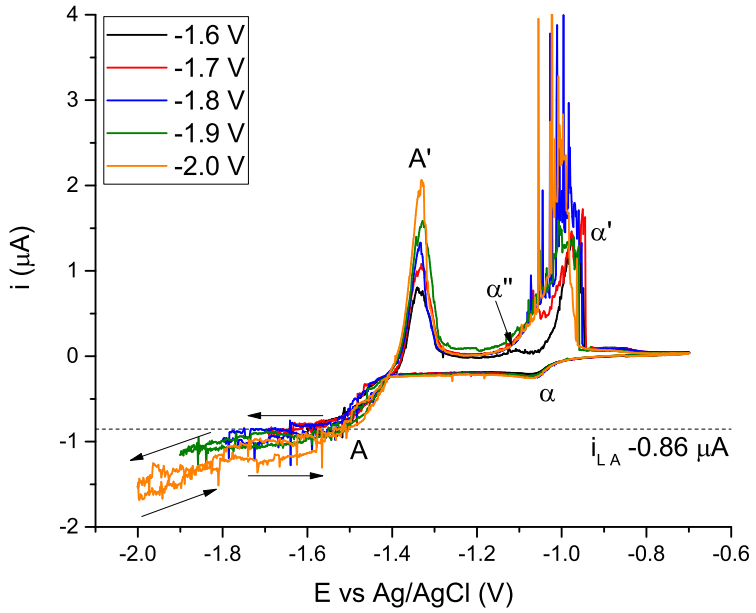

Figure 7.7: CVs of aluminium and cerium co-deposition on a tungsten microelectrode (TT, $r = 25$ µm) over a number of potential windows. $[AlCl_3] = 1.74$ mM, $[CeCl_3] = 20$ mM, $\nu = 100$ mVs^{-1}, $T = 723$ K.

Figure 7.8 shows the m values calculated from CVs in Figure 7.7. Over different potential windows the m values followed the same pattern, indicating that the alloy formation reactions were repeatable over these CVs. In the region -1.55 to -1.7 V, where the alloying current A was limiting, the average m value was found to be 3.2 ± 0.3. The magnitude of this increase from 2.0 ± 0.4 was expected, as the $[CeCl_3]$:$[AlCl_3]$ ratio increased from 4.5:1 to 10:1. This constant m value between -1.55 and -1.7 V suggested that co-deposition on microelectrodes is controlled by the flux of each species to the electrode surface for approximately 0.2 V, before other processes start to affect the co-deposition. Further work at an even greater $[CeCl_3]$:$[AlCl_3]$ ratio is required to determine if m is always dictated by the flux ratio, or if there is some maximum Ce:Al ratio that can be produced at potentials more positive than pure cerium plating.

More negative of -1.7 V the m value increased. This may have been due to an increased surface area, meaning that $i_{L\,A}$ was undervalued at these potentials, or lithium may have been co-depositing with cerium

and aluminium, as lithium reduction was seen to begin around these potentials on a bulk aluminium macroelectrode (Figure 4.1). In either case the m value was no longer a valid description of the co-deposition ratio of cerium and aluminium at these potentials.

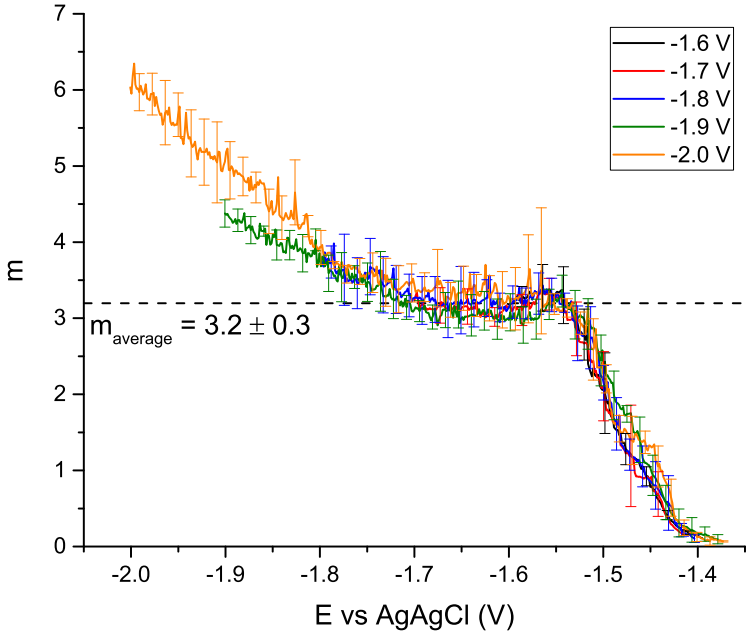

Figure 7.8: m values calculated from the forward scans of Figure 7.7. Every 10th error bar is shown for clarity. Average m value was taken from each potential window using data between -1.55 and -1.7 V where the alloying current A was limiting.

Figure 7.9 shows the Ce:Al ratio calculated from the CVs using the reduction charges as well as the oxidation charges:

$$\text{Ce:Al}_{\text{co-deposit}} = \frac{\text{Q}_{\text{Ce co-deposited}}}{\text{Q}_{\text{Al co-deposited}}} = \frac{\nu * \int_{-1.5}^{-2.0} (i - i_{lim\,\alpha})\, dV}{\nu * i_{lim\,\alpha} * (2 - 1.5)} \tag{7.1}$$

$$\text{Ce:Al}_{\text{total-deposit}} = \frac{\text{Q}_{\text{Ce co-deposited}}}{\text{Q}_{\text{Al co-deposited}} + \text{Q}_{\text{Al pre-deposited}}} = \frac{\nu * \int_{-1.5}^{-2.0} (i - i_{lim\,\alpha})\, dV}{\nu * (i_{lim\,\alpha} * (2 - 1.5) + \int_{-1.1}^{-1.5} i\, dV)} \tag{7.2}$$

$$\text{Ce:Al}_{\text{ox}} = \frac{\text{Q}_{\text{A'}}}{\text{Q}_{\alpha\text{'}+\alpha\text{''}}} = \frac{\int_{-1.6}^{-1.2} i\, dV}{\int_{-1.2}^{-1.0} i\, dV} \tag{7.3}$$

The ratio of the oxidation peaks (Ce:Al_{ox}) were the same at all potential windows with an average value of 0.58 ± 0.15. This was lower than the m value, which was expected as Ce:Al_{ox} included bulk aluminium deposited before co-deposition. This was because α' and α'' were not resolvable, and so Ce:Al_{ox} was a measure of the global composition. This was interesting, as the oxidation peak areas for A' and α' both grew in as

the potential window of the CVs were widened, implying that there was a cerium content of the alloy that was more mechanically stable and was not lost from the electrode surface.

Ce:Al ratios calculated from the reduction charges were significantly greater and increased over wider potential windows. As discussed for the m values, negative of -1.7 V it was difficult to properly attribute the current due to each species since either: the surface area was increasing, thus $i_{L\,\alpha}$ was undervalued, or Li^+ started to reduce and the increase in current was not due to Ce^{3+}. Thus only the Ce:Al values at -1.6 and -1.7 V are reliable for discussion of co-deposition. For both $Ce{:}Al_{\text{co-deposit}}$ and $Ce{:}Al_{\text{total-deposit}}$, the values were greater than $Ce{:}Al_{\text{ox}}$. $Ce{:}Al_{\text{co-deposit}}$ had the greatest value of 2.33 ± 0.03 at -1.7 V, in contrast to $Ce{:}Al_{\text{total-deposit}}$ 1.41 ± 0.02. The $Ce{:}Al_{\text{co-deposit}}$ value was lower than the m value as the integration covered a potential range before the co-deposition current became limiting. At wider potential windows if $i_{L\,A}$ had remained constant, $Ce{:}Al_{\text{co-deposit}}$ would have been expected to tend towards the m value.

For macroelectrodes, where the m value could not be used reliably to understand co-deposition, Ce:Al was a necessary alternative form of analysis. For microelectrodes, the m value shows that the flux ratio dictates the ratio of species being reduced, and there are no effects of increasing surface area or phase kinetic factors, at least over a specific range of potentials. On microelectrodes, combined analysis using the m value and Ce:Al ratios is useful for understanding co-deposition as the alloy composition still did not reach a limiting case.

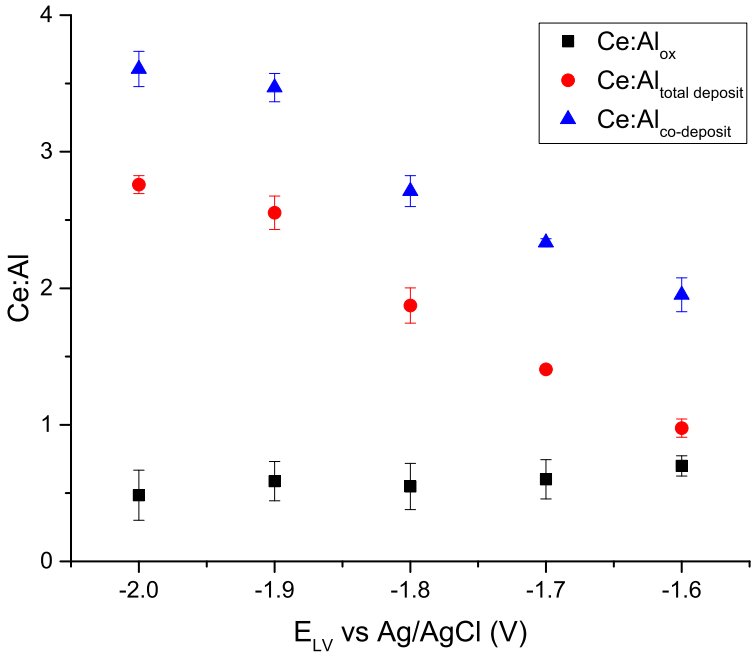

Figure 7.9: Ce:Al ratios calculated from the reduction and oxidation charges from CVs in Figure 7.7.

Figure 7.10 shows the efficiency of the α/α' and A/A' reactions. The efficiency of the aluminium plating/stripping reaction was constant (50-60%) over these potential windows, due to the large errors. The low efficiencies of the aluminium plating/stripping during co-deposition versus only plating and stripping (Figure 7.5), reflected the decrease of bulk aluminium present due to cerium insertion. This resulted in mechanically unstable (previously alloyed) aluminium, which detached and produced spikes in the CV currents, which resulted in the large errors due to there being large variation between each of the five CVs at a single potential window. The efficiency of the alloying reaction (A/A') was low at 30% even on the narrowest potential window, and decreased as the potential window was widened. This was in contrast to the efficiency of the alloying reaction on a bulk aluminium macroelectrode of >75%. This was expected due to the much higher current density on microelectrodes, which is known to promote the formation of dendrites. In the lower flux ratio co-deposition measurements, the alloy oxidation peak had very high n values (Figure 7.6), which, in macroelectrode work, corresponded to low efficiencies. The low efficiencies here were attributed to the greater flux ratio, and therefore even higher current density, which resulted in less mechanically stable alloy deposits, i.e. co-deposition with more cerium relative to aluminium, resulted in less mechanically stable deposits, causing more loss of the reduced cerium from the electrode surface.

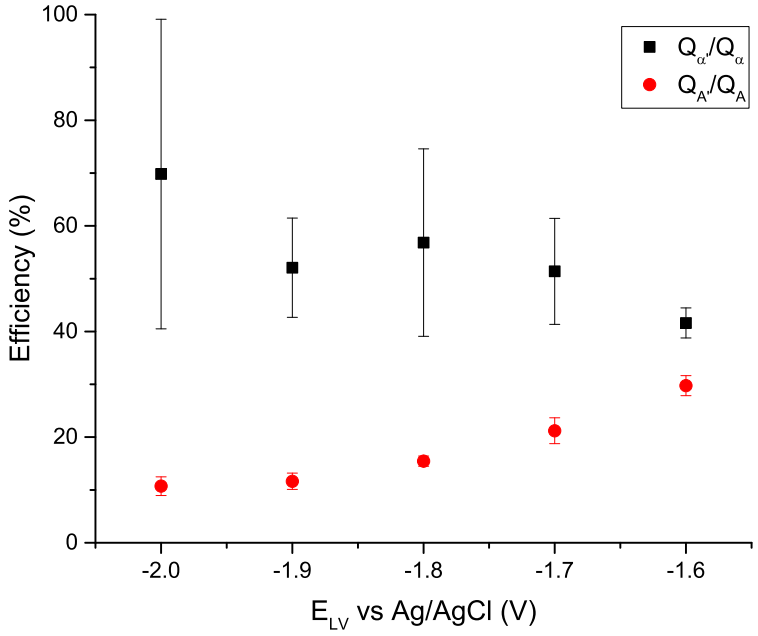

Figure 7.10: Efficiency of the cerium and aluminium reactions by taking the ratio of oxidation to reduction charge for each reaction from Figure 7.7.

Figure 7.11 shows the n values obtained by fitting the alloy oxidation peak (A') using Equation 4.1. As before n is related to the peak width, and was expected to have a value of 3. The obtained n value was constant within experimental error with an average value of 4.76 ± 0.57. Since this value was above 3, this implied

that the deposit was homogeneous with well interconnected grain structure, thus a low spread of surface energies. This was in contrast to the n values obtained for this same oxidation peak on macroelectrodes, where different scan rates (different times spent alloying) produced varying n values due to the large kinetic contribution to the formation of alloy (Figure 6.23). Since microelectrode co-deposition is determined by the flux of each species to the surface, these same kinetic factors are less prevalent and so at each potential window the composition and structure of the alloy are very similar. These n values were smaller than those obtained on microelectrodes at a lower flux ratio (Figure 7.6), which implied that at a higher current density the crystal grains were less well connected. This was not expected and may have been an artifact: well connected crystal grains would have produced less mechanically stable alloy, a lot of which detached; the less well connected grains produced a more stable alloy, which did not suffer as much detachment and so remained to be electrochemically oxidised. This agreed with the very low efficiencies (<30%) of the A/A' reaction at this high flux ratio (Figure 7.10).

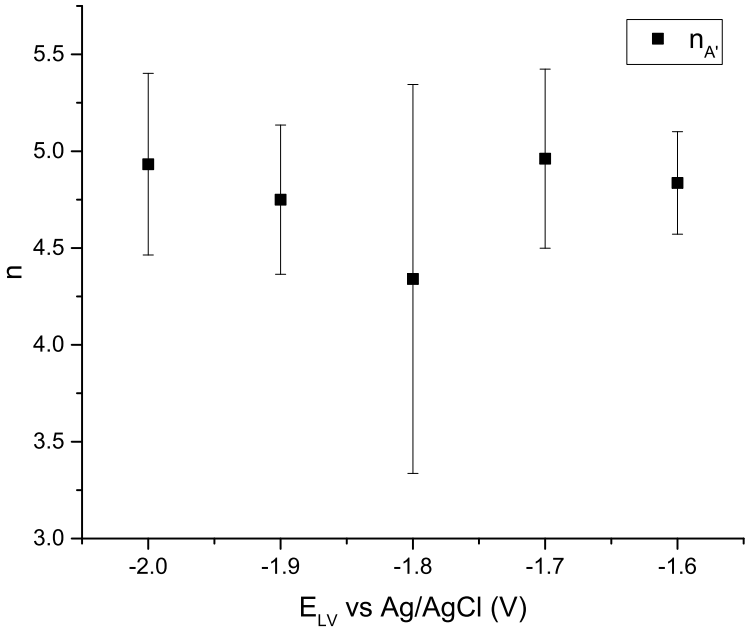

Figure 7.11: n values obtained from fitting A' peak in Figure 7.7 with Equation 4.1.

7.2.4 Co-deposition over a Wide Potential Window

Figure 7.12 shows a CV with a lower vertex potential of -2.2 V. The reaction β was observed to begin at approximately -1.8 V. Below -2.15 V the γ/γ' reaction was observed. It is interesting to note that the β reaction looked most similar to the reduction of lithium into a bulk aluminium macroelectrode in Figure 4.1, whereas the γ/γ' reaction looked most similar to the reduction of lithium in a thin film macroelectrode in

Figures 4.16 (LKE-$AlCl_3$) and 6.21 (LKE-$CeCl_3$-$AlCl_3$). During co-deposition on macroelectrodes γ/γ' was only observed with a lower [$CeCl_3$]:[$AlCl_3$] ratio, i.e. if the flux of cerium was high enough, the aluminium preferred to co-deposit with cerium rather than lithium, and more cerium-aluminium phases were observed. On microelectrodes the Ce:Al ratios are larger than on macroelectrodes, however the lack of more cerium-aluminium alloy peaks implies that the alloy was amorphous. Thus these β and γ/γ' reactions are not due to lithium alloying with "free" aluminium, but rather is the formation of ternary lithium-cerium-aluminium amorphous alloy. Since currents observed negative of -1.7 V in Figure 7.7 were due to the reduction of Li^+, so studies of the cerium-aluminium system on microelectrodes, where there is only one reaction attributable to cerium-aluminium alloying, should be confined to a potential window positive of -1.7 V.

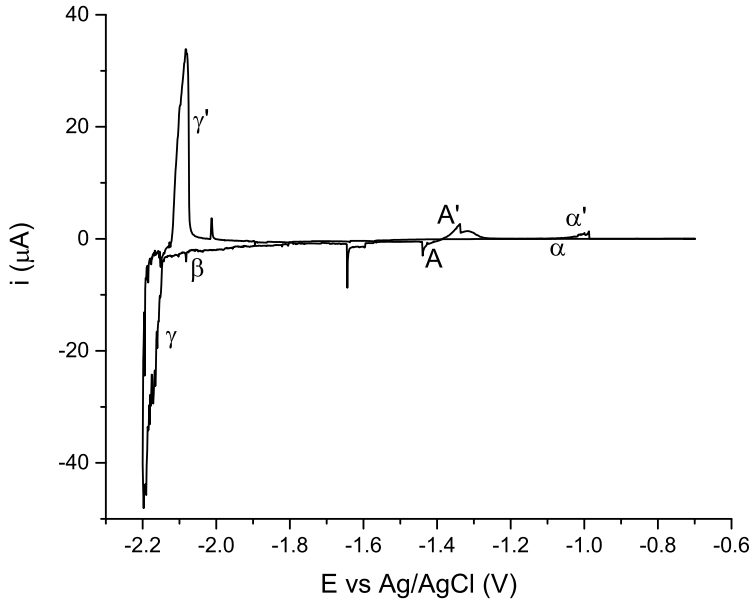

Figure 7.12: CV of aluminium and cerium co-deposition on a tungsten microelectrode (TT, r = 25 μm) over a much wider potential window, [$AlCl_3$] = 1.74 mM, [$CeCl_3$] = 20 mM, ν = 100 mVs^{-1}, T = 723 K.

With a high flux of cerium, on macroelectrodes five cerium-aluminium phases were observed; on microelectrodes only one cerium-aluminium phase (and lithium-aluminium or lithium-cerium-aluminium) was observed. The presence of only one alloy peak on microelectrodes (that is sharper than expected for n = 3), implied that initial deposition produced an amorphous alloy. Whether or not crystallisation occurred is unclear, as with a high enough Ce:Al ratio the formation of higher cerium content crystalline Ce_xAl_y phases would not result in extra current, as reduction of Ce^{3+} was already occurring at its maximum diffusion limited rate. Since no extra oxidation peaks were observed in the microelectrode CVs over wide potential windows, phase changes from higher to lower cerium content crystalline Ce_xAl_y phases did not require cerium to be expelled by oxidation, i.e. there must have been a phase where this "excess" cerium could reside. To explain this behaviour for the reductive and oxidative scans, an amorphous alloy which can "donate" or "accept"

cerium would allow phase changes between the Ce_xAl_y crystal phases to occur without changing the rate of reduction/oxidation. As previously mentioned, this amorphous phase would not be thermodynamically stable as it does not appear on the cerium-aluminium binary phase diagram (Figure 2.11), but rather it would be a metastable phase. This would seem to be a metallic glass[108–111] that has been produced electrochemically, rather than by rapid cooling of a liquid alloy. It would then seem that peak A/A', which was attributed to Ce_3Al_{11}, should, in fact, be attributed to amorphous cerium-aluminium alloy (perhaps in combination with some crystalline Ce_3Al_{11}).

In some way this lack of extra electrochemical peaks may be a negative, as a fingerprint of peaks might be expected to be more useful for species identification and can be achieved by using high flux ratios. However, co-deposition is unlikely to be the final sensor design as it would be undesirable to add another redox species in order to allow for on-line monitoring, due to the already complex nature of nuclear waste. Instead, co-deposition has been useful for understanding the electrochemical response based on electrode size and salt composition. It is now necessary to understand the electrochemical response on a fixed volume thin film aluminium microelectrode, which would be a better candidate for a sensor.

7.3 Thin Film Aluminium Microelectrodes

To avoid addition of $AlCl_3$ to LKE, it would be preferable to use a thin film aluminium microelectrode. Microfabricated thin film aluminium electrodes have 200 nm of aluminium deposited onto tungsten STT microelectrodes. The radius of the aluminium surface is 5 μm greater than the radius of the exposed tungsten surface, such that there is a ring of aluminium deposited on the surrounding Si_3N_4 (insulator), to ensure full surface coverage of the tungsten. Radii given for thin film aluminium microelectrodes are those of the underlying tungsten microelectrode. Figure 7.13 shows a typical CV of a newly microfabricated thin film aluminium microelectrode. There was a resistive slope, and capacitance to the response. While resistive features can mask reduction currents, oxidation peaks have often been easier to observe. No response from Ce^{3+} alloying with aluminium (A/A') was observed. Aluminium oxide is known to form rapidly in air, which is self passivating and is an effective barrier to intermetallic formation.[112] The exact structural form, thickness and morphology is known to be highly dependent on the environmental conditions during its formation, with only single nanometer thicknesses from atmospheric air exposure.[113–115]

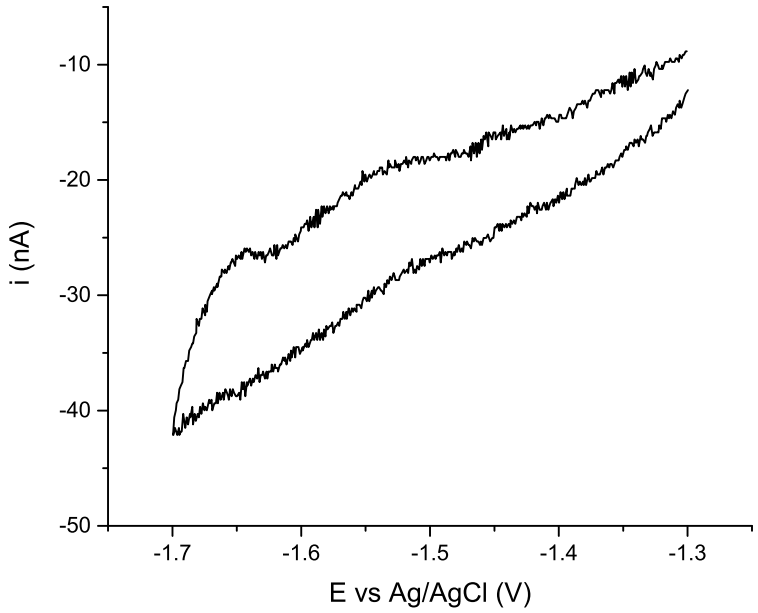

Figure 7.13: CV on a thin film aluminium microelectrode, $r = 25$ μm, $[CeCl_3] = 10$ mM, $\nu = 100$ mVs^{-1}, $T = 723$ K

7.3.1 Stability of the Al/Al_xO_y Thin Films

A key practical consideration is the stability of aluminium metal and aluminium oxide in LKE and whether aluminium oxide would preferentially dissolve, leaving behind the pure aluminium layer. Since the aluminium layer on the microelectrodes is 200 nm it can be expected that, even with poor solubility, if all the metal was removed the bulk concentration would stay below the solubility limit. The plating/stripping reaction of Al^{3+}/Al^0 occurs around -1.2 ± 0.1 V. When placed in LKE, bulk aluminium macroelectrodes, and thin film aluminium microelectrodes, show matching OCPs. To see whether the metal is lost, the OCP of a microelectrode was measured over time (Figure 7.14). The potential rested at -1.1 V for approximately 5 minutes before rapidly becoming positive and tending toward the OCP for a clean salt on tungsten (approximately -0.45 V). This gave an etching/dissolution rate of 0.67 nm s^{-1} for all the aluminium, assuming a constant rate across the entire surface area.

Before and after optical microscopy images are seen in Figure 7.15. After immersion the aluminium looked to have been completely lost from the electrode surface, both on the tungsten and overlying Si_3N_4.

Table 7.1 shows the EDX (energy dispersive x-ray spectroscopy) measurements on the surface on the microelectrode after immersion in LKE. These measurements confirmed the visual observations that no aluminium remained on the tungsten surface. At the step edge of the Si_3N_4 there appeared to be a small amount of aluminium, however it was a small value when compared to every other element.

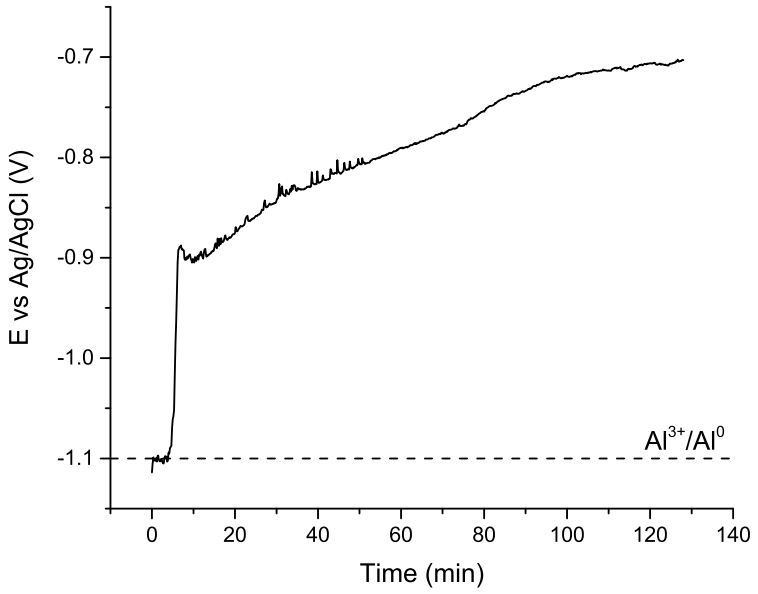

Figure 7.14: OCP over time on a thin film aluminium microelectrode, $r = 50$ μm, $T = 712$ K

Table 7.1: Normalised atomic percentages from EDX of a used thin film aluminium microelectrode (Figure 7.15).

Location	Tungsten	Aluminium	Silicon	Nitrogen	Oxygen
X_1	91.45	0.03	2.03	0.04	6.44
X_2	50.52	0.80	21.20	25.05	2.39

The solubility of aluminium oxide in LKE is on the order of $\times 10^{-6}$ mol l^{-1}.[89] For the largest size microelectrode ($r = 50$ μm), if there was enough oxide present that the entire aluminium volume was converted to oxide (assuming the sparge cleaning method was not 100% effective, such that the remaining oxide was not noticed during macroelectrode experiments), the resulting aluminium oxide concentration would be $\sim 6 \times 10^{-9}$ mol l^{-1}, three orders of magnitude below the solubility limit. For a bulk aluminium macroelectrode of 0.05 cm radius, immersed 1 cm into the salt, the radius would only change by 0.67 μm to reach the solubility limit of aluminium oxide, thus if this oxide mechanism occurred it would not have been observed from macroelectrode measurements. This provides a possible mechanism for the loss of aluminium from microelectrodes. A salt was prepared with approximately 16 mM of Al_2O_3 (solubility $\times 10^{-6}$ mol $l^{-1} \approx 0.01$ mM), two orders of magnitude above the solubility limit. To ensure the LKE was saturated with Al_2O_3, the LKE-Al_2O_3 was heated above 873 K and held for at least one hour before cooling back to 723 K. Thin film aluminium microelectrodes immersed in this salt were found to lose all aluminium within 3 hours. This suggested that formation and dissolution of aluminium oxide cannot be the mechanism for the loss of all aluminium from the electrode surface.

It was thought that if the loss mechanism of aluminium was some other chemical reaction, then a holding

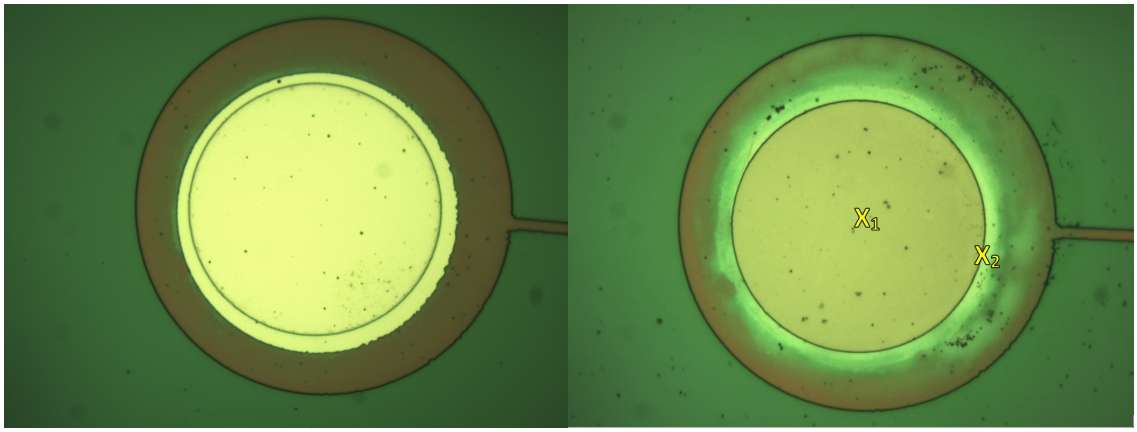

Figure 7.15: Optical microscopy of a thin film aluminium microelectrode at 500X magnification, $r = 50$ μm. (Left) Before immersion in LKE. (Right) After OCP measurement in LKE. X_n marks the points at which EDX measurements were taken, see Table 7.1

potential, below that of the aluminium plating potential, may prevent the loss of aluminium. Figure 7.16 shows the current and cumulative charge passed for a thin film aluminium microelectrode held at -1.4 V in LKE. The current was quite large, as the expected limiting current for a redox couple in this system would be expected to be on the order of magnitude of approximately -0.1 μA. The current increased over time, which indicated an increasing surface area and/or an increase in capacitive current. When the microelectrode was removed from the salt, it was still held at -1.4 V as the salt cooled, which is why the current dropped to 0 A at the end of the experiment.

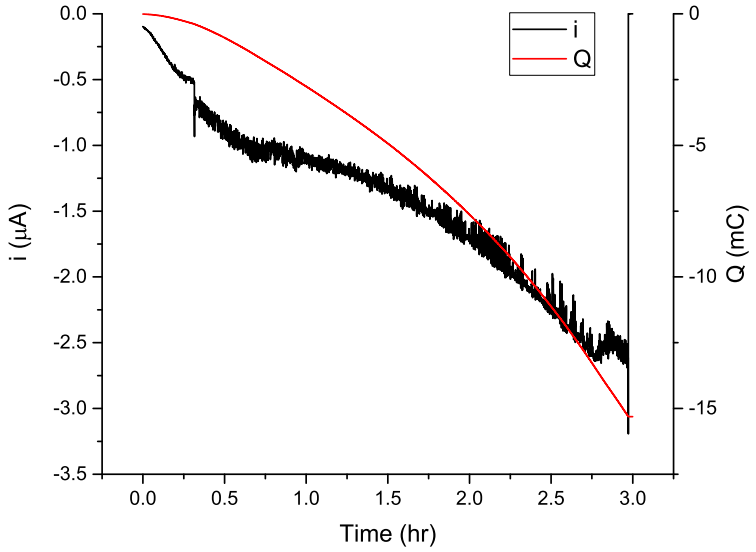

Figure 7.16: Current and cumulative charge passed for a thin film aluminium microelectrode ($r = 15$ μm, $T = 723$ K) held at -1.4 V in LKE.

Figure 7.17 shows optical microscopy images of the electrode before and after being held at -1.4 V for 3 hours. By visual inspection there was a large degree of damage to the electrode: missing Si_3N_4 as well as

cracks. The damage to the Si_3N_4 insulator has been observed multiple times within the research group after prolonged use (>1 hour) or negative applied potentials (<-1 V).[64] The exposed tungsten then results in a larger surface area, one reason why the current in Figure 7.16 increased over time. The cause of the damage to the Si_3N_4 is outside the scope of this thesis and so was not investigated. Most of the bright metal (assumed to be aluminium) in the inner disc remained, as did some on the Si_3N_4 (outer ring).

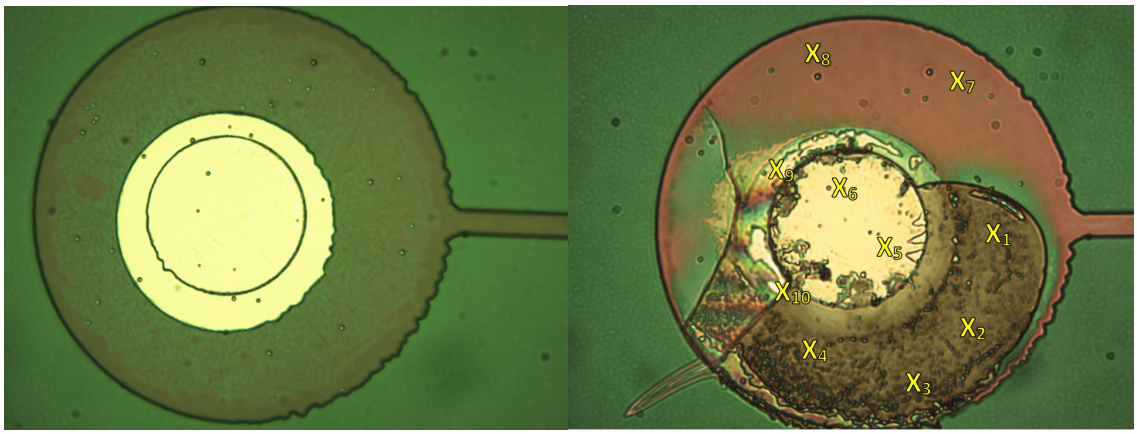

Figure 7.17: Optical microscopy of a thin film aluminium microelectrode at 500X magnification, r = 15 μm. (Left) Before immersion in LKE. (Right) After immersion in LKE for 3 hours at -1.4 V. X_n marks the locations of EDX measurements.

Table 7.2 shows the results of EDX on the microelectrode. The EDX measurements confirmed the presence of aluminium in locations where bright metal was visually observed: specifically on the inner disc and in some locations on the Si_3N_4. EDX also confirmed the loss of a large section of Si_3N_4 by comparison of silicon and nitrogen levels at different locations. By holding the electrode at a potential more negative than the aluminium plating potential, the loss of aluminium was prevented, which implied that the loss of aluminium in the absence of an applied potential is due to chemical oxidation, but not from water based impurities (e.g. oxide and hydroxide). It was possible that this chemical oxidant was a species such as Cl_2, which was produced during sparge cleaning, that remained dissolved and reactive even after a few hours.

Table 7.2: Normalised atomic percentages from EDX of a thin film aluminium microelectrode after being held at -1.4 V for approximately 3 hours.

Location	Tungsten	Aluminium	Silicon	Nitrogen	Oxygen	Titanium
X_1	77.8	0.0	8.5	1.0	12.0	0.8
X_2	80.0	0.0	7.2	0.8	11.4	0.6
X_3	77.6	0.0	8.6	1.0	12.2	0.6
X_4	81.5	0.0	7.0	1.0	7.0	0.4
X_5	60.6	19.4	5.0	0.0	14.4	0.6
X_6	59.6	18.4	6.4	0.0	14.9	0.7
X_7	23.9	0.0	30.5	43.2	2.4	0.0
X_8	23.9	0.0	30.9	45.2	0.0	0.0
X_9	14.7	4.3	34.3	34.9	11.8	0.0
X_{10}	53.6	18.9	6.4	0.0	20.7	0.4

7.3.2 Anodic Cycling

The left hand graph in Figure 7.18 shows CVs scanned positively of the aluminium reduction potential (-1.2 V). This was done to test whether some aluminium metal, or Al_2O_3, could be converted to $AlCl_3$, then reduced back to aluminium metal on the surface of the electrode, possibly disturbing the aluminium oxide layer. After performing these anodic scans, the potential window was reverted to -1.3 to -1.7 V (right hand graph of Figure 7.18), where Ce^{3+} reduction to cerium-aluminium alloy (A/A') was then observed.

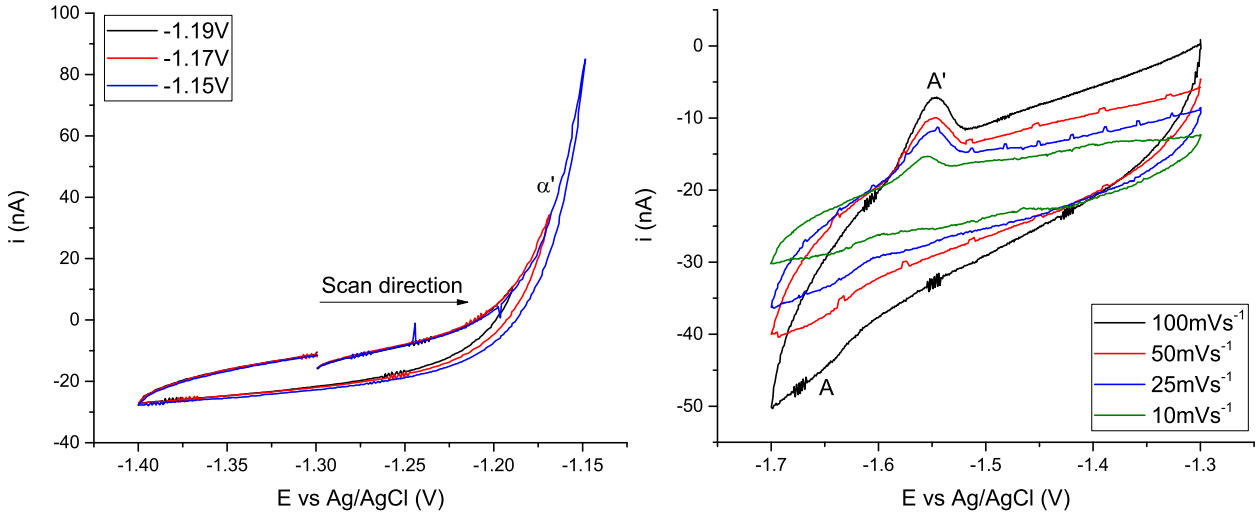

Figure 7.18: CVs on a thin film aluminium microelectrode, r = 25 µm, [$CeCl_3$] = 10 mM, ν = 100 mVs^{-1}, T = 723 K. (Left) Anodic cycling to -1.15 V. (Right) CVs over the cerium-aluminium alloying potential window.

The onset potential of $i_{L\,A}$ began at approximately -1.625 V at all scan rates. The $E_{p\,A'}$ was approximately -1.55 V at all scan rates. There was however a significant background current as well as capacitance, as evidenced by the increase of background currents with scan rate. This implied that there was a reaction occurring over this potential window in addition to Ce^{3+} reduction. It was seen in Section 7.3.1 that

aluminium spontaneously dissolves from the surface due to a chemical oxidant producing Al^{3+}. This unknown background reaction could then be the reduction of Al^{3+} which has been generated locally at the electrode surface. The alloying currents observed would then be co-deposition, rather than insertion of cerium into aluminium which would kinetically limited. It should be noted that any Al^{3+} produced at the electrode surface will diffuse away from the electrode, therefore only a fraction of the Al^{3+} generated chemically could be reduced for co-deposition.

It was attempted to improve the response of alloying by applying more positive potentials as well as applying oxidising potentials for longer, by scanning at slower scan rates. Unfortunately this did not result in larger, or more well defined, alloying currents. Instead it resulted in aluminium being lost from the surface, as more time was given for Al^{3+} to diffuse away from the electrode, and so all alloying current disappeared more rapidly.

7.3.3 Repeat CVs over Cerium-Aluminium Alloying Window

With some tungsten microelectrodes, there is initially a poor response but by performing a few CVs the signal improves. It is thought that this is due to the molten salt cleaning the oxide from the tungsten surface.[64] Aluminium oxide has a low solubility in LKE,[89] however since the total quantity of aluminium oxide on a microelectrode should be very low, it could dissolve leaving a pure aluminium layer. Thus by performing CVs continuously (below the aluminium stripping potential), it was hoped that aluminium oxide would dissolve while the aluminium underneath would remain, allowing for alloying to occur. CVs were performed every 5 minutes for one thin film aluminium microelectrode, and CVs were performed continuously on another thin film aluminium microelectrode (left and right hand graphs in Figure 7.19, respectively). While there were changes in the response as time increased, no cerium-aluminium alloying was observed and so this did not result in aluminium oxide free thin film aluminium microelectrodes.

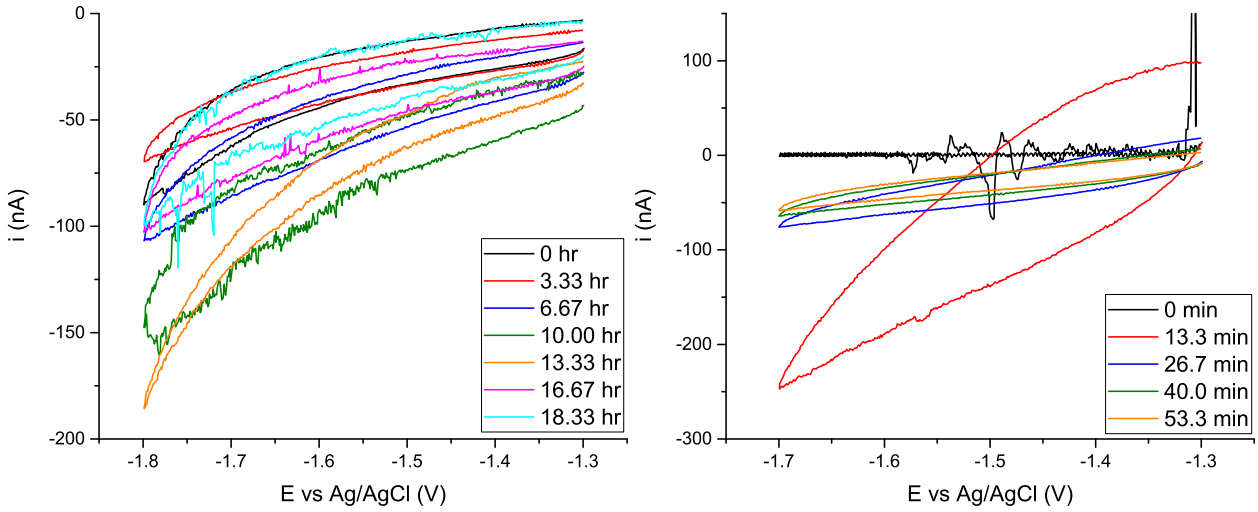

Figure 7.19: CVs on thin film aluminium microelectrodes [$CeCl_3$] = 20 mM, ν = 200 mVs^{-1}, T = 686 K. (Left) r = 10 μm, CVs performed every five minutes for 19 hours, with a holding potential of -1.3 V applied between CVs. (Right) r = 25 μm, CVs performed continuously over 1 hour.

7.3.4 Cathodic Cycling

It was observed on bulk aluminium macroelectrodes, that scanning out to lithium alloying potentials (approximately -2.0 V) would result in the improvement of the signal response of the α/α' (pure aluminium) and A/A' (cerium-aluminium alloying) reactions compared to a brand new electrode that had a native oxide layer.

In Figure 7.20 CVs were performed by decreasing the lower vertex potential. Below -1.9 V, the negative current for reaction β increased rapidly. Al_2O_3 is known to incorporate Li^+ at low temperatures and irreversibly form a highly stable Al-O-Li amorphous phase which has a high Li^+ conductivity.[116,117] This permeability to Li^+ allows the reference electrode, which has a aluminosilicate sheath, to work. There was no β' oxidation observed on narrow potential windows, which was observed over similar potential windows for bulk aluminium macroelectrodes (Figure 4.1). When scanned to -2.3 V, the γ/γ' reaction and the β' oxidation were observed. These are the same lithium-aluminium alloying reactions observed on a bulk aluminium macroelectrode (Figure 4.1). Three scans were performed at each potential window, with small increases in the magnitude of currents on repeat scans. For the scans to -2.3 V, there was a much larger difference between the first and second scan, i.e. β showed little change on repeat scans, therefore it had little effect on the aluminium layer, whereas γ/γ' showed larger changes on repeat scans, therefore it had a much greater effect on the aluminium layer. This can be explained as the large flux of lithium causing a sizable volume expansion which leads to an increase in the electrode surface roughness and area. This was used to "prepare" the aluminium surface for a bulk macroelectrode, as multiple lithium alloying cycles could be performed without losing all of the bulk

aluminium. Despite the presence of $CeCl_3$ in this salt, there was no observed cerium-aluminium alloying, as the capacitance (difference between the negative and positive currents on the forward and backward scans) was quite large (approximately 100 nA, which was comparable to the expected alloying current).

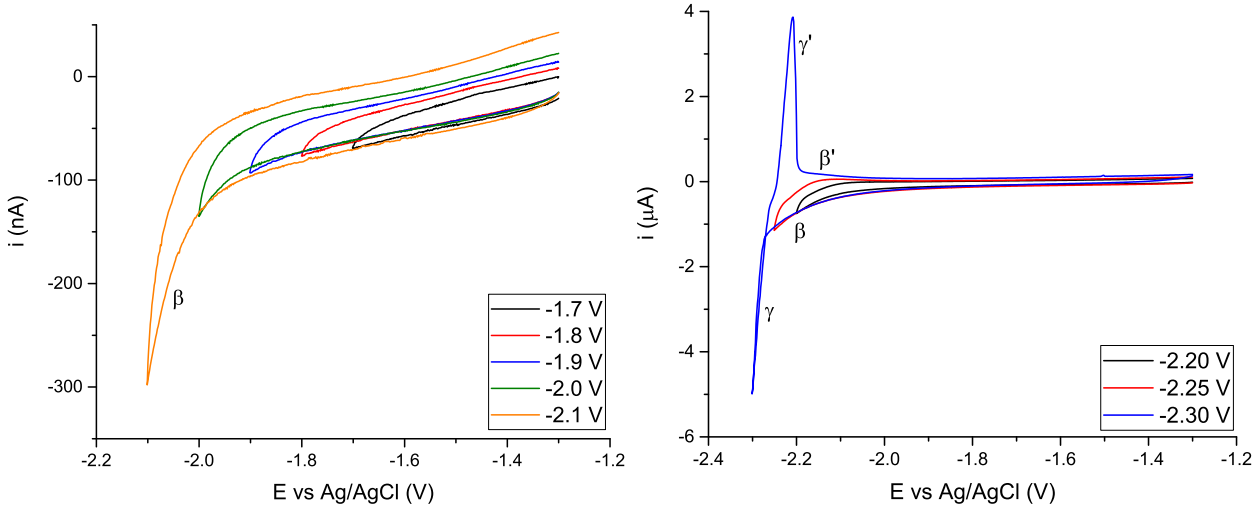

Figure 7.20: CVs with wide potential windows performed on a thin film aluminium microelectrode, r = 25 μm, [$CeCl_3$] = 20 mM, ν = 200 mVs^{-1}, T = 686 K.

Li^+ reduction was performed at different scan rates (Figure 7.21) on the same thin film aluminium microelectrode. At higher scan rates, the currents of β and β' increased, whereas γ and γ' both became smaller. This i_p versus ν^{-x} relationship for the γ/γ' reaction was also observed on bulk aluminium macroelectrodes (Figure 4.1). Over five CVs at each scan rate there was no degradation to the signal, despite these applied potentials usually causing instantaneous degradation of the signal response on in-house developed tungsten and platinum microelectrodes.[64] This implied that the layer of aluminium protected some surface on the microelectrode from unwanted reactions caused by applying these negative potentials.

CVs were then performed over the expected cerium-aluminium reduction window on the same thin film aluminium microelectrode (Figure 7.22). Clear cerium-aluminium alloying features were observed (A/A'). The reduction current (A), appeared to give a peak type response above 100 mVs^{-1} and the oxidation peak potential $E_{p\,A'}$ was constant within experimental error. This size of microelectrode (r = 25 μm) was known to be on the border of micro- and macro- type response based on scan rates used in this work.[48] At 100 mVs^{-1} and below, the reduction current showed the expected limiting current type response. At all scan rates there was a significant background current and capacitance. This capacitance changed the observed limiting currents at each scan rate. As the scan rate decreased, the reduction current became more limiting but the current was less smooth. This may be an effect of detaching mechanically unstable alloy, or this may be due to external electromagnetic noise, since the Faraday "cage" did not surround the entire electrochemical cell

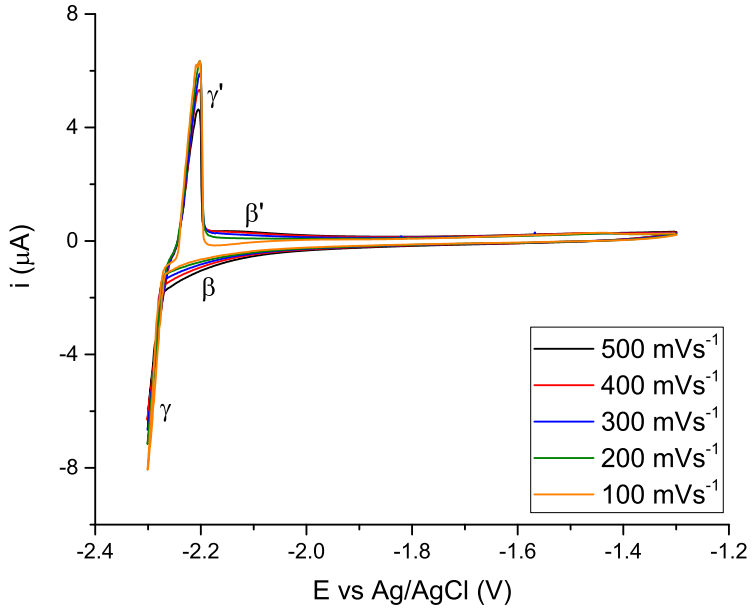

Figure 7.21: CVs performed on a thin film aluminium microelectrode at multiple scan rates, $r = 25$ μm, [$CeCl_3$] = 20 mM, $T = 686$ K.

and these Faradaic currents were very small. The background current was similar to that observed during anodic cycling (Figure 7.18). In both cases aluminium had been exposed to the salt and Al^{3+} may have been generated by a chemical oxidant (e.g. dissolved Cl_2). The background current may then be reduction of Al^{3+} and the alloying would then be co-deposition of Ce^{3+} and Al^{3+}. The aluminium current was not limiting, i.e. the slope of aluminium reduction current was different to the slope of the co-deposition current, and the slope of aluminium reduction current changed with scan rate. This made an m value very difficult to calculate accurately.

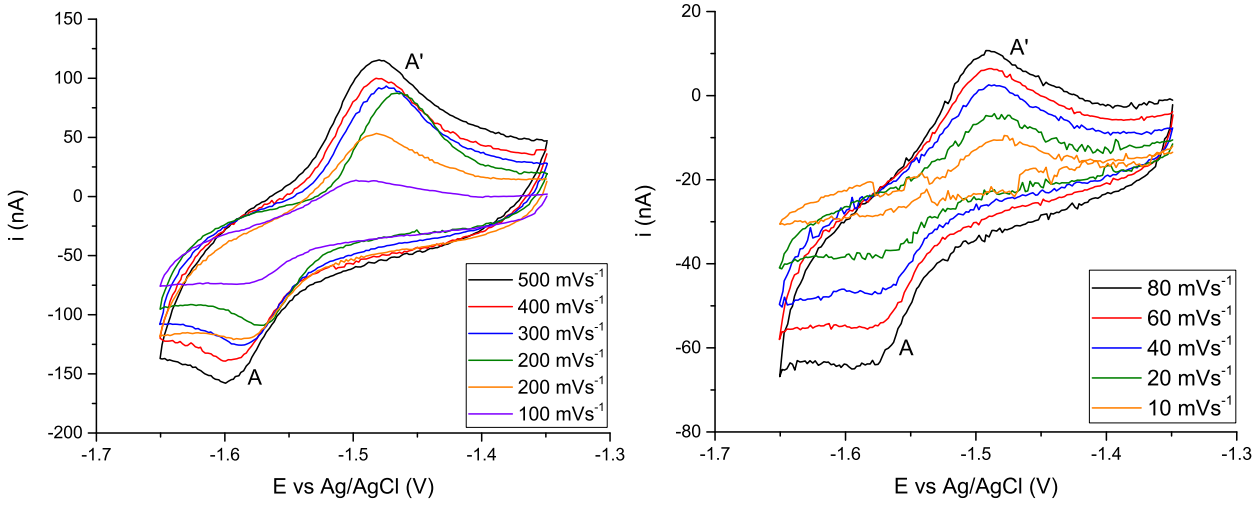

Figure 7.22: CVs at multiple scan rates on a thin film aluminium microelectrode after Li^+ reduction, $r = 25$ μm, [$CeCl_3$] = 20 mM, $T = 686$ K (Left) $\nu = 500 \rightarrow 100$ mVs^{-1} (Right) $\nu = 80 \rightarrow 10$ mVs^{-1}

A possible mechanism of oxide removal could be as follows. The oxide film is permeable to Li^+ ions,[116] allowing the transport of Li^+ to the aluminium surface. The reduction of Li^+ to form lithium-aluminium alloy results in a large volume expansion at the Al-Al_xO_y interface. This causes stress to the oxide film, which results in cracking, allowing salt to reach the pure aluminium underneath. When the lithium is oxidised, the remaining aluminium is likely to be structurally altered (different morphology and grain boundaries), affecting future reactions. Since the microelectrode film has a large surface to volume ratio, this new aluminium structure is the predominant one that is involved in further reactions. It was hoped that further reduction of Li^+ would cause more cracking, and thus more pure aluminium surface area to be exposed, leading to the improvement of the Ce^{3+} reduction signal, until the point at which the entire Al surface would be exposed to the salt.

7.3.5 Study of Li^+ Reduction on the Sensing Ability of Ce^{3+}

On a new thin film aluminium electrode (r = 15 μm) CVs were performed over the Ce^{3+} and Li^+ reduction windows (-1.3 to -1.7 V and -1.3 to -2.3 V, respectively) in alternation (Figure 7.23). There was significant capacitance in the microelectrode response over the Ce^{3+} reduction window. The raw data was also resistive, but this was removed by background correction to allow direct comparison of the reduction currents on successive CVs. While there was an improvement in the Ce^{3+} signal (increasing reduction and oxidation currents), this diminished as further Li^+ reduction CVs were performed. In Figure 7.23 the Li^+ reduction signal became smaller with time and spikes started to appear in the current. By CV 52 $i_{p\,\gamma}$ was only approximately -1 μA, whereas on CV 16 it was approximately -5.5 μA. Since both alloying reactions were diminishing, this indicated damage to the aluminium layer as the electroactive area initially increased, but then subsequently decreased due to repeat alloying/de-alloying cycles leading to pulverisation (electrically disconnected grains resulting from the quasi-reversible expansion of LiAl) of the thin aluminium film (as seen for aluminium nanowires).[117, 118] On microelectrodes this pulverisation would reduce the electroactive area, decreasing the response of Li^+ and Ce^{3+} reduction. Controlling the Li^+ reduction, e.g. not scanning as negatively and therefore reducing less Li^+, may help to prevent this pulverisation.

On a new thin film aluminium microelectrode (of the same 15 μm radius), this same alternation of potential windows was performed, but only scanning to -2.25 V rather than -2.3 V. Figure 7.24 shows that this potential window allowed lithium reduction via the β/β' reaction, but the γ/γ' reaction (which has much greater currents and so was expected to deteriorate the aluminium layer more rapidly) was not observed. Cerium-aluminium alloy reactions were then observed when scanning over the wider potential window. In addition to A/A' there was another cerium oxidation peak (B') just negative of A', which was attributed to $CeAl_3$

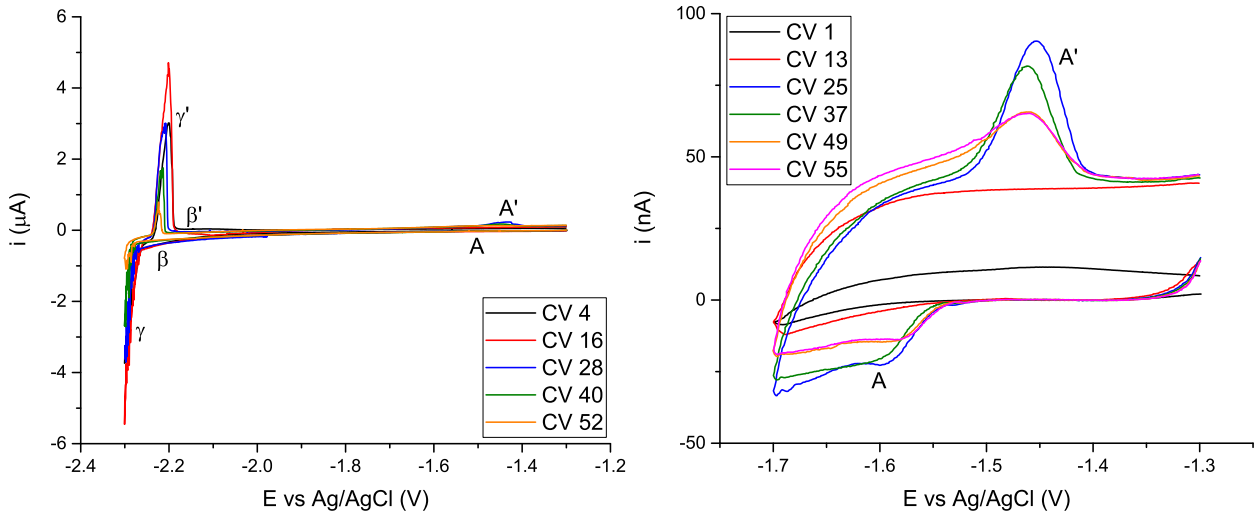

Figure 7.23: CVs alternating over two potentials windows on a thin film aluminium microelectrode, $r = 15$ μm, $[CeCl_3] = 20$mM, $\nu = 200$ mVs^{-1}, $T = 684$ K. Three CVs are run over each potential window, before changing the potential window. The CV numbers in the legends correspond to the chronological order of CVs run over both potential windows. (Left) -1.3 to-2.3 V to reduce Li^+ (Right) -1.3 to -1.7 V to reduce Ce^{3+}, background corrected using -1.375 to -1.475 V as the linear baseline.

(Section 6.4.1). The potential separation between $E_{p\,A'}$ and $E_{p\,B'}$ was similar to that on macroelectrodes (Figure 6.1). Over the first few scans of Li^+ reduction, the response during oxidation (β') changed from peak shape oxidation to the shoulder like shape, which was thought to be due to the lithium-aluminium alloying process. The reduction current at the lower vertex potential then became more consistent between scans, remaining between -1 and -0.5 μA. On this scale the Ce^{3+} reduction and oxidation were easily observed, and showed the same increase in oxidation current with scan number. This could not be observed on the previous thin film aluminium microelectrode when scanning to -2.3 V (Figure 7.23). The Ce^{3+} response was much improved from the previous electrode. While the contribution of capacitance to the current looked to be similar (approximately 50 nA based upon the current separation at -1.3 V), the redox peak currents were much larger. Since the $CeCl_3$ concentration and geometric radius for each experiment were the same, the electroactive area resulting from Li^+ reduction was judged to be greater by pre-conditioning the electrode more "gently".

Once the thin film microelectrode electrode was "preconditioned" a scan rate study was performed (Figure 7.25). In the raw data, the currents and magnitude of the slope both increased with scan rate. Once background corrected, the alloying current was observed to be limiting at each scan rate. The expected limiting current for this reaction was approximately 350 nA (assuming $r = 15$ μm and that the reaction was limited by Ce^{3+} diffusion), which was far above any observed value. Using the limiting current at 10 mVs^{-1} (with the least contribution of capacitive current), the area of the electrode was calculated to be approximately 1.4% of the geometric area. Clearly the electrode surface had not become pure aluminium. Further CVs to

reduce more lithium resulted in loss of all previously observable reactions, i.e. all the aluminium had been lost from the tungsten surface, which was confirmed by optical microscopy.

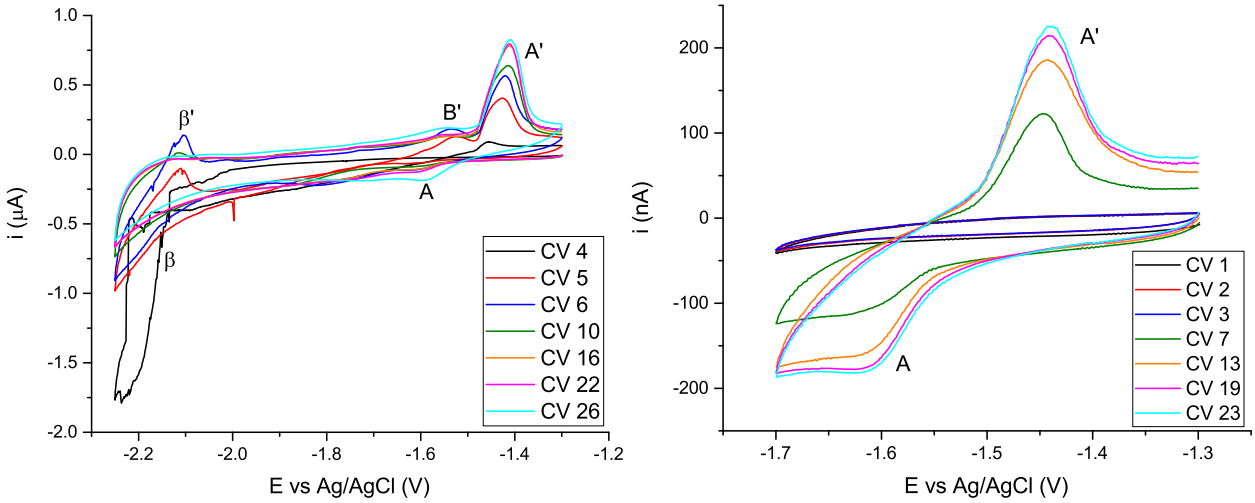

Figure 7.24: CVs alternating over two potential windows on a thin film aluminium microelectrode, r = 15 μm, [$CeCl_3$] = 20 mM, ν = 200 mVs^{-1}, T = 684 K. Three CVs are run over each potential window, before changing the potential window. The CV numbers in the legends correspond to the chronological order of CVs run over both potential windows. (Left) -1.3 to -2.25 V to reduce Li^+ (Right) -1.3 to -1.7 V to reduce Ce^{3+}.

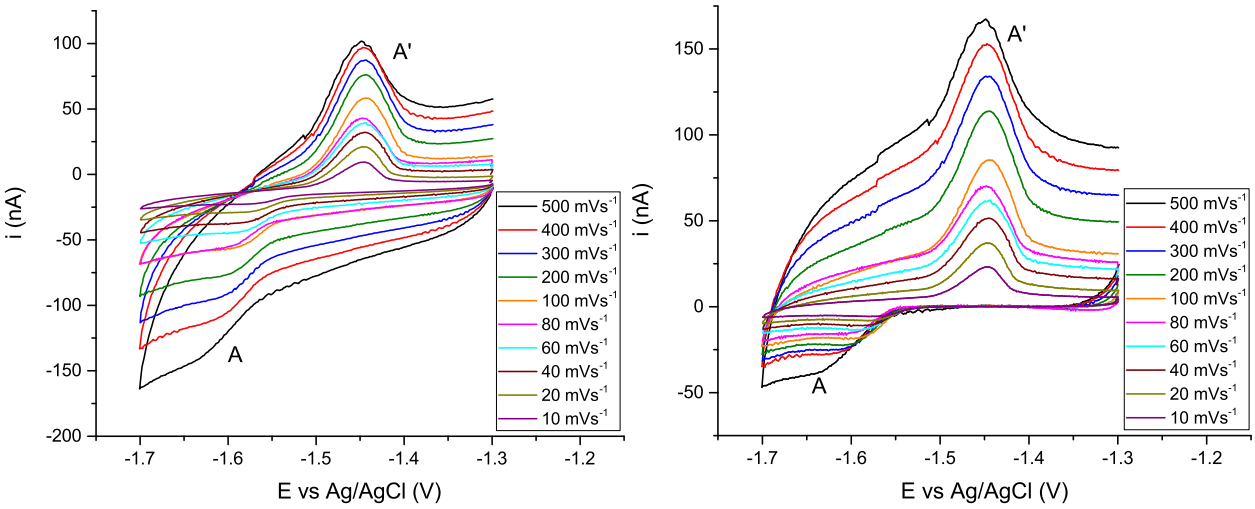

Figure 7.25: Scan rate study of the cerium-aluminium alloying reaction (A/A') after pre-conditioning performed in Figure 7.24. Thin film aluminium microelectrode, r = 15 μm, [$CeCl_3$] = 20 mM, T = 684 K. (Left) Raw data. (Right) Background corrected using -1.375 to -1.475 V as the linear baseline.

7.4 Conclusions

Co-deposition on a microelectrode had greater Ce:Al values than macroelectrodes due to the higher current density of microelectrodes. Despite Ce:Al ratios great enough for multiple Ce_xAl_y intermetallics to have

formed during CVs on microelectrodes, only one reaction was observed for cerium-aluminium alloying for CVs over wide potential windows. This was different to macroelectrodes where up to five oxidation peaks were observed and attributed to Ce_xAl_y intermetallics, at a similar $[CeCl_3]$:$[AlCl_3]$ ratio as used for these microelectrode experiments. The high current density on microelectrodes resulted in highly dendritic deposits, which detached from the electrode surface leading to low current efficiencies. This is acceptable for studying the fundamentals of cerium-aluminium alloying, but not for concentration monitoring. Co-deposition is not the method that would be used for the final sensor, as a fixed volume thin film aluminium microelectrode would be preferred to give a repeatable response without generating dendritic structures. From a combination of macroelectrode and microelectrode co-deposition measurements, it was found that more cerium was present in the alloy than could be explained by the number of observed crystal phases. This was explained by the electrochemical formation of a metallic glass of cerium-aluminium , which is a metastable amorphous phase, usually formed in the literature by rapid cooling of liquid alloys.

The use of microfabricated thin film aluminium microelectrodes was difficult due to the formation of a highly stable oxide film after aluminium deposition during microfabrication. The oxide film could be overcome by the reduction of Li^+ to result in the observation of cerium-aluminium alloying. This was thought to be due to lithium-aluminium alloying resulting in significant volume expansion which resulted in surface roughening, providing free aluminium surfaces. As with co-deposition, only one cerium-aluminium alloy reaction could be observed, even over wide potential windows. Unfortunately these CVs had large background resistances, high capacitances and a smaller electroactive area than geometric area. These are critical factors for the applicability of these microelectrodes as sensors and so the removal, or prevention, of the oxide layer is highly desirable. The oxide film, as well as the aluminium layer, were lost spontaneously when immersed in LKE with no applied potential. If a potential negative of the aluminium plating potential was applied, aluminium would remain on the electrode. This implied that the loss mechanism is chemical rather than mechanical. Oxygen based oxidants (O_2 or H_2O) are unlikely to be the cause, since saturation of LKE with Al_2O_3 did not prevent aluminium loss. A different oxidant in LKE, perhaps Cl_2 generated by electrochemical sparge cleaning, may have caused the chemical oxidation and dissolution of aluminium. Unfortunately, continuous CVs for hours (long enough for dissolution/removal of the top oxide layer) did not result in observable alloying, which suggested that the negative potential was also preventing the aluminium oxide from being removed.

Future steps to improve device performance would be to attempt depositing sacrificial metal layer onto aluminium, which could selectively be stripped from the electrode surface. This would be done by preventing exposure to air between the deposition of aluminium and the sacrificial metal, or by argon milling any formed oxide layer before deposition of the sacrificial metal. Alternatively, aluminium oxide could be

chemically/electrochemically etched (in solvent other than molten salt) before transferring to an LKE-$CeCl_3$ salt without exposing the electrode to an oxygen containing atmosphere. Aluminium could also be plated onto a tungsten microelectrode from a different solvent (molten salt or ionic liquid plating bath) and then transferred to LKE-$CeCl_3$, as long as both solutions are under an inert atmosphere. This would have the benefit of selectively depositing the aluminium inside the Si_3N_4 cavity, as opposed to the microfabricated electrodes which have some aluminium deposited outside the cavity leading to some uncertainty in the total surface area, volume and geometry of the aluminium layer. This would also allow the use of thin film aluminium microelectrodes with different layer thickness, which may affect the kinetics of cerium insertion (which unfortunately could not be investigated in this work). If these issues with the native aluminium oxide can be overcome, it is expected that the enhanced diffusion properties, which significantly simplified the co-deposition signal by the transition of kinetic (macro-) to thermodynamic (micro-) control, would improve the response of alloying with a fixed metal volume. This would ultimately prove that such microelectrodes are ideal for on-line monitoring in nuclear pyroprocessing.

Chapter 8

Conclusions and Further Work

Nuclear pyroprocessing requires fundamental understanding of alloying systems as well as development of on-line monitoring sensors. For this purpose, cerium-aluminium was studied as a surrogate system for plutonium-aluminium, and macro- and microelectrodes were used to compare their applicability as sensors from the obtained electrochemical responses. In Chapter 4 fundamental alloying behaviour of cerium-aluminium was studied on a bulk aluminium macroelectrode, and the electrodeposition of each metal was studied on a tungsten macroelectrode. To study these reactions, cyclic voltammetry was predominantly performed using multiple analytical techniques to analyse the data which included: background correction, iR drop correction, convolution and oxidation/reduction efficiency. Once the electrochemical behaviour of electrodeposition of each metal was understood, studies of alloying was performed by reduction of cerium into a bulk aluminium electrode. One alloying reaction was observed, which was found to have a large kinetic barrier to alloy formation (evidenced by the apparent resistance being approximately 4 Ω greater than the solution resistance). While the i_p versus $\nu^{0.5}$ relationship was found to be linear, which indicated diffusion control of the reaction at the peak potential, the calculated Ce^{3+} concentration was approximately 50% of the amount added by mass. In addition, convolution (which should produce a steady state convolved current for a diffusion controlled reaction) yielded an increasing convolved current negative of the peak potential. It is highly likely that the insertion of cerium into the aluminium lattice results in a high degree of surface roughening and an increasing surface area during alloy formation. Fitting the alloy oxidation peak to an expression which describes the peak shape of a monolayer, it was observed that there was a high degree of phase change occurring within the aluminium lattice, with increasing crystal grain growth at slower scan rates where more time was given for nucleation and growth. This highlighted that the cerium insertion was deeper than a monolayer, which

will continue to change the surface properties of the electrode as further alloying occurs. The inability to determine the electrochemical surface area prohibits the use of a bulk aluminium macroelectrode as a sensor.

Co-deposition of Ce^{3+} and Al^{3+} showed more alloying behaviour with less of a kinetic barrier, and was found to be affected by the $[CeCl_3]$:$[AlCl_3]$ ratio. The Al^{3+} was added via two methods: addition of a particular mass of $AlCl_3$ powder; and by passing a specific charge during electrochemical dissolution of an aluminium electrode. In Chapter 5, the $AlCl_3$ concentration decrease over time was studied from both methods of addition. Simultaneous measurement of the counter electrode potentials resulted in observation of large quantities of lithium metal produced during electrochemical dissolution, which would then chemically react to regenerate Li^+ and aluminium metal (called a "short circuit" reaction due to the similarity with the same phenomenon in batteries). This "short circuit" reaction was found to be <100% efficient: some lithium metal reacted with remaining water based impurities in the molten salt, thus there was always some Al^{3+} which remained in solution at the end of the "short circuit" reaction. This "short circuit" reaction usually took 10-20 hours to complete, and had 2nd order kinetics. This was attributed to the stability of lithium clusters in LKE, which allowed the reaction to be simplified to a two species reaction rather than a four species reaction as might first be assumed. The concentration change of Al^{3+} was monitored by performing CVs and obtaining the peak potentials and peak currents of the aluminium plating reaction. The peak potential change over time did not follow expected Nernstian behaviour, and so could not be used to estimate concentration. The peak currents decreased over time as expected, however the macroelectrodes used did not have a fixed area and so only the relative concentration change could be obtained. By performing chronoamperometry on a microelectrode (with a well defined area) it was possible to determine the concentration once the "short circuit" reaction had stopped. The Al^{3+} concentration was approximately 2 mM at the completion of the short circuit reaction (10% of the amount added), however the peak current as the same time was 25% of the peak current at the beginning of concentration monitoring. This disparity was caused by the rapid rate of the "short circuit" reaction, which means that the concentration at the end of electrochemical dissolution was always less than the total amount added by the charge passed. The production of lithium metal during electrochemical dissolution is important to be aware of for the industrial scale electrochemical dissolution of nuclear waste, as this "short circuit" reaction would cause the dissolved waste to precipitate out, preventing extraction of the actinides. It may be possible to overcome this issue by surrounding the counter electrode with a frit, and adding oxide/oxygen to convert the highly reactive lithium metal to lithium oxide and precipitate out.

Addition of $AlCl_3$ powder showed a much slower rate of loss, on the order of days rather than tens of hours. This loss is thought to be due to volatility of $AlCl_3$ from LKE, since the sublimation point of $AlCl_3$ is

approximately 270 °C below the operating temperature. Due to the sampling method used, not enough data points were collected to accurately determine the kinetics of the loss rate. Unfortunately addition of $AlCl_3$ powder also appeared to introduce some impurities, possibly in the form of metal chlorides. These did not initially produce observable reactions, however repeat voltammetry showed reactions growing in positive of the cerium-aluminium system, thought to be due to aluminium alloying with the metals which had gradually been electrodeposited on the electrode surface. These reactions then interfere with the study of the cerium-aluminium system. These unknown metal deposits could be removed by repeating the cleaning procedure (CVs over the entire solvent window while sparging with argon gas), allowing the cerium-aluminium to be studied without interference for a time. Since the Al^{3+} concentration change from volatilisation was far less rapid than that from the "short circuit reaction", addition of $AlCl_3$ powder allowed co-deposition to be studied at a $[CeCl_3]$:$[AlCl_3]$ ratio that was fixed within the experimental timeframe.

In Chapter 6 the co-deposition of Ce^{3+} and Al^{3+} was studied in more detail by studying a changing $[CeCl_3]$:$[AlCl_3]$ ratio by addition of Al^{3+} by electrochemical dissolution, and at two fixed $[CeCl_3]$:$[AlCl_3]$ ratios by addition of $AlCl_3$ powder. As the $[CeCl_3]$:$[AlCl_3]$ ratio increased due to the "short circuit" reaction, the reduction peak current for cerium alloying remained constant indicating that the alloying was controlled by the diffusion of Ce^{3+}. A second aluminium stripping peak was observed, that was attributed to aluminium that remained after cerium-aluminium alloy oxidation, was found to to be less stable that bulk (non alloyed) aluminium. This was attributed to the roughened nature of the de-alloying aluminium, the proportion of which increased with the $[CeCl_3]$:$[AlCl_3]$ ratio. Convolution of the co-deposition current did not result in a steady state current for alloying, but instead the convolved current increased negative of the peak potential. As with alloying on the bulk aluminium electrode, this suggested that electrodeposition of a cerium-aluminium alloy resulted in a significant surface area increase that did not occur when plating only one metal. m values obtained at the peak potential smoothly increased over time (up to 1.5 over the timeframe studied), as the $[CeCl_3]$:$[AlCl_3]$ ratio increased. Charge analysis of the reductive and oxidative scans also showed that the ratio of cerium to aluminium (Ce:Al) in the alloy increased (up to 2.0 over the timeframe studied) with the increasing $[CeCl_3]$:$[AlCl_3]$ ratio. While the alloying reaction was found to be mass transport limited at the peak potential, the fluxes of Ce^{3+} and Al^{3+}, and so m values, varied with time during the course of the CVs on macroelectrodes due to convection and a changing surface area.

The fixed $[CeCl_3]$:$[AlCl_3]$ ratios showed two regimes: at a low $[CeCl_3]$:$[AlCl_3]$ ratio and at a high $[CeCl_3]$:$[AlCl_3]$ ratio. At the low $[CeCl_3]$:$[AlCl_3]$ ratio, two alloying reactions were observed, as well as lithium-aluminium alloying at more negative potentials. Charge analysis showed the Ce:Al ratio was great enough for the formation of three Ce_xAl_y intermetallics, despite only observing two reactions. At the high $[CeCl_3]$:$[AlCl_3]$

ratio five alloying reactions were observed, as well as pure cerium plating instead of lithium-aluminium alloying. Charge analysis of the oxidation peaks confirmed that these correspond to the five crystalline Ce_xAl_y phases in the binary phase diagram.

From all the macroelectrode co-deposition studies, it appeared that an amorphous cerium-aluminium alloy (also known in the literature as a metallic glass) was formed electrochemically, which had a variable Ce:Al ratio and m value, rather than only specific values as would be expected from crystalline phase formation (as seen for the cerium-bismuth alloying system in other work). The electrochemical formation of this metastable metallic glass from mixing two solids appears to be novel; such metallic glasses are normally produced in the literature by rapid cooling of liquid alloys at specific compositions. In previous studies of cerium-aluminium co-deposition in literature the observed alloying peaks have only ever been attributed to specific crystalline phases by the use of ex-situ XRD. This work shows the formation of the cerium-aluminium amorphous phase under non-equilibrium conditions. By increasing the Ce:Al ratio in the alloy significantly, and plating cerium, the conversion from amorphous to crystalline phases was promoted, which resulted in the greater number of observed peaks, as phase change between crystalline phases (without an amorphous phase "buffer") required the reduction and oxidation of cerium at different potentials. While a lot was learned about the limiting factors of formation of the different alloy phases, the electrochemical response on macroelectrodes could not be used to accurately calculate the Ce^{3+} concentration, which is required for a sensor.

Chapter 7 studied alloying behaviour by co-deposition and insertion on microelectrodes. Co-deposition on tungsten microelectrodes was found to result in steady state alloying current that was scan rate independent, as expected for microelectrodes. This made analysis of co-deposition currents much simpler to perform than on macroelectrodes, and meant that the alloying was diffusion limited by Ce^{3+} on the microelectrodes. There were two aluminium stripping peaks, as there were for macroelectrode co-deposition, resulting from a combination of bulk (non alloyed) aluminium and roughened (alloyed) aluminium. From the amount of each form of aluminium present, it was found that the degree of mixing of the co-deposited cerium-aluminium phase and the pre-deposited bulk aluminium phase was negligible, which is consistent with a large kinetic barrier for cerium insertion. The ratio of Ce:Al obtained from charge analysis (both reductive and oxidative), as well as the m value for co-deposition, agreed with the expected ratio of the flux of each species to the electrode, which happened to be the same value as required for the most cerium rich intermetallic Ce_3Al. Only one cerium-aluminium alloying reaction was observed, with lithium-aluminium alloying occurring at more negative potentials. This implied on the microelectrodes the amorphous phase did not nucleate into crystalline phases, and that co-deposition did not have the same kinetic barrier as on macroelectrodes, thus both species were diffusion limited and were deposited at their maximum rate. Due to this behaviour on

microelectrodes, the Ce^{3+} concentration was accurately calculated from the reduction co-deposition current, which is ideal for on-line monitoring.

Co-deposition on an industrial scale pyroprocessing system would not be practical, as it requires the addition of Al^{3+} to an already highly complex mixture, and so the final sensor design would be a thin film aluminium microelectrode. Thin film microelectrodes were microfabricated in-house by deposition of 200 nm of aluminium onto existing in-house microfabricated tungsten microelectrodes. Insertion of cerium into thin film aluminium microelectrodes was hampered by the formation of a highly stable aluminium oxide layer. This oxide layer was electrically conductive, but not conductive to Ce^{3+} and so prevented the alloying of cerium with the pure aluminium layer underneath. This oxide layer was conductive to Li^{+}, allowing the formation of lithium-aluminium alloy which caused volume expansion, resulting in mechanical damage to the oxide layer. This process allowed cerium-aluminium alloying to occur, although the surface area of the exposed aluminium was far less than the geometric area of the microelectrode, preventing accurate calculations of the Ce^{3+} concentration. Further lithium-aluminium alloying did lead to some improvement of the cerium-aluminium alloying response (larger currents, more well defined limiting reduction currents and oxidation peaks), however this eventually resulted in irreversible damage and total loss of the aluminium. In addition, the thin (200 nm) aluminium layer spontaneously disappeared within three hours when immersed in LKE. This could be prevented by the application of a reducing potential, indicating that the loss of aluminium was chemical rather than mechanical. The chemical oxidant was found not to be from water based impurities, as aluminium was still lost from a salt saturated with Al_2O_3 (the expected product of an aluminium reaction with water based impurities). Unfortunately applying a reducing potential to prevent aluminium loss also prevented the loss of aluminium oxide, preventing the selective removal of the oxide layer.

It has been shown that the well known advantages of microelectrodes under ambient conditions also extend to these molten salt conditions, and that these advantages significantly improve the electrochemical alloying response of co-deposition, making it easier to analyse and therefore determine concentrations of species in solution, which is essential for on-line monitoring in pyroprocessing. The gained understanding of electrochemically induced alloying in macro- and microelectrodes will be beneficial for informing the industrial scale extraction process. In the short-term it would be of benefit to develop aluminium microelectrodes that do not form an oxide layer (sacrificial metal in microfabrication/plating aluminium electrochemically in an inert atmosphere), to determine if the insertion type alloying reaction can be used for on-line monitoring. In addition it may be useful to co-deposit cerium and aluminium on a microelectrode with the cerium in greater excess to determine if the reaction ever becomes limited by Al^{3+} and if other crystal phase formation can be observed under these conditions. It would be beneficial to repeat these experiments with plutonium

(in facilities at the National Nuclear Laboratory) to show the applicability of this work to the real alloying system of interest. Performing experiments with more redox species (multiple lanthanides and actinides) is also critical for understanding the competition of alloy formation, and if concentrations for each redox species can be still be extracted in a more complex and realistic system. To better understand the formation of crystal phases, other analytical techniques may be of benefit, e.g. x-ray and/or neutron diffraction, if they could be performed in-situ during electrochemistry to understand phase changes and phase formation on short timescales (unlike ex-situ techniques which would require hours for sample cooling and transferal).

In addition to pyroprocessing, the work in this thesis may have applications in others sectors. For example molten salts are also used for the production of aluminium, and formation of carbon nanostructures. Lithium-aluminium alloying behaviour was also studied which may provide for an alternative route to the industrial production of lithium-aluminium alloys which are very important as a low density, high strength material for aeronautical, and other, applications. Electrochemical alloy formation in molten salts may be of use for many other industries, where the combination of potential and high temperature may allow for finer control over the composition and distribution of alloy within a material. Of particular note is the ability to form metallic glass electrochemically, which are advantageous for many applications due to their amorphous, rather than crystalline, structure. Electrochemical formation (insertion or co-deposition) of metallic glasses may provide a route to form a variety of these glasses in the solid state, rather than rapid cooling of liquid alloys which is the predominant way such glasses are formed in the literature.

Chapter 9

Bibliography

[1] S. Bertozzi, G. Carvalho, P. Dechamps, V. Gaspar, M. Larch, and M. Sochacki, "Bepa Monthly Brief," *Bepa Monthly Brief*, no. 21, pp. 0–32, 2008.

[2] R. E. H. Sims, H.-H. Rogner, and K. Gregory, "Carbon emission and mitigation cost comparisons between fossil fuel, nuclear and renewable energy resources for electricity generation," *Energy Policy*, vol. 31, pp. 1315–1326, 2003.

[3] A. Adamantiades and I. Kessides, "Nuclear power for sustainable development: Current status and future prospects," *Energy Policy*, vol. 37, no. 12, pp. 5149–5166, 2009.

[4] F. L. Toth and H.-H. Rogner, "Oil and nuclear power: Past, present, and future," *Energy Economics*, vol. 28, no. 1, pp. 1–25, 2006.

[5] L. Mez, "Nuclear energy - Any solution for sustainability and climate protection?," *Energy Policy*, vol. 48, pp. 56–63, 2012.

[6] J. Emsley, *Nature's Building Blocks*. OUP Oxford, 2011.

[7] World Nuclear Association, "Physics of Uranium and Nuclear Energy," 2016.

[8] J. P. Elliott, *A Study of Alloying in LiCl-KCl Eutectic: Development of Liquid Thin Film Bismuth Macro- and Microelectrodes*. Ph.d., The University of Edinburgh, 2017.

[9] GEN IV International Forum, "GIF Annual Report 2016," 2016.

[10] World Nuclear Association, "Fast Neutron Reactors," 2017.

[11] World Nuclear Association, "Processing of Used Nuclear Fuel," 2017.

[12] IAEA, "Fast Reactors and Related Fuel Cycles: Challenges and Opportunities," tech. rep., International Atomic Energy Agency, 2009.

[13] IAEA, "Assessment of Nuclear Energy Systems Based on a Closed Nuclear Fuel Cycle with Fast Reactors," tech. rep., International Atomic Energy Agency, 2010.

[14] E. S. Beckjord, "The Future of Nuclear Power - An Interdisciplinary MIT Study," tech. rep., Massachusetts Institute of technology, 2003.

[15] IAEA, "Status of Developments in the Back End of the Fast Reactor Fuel Cycle," tech. rep., International Atomic Energy Agency, 2011.

[16] G. Uchiyama, T. Asakura, S. Hotoku, H. Mineo, K. Kamei, M. Watanabe, and S. Fujine, "Solvent extraction behavior of minor nuclides in nuclear fuel reprocessing process," *Journal of Radioanalytical and Nuclear Chemistry*, vol. 246, no. 3, pp. 683–688, 2000.

[17] J. E. Birkett, M. J. Carrott, O. D. Fox, C. J. Jones, C. J. Maher, C. V. Roube, R. J. Taylor, and D. A. Woodhead, "Controlling neptunium and plutonium within single cycle solvent extraction flowsheets for advanced fuel cycles," *Journal of Nuclear Science and Technology*, vol. 44, no. 3, pp. 337–343, 2007.

[18] R. J. Taylor, C. R. Gregson, M. J. Carrott, C. Mason, and M. J. Sarsfield, "Progress towards the Full Recovery of Neptunium in an Advanced PUREX Process," *Solvent Extraction and Ion Exchange*, vol. 31, no. 4, pp. 442–462, 2013.

[19] S. W. Kwon, D. H. Ahn, E. H. Kim, and H. G. Ahn, "A study on the recovery of actinide elements from molten LiCl-KCl eutectic salt by an electrochemical separation," *Journal of Industrial and Engineering Chemistry*, vol. 15, no. 1, pp. 86–91, 2009.

[20] M. Iizuka, T. Koyama, N. Kondo, R. Fujita, and H. Tanaka, "Actinides recovery from molten salt/liquid metal system by electrochemical methods," *Journal of Nuclear Materials*, vol. 247, pp. 183–190, 1997.

[21] J. Serp, M. Allibert, A. L. Terrier, R. Malmbeck, M. Ougier, J. Rebizant, and J.-P. Glatz, "Electroseparation of Actinides from Lanthanides on Solid Aluminum Electrode in LiCl-KCl Eutectic Melts," *Journal of Electrochemical Society*, vol. 152, no. 3, pp. C167–C172, 2005.

[22] J. Zhang, "Electrochemistry of actinides and fission products in molten salts - Data review," *Journal of Nuclear Materials*, vol. 447, no. 1-3, pp. 271–284, 2014.

[23] J. Zhang, E. A. Lahti, and W. Zhou, "Thermodynamic properties of actinides and rare earth fission products in liquid cadmium," *Journal of Radioanalytical and Nuclear Chemistry*, pp. 1637–1648, 2015.

[24] J. Zhang, E. A. Lahti, and E. Wu, "Thermodynamic properties of actinides and fission products in liquid bismuth," *Progress in Nuclear Energy*, vol. 81, pp. 67–77, 2015.

[25] L. Cassayre, R. Malmbeck, P. Masset, J. Rebizant, J. Serp, P. Soucek, and J. P. Glatz, "Investigation of electrorefining of metallic alloy fuel onto solid Al cathodes," *Journal of Nuclear Materials*, vol. 360, no. 1 SPEC. ISS., pp. 49–57, 2007.

[26] L. Cassayre, C. Caravaca, R. Jardin, R. Malmbeck, P. Masset, E. Mendes, J. Serp, P. Soucek, and J. P. Glatz, "On the formation of U-Al alloys in the molten LiCl-KCl eutectic," *Journal of Nuclear Materials*, vol. 378, no. 1, pp. 79–85, 2008.

[27] P. Souček, R. Malmbeck, E. Mendes, C. Nourry, D. Sedmidubský, and J. P. Glatz, "Study of thermodynamic properties of Np-Al alloys in molten LiCl-KCl eutectic," *Journal of Nuclear Materials*, vol. 394, no. 1, pp. 26–33, 2009.

[28] Y. Castrillejo, R. Bermejo, A. M. Martínez, E. Barrado, and P. Díaz Arocas, "Application of electrochemical techniques in pyrochemical processes - Electrochemical behaviour of rare earths at W, Cd, Bi and Al electrodes," *Journal of Nuclear Materials*, vol. 360, pp. 32–42, 2007.

[29] D.-B. Ji, Y.-D. Yan, M.-L. Zhang, X. Li, X.-Y. Jing, W. Han, Y. Xue, and Z.-J. Zhang, "Separation of lanthanum from samarium on solid aluminum electrode in LiCl-KCl eutectic melts," *Journal of Radioanalytical and Nuclear Chemistry*, vol. 304, no. 3, pp. 1123–1132, 2015.

[30] Y. Castrillejo, M. R. Bermejo, P. Díaz Arocas, A. M. Martínez, and E. Barrado, "Electrochemical behaviour of praseodymium (III) in molten chlorides," *Journal of Electroanalytical Chemistry*, vol. 575, no. 1, pp. 61–74, 2005.

[31] Y. Castrillejo, P. Fernández, J. Medina, P. Hernández, and E. Barrado, "Electrochemical extraction of samarium from molten chlorides in pyrochemical processes," *Electrochimica Acta*, vol. 56, no. 24, pp. 8638–8644, 2011.

[32] S. E. Bae, Y. J. Park, S. K. Min, Y. H. Cho, and K. Song, "Aluminum assisted electrodeposition of europium in LiCl-KCl molten salt," *Electrochimica Acta*, vol. 55, no. 8, pp. 3022–3025, 2010.

[33] M. R. Bermejo, J. Gómez, J. Medina, A. M. Martínez, and Y. Castrillejo, "The electrochemistry of gadolinium in the eutectic LiCl-KCl on W and Al electrodes," *Journal of Electroanalytical Chemistry*, vol. 588, no. 2, p. 253 266, 2006.

[34] Y. Castrillejo, M. R. Bermejo, A. I. Barrado, and A. M. Martínez, "Electrochemical behaviour of erbium in the eutectic LiCl-KCl at W and Al electrodes," *Electrochimica Acta*, vol. 51, pp. 1941–1951, 2006.

[35] M. Zhang, H. Wang, W. Han, M. Zhang, Y. Li, Y. Wang, Y. Xue, F. Ma, and X. Zhang, "Electrochemical extraction of cerium and formation of Al-Ce alloy from CeO2 assisted by AlCl3 in LiCl-KCl melts," *Science China Chemistry*, vol. 57, no. 11, pp. 1477–1482, 2014.

[36] M. Zhang, Y. Li, W. Han, M. Zhang, Y. Xue, Y. Wang, Gao, and Yang, "Underpotential Deposition of Al-Ce Alloys at an Al Electrode from LiCl-KCl-CeCl3 Melts," *Rare Metal Materials and Engineering*, vol. 45, no. 8, pp. 1956–1960, 2016.

[37] Y.-L. Liu, K. Liu, L.-Y. Yuan, Z.-F. Chai, and W.-Q. Shi, "Estimation of the composition of intermetallic compounds in LiCl-KCl molten salt by cyclic voltammetry," *Faraday Discussions*, vol. 190, pp. 387–398, 2016.

[38] L. Wang, Y.-L. Liu, K. Liu, S.-L. Tang, L.-Y. Yuan, L.-L. Su, Z.-F. Chai, and W.-Q. Shi, "Electrochemical extraction of cerium from CeO2 assisted by AlCl3 in molten LiCl-KCl," *Electrochimica Acta*, vol. 147, pp. 385–391, 2014.

[39] M. D. Adams, A. D. Wenz, and R. K. Steunenberg, "Observation of a uranium(V) species in molten chloride salt solutions," *The Journal of Physical Chemistry*, vol. 67, pp. 1939–1941, 1969.

[40] B. Y. Kim and J.-I. Yun, "Reduction of Trivalent Europium in Molten LiCl-KCl Eutectic Observed by In-Situ Laser Spectroscopic Techniques," *ECS Electrochemistry Letters*, vol. 2, no. 11, pp. H54–H57, 2013.

[41] S. Y. Oh, J. Y. Kim, S. E. Bae, Y. H. Cho, J. W. Yeon, and K. Song, "Spectroscopic analysis of trivalent cerium and holmium ions in LiCl-KCl eutectic melt at high temperature," *Journal of Luminescence*, vol. 134, pp. 706–709, 2013.

[42] C. A. Schroll, S. Chatterjee, T. G. Levitskaia, W. R. Heineman, and S. A. Bryan, "Electrochemistry and spectroelectrochemistry of europium(III) chloride in 3LiCl-2KCl from 643 to 1123 K," *Analytical Chemistry*, vol. 85, no. 20, pp. 9924–9931, 2013.

[43] G. P. Smith, D. W. James, and C. R. Boston, "Optical Spectra of Tl+, Pb2+, and Bi3+ in the Molten Lithium Chloride-Potassium Chloride Eutectic," *The Journal of Chemical Physics*, vol. 42, pp. 2249–2250, 1965.

[44] V. A. Volkovich, A. I. Bhatt, I. May, T. R. Griffiths, and R. C. Thied, "A Spectroscopic Study of Uranium Species Formed in Chloride Melts," *Journal of Nuclear Science and Technology*, vol. Supplement, pp. 595–598, 2002.

[45] P. Pint, "The Behavior of an Oscillating Solid Microelectrode for Voltammetric Studies in Aqueous and Molten Salt Solutions," *Journal of The Electrochemical Society*, vol. 123, no. 7, p. 1042, 1976.

[46] R. T. Carlin, "Deposition Studies of Lithium and Bismuth at Tungsten Microelectrodes in LiCl:KCl Eutectic," *Journal of The Electrochemical Society*, vol. 136, no. 5, p. 1249, 1989.

[47] P. Atkins and J. de Paula, *Physical Chemistry*. Oxford University Press, 8th ed., 2006.

[48] A. J. Bard and L. R. Faulkner, *Electrochemical Methods: Fundamentals and Applications*. John Wiley & Sons, Inc., 2nd ed., 2001.

[49] C. G. Zoski, *Handbook of Electrochemistry*. Elsevier, 1st ed., 2007.

[50] J. Heinze, "Ultramicroelectrodes in Electrochemistry," *Angewandte Chemie International Edition*, vol. 32, no. 9, pp. 1268–1288, 1993.

[51] K. Stulík, C. Amatore, K. Holub, V. Marecek, and W. Kutner, "Microelectrodes. Definitions, characterization, and applications (Technical report)," *Pure and Applied Chemistry*, vol. 72, no. 8, pp. 1483–92, 2000.

[52] A. M. Bond, "Past, present and future contributions of microelectrodes to analytical studies employing voltammetric detection. A review," *The Analyst*, vol. 119, no. 11, p. 1R, 1994.

[53] R. G. Compton and C. E. Banks, *Understanding Voltammetry*. Imperial College Press, 2nd ed., 2014.

[54] X. Liu, C. Giordano, and M. Antonietti, "A facile molten-salt route to graphene synthesis," *Small*, vol. 10, no. 1, pp. 193–200, 2014.

[55] J. Wang, B. Ding, X. Hao, Y. Xu, Y. Wang, L. Shen, H. Dou, and X. Zhang, "A modified molten-salt method to prepare graphene electrode with high capacitance and low self-discharge rate," *Carbon*, vol. 102, pp. 255–261, 2016.

[56] A. R. Kamali, C. Schwandt, and D. J. Fray, "Effect of the graphite electrode material on the characteristics of molten salt electrolytically produced carbon nanomaterials," *Materials Characterization*, vol. 62, no. 10, pp. 987–994, 2011.

[57] J. B. Bai, A. L. Hamon, A. Marraud, B. Jouffrey, and V. Zymla, "Synthesis of SWNTs and MWNTs by a molten salt (NcCl) method," *Chemical Physics Letters*, vol. 365, no. 1-2, pp. 184–188, 2002.

[58] J. Y. Kim, S. E. Bae, D. H. Kim, Y. S. Choi, J. W. Yeon, and K. Song, "High-temperature viscosity measurement of LiCl-KCl molten salts comprising actinides and lanthanides," *Bulletin of the Korean Chemical Society*, vol. 33, no. 11, pp. 3871–3874, 2012.

[59] E. V. Artsdalen and I. Yaffe, "Electrical conductance and density of molten salt systems: KCl-LiCl, KCl-NaCl and KCl-KI," *The Journal of Physical Chemistry*, vol. 59, no. 1953, pp. 118–127, 1955.

[60] CRCT, "FactSage FT salt database:List of systems and phases.," 2017.

[61] G. Bourgès, D. Lambertin, S. Rochefort, S. Delpech, and G. Picard, "Electrochemical studies on plutonium in molten salts," *Journal of Alloys and Compounds*, vol. 444-445, pp. 404–409, 2007.

[62] Y. B. Kang, A. D. Pelton, P. Chartrand, and F. C. D, "Critical evaluation and thermodynamic optimization of the Al-Ce, Al-Y, Al-Sc and Mg-Sc binary systems," *CALPHAD: Comput. Coupling Phase Diagrams Thermochem.*, vol. 32, pp. 413–422, 2008.

[63] M. E. Kassner and D. E. Peterson, "Al-Pu (Aluminium-Plutonium)," *Binary Alloy Phase Diagrams, II Ed., Ed. T.B. Massalski*, vol. 1, pp. 197–200, 1990.

[64] E. O. Blair, *The Optimisation and Characterisation of Durable Microelectrodes for Electroanalysis in Molten Salt.* Ph.d., The University of Edinburgh, 2016.

[65] M. R. Bermejo, F. de la Rosa, E. Barrado, and Y. Castrillejo, "Cathodic behaviour of europium (III) on glassy carbon, electrochemical formation of Al4Eu, and oxoacidity reactions in the eutectic LiCl-KCl," *Journal of Electroanalytical Chemistry*, vol. 603, no. 1, pp. 81–95, 2007.

[66] M. R. Bermejo, E. Barrado, A. M. Martínez, and Y. Castrillejo, "Electrodeposition of Lu on W and Al electrodes: Electrochemical formation of Lu-Al alloys and oxoacidity reactions of Lu(III) in the eutectic LiCl-KCl," *Journal of Electroanalytical Chemistry*, vol. 617, no. 1, pp. 85–100, 2008.

[67] K. Liu, Y.-L. Liu, L.-Y. Yuan, and X.-L. Zhao, "Electroextraction of gadolinium from Gd2O3 in LiCl-KCl-AlCl3 molten salts," *Electrochimica Acta*, vol. 109, pp. 732–740, 2013.

[68] Y. Sun, M. Zhang, W. Han, Y. Yan, Y. Yang, and Y. Sun, "Electrochemical behaviour and codeposition of Al-Li-Er alloys in," *Journal of Rare Earths*, vol. 31, no. 2, pp. 192–197, 2013.

[69] Y. Castrillejo, M. R. Bermejo, A. I. Barrado, R. Pardo, E. Barrado, and A. M. Martínez, "Electrochemical behaviour of dysprosium in the eutectic LiCl-KCl at W and Al electrodes," *Electrochimica Acta*, vol. 50, no. 10, pp. 2047–2057, 2005.

[70] L.-L. Su, K. Liu, Y.-L. Liu, L. Wang, L.-Y. Yuan, L. Wang, Z.-J. Li, X.-L. Zhao, Z.-F. Chai, and W.-Q. Shi, "Electrochemical behaviors of Dy(III) and its co-reduction with Al(III) in molten LiCl-KCl salts," *Electrochimica Acta*, vol. 147, pp. 87–95, 2014.

[71] G. De Cordoba, A. Laplace, O. Conocar, J. Lacquement, and C. Caravaca, "Determination of the activity coefficient of neodymium in liquid aluminium by potentiometric methods," *Electrochimica Acta*, vol. 54, no. 2, pp. 280–288, 2008.

[72] Y.-L. Liu, L.-Y. Yuan, G.-A. Ye, Kui-Liu, L. Zhu, M.-L. Zhang, Z.-F. Chai, and W.-Q. Shi, "Co-reduction behaviors of lanthanum and aluminium ions in LiCl-KCl eutectic," *Electrochimica Acta*, vol. 147, pp. 104–113, 2014.

[73] D.-B. Ji, Y.-D. Yan, M.-L. Zhang, P. Wang, X. Yang, X.-Y. Jing, Y. Xue, W. Han, and T. Hartmann, "Study on Electrochemical Behavior of La(III) and Preparation of Al-La Intermetallic Compound Whiskers in Chloride Melt," *Journal of The Electrochemical Society*, vol. 163, no. 2, pp. D1–D8, 2016.

[74] H. Tang, Y.-d. Yan, M.-l. Zhang, X. Li, Y. Huang, Y.-l. Xu, and Y. Xue, "Electrochimica Acta AlCl3 aided extraction of praseodymium from Pr6O11 in LiCl-KCl eutectic melts," *Electrochimica Acta*, vol. 88, pp. 457–462, 2013.

[75] Y. Xue, Q. Wang, Y.-d. Yan, L. Chen, M.-l. Zhang, and J. Zhang, "Asian Nuclear Prospects 2012 Cathodic behaviour of samarium(III) in LiCl-KCl melts on molybdenum and aluminium electrodes," *Energy Procedia*, vol. 39, pp. 474–479, 2013.

[76] Y. D. Yan, H. Tang, M. L. Zhang, Y. Xue, W. Han, D. X. Cao, and Z. J. Zhang, "Electrochimica Acta Extraction of europium and electrodeposition of Al-Li-Eu alloy from Eu2O3 assisted by AlCl3 in LiCl-KCl melt," *Electrochimica Acta*, vol. 59, pp. 531–537, 2012.

[77] Y.-d. Yan, Y.-l. Xu, M.-l. Zhang, Y. Xue, W. Han, Y. Huang, and Q. Chen, "Electrochemical extraction of neodymium by co-reduction with aluminum in LiCl-KCl molten salt," *Journal of Nuclear Materials*, vol. 433, no. 1-3, pp. 152–159, 2013.

[78] Y. Yongde, H. Ying, X. Yun, Z. Milin, H. Wei, and Z. Zhijian, "Direct Electrochemical Formation of Different Phases Al-Y Alloys by Codeposition in LiCl-KCl Melts," *Rare Metal Materials and Engineering*, vol. 45, no. 2, pp. 272–276, 2016.

[79] G. De Córdoba, A. Laplace, O. Conocar, and J. Lacquement, "Determination of the activity coefficient of Am in liquid Al by electrochemical methods," *Journal of Nuclear Materials*, vol. 393, no. 3, pp. 459–464, 2009.

[80] K. Liu, L.-Y. Yuan, Y.-L. Liu, X.-L. Zhao, H. He, and G.-a. Ye, "Electrochemical reactions of the Th4+/Th couple on the tungsten, aluminum and bismuth electrodes in chloride molten salt," *Electrochimica Acta*, vol. 130, pp. 650–659, 2014.

[81] Y.-L. Liu, Y.-D. Yan, W. Han, M.-L. Zhang, L.-Y. Yuan, R.-S. Lin, G.-A. Ye, H. He, Z.-F. Chai, and W.-Q. Shi, "Electrochemical separation of Th from ThO2 and Eu2O3 assisted by AlCl3 in molten LiCl-KCl," *Electrochimica Acta*, vol. 114, pp. 180–188, 2013.

[82] Y. Castrillejo, P. Fernández, M. R. Bermejo, E. Barrado, and A. M. Martínez, "Electrochemistry of thulium on inert electrodes and electrochemical formation of a Tm-Al alloy from molten chlorides," *Electrochimica Acta*, vol. 54, no. 26, pp. 6212–6222, 2009.

[83] X. Li, Y.-d. Yan, M.-l. Zhang, H. Tang, D.-b. Ji, W. Han, Y. Xue, and Z.-j. Zhang, "Electrochemical formation of Al-Tm intermetallics in eutectic LiCl-KCl melt containing Tm and Al ions," *Journal of Nuclear Materials*, vol. 452, no. 1-3, pp. 197–204, 2014.

[84] Y. Castrillejo, A. Vega, M. Vega, P. Hernández, J. Rodriguez, and E. Barrado, "Electrochemical formation of Sc-Al intermetallic compounds in the eutectic LiCl-KCl. Determination of thermodynamic properties.," *Electrochimica Acta*, vol. 118, pp. 58–66, 2014.

[85] M. Mohamedi, N. Kawaguchi, Y. Sato, and T. Yamamura, "Electrochemical study of the mechanism of formation of the surface alloy of aluminum-niobium in LiCl-KCl eutectic melt," *Journal of Alloys and Compounds*, vol. 287, no. 1-2, pp. 91–97, 1999.

[86] B. Hallstedt and O. Kim, "Thermodynamic assessment of the Al-Li system," *International Journal of Materials Research*, vol. 98, no. 10, pp. 961–969, 2007.

[87] D. K. Corrigan, J. P. Elliott, E. O. Blair, S. J. Reeves, I. Schmuser, A. J. Walton, and A. R. Mount, "Advances in electroanalysis, sensing and monitoring in molten salts," *Faraday Discussions*, vol. 190, pp. 351–366, 2016.

[88] N. Brockie, *Applications of Liquid Cathode Electrochemistry Towards the Nuclear Industry*. Ph.d., The University of Edinburgh, 2011.

[89] R. D. Janeiro and K. Polytechnic, "II . A potentiometric study of alumina solubility and the influence of complexing by fluoride ions in LiCl-KCl," *Journal of Applied Electrochemistry*, vol. 8, pp. 273–276, 1978.

[90] S. U. N. Yi, Z. Mi-lin, H. A. N. Wei, L. I. Mei, and Y. Yu-sheng, "Electrochemical Formation of Al-Li Alloys by Codeposition of Al and Li from LiCl-KCl-AlF3 Melts at 853 K," *Chemical Journal of Chinese Universities*, vol. 29, no. 2, pp. 324–328, 2013.

[91] O. Shirai, M. Iizuka, T. Iwai, and Y. Arai, "Electrode reaction of Pu3+/Pu couple in LiCl-KCl eutectic melts: comparison of the electrode reaction at the surface of liquid Bi with that at a solid Mo electrode.," *Analytical sciences : the international journal of the Japan Society for Analytical Chemistry*, vol. 17, no. 1, pp. 51–57, 2001.

[92] D. K. Corrigan, E. O. Blair, J. G. Terry, A. J. Walton, and A. R. Mount, "Enhanced electroanalysis in lithium potassium eutectic (LKE) using microfabricated square microelectrodes," *Analytical Chemistry*, vol. 86, no. 22, pp. 11342–11348, 2014.

[93] Y. Yan, X. Li, M. Zhang, H. Tang, W. Han, Y. Xue, and Z. Zhang, "The Solubility of Rare Earth with Variable Valent and Electrochemical Behavior in LiCl-KCl-AlCl3 Melts," *Energy Procedia*, vol. 39, pp. 408–414, 2013.

[94] D. Sedmidubský, R. J. M. Konings, and P. Souček, "Ab-initio calculations and phase diagram assessments of An-Al systems (An = U, Np, Pu)," *Journal of Nuclear Materials*, vol. 397, no. 1-3, pp. 1–7, 2010.

[95] D. R. Lide, *CRC Handbook of Chemistry and Physics, Internet Version*. CRC Press, 85th ed., 2003.

[96] Y. Sakamura, T. Inoue, T. Iwai, and H. Moriyama, "Chlorination of UO2, PuO2 and rare earth oxides using ZrCl4 in LiCl-KCl eutectic melt," *Journal of Nuclear Materials*, vol. 340, no. 1, pp. 39–51, 2005.

[97] K. Liu, Y.-L. Liu, L.-Y. Yuan, X.-L. Zhao, and H. He, "Electrochemical formation of erbium-aluminum alloys from erbia in the chloride melts," *Electrochimica Acta*, vol. 116, pp. 434–441, 2014.

[98] A. M. Martinez, Y. Castrillejo, B. Borresen, M. R. Bermejo, and M. Vega, "Chemical and electrochemical behaviour of chromium in molten chlorides," *Journal of Electroanalytical Chemistry*, vol. 493, pp. 1–14, 2000.

[99] Y.-H. Liu, Y.-D. Yan, M.-L. Zhang, J.-N. Zheng, Yang-Zhao, P. Wang, T.-Q. Yin, Y. Xue, X.-Y. Jing, and W. Han, "Electrochemical Synthesis of Sm-Ni Alloy Magnetic Materials by Co-reduction of Sm(III)

and Ni(II) in LiCl-KCl-SmCl3-NiCl2 Melt," *Journal of The Electrochemical Society*, vol. 163, no. 13, pp. D672–D681, 2016.

[100] A. Merwin, W. C. Phillips, M. A. Williamson, J. L. Willit, P. N. Motsegood, and D. Chidambaram, "Presence of Li Clusters in Molten LiCl-Li," *Scientific Reports*, vol. 6, no. October 2015, p. 25435, 2016.

[101] Y. D. Yan, M. L. Zhang, Y. Xue, W. Han, D. X. Cao, and L. Y. He, "Electrochemical study of the codeposition of Mg-Li-Al alloys from LiCl-KCl-MgCl2-AlCl3 melts," *Journal of Applied Electrochemistry*, vol. 39, pp. 455–461, 2009.

[102] M. Shen, B. Li, S. Z. Li, and J. G. Yu, "Electrochemical Removal of AlCl3 from LiCl-KCl Melts," *Metallurgical and Materials Transactions A*, vol. 43A, pp. 1662–1669, 2011.

[103] J. Sang Mun, J.-M. Hur, H. Sun Seok, K. Dae Seung, C. Myoung Soo, C.-S. Seo, J.-S. Yoon, and S.-W. Park, "an Electrochemical Reduction of Uranium Oxide in the Advanced Spent-Fuel Conditioning Process," *Nuclear technology*, vol. 162, no. 2, pp. 184–191, 2010.

[104] S. M. Jeong, S. B. Park, S. S. Hong, C. S. Seo, and S. W. Park, "Electrolytic production of metallic uranium from U3O8 in a 20-kg batch scale reactor," *Journal of Radioanalytical and Nuclear Chemistry*, vol. 268, no. 2, pp. 349–356, 2006.

[105] E. O. Blair, D. K. Corrigan, J. G. Terry, A. R. Mount, and A. J. Walton, "Development and Optimization of Durable Microelectrodes for Quantitative Electroanalysis in Molten Salt," *Journal of Microelectromechanical Systems*, vol. 24, no. 5, pp. 1346–1354, 2015.

[106] E. O. Blair, D. K. Corrigan, H. J. Levene, I. Schmueser, J. G. Terry, S. Smith, A. R. Mount, and A. J. Walton, "Improving the Yield and Lifetime of Microfabricated Sensors for Harsh Environments," *IEEE Transactions on Semiconductor Manufacturing*, vol. 30, no. 3, pp. 192–200, 2017.

[107] A. D. Shamsiddinov, I. N. Gaeniev, V. V. Kinzhibalo, and N. K. Karimov, "Isothermal cross-solutions of the phase diagrams of the systems Al-Li-La and Al-Li-Ce at 823-423 K," *Izv. Vyssh. Uchebn. Zaved., Tsvetn. Metall.*, pp. 86–90, 1991.

[108] W. H. Wang, C. Dong, and C. H. Shek, "Bulk metallic glasses," *Materials Science and Engineering R: Reports*, vol. 44, no. 2-3, pp. 45–90, 2004.

[109] A. Inoue, "Stabilization of metallic supercooled liquid and bulk amorphous alloys," *Acta Materialia*, vol. 48, no. 1, pp. 279–306, 2000.

[110] B. Zhang, R. J. Wang, D. Q. Zhao, M. X. Pan, and W. H. Wang, "Superior glass-forming ability through microalloying in cerium-based alloys," *Physical Review B - Condensed Matter and Materials Physics*, vol. 73, no. 9, pp. 1–4, 2006.

[111] G. Orveillon, O. N. Senkov, J. L. Soubeyroux, B. Chevalier, and S. Gorsse, "Composition selection and glass forming ability of Ce-based amorphous alloys," *Advanced Engineering Materials*, vol. 9, no. 6, pp. 483–486, 2007.

[112] J. L. Provo, "Use of aluminum oxide as a permeation barrier for producing thin films on aluminum substrates," *Journal of Vacuum Science and Technology A*, vol. 34, no. 4, pp. 041503–1 – 041503–7, 2016.

[113] P. C. Snijders, L. P. H. Jeurgens, and W. G. Sloof, "Structure of thin aluminium-oxide films determined from valence band spectra measured using XPS," *Surface Science*, vol. 496, pp. 97–109, 2002.

[114] L. P. H. Jeurgens, W. G. Sloof, F. D. Tichelaar, and E. J. Mittemeijer, "Structure and morphology of aluminium-oxide films formed by thermal oxidation of aluminium," *Thin Solid Films*, vol. 418, pp. 89–101, 2002.

[115] L. P. H. Jeurgens, W. G. Sloof, F. D. Tichelaar, C. G. Borsboom, and E. J. Mittemeijer, "Determination of thickness and composition of aluminium-oxide overlayers on aluminium substrates," *Applied Surface Science*, vol. 144-145, pp. 11–15, 1999.

[116] C. Gong, D. Ruzmetov, A. Pearse, D. Ma, J. N. Munday, G. Rublo, A. A. Talin, and M. S. Leite, "Surface/Interface Effects on High-Performance Thin-Film All-Solid- State Li-Ion Batteries," *Applied Materials and Interfaces*, vol. 7, pp. 26007–26011, 2015.

[117] Y. Liu, N. S. Hudak, D. L. Huber, S. J. Limmer, J. P. Sullivan, and J. Y. Huang, "In Situ Transmission Electron Microscopy Observation of Pulverization of Aluminum Nanowires and Evolution of the Thin Surface Al2O3 Layers during Lithiation-Delithiation Cycles," *Nano Letters*, vol. 11, pp. 4188–4194, 2011.

[118] K. Nishio, T. Yanagishita, M. Yoshida, T. Hayakawa, and H. Masuda, "Enlargement of surface area of Al by electrochemical insertion and deinsertion of Li," *Electrochemistry Communications*, vol. 59, pp. 13–15, 2015.